EXPLORING CONTINUUM COMPUTATIONAL MODELS FOR NEUTRAL GAS FLOW IN THE JET NEUTRALISER

By

Michael Porton

A THESIS SUBMITTED IN PARTIAL FULFILLMENT
OF THE REQUIREMENTS FOR THE DEGREE OF
DOCTOR OF PHILOSOPHY

Cranfield University
School of Engineering
November 2010

Supervisors: Prof D. Drikakis, Dr E. Shapiro & Dr E. Surrey

Exploring continuum computational models for neutral gas flow in the JET neutraliser

Michael Porton

November 2, 2010

Abstract

Effective understanding of gas flow is important to ensure efficient operation of gas neutraliser systems such as those used at the Joint European Torus (JET), which form part of invaluable heating systems for nuclear fusion experiments. Computational fluid dynamics modelling of the neutral gas flow in the JET neutraliser has been undertaken, motivated by the shortfall in neutralisation efficiency and apparent loss of gas target observed in the JET neutraliser system. This has presented a challenging modelling endeavour due to the interaction of beam, background plasma and rarefied neutral gas. Utilising the continuum flow approximation, the Navier-Stokes and Augmented Burnett equations have been implemented and applied in conjunction with second-order slip boundary conditions to form a gas solver accurate within the continuum-transition regime.

Simulations in the presence of the ionic beam and background neutraliser plasma encountered during tokamak heating operations have been achieved via the development of a coupled beam-plasma-gas solver. The gas flow governing equations have been supplemented by a series of source/sink terms for mass/energy that describe the complex web of interactions between the neutraliser constituents.

The developed solver has been validated against experimental data, both in the absence and presence of beam. The design of future gas neutraliser systems has also been considered, with variation of several model and geometry parameters in order to better understand the loss of neutralisation efficiency and how future systems might be optimised. The neutraliser design for the forthcoming International Thermonuclear Experimental Reactor (ITER) has also been evaluated.

Acknowledgements

I would like to thank the United Kingdom Atomic Energy Authority and Cranfield University for the opportunity to undertake this PhD. At times a fearsome challenge, I am truly grateful to my supervisors Dr Elisabeth Surrey, Prof Dimitris Drikakis and Dr Evgeniy Shapiro for their constant guidance and encouragement.

The culmination of an academic journey, there are many without whom this point could not have been reached. Most notable is the contribution of Derwyn Parry, a friend and mentor to whom I am indebted for first inspiring my love of mathematics.

Finally, I wish to thank my family. They have always been immensely supportive and are key to all that I have been able to achieve. The last three years have proved truly testing and I thank them, both in the UK and US, for their unwavering faith in me. None of this would have been possible without them.

Michael Porton

Contents

Abstract i

Acknowledgements iii

Contents v

List of Figures ix

List of Tables xv

Nomenclature xvii

1 Introduction 1
- 1.1 Neutraliser Physics . . . 5
- 1.2 Modelling of Rarefied Gas Flow . . . 6
- 1.3 Wall Interaction Effects . . . 8
- 1.4 Scope and Objectives . . . 10
- 1.5 Thesis Structure . . . 11

2 The Problem in Detail 13
- 2.1 Neutral Beam Heating (NBH) . . . 13
- 2.2 Gas Neutralisers . . . 17
- 2.3 Evolution of JET Neutraliser Understanding . . . 19
- 2.4 Modelling of the Neutraliser Constituents . . . 24
  - 2.4.1 Beam Modelling . . . 24
  - 2.4.2 Plasma Modelling . . . 25
  - 2.4.3 Gas Modelling in the Continuum-Transition Regime . . . 25
  - 2.4.4 Coupling Modelling Systems . . . 27
- 2.5 Wall Interaction . . . 28
- 2.6 Summary . . . 30

3 Modelling Approach 31
- 3.1 Outline of the Governing Equations . . . 31
- 3.2 Neutraliser Physics Summary & Interaction Model . . . 35

3.2.1 Beam . . . 38
3.2.2 Energy to the Background Gas . . . 45
3.2.3 Momentum Transfer Cross-Section . . . 56
3.2.4 Plasma . . . 58
3.2.5 Gas Sources & Sinks . . . 62
3.3 Finalised Governing Equations . . . 67
3.4 Numerical Framework . . . 70
3.4.1 Finite Volume Method . . . 71
3.4.2 Generalised Curvilinear Co-ordinates . . . 71
3.4.3 Spatial discretisation . . . 72
3.4.4 Time Integration . . . 75
3.4.5 Boundary Conditions . . . 76
3.4.6 Neutraliser Source/Sink & Pressure Evaluation . . . 79
3.4.7 Domain Decomposition . . . 80
3.5 Summary . . . 80

4 Development of Continuum-Transition Solver 85
4.1 1D Hypersonic Shock . . . 86
4.1.1 Boundary Conditions and Flow Parameters . . . 86
4.1.2 Convergence Study & Comparison with Published Works . . . 87
4.1.3 Instability of the Conventional Burnett Equations . . . 89
4.1.4 Assessment of Novel Timestep Limits . . . 91
4.2 2D Hypersonic Flow about Blunt Body . . . 93
4.2.1 Boundary Conditions and Flow Parameters . . . 95
4.2.2 Convergence Study & Comparison with Published Works . . . 95
4.2.3 Assessment of Novel Timestep Limits . . . 96
4.3 2D Microchannel . . . 99
4.3.1 Boundary Conditions and Flow Parameters. . . . 99
4.3.2 Analytical Models . . . 101
4.3.3 Results . . . 102
4.4 3D Microchannel . . . 103
4.4.1 Boundary Conditions and Flow Parameters. . . . 104
4.4.2 Analytical Models . . . 104
4.4.3 Results . . . 105
4.5 2D JET Neutraliser . . . 108
4.5.1 Boundary Conditions and Flow Parameters . . . 108
4.5.2 Results . . . 112
4.6 3D JET Neutraliser . . . 118
4.6.1 Boundary Conditions and Flow Parameters . . . 118
4.6.2 Results . . . 118
4.7 Summary . . . 119

5 Application of the Coupled Beam-Plasma-Gas Solver **123**
5.1 2D JET Neutraliser . . . 123
5.1.1 Boundary Conditions and Flow Parameters . . . 126
5.1.2 Grid Development . . . 130
5.1.3 In the Absence of Beam . . . 135
5.1.4 In the Presence of Beam . . . 136
5.2 2D ITER Neutraliser . . . 155
5.2.1 Boundary Conditions and Flow Parameters . . . 157
5.2.2 In the Absence of Beam . . . 159
5.2.3 In the Presence of Beam . . . 160
5.3 3D JET Neutraliser . . . 172
5.3.1 Boundary Conditions and Flow Parameters . . . 174
5.3.2 In the Absence of Beam . . . 176
5.3.3 In the Presence of Beam . . . 177
5.4 JET Neutraliser Optimisation . . . 181
5.5 Summary . . . 182

6 Conclusions and Future Work **193**
6.1 Conclusions . . . 194
6.2 Future Work . . . 196

List of Figures

1.1 Reactants and products of Deuterium-Tritium fusion . . . 2
1.2 The Tokamak reactor concept[?] . . . 3
1.3 Elevation view of a JET neutral injector box . . . 5
1.4 Outline of rarefied flow regimes and modelling techniques . . . 9

2.1 Progression of beam within the JET beamline . . . 15
2.2 Plan view of the JET neutral beam injector . . . 16
2.3 Plan view of the ITER neutral beam injector . . . 17
2.4 JET neutraliser geometry . . . 20
2.5 Longitudinal section of ITER neutraliser geometry[?] . . . 21
2.6 Equilibrium species fractions for initially positive and negative polarity beams . . . 22
2.7 The JET neutraliser in the absence and presence of beam . . . 23
2.8 Outline of development of the Burnett Equations . . . 27

3.1 Summary of gas sources and sinks as described by the interaction model . . . 37
3.2 Outline of the infinitesimal neutraliser slice concept . . . 39
3.3 Optimum perveance versus power for several exemplar JET PINIs . . . 40
3.4 Beam profile sections along the JET neutraliser from the PINI Simulator[?] . . . 46
3.5 Potential energy curves for hydrogen[?] . . . 49
3.6 Dissociation reaction cross-sections for differing projectile electron energies . . . 55
3.7 Published and fitted reflection coefficients for hydrogen on copper[?] . . . 56
3.8 Comparison of momentum transfer cross-sections of *Pamela*[?] and *Phelps*[?] . . . 59
3.9 Beam deposited power balance . . . 61
3.10 Exemplar finite volume method 2D and 3D computational cells . . . 81
3.11 Visual outline of the discretisation and reconstruction process . . . 82
3.12 Visual summary of notation for demonstration of boundary conditions . . . 82
3.13 Visual summary of notation for demonstration of slip condition evaluation . . . 83
3.14 Exemplar partitioning of simulation amongst several MPI processes . . . 83

4.1 Schematic of 1D hypersonic shock test case . . . 87
4.2 Results of Maxwellian 1D hypersonic shock study . . . 88
4.3 Results of argon 1D hypersonic shock study . . . 89

4.4 Navier-Stokes Mach 20 Maxwellian 1D shock profiles near shock interface 91
4.5 Maximum mean free path as a function of timestep for Conventional Burnett Mach 20 Maxwellian 1D shock 92
4.6 Observed limits for 1D shock and conjectured additional *CFL* factors 94
4.7 2D bow shock grid convergence study - temperature along the stagnation streamline 97
4.8 Comparison of 2D bow shock results with published data along the stagnation streamline 98
4.9 2D bow shock temperature contours comparing Navier-Stokes and Augmented Burnett solutions 106
4.10 Comparison of observed 1D shock and 2D bow-shock *CFL* factors 107
4.11 Exemplar pressure distribution for a Navier-Stokes 2D microchannel simulation . 107
4.12 Centreline velocity and temperature profiles for 2D microchannel simulations with differing slip models 108
4.13 Sections indicating velocity profiles at 2D microchannel midpoint for differing slip models 109
4.14 2D microchannel wall slip velocity and temperature for differing slip models . . . 110
4.15 Sections indicating variable profiles at 2D microchannel midpoint for differing viscous models 111
4.16 Centreline velocity and temperature profiles for 3D microchannel simulations with differing slip models at $AR = 1$ 113
4.17 2D JET Neutraliser computational geometries (without diagnostic collar) 114
4.18 2D JET neutraliser flow vector plots (geometry A). Dashed line shows approximate position of the recirculation zone 115
4.19 2D JET neutraliser centreline velocity and temperature profiles for geometry A . . 115
4.20 2D JET neutraliser transverse outlet velocity and temperature profiles for geometry A 116
4.21 2D JET neutraliser centreline pressure for geometry A (Navier-Stokes & Augmented Burnett) 116
4.22 2D JET neutraliser centreline pressure profiles for geometries A, B & C (Augmented Burnett) 116
4.23 Various 2D JET neutraliser centreline profiles for geometry C (Navier-Stokes & Augmented Burnett) 121
4.24 Comparing 2D and 3D JET neutraliser centreline pressure profiles 122
4.25 Comparing 2D and 3D JET neutraliser centreline *Kn* profiles 122

5.1 JET Neutral Beam Test Bed diagnostic collar 126
5.2 JET neutraliser experimental data and trends, with exemplar error bars 127
5.3 JET 2D computational geometry including diagnostic collar 130
5.4 Fictitious boundary cell issues for the 2D JET neutraliser geometry the including diagnostic collar 131

5.5 JET 2D neutraliser with collar - flow vector diagrams for Navier-Stokes simulations upon grids 1 & 2 . . . 133
5.6 JET 2D neutraliser grid with collar - Exemplar flow vector diagrams in the absence of beam . . . 136
5.7 JET 2D neutraliser grid with collar - exemplar centreline pressure and temperature profiles in the absence of beam . . . 137
5.8 JET 2D neutraliser grid with collar - neutraliser cold gas targets with varying gas flow . . . 137
5.9 JET 2D neutraliser with collar - α_{Hot} scan comparison to experimental data (experimental trend is indicated at $\alpha_{hot} = 0.37$) . . . 139
5.10 JET 2D neutraliser with collar - summary of α_{hot} scan error to experimental data . 140
5.11 JET 2D neutraliser grid with collar - centreline gas density and temperature for $P_b = 6MW$ . . . 142
5.12 JET 2D neutraliser grid with collar - gas temperature and density contours for $P_b = 6MW$ . . . 143
5.13 JET 2D neutraliser grid with collar - gas temperature and density at the diagnostic collar for $P_b = 6MW$ . . . 143
5.14 JET 2D neutraliser grid with collar - beam composition for $P_b = 6MW$ . . . 144
5.15 JET 2D neutraliser grid with collar - plasma electron density and temperature for $P_b = 6MW$ . . . 145
5.16 JET 2D neutraliser grid with collar - fractional contribution of each mass and energy source type for $P_b = 6MW$ . . . 146
5.17 JET 2D neutraliser grid with collar - magnitude of each mass and energy source type for $P_b = 6MW$ . . . 147
5.18 JET 2D neutraliser grid with collar - energy deposited per source particle for each source type at $P_b = 6MW$ . . . 149
5.19 JET 2D neutraliser grid with collar - primary and stripped electron details for $P_b = 6MW$ . . . 149
5.20 JET 2D neutraliser grid with collar - comparison of P_b scan to experiment . . . 150
5.21 JET 2D neutraliser grid with collar - P_b scan centreline density and temperature profiles . . . 151
5.22 JET 2D neutraliser grid with collar - P_b scan electron density and temperature longitudinal profiles . . . 151
5.23 JET 2D neutraliser grid with collar - T_w scan cold gas target and neutral beam fractions . . . 152
5.24 JET 2D neutraliser grid with collar - Q_n scan longitudinal gas density and temperature profiles . . . 153
5.25 JET 2D neutraliser grid with collar - Q_n scan gas targets . . . 153
5.26 JET 2D neutraliser grid with collar - Q_n scan comparison of gas temperature at the diagnostic collar with experiment . . . 154
5.27 JET 2D neutraliser grid with collar - Q_n scan electron temperature profiles . . . 155

5.28 JET 2D neutraliser grid with collar - Q_s scan gas targets . . . 156
5.29 JET 2D neutraliser grid with collar - B_w scan gas targets . . . 157
5.30 2D ITER relevant computational geometries . . . 159
5.31 2D ITER neutraliser - centreline gas density and temperature in the absence of beam 162
5.32 2D ITER neutraliser - velocity vector plot in the absence of beam . . . 162
5.33 2D ITER neutraliser - centreline gas density profiles in the absence and presence of beam, with comparison to 2D JET neutraliser with collar . . . 165
5.34 2D ITER neutraliser - centreline gas temperature in the presence of beam, with comparison to 2D JET neutraliser with collar . . . 167
5.35 Energy deposited by energetic neutralised plasma ions for ITER and JET simulations in HiReCom . . . 168
5.36 2D ITER neutraliser - plasma density, with comparison to 2D JET neutraliser with collar . . . 169
5.37 2D ITER neutraliser - electron temperature, with comparison to 2D JET neutraliser with collar . . . 170
5.38 2D ITER neutraliser - stripped electron density and temperature, with comparison to 2D JET neutraliser with collar . . . 171
5.39 2D ITER neutraliser - fractional and actual contribution of each source type to total Energy source . . . 171
5.40 2D ITER neutraliser - beam composition along the neutraliser . . . 172
5.41 2D Symmetric & Asymmetric neutralisers - $S1$ vs A velocity vector comparison . . 174
5.42 2D Symmetric & Asymmetric neutralisers - $S1$ vs A transverse density and temperature comparisons . . . 175
5.43 2D Symmetric neutraliser - I_b scan centreline gas density and temperature profiles 176
5.44 2D Symmetric neutraliser - I_b scan hot gas target and fraction of cold target 177
5.45 2D Symmetric neutraliser - I_b scan wall plasma and stripped electron density . . . 178
5.46 2D Symmetric neutraliser - N_w scan centreline gas density profiles in the absence of beam . . . 179
5.47 2D Symmetric neutraliser - N_w scan centreline gas density and temperature profiles in the presence of beam . . . 180
5.48 2D Symmetric neutraliser - N_w scan wall plasma electron density profiles in the presence of beam . . . 181
5.49 2D Symmetric neutraliser - N_w scan total energy source to each computational slice 182
5.50 2D Symmetric neutraliser - N_w scan energy deposition by plasma source particles 183
5.51 3D JET neutraliser computational geometries . . . 185
5.52 3D JET neutraliser with and without septum - $y = z = 0$ centreline pressure and target . . . 186
5.53 3D JET neutraliser with and without septum - longitudinal velocity at $y = 0$, $x = 0.4m$ . . . 186
5.54 2D and 3D JET neutraliser - gas density and temperature profiles at $y = z = 0$ . . . 187
5.55 2D and 3D JET neutraliser - transverse temperature profiles at $(x, z) = (0.03, 0)$ . . 187

5.56 2D and 3D JET neutraliser - wall plasma density profiles at $y = z = 0$ 188
5.57 2D and 3D JET neutraliser - D_{source} at the midpoint interspace $(x = 0.03m)$ 188
5.58 3D JET neutraliser with and without Septum - Comparison to experiment 189
5.59 3D JET neutraliser with and without Septum - gas density in beam path and centreline temperature (at $y = z = 0$) 190
5.60 3D JET neutraliser with and without Septum - total energy source to slice 190
5.61 3D JET neutraliser with and without Septum - plasma ion reflection energy source to slice and energy deposited per source particle 191
5.62 3D JET neutraliser with and without Septum - average neutraliser half width $\overline{N_{hw}}$ 191

List of Tables

3.1 Molecular interaction force models for differing viscosity interaction model exponents . . . 33
3.2 Ion beam species fractions for JET beam source . . . 40
3.3 Exemplar beam projectiles cross-section table for 80,100,120 keV . . . 42
3.4 Supporting constants for cross-sections evaluation by Chebyschev polynomials[?] 44
3.5 Ratio of atomic to total stopping power for a hydrogen beam [?] . . . 45
3.6 Typical experimental values for the JET neutraliser contents subject to 120kv 60A beam . . . 45
3.7 Table of dissociation by beam ion cross sections[? ?] . . . 47
3.8 Cross sections for electron induced processes[? ?] . . . 52
3.9 Comparison of momentum transfer cross-sections of *Pamela*[?] and *Phelps*[?] . . . 58

4.1 Gas parameters utilised in 1D hypersonic shock simulation . . . 87
4.2 Convergence study for Navier-Stokes argon 1D shocks . . . 88
4.3 Onset of instability for Conventional Burnett Equations due to increasing grid refinement . . . 90
4.4 Onset of instability in 1D shock for differing variable reconstruction schemes . . . 91
4.5 Comparison of the computational stability limits for 1D shock subject to differing variable reconstruction schemes . . . 93
4.6 Freestream boundary conditions utilised in 2D bow shock simulation . . . 95
4.7 Gas parameters utilised in 2D bow shock simulation . . . 95
4.8 Comparison of the computational stability limits for differing variable reconstruction schemes . . . 99
4.9 2D microchannel geometry and gas parameters . . . 101
4.10 Grid convergence study results for the 2D microchannel test case . . . 102
4.11 Comparison of Navier-Stokes 2D microchannel simulations with an analytical model 103
4.12 3D microchannel geometry and gas parameters . . . 104
4.13 Grid convergence study results for the 3D microchannel test case . . . 105
4.14 Comparison of HiReCom Navier-Stokes 3D microchannel simulations with an analytical pressure model . . . 106
4.15 Comparison of HiReCom Navier-Stokes microchannel simulations with an analytical volumetric flow rate model . . . 112

4.16 Summary of 2D JET neutraliser gas and wall parameters for hydrogen 112
4.17 Summary of 2D JET neutraliser results with Deissler slip boundary conditions . . . 112

5.1 Functional fits to JET neutraliser experimental data 126
5.2 Gas parameters for deuterium simulations of the JET and ITER neutralisers 130
5.3 JET 2D neutraliser grid with collar - development study simulation parameters . . 131
5.4 JET 2D neutraliser with collar - grid resolution study results summary 134
5.5 JET 2D neutraliser with collar - grid resolution study simulation parameters 135
5.6 JET 2D neutraliser with collar - gas targets in the absence of beam 137
5.7 JET 2D neutraliser with collar - α_{Hot} scan model parameters 138
5.8 JET 2D neutraliser grid with collar - values supporting electron temperature evaluation for P_b scan 148
5.9 JET 2D neutraliser grid with collar - P_b scan model parameters 149
5.10 JET 2D neutraliser grid with collar - T_w scan model parameters 151
5.11 JET 2D neutraliser grid with collar - Q_n scan model parameters 153
5.12 JET 2D neutraliser grid with collar - Q_s scan model parameters 154
5.13 JET 2D neutraliser grid with collar - B_w scan beam parameters 155
5.14 Comparison of neutraliser and beam parameters for ITER and JET 157
5.15 Table of 2D ITER model parameters 160
5.16 Table of convergence study upon ITER relevant neutraliser geometry A 160
5.17 2D ITER neutraliser - gas targets in the absence of beam 161
5.18 2D ITER neutraliser - model parameters in the presence of beam 162
5.19 Plasma production cross-sections and energy deposition rates for the JET and ITER beams 163
5.20 2D ITER neutrlaiser - gas targets in the presence of beam - 166
5.21 2D Symmetric neutraliser - I_b scan model parameters 167
5.22 2D Symmetric neutraliser - I_b scan gas targets and estimated beam neutral fractions 168
5.23 2D Symmetric neutraliser - N_w scan model parameters 169
5.24 2D Symmetric neutraliser - N_w scan gas targets and estimated beam neutral fractions 170
5.25 2D Symmetric neutraliser - partitioning study parameters 171
5.26 2D Symmetric neutraliser - partitioning study gas targets and estimated beam neutral fractions 173
5.27 3D JET neutraliser with and without septum - model parameters 184

Nomenclature

Acronyms

CCFE	Culham Centre for Fusion Energy
CFD	Computational Fluid Dynamics
CFL	Courant-Friedrich-Lewy
DDD	Design Description Document
DEMO	Demonstration Power Plant
DPD	Dissipative Particle Dynamics
DSMC	Direct Simulation Monte Carlo
EFDA	European Fusion Development Agreement
ENO	Essentially Non-Oscillatory
GHE	Generalised Hydrodynamics Equations
HiReCom	High Resolution Computing
ICF	Inertial Confinement Fusion
IFMIF	International Fusion Materaials Irradiation Facility
ITER	International Thermonuclear Experimental Reactor
JET	Joint European Torus
LBM	Linearised Boltzmann Method
MCF	Magnetic Confinement Fusion
MD	Molecular Dynamics
MUSCL	Monotonic Upwind Scheme for scalar Conservation Laws
NBH	Neutral Beam Heating
NINI	Negative Ion Neutral Injector
PIC	Particle-in-Cell
PINI	Positive Ion Neutral Injector
UKAEA	United Kingdom Atomic Energy Authority
WENO	Weighted Essentially Non-Oscillatory

Continuum-Transition Gas Solver

Conservation equations and flow variables

t	Time (s)
$\boldsymbol{r} = (x, y, z)$	Cartesian co-ordinates (m)
$\boldsymbol{\delta r} = (\delta x, \delta y, \delta z)$	Infinitesimal distances (m)
ξ, η, ζ	Curvilinear co-ordinates
ρ	Density (kgm^{-3})
u, v, w	Cartesian velocities (ms^{-1})
$\boldsymbol{e}$	Total energy per unit volume (Jm^{-3})
T	Temperature (K)
p	Pressure (Pa)
Kn	Knudsen number
$\boldsymbol{\sigma} = \sigma_{ij}$	Viscous stress tensor
$\boldsymbol{q} = q_i$	Heat flux
μ	Dynamic viscosity ($kgm^{-1}s^{-1}$)
γ	Ratio of specific heats or adiabatic index
R	Gas constant ($Jkg^{-1}K^{-1}$)
c_v	Specific heat capacity with constant volume ($Jkg^{-1}K^{-1}$)
$\boldsymbol{I}$	Identity tensor
λ_b	Bulk viscosity coefficient ($kgm^{-1}s^{-1}$)
μ_0, T_0, T_s	Viscosity law parameters ($kgm^{-1}s^{-1}$, K, K)
ω	Interaction law exponent
κ	Thermal conductivity coefficient ($WK^{-1}m^{-1}$)
λ	Mean free path (m)
M	Mach number
Re	Reynolds number
Pr	Prandtl number
ω_i, θ_i	Burnett equation coefficients
$\boldsymbol{U}$	Conserved variables
$\boldsymbol{E}, \boldsymbol{F}, \boldsymbol{G}$	Inviscid fluxes in cartesian co-ordinates
$\boldsymbol{E}_v, \boldsymbol{F}_v, \boldsymbol{G}_v$	Viscous fluxes in cartesian co-ordinates
$\widetilde{\boldsymbol{E}}, \widetilde{\boldsymbol{F}}, \widetilde{\boldsymbol{G}}$	Inviscid fluxes in curvilinear co-ordinates
$\widetilde{\boldsymbol{E}_v}, \widetilde{\boldsymbol{F}_v}, \widetilde{\boldsymbol{G}_v}$	Viscous fluxes in curvilinear co-ordinates
$\boldsymbol{J}$	Jacobian
$\lvert\boldsymbol{J}\rvert$	Determinant of the Jacobian

Grid Metrics

I, J, K	Cell reference variables
I_c, J_c, K_c	Cycling cell references
$*_x, *_y, *_z$	Partial derivatives with respect to Cartesian co-ordinates
$*_\xi, *_\eta, *_\zeta$	Partial derivatives with respect to curvilinear co-ordinates

Variable Reconsruction Schemes

$\boldsymbol{u}_L, \boldsymbol{u}_R$	Left and right variable states
k	MUSCL parameter
$\widetilde{\phi_L}, \widetilde{\phi_R}$	MUSCL limiter fuction
r_L, r_R	MUSCL slope ratio
$S_{*,L}, S_{*,R}$	WENO stencils
$p_{n,*}$	WENO polynomial candidates
I_n	WENO smoothness candidates
α_n	WENO weighting factors
c_n	WENO multipliers

Boundary conditions

Boundary values

$\rho_{in}, \rho_{out}, \rho_\infty$	Inlet, outlet and freestream densities (kgm^{-3})
$p_{in}, p_{out}, p_\infty$	Inlet, outlet and freestream pressure (Pa)
$T_{in}, T_{out}, T_\infty$	Inlet, outlet and freestream temperatures (K)
$M_\infty, Re_\infty, Kn_\infty$	Freestream Mach, Reynolds and Knudsen numbers
A_{in}	Inlet flow area (m^{-2})
u_{in}, v_{in}, w_{in}	Inlet velocities (ms^{-1})
$\dot{Q_{in}}, \dot{Q_{mid}}, \dot{Q_{out}}$	Inlet, midpoint and outlet volumetric flow rates (m^3s^{-1})
Kn_{in}, Kn_{out}	Inlet and outlet Knudsen

Slip boundary conditions

u_s, v_s, w_s	Wall slip velocities (ms^{-1})
T_s	Wall slip temperature (K)
T_w	Wall temperature (K)
σ	Momentum accommodation co-efficient
α	Energy accommodation co-efficient (typical)
$\widetilde{n}, \widetilde{p}$	Distances normal and parallel to wall (m)

Coupled Beam-Plasma-Gas Solver

Additions to conservation equations

$\boldsymbol{L}$,$\boldsymbol{S}$	Generic source and sink terms
L^{ρ}	Generic mass loss term ($kgm^{-3}s^{-1}$)
S^{ρ}	Generic mass source term ($kgm^{-3}s^{-1}$)
S^{e}	Generic additional energy source term ($Jm^{-3}s^{-1}$)
$\widehat{p}$	Modified pressure (Pa)
p_p	Plasma pressure (Pa)

Boundary conditions

$Q_n, Q_s, Q_s^{'}$	Throughput via neutraliser interspace, throughput to beam source and suplus throughput from beam source to neutraliser in the presence of beam ($mbarls^{-1}$)
T_{inj}, p_{inj}	Temperature and presure at upstream neutraliser boundary (K, Pa)
T_{mid}	Temperature of gas entering at neutraliser interspace inlet (K)

Experimental quantities

$\overline{T}_{gas}$	Gas temperature measured at the JET Neutral Beam Test Bed diagnostic collar (K)
$\overline{T}_e$,$\overline{n}_e$	Electron temperature and density measured at the JET Neutral Beam Test Bed diagnostic collar (eV,m^{-3})
$\overline{p}_{col}$	Gas pressure measured at the JET Neutral Beam Test Bed diagnostic collar (Pa)
$\overline{F}_c$	Fraction of cold target deduced from JET
$p_{correct}, p_{baratron}$	Corrected gas pressure and original experimental pressure measured by baratron (Pa)
$T_{correct}, T_{baratron}$	Corrected gas temperature and original experimental temperature measured by baratron (K)

Geometry description

A_n	Neutraliser cross-sectional area (m^2)
N_w,N_{hw},N_d	Half of neutraliser width, half width and depth (m)
Δx_{col}, Δx_{out}	Longitudinal grid spacing inside and outside of diagnostic collar (m)
Δy, Δz	Transverse grid spacings (m)
y_{low}, y_{high}, z_{low}, z_{high}	Transverse cell extremities (m)
Vol_{gas}, Vol_{beam}	Volumes of beam and gas within a cell (m^{-3})
f_{beam}	Fraction of cell volume containing beam
Vol_{gas}^{Total}, Vol_{beam}^{Total}	Total volumes of beam and gas within a transverse neutraliser slice (m^{-3})
$(J_{inner}^{Qi}, K_{inner}^{Qi})$, D_{inner}^{Qi}	Reference and distance to beam centre of innermost cell of quadrant i
$(J_{outer_n}^{Qi}, K_{outer_n}^{Qi})$, D_{inner}^{Qi}	Reference and distance to beam centre of outer neighbours of innermost cells of quadrant i
J_{inner}^{Hi}, D_{inner}^{Hi}	Reference and distance to beam centre of innermost cell of half i
J_{outer}^{Hi}, D_{outer}^{Hi}	Reference and distance to beam centre of outer neighbours of innermost cells of half i
$\overline{D_{inner}}$, $\overline{D_{outer}}$	Average distance over all quadrants of innermost and outer cells to beam centre (m)
N_w^{Qi}, N_{hw}^{Qi}, N_d^{Qi}	Neutraliser width, half width and depth for quadrant i
N_w^{Hi}	Neutraliser width for half i
$\overline{N_{hw}}$,$\overline{B_{hw}}$	Neutraliser and beam half-width averaged over transversed slice
f_{sym}	Geometry symmetry factor

Useful constants

m_e	Electron mass (kg)
m_b	Beam projectile mass (kg)
m_D	Atomic deuterium mass (kg)
N_0	Loschmidt's Number (m^{-3})
l_b	Beam path length in neutraliser (m)
e	Electron charge (C)

Gas density

n	Gas number density (m^{-3})
$\overline{n}$	Gas number density average in beam path(m^{-3})
$\overline{n_{inner}}$, $\overline{n_{outer}}$	Gas number density average over all quadrants of innermost and outer cells to beam centre(m^{-3})
$\widetilde{n}$	Linearised gas density profile (m^{-3})
a_0, a_1	Gas density distribution in beam path coefficients

Beam properties

$Perv$	Beam perveance (Pv)
I_b	Beam current (A)
V_b	Beam voltage (V)
A_b	Beam area (m^2)
A_b^{ext}	External beam area (m^2)
B_w, B_d	Beam width and depth (m)
v_b	Beam velocity (ms^{-1})
E_b	Total beam energy (eV)
U_b	Beam energy per atomic mass unit ($keVamu^{-1}$)
n_b	Total beam density (m^{-3})
$\overline{n_b^0}$, $\overline{n_b^+}$, $\overline{n_b^-}$	Beam neutral, positive ion and negative ion densities (m^{-3})
H_{Stop}	Ionic stopping power ($eV.mol-1$)
H_{low}, H_{high}	Ionic stopping power components ($eV.mol-1$)
χ	Ratio of atomic to total beam stopping power
Δx	Distance traversed by beam (m)
P_b^{neut}	Beam power loss to neutraliser contents ($eV.s^{-1}$)
P_b^p, P_b^{se}	Beam power deposited in neutraliser plasma and stripped electrons (eVs^{-1})

Sink terms

L_b^ρ, $L_b^{\rho \boldsymbol{u}}$, L_b^e	Density, momentum and energy loss due to ionisation by the beam ($kgm^{-3}s^{-1}$, $kgm^{-2}s^{-2}$, $Jm^{-3}s^{-1}$)

Selected beam cross-sections

σ_{CE}, $\sigma_{\widetilde{CE}}$	Cross sections of charge exchange on molecules and atoms (m^2)
σ_{DCE}	Cross section of double electron capture (m^2)
σ_{EC}	Cross section of single electron capture by neutral projectile (m^2)
σ_{PL_0}	Cross section of electron loss by neutral projectile (m^2)
$\sigma_{PL^1_-}$, $\sigma_{PL^2_-}$	Cross section of single and double electron loss by negative projectile (m^2)
σ_0, σ_+	Cross sections of ionisation by neutral and positive projectiles (m^2)
σ_{01}, $\sigma_{0\bar{1}}$	Cross sections of change in projectile composition from neutral to positive and negative (m^2)
σ_{10}, $\sigma_{1\bar{1}}$	Cross sections of change in projectile composition from positive to neutral and negative (m^2)
$\sigma_{\bar{1}0}$, $\sigma_{\bar{1}1}$	Cross sections of change in projectile composition from negative to neutral and positive (m^2)
$\widetilde{C_n}$	Chebyschev polynomial of order n

Transverse slice properties

$\overline{T_{neut}}$	Gas temperature average over the transverse slice of the neutraliser (K)
$\overline{n_{neut}}$	Gas density average over the transverse slice of the neutraliser (m^{-3})
$\overline{d_{neut}}$	Distance between walls averaged over the transverse slice of the neutraliser (m)

Product energy deposition framework

$N^{Reflect}$, $E^{Reflect}$	Number and energy reflection coefficient for wall incident ions
E_{Ion}	Wall incident ion energy per atom ($eVatom^{-}1$)
σ_{mom}	Momentum transfer cross-section (m^2)
$f^{dep_0}_{total}$, $f^{dep_+}_{total}$, $f^{dep_p}_{total}$	Total energy deposited in the neutral gas by neutral and ionic reaction products, and wall incident plasma ions (eV)
$f^{dep_0}_1$, $f^{dep_+}_1$	Typical fraction of energy deposited by neutral and ionic product before first incidence with neutraliser wall (eV)
α_{hot}	Energy accommodation co-efficient (fast particles)
D_{source}, D^{beam}_{source}	Distribution factors for source terms across the entire infinitesimal transverse neutraliser slice and solely within the beam path
$\overline{E^0_{source}}$,$\overline{E^+_{source}}$	Exemplar neutral and ionic source product characteristic energies (eV)
$\overline{E_{reflected}}$	Energy of product following reflection from wall (eV)
$\overline{E^{dep_0}_{source}}$,$\overline{E^{dep_+}_{source}}$	Energy deposited by neutral and ionic source products (eV)

Beam ion induced dissociation

Production and properties

σ_{BD1}, σ_{BD2}, σ_{BD3}, σ_{BD4}	Cross sections of beam ion induced dissociation reactions (m^2)
E_{BD1}, E_{BD2}, E_{BD3}, E_{BD4}	Energies of products from beam ion induced dissociation reactions (eV)
$\sigma_{b.diss}^{total}$	Total cross section of beam ion induced dissociation (m^2)
$\sigma_{b.diss}^{prod_0}$, $\sigma_{b.diss}^{prod_+}$	Neutral and ionic product production cross section of beam ion induced dissociation (m^2)
$\overline{E_{b.diss}^0}$, $\overline{E_{b.diss}^+}$	Characteristic energy of neutral and ionic products of beam ion induced dissociation (eV)

Sink and Source terms

$N_{b.diss}^0$, $N_{b.diss}^+$	Neutral and ionic product production rate due to beam ion induced dissociation (s^{-1})
$N_{b.diss}^{Reflect}$, $E_{b.diss}^{Reflect}$	Number and energy reflection coefficient for ionic products from beam ion induced dissociation
$L_{b.diss}^{\rho}$, $L_{b.diss}^{\rho \boldsymbol{u}}$, $L_{b.diss}^{e}$	Density, momentum and energy loss due to beam ion induced dissociation ($kgm^{-3}s^{-1}$, $kgm^{-2}s^{-2}$, $Jm^{-3}s^{-1}$)
$S_{b.diss}^{\rho}$, $S_{b.diss}^{\rho \boldsymbol{u}}$, $S_{b.diss}^{e}$	Density, momentum and energy source due to beam ion induced dissociation ($kgm^{-3}s^{-1}$, $kgm^{-2}s^{-2}$, $Jm^{-3}s^{-1}$)
$\widetilde{N_{b.diss}^+}$	Rate of reflection of ionic products of beam ion induced dissociation (s^{-1})
$\widetilde{E_{b.diss}^+}$	Characteristic energy of reflected ionic products of beam ion induced dissociation (eV)
$E_{b.diss}^{dep_0}$, $E_{b.diss}^{dep_+}$	Energy deposited in background gas by each neutral and ionic product of beam ion induced dissociation dissociation (eV)
$s_{b.diss}^{\rho}$, $s_{b.diss}^{e}$	Total density and energy source to infinitesimal transverse neutraliser slice due to beam ion induced dissociation ($kgm^{-3}s^{-1}$, $Jm^{-3}s^{-1}$)

Primary electron

Production and properties

σ_{pe}	Primary electron production cross section for composite beam (m^2)
$\overline{E_{pe}}$	Characteristic primary electron energy for composite beam (m^2)
$\sigma_{pe}^{H^+}$, $\sigma_{pe}^{H^0}$	Primary electron production cross section for proton and neutral hydrogen projectiles into hydrogen gas (m^2)
$\sigma_{pe}^{He^+}$, $\sigma_{pe}^{He^0}$	Primary electron production cross section for proton and neutral hydrogen projectiles into helium gas (m^2)
$\overline{E_{pe}^{H^+}}$, $\overline{E_{pe}^{H^0}}$	Characteristic primary electron energy for proton and neutral hydrogen projectiles into hydrogen gas (m^2)
$\overline{E_{pe}^{He^+}}$, $\overline{E_{pe}^{He^0}}$	Characteristic primary electron energy for proton and neutral hydrogen projectiles into helium gas (m^2)
$\overline{n_{pe}}$	Primary electron density (m^{-3})
$\overline{v_{pe}}$	Characteristic primary electron velocity (ms^{-1})

Dissociation

$\sigma_{pe.diss}^{total}$	Total cross section of primary electron induced dissociation (m^2)
$\sigma_{pe.diss}^{prod_0}$, $\sigma_{pe.diss}^{prod_+}$	Neutral and ionic product production cross section of primary electron induced dissociation (m^2)
$\overline{E_{pe.diss}^{0}}$, $\overline{E_{pe.diss}^{+}}$	Characteristic energy of neutral and ionic products of primary electron induced dissociation (eV)
σ_{ED1}, σ_{ED2}	Cross sections of electron induced dissociation reactions (m^2)
E_{ED1}, E_{ED2}	Energy of products from electron induced dissociation reactions (eV)

Sink and Source terms

$N_{pe.diss}^{0}$, $N_{pe.diss}^{+}$	Neutral and ionic product production rate due to primary electron induced dissociation (s^{-1})
$L_{pe.diss}^{\rho}$, $L_{pe.diss}^{\rho \boldsymbol{u}}$, $L_{pe.diss}^{e}$	Density, momentum and energy loss due to primary electron induced dissociation ($kgm^{-3}s^{-1}$, $kgm^{-2}s^{-2}$, $Jm^{-3}s^{-1}$)
$S_{pe.diss}^{\rho}$, $S_{pe.diss}^{\rho \boldsymbol{u}}$, $S_{pe.diss}^{e}$	Density, momentum and energy source due to primary electron induced dissociation ($kgm^{-3}s^{-1}$, $kgm^{-2}s^{-2}$, $Jm^{-3}s^{-1}$)
$E_{pe.diss}^{dep_0}$, $E_{pe.diss}^{dep_+}$	Energy deposited in background gas by each neutral and ionic product of primary electron induced dissociation
$s_{pe.diss}^{\rho}$, $s_{pe.diss}^{e}$	Total density and energy source to infinitesimal transverse neutraliser slice due to primary electron induced dissociation ($kgm^{-3}s^{-1}$, $Jm^{-3}s^{-1}$)

Stripped electrons

Production and properties

σ_{se_+}, σ_{se_-}	Stripped electron production cross section for neutral and negative projectiles (m^2)
E^0_{se}	Initial stripped electron energy (eV)
v^0_{se}	Initial stripped electron velocity ($m.s^{-1}$)
$\overline{n_{se}}$	Average stripped electron density in beam path(m^{-3})
$\overline{v_{se}}$	Stripped electron velocity in beam path ($m.s^{-1}$)
$\overline{E_{se}}$	Stripped electron energy in beam path (eV)
e^{Total}_{se}	Total stripped electron energy per unit volume (eVm^{-3})
K_{in}	Energy deposition rate in gas due to inelastic collision with stripped electrons (eVm^3s^{-1})

Dissociation

$\sigma^{total}_{se.diss}$	Total cross section of stripped electron induced dissociation (m^2)
$\sigma^{prod_0}_{se.diss}$, $\sigma^{prod_+}_{se.diss}$	Neutral and ionic product production cross section of stripped electron induced dissociation (m^2)
$\overline{E^0_{se.diss}}$, $\overline{E^+_{se.diss}}$	Characteristic energy of neutral and ionic products of stripped electron induced dissociation (eV)

Sink and Source terms

$N^0_{se.diss}$, $N^+_{se.diss}$	Neutral and ionic product production rate due to stripped electron induced dissociation (s^{-1})
$N^{Reflect}_{se.diss}$, $E^{Reflect}_{se.diss}$	Number and energy reflection coefficient for ionic products from stripped electron induced dissociation
$L^{\rho}_{se.diss}$, $L^{\rho \boldsymbol{u}}_{se.diss}$, $L^{e}_{se.diss}$	Density, momentum and energy loss due to stripped electron induced dissociation ($kgm^{-3}s^{-1}$, $kgm^{-2}s^{-2}$, $Jm^{-3}s^{-1}$)
$S^{\rho}_{se.diss}$, $S^{\rho \boldsymbol{u}}_{se.diss}$, $S^{e}_{se.diss}$	Density, momentum and energy source due to stripped electron induced dissociation ($kgm^{-3}s^{-1}$, $kgm^{-2}s^{-2}$, $Jm^{-3}s^{-1}$)
$S^{e}_{se.inelastic}$	Energy source due to inelastic collision of stripped electrons with gas molecules ($Jm^{-3}s^{-1}$)
$E^{dep_0}_{se.diss}$, $E^{dep_+}_{se.diss}$	Energy deposited in background gas by each neutral and ionic product of stripped electron induced dissociation
$s^{\rho}_{se.diss}$, $s^{e}_{se.diss}$	Total density and energy source to infinitesimal transverse neutraliser slice due to stripped electron induced dissociation ($kgm^{-3}s^{-1}$, $Jm^{-3}s^{-1}$)
$s^{e}_{se.inelastic}$	Total energy source to infinitesimal transverse neutraliser slice due to inelastic collision of stripped electrons with gas molecules ($Jm^{-3}s^{-1}$)

Plasma

Properties

n_p	Plasma number density (m^{-3})
$\widetilde{n_p}$	Plasma density distribution (m^{-3})
n_{wi}	Plasma ion number density at wall (m^{-3})
T_e	Electron temperature (eV)
ψ	Ratio of charge exchange ion production to total ion production
η	Ratio of plasma sheath potential to electron temperature
ϕ	Plasma sheath potential (eV)
$\alpha_0, \alpha_1, \alpha_2, \alpha_3, \alpha_4$	Plasma distribution coefficients in beam path
$\gamma_0, \gamma_1, \gamma_2$	Plasma distribution coefficients outside beam path
θ_c	Angle of chord to $z = 0$
B_c, N_c, δ_c	Distance along chord to beam edge, neutraliser wall and cell centre (m)

Model formulation

$\widetilde{D_i}$	Generalised diffusion coefficient
J_p^b	Plasma ion flux from beam path ($m^{-2}s^{-1}$)
S_i, S_e	Ion and electron source terms ($m^{-3}s^{-1}$)
J_i, J_e	Flux of ions and electrons ($m^{-2}s^{-1}$)
D_i, D_e	Ion and electron diffusion coefficients
τ_i, τ_e	Ion and electron relaxation times (s)
$\sigma_{ni}^{col}, \sigma_{ne}^{col}$	Ion and electron collision cross-sections (m^{-2})
v_i, v_e	Ion and electron characteristic velocities (ms^{-1})
C_{CX},	Ratio of electron flux to ion flux
m_i	Ion mass (kg)
c_s	Ion sound speed (ms^{-1})
n_{wi}	Ion density at wall (m^{-3})
c_{diff}	Simplifying diffusion factor
f_{source}	Simplifying source factor

Source terms

P_p^{wall}	Power deposited upon neutraliser walls by plasma (eVs^{-1})
N_p^+	Plasma ion production rate (s^{-1})
$\widetilde{N_p^+}$	Rate of reflection of wall incident plasma ions
$N_p^{Reflect}$, $E_p^{Reflect}$	Number and energy reflection coefficient for ionic products from stripped electron induced dissociation
E_p^{dep}	Energy deposited in background gas by each wall incident plasma ion
s_p^{ρ}, s_p^e	Total density and energy source to infinitesimal transverse neutraliser slice due to reflection of wall incident plasma ions ($kgm^{-3}s^{-1}$, $Jm^{-3}s^{-1}$)
$S_{se.diss}^{\rho}$, $S_{se.diss}^{\rho \boldsymbol{u}}$, $S_{se.diss}^e$	Density, momentum and energy source due to reflection of wall incident plasma ions ($kgm^{-3}s^{-1}$, $kgm^{-2}s^{-2}$, $Jm^{-3}s^{-1}$)

1 Introduction

Nuclear fusion, the process that powers stars, is currently the subject of an extensive world-wide research effort with the intention of providing a viable alternative energy supply to meet growing worldwide needs. Most advanced at present is the approach of magnetic confinement fusion, which aims to utilise the energy released by the fusion of two hydrogenic species - deuterium and tritium - to ultimately provide electricity. Whilst deuterium is an abundant resource, found in seawater and typically forming approximately 1 in 6300 of all water molecules[**?**], tritium would be required to be made within a future reactor.

From the fusion of a deuterium and tritium nucleus, an alpha particle is produced and a neutron released, as summarised in figure 1.1. The overall reduction in mass that occurs results in the release of significant energy, some 17.6 MeV, the bulk of which is resultant in neutron kinetic energy. It is this energy release that would be harnessed to provide both electricity and to breed tritium within a reactor via interaction with lithium, which exists in abundant supply[**?**]. Power plant design studies conjecture that the current reserves of deuterium and lithium could produce enough fusion energy to supply the world's energy needs for millions of years[**?** **?**]. To offer context, the energy released by this process is so plentiful that the amount of lithium contained in a laptop battery, and the amount of deuterium found in half a bathtub of seawater would provide enough material for nuclear fusion to meet the average European's energy consumption for 30 years[**?**]. If successfully developed, nuclear fusion power would offer abundant energy, with relatively small amounts of long-lived radioactive waste, present a minimal proliferation risk and be intrinsically safe due to the very particular conditions required for fusion to take place[**?**].

Indeed, for fusion to occur, it is necessary to provide sufficient energy to the reactants to allow

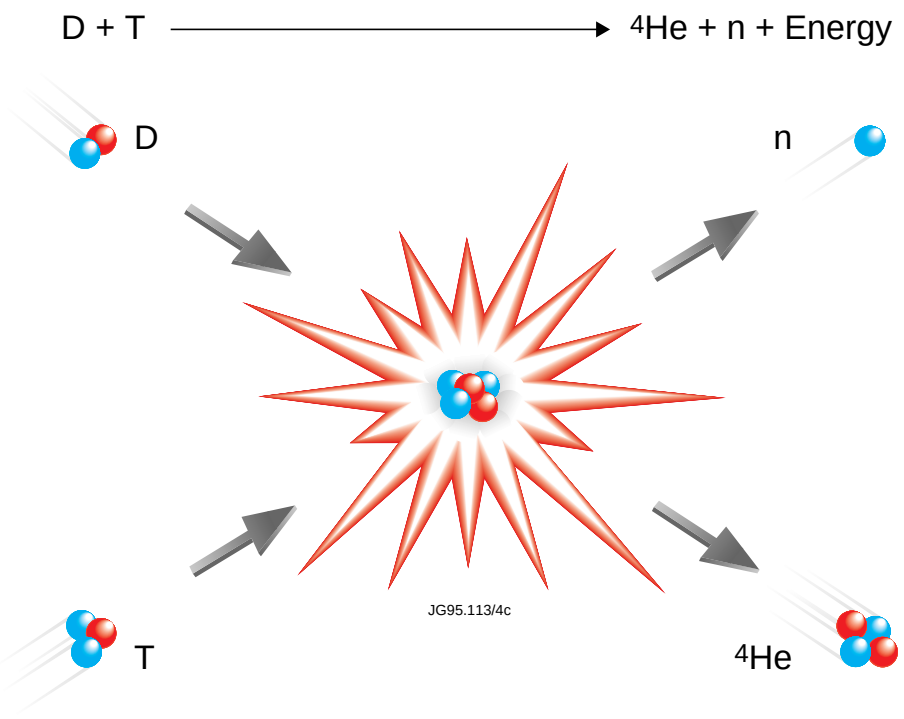

FIGURE 1.1: Reactants and products of Deuterium-Tritium fusion

them to overcome Coulomb repulsion as they approach one another. Thus fusion only occurs at very high temperatures, typically 100 million K[**?**]. At such elevated temperatures, the reactants form a plasma, wherein the electrons possess enough energy to separate from the ionic nuclei to form a fully ionized, though electrostatically neutral, gas.

Since temperatures of this magnitude are beyond confinement by material walls, alternative approaches are necessary. Two confinement techniques dominate fusion energy research at present, namely inertial confinement fusion (ICF) and magnetic confinement fusion (MCF). The former seeks to simultaneously compress and heat a pellet of fuel to very high pressure and temperature via imparting a rapid pulse of energy upon the pellet surface. This pulse of energy is typically provided by lasers in the most successful ICF facilities. When the fuel becomes sufficiently dense and hot, fusion occurs and can burn a significant fraction of the fuel before dissipating. Therefore, this technique utilises very dense fuels and produces very short bursts of fusion energy. By contrast, MCF seeks to use low density gases and provide a stable prolonged source of fusion energy. MCF exploits the charged nature of plasma particles, and the fact they follow magnetic field lines, by confining the plasma within a magnetic bottle. Such a magnetic confinement approach forms the basis of the 'tokamak', a device invented in the Soviet Union in the late 1950s[**?**]. The most successful fusion reactor design to date, tokamaks utilise both toroidal and poloidal coils, to form a helical magnetic field that serves to confine the plasma away from the walls of a torus-shaped reactor vessel, as summarised in figure 1.2.

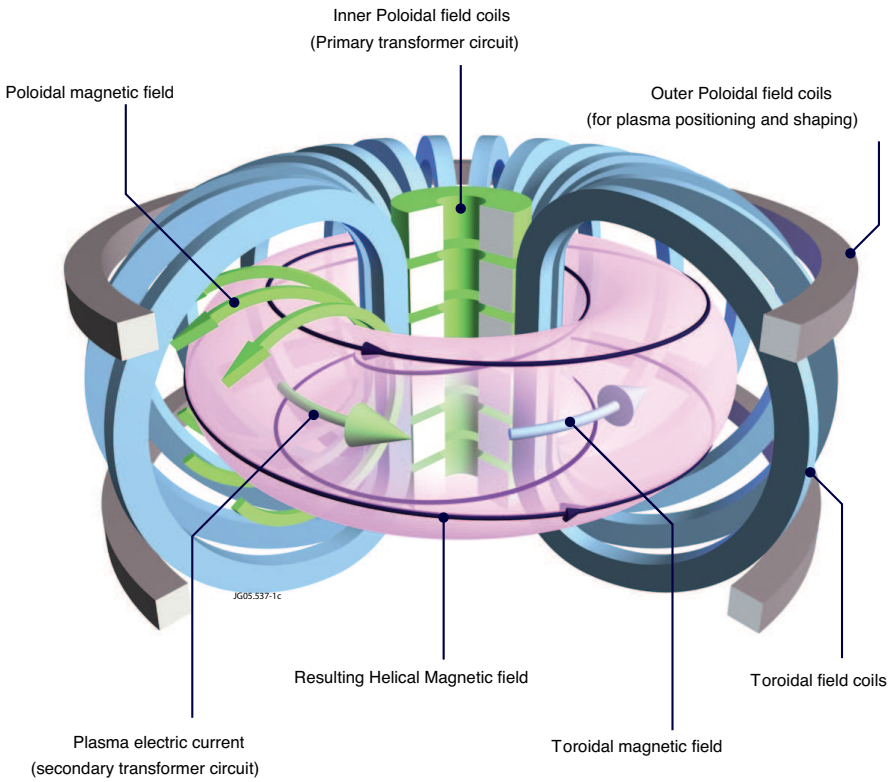

FIGURE 1.2: The Tokamak reactor concept[**?**]

The largest tokamak in the world is the Joint European Torus (JET)[**?**], sited in the UK near Oxford. Operational since 1983, on a pulsed basis for up to 60 seconds, some 79000 experimental pulses have been undertaken to date. JET holds the world record for the largest amount of fusion power produced in a reactor, namely 16 MW of fusion power achieved in 1997. Having proved hugely successful in demonstrating the physics basis for fusion, the next step after JET on the 'road map' to fusion power is the International Thermonuclear Experimental Reactor (ITER)[**?**]. Due to be operational in 2016, ITER represents a huge international collaboration to produce a tokamak posessing a major radius more than twice that of JET, which will be capable of experimental pulses lasting up to an hour. This increase in size will facilitate a 'burning' plasma wherein the energy produced by fusion reactions will surpass that needed for heating of the experiment, implying a net energy gain for the first time in a tokamak. Should ITER prove a success, fusion power should then be realisable with the envisaged contruction of a Demonstration Power Plant (DEMO)[**?**].

From an engineering viewpoint, there are several important challenges still to be overcome. For example, the development of low-activation materials capable of withstanding irradiation by the fast neutrons resultant from fusion is of paramount importance and is to be addressed via the construction of a specialist materials testing facility, the International Fusion Materials Irradiation

Facility (IFMIF)[**?**]. Similarly, the design of blankets capable of breeding tritium is imperative in order to allow any future fusion reactor to be sustainable, whilst an effective exhausting system capable of extracting helium 'ash' from the vessel is key to ensuring a hot, stable plasma. Indeed, how to obtain and control high temperature plasmas over prolonged periods in such a way that fusion reactions may be sustained, is one of the most significant technical challenges for fusion[**?**].

At present, JET requires the delivery of Megawatts of heating power to the reactor vessel in order to achieve and sustain the very high temperatures that facilitate fusion reactions. The vast majority of this heating occurs via neutral beam heating (NBH)[**?**]. A stream of highly energetic neutral atoms are injected into the tokamak and give up their energy to the plasma electrons and ions via collisions, serving to heat and simultaneously fuel the plasma. Typically deuterium, these energetic neutral atoms result from ions acclerated through large voltages before undergoing neutralisation of their charge. This neutralisation of charge allows penetration of the intense magnetic fields in the vicinity of the tokamak vessel. This process is achieved through charge exchange as the beam of energetic particles pass through a body of gas, contained within the 'neutraliser'.

The JET NBH consists of 16 neutral injectors located in two neutral injector boxes, with internal layout as given in figure 1.3. Each of these injectors is capable of producing a $7.5MW$ positive ion beam at its source. However, only a fraction of these extracted ions are succesfully neutralised and the residual beam ions are removed from the beam upon exit from the neutraliser via the use of bending magnets. The remaining neutral beam atoms proceed along the beamline towards the tokamak. Thus the JET NBH is currently capable of injecting a total neutral beam power of $23MW$. Ultimately, it is the neutraliser and the processes that occur within it that are of paramount importance in maximising the power injected to the tokamak.

A long standing problem has been encountered in the use of JET's positive-ion based neutral beams; the gas neutralisation process has consistently proven to be less efficient than originally predicted by both theory[**? ? ?**] and experimental development work[**?**] that contributed to its design. It is thought that the cause of this loss of efficiency is fairly well understood following experimental validation[**? ? ?**] of existing gas heating models[**? ?**] based upon a global energy balance. However, modifications of the neutraliser design to alleviate these effects have brought no definitive improvement[**?**]. Ultimately, as fusion moves towards power plant realisation, system efficiency and availability will dominate all aspects of design in order to ensure it represents a financially competitive energy production technology. This has motivated the pursuit of a more definitive model to better understand the physics of gas neutraliser systems, and has culminated in this research thesis.

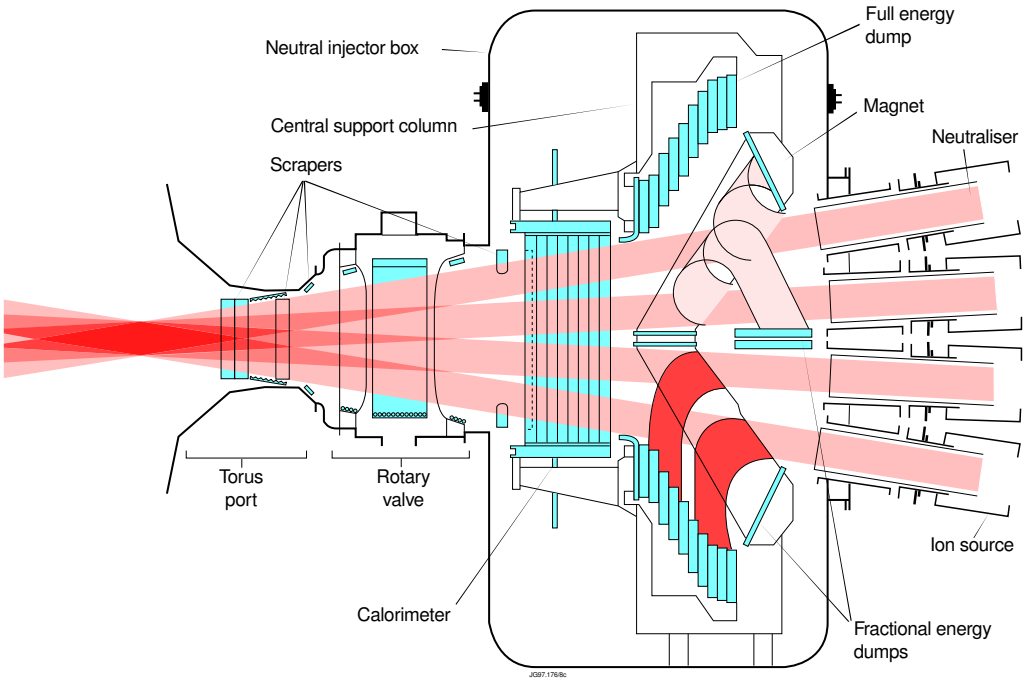

FIGURE 1.3: Elevation view of a JET neutral injector box

1.1 Neutraliser Physics

Present gas neutraliser designs consist of a box of gas through which the beam passes. Examination of present neutraliser understanding reveals three distinct sytem components: the background gas, the injected ion beam and the plasma generated within the neutraliser. The incident beam is initially wholly ionic but undergoes interaction with the background gas that serves to neutralise some fraction of the beam as it progresses along the neutraliser. As well as charge exchange interactions, the beam may ionise or dissociate the background gas molecules and thus induces a significant gas mass/energy sink. Many products of these interactions serve to form a background plasma within the neutraliser[**? ?**].

Rather than direct momentum transfer from the beam to the gas, it is this background plasma that previous modelling endeavours have identified as capable of providing significant energy to the background gas; plasma ions are subject to acceleration at the plasma sheath, are neutralised at the neutraliser wall and reflected back with significant energy that they then deposit within the background gas as they reach thermal equilibrium[**? ?**]. It is this heating of the background gas that is believed to provide reduced gas density and thus reduced beam neutralisation.

There exist previous modelling attempts applicable to each of the three system components; in addition to the global gas heating model mentioned above, stand-alone models exist for both the beam and background plasma[**? ?**]. The former evaluates the composition of the beam along the length of the neutraliser, whilst the latter utilises diffusion equations to provide a series of 1D plasma distributions along the length of the neutraliser. Coupling of these beam, plasma and

gas models was attempted by Surrey for both the JET and ITER systems. The failure of these models to formulate successful gas heating reduction strategies highlights the limitations of these models, which are unable to resolve the effects of gas flow [**?** **?**]. Such an extension of previous work to evaluate neutraliser gas dynamics subject to the various gas sources and sinks resulting from interaction with the beam and background plasma has never been attempted. The difficulty of such an endeavour is compounded by the gas regime encountered in the system; during typical operations the system contains rarefied gas that lies within the continuum-transition regime[**?**].

1.2 Modelling of Rarefied Gas Flow

The vast majority of modelling approaches are originally based upon the Boltzmann transport equations, which describe the statistical distribution of particles in a fluid and have been demonstrated to be valid for any flow regime. The classical equation from which they are formulated, utilises a collision integral based upon the kinetic gas theory; this collision integral assumes binary collisions, molecular chaos and point mass molecules. Solution of the transport equation is difficult for general applications and thus restricted to simplistic cases. Ideally, one would apply deterministic simulation of the motion of all atoms within the system of interest, with any desired macroscopic variable then obtained as the statistical average of this detailed molecular data. However, such an approach is beyond the computational limits of modern computing and instead a range of modelling approaches for complex geometries and flow types have been developed, with the applicability of each approach heavily dependent upon the rarefaction and length scale of the system to be modelled.

Rarefaction is indicated by the Knudsen number $Kn = \lambda/l$, the ratio of the atomic mean free path between collisions λ to the characteristic length of the system l. As summarised in figure 1.4, a gas is said to belong to the continuum regime for low levels of Knudsen, i.e. $Kn \leq 10^{-1}$, a regime wherein a gas can be considered to be in local thermodynamic equilibrium. By contrast, $Kn > 1$ encompasses the molecular regime wherein strong local thermodynamic nonequilibrium is encountered. The intermediate values constitute the continuum-transition regime. Since gas neutralisers typically possess continuum-transition flow, their simulation presents a significant modelling challenge. Neither traditional continuum nor molecular flow simulation methods prove accurate for nonisothermal flows in this gas regime, as can be seen from examination of each modelling technique in turn.

The molecular regime typically requires application of pseudo particle methods to simulate some sample of the molecules in the system. The most renowned of these are the Direct Simulation Monte-Carlo method (DSMC), Lattice-Boltzmann Method (LBM), Molecular Dynamics (MD) and the Dissipative Particle Dynamics (DPD).

DSMC was proposed by *Bird*[**?**] and utilises a series of simulation molecules, evaluating their motion and collision interactions to provide macroscopic flow properties according to the conservation laws applied to each molecule. Both their motion and collisions, which may consist of intermolecular collisions and surface-molecule interactions, are evaluated by probabilistic distributions and several possible collision models. A powerful modelling approach, it represents the

only means of simulating molecular flow in complex geometries [**?**] and has been successfully extended to near molecular flows $Kn < 1$. However, such work has been hampered by both poor convergence and large statistical scatter since at continuum-transition levels the density of the flow is much higher than for molecular flow; given limited computational resources, DSMC methods simulate only some fraction of the real molecules and since statistical scatter of the solution is increased if the sample represents a smaller fraction of the real molecules, continuum-transition simulations are subject to significant errors. To alleviate this, a larger sample size may be attempted, however this increases demand upon computational resources, and slows convergence.

LBM uses simulation particles to solve a simplified Boltzmann equation, but confines their movements to a lattice with the collison of two particles deemed to occur upon their moving to the same lattice point. Representing the fluid as an ensemble of interacting particles, macroscopic flow properties are provided by averaging over a number of lattice sites, with significant computational savings possible against DSMC. The subject of significant academic attention in recent years, the traditional LBM is successful for isothermal flows, but issues have been identified in its application to non-isothermal flows and also in its entropy development[**?**]. An alternative entropic approach has recently been developed, utilising application of the Boltzmann H-theorem to ensure correct performance with regards to entropy[**?**]. However, its extension to nonisothermal and complex flows had not been rigorously established at the outset of this project.

MD seeks to model systems on the atomistic level and is suitable only for simulating very small volumes of liquid over very short timescales. DPD seeks to utilise features of both MD and LBM to model molecular clusters rather than individual atoms, with the use of soft repulsive forces extending the time scales that may be achieved beyond MD and requiring far fewer simulation particles to achieve hydrodynamic behaviour[**?**]. Whilst each has been successfully applied to a range of systems [**? ? ? ?**] neither is able to include reactions such as dissociation and ionisation, which are important inclusions if neutraliser gas dynamics are to be effectively modelled.

By contrast, modelling with the continuum approach allows the microscopic behaviour of a gas to be described entirely by macroscopic variables - the material properties describing kinematic, thermodynamic and transport quantities - and avoids simulation of individual particles. It utilises a series of conservation equations derived as the moment equations of the Boltzmann equation, requirings constitutive relations to provide a complete set of equations. These constitutive relations for transport phenomena such as viscous stress and heat flux can be derived by the Chapman-Enskog method[**?**]. The Navier-Stokes are the first order solutions from this approach, which assume near linear relations of stress to rate-of-strain and heat flux to temperature gradient and thus require that the flow be near local thermodynamic equilibrium throughout the domain. Whilst significantly more computationally efficient than any of the molecular modelling methods within the continuum-transition regime, the increased thermodynamic nonequilibrium of this regime renders invalid the near linear relationships of the constitutive relations, and the Navier-Stokes equations become increasingly inaccurate with increased Kn[**?**].

Thus of the 'traditional' molecular and continuum modelling approaches none may be straightforwardly applied to the continuum-transition regime, with each either inappropriate, computationally expensive or providing significant possible errors. To address this gap and retain the computational savings of the continuum approach, there exist several novel generalized hydrodynamic equations (GHEs) that extend the accuracy of a fluid-based approach into the continuum-transition regime. These GHEs either introduce additional moments or extend the accuracy of existing methods to higher-orders.

The most notable methods introducing additional moments are the Grad 13 moment[**?**] and Struchtrup 13 moment[**?**] systems. Each includes 13 additional moment equations for the dependent variables within the governing equations, significantly increasing the complexity of the system[**?**]. At the outset of this research, test cases were minimal in number without any apparent application of the system to complex flows of more than a single dimension[**?**]. However, they hold promise for the future having recently been successfully applied to produce analytical solutions to both Couette and Poiseuille flows[**? ?**].

The alternative GHE approach is to extend the constitutive relations for stress and heat flux to include additional higher-order terms beyond Navier-Stokes, with inclusion of second order terms providing the Burnett equations[**?**]. Highly non-linear, this equation system retains the computational savings of continuum modelling whilst offering a suitably accurate model of gas within the continuum-transition regime. Previous applications include microfluidics[**?**], hypersonic shock structures[**? ?**] and chemically reacting flows[**?**] and demonstrate the enhanced accuracy of the Burnett equations within the continuum-transition regime when compared with the Navier-Stokes equations. Several versions of the equation system exist since the Conventional Burnett equations were demonstrated to develop instability upon excessively refined grids; linearized stability analysis has shown that the characteristic stability trajectories grow exponentially when the system is subject to a periodic perturbation of wavelength less than some critical length, which is linked to the mean free path [**? ?**]. Unconditional stability has since been delivered via the inclusion of either several ad-hoc conditions or the use of an alternative collision model in their derivation[**? ?**]. Therefore at the outset of this research, the Burnett equations represented the most appropriate method for evaluation of continuum-transition flows in multiple dimensions; offering the computational efficiency of a continuum-based method whilst of significantly enhanced accuracy when compared with traditional continuum approaches, with a significant number of pre-existing test cases in several dimensions.

1.3 Wall Interaction Effects

In modelling continuum-transition flows, one must consider the effects of the interaction of incident gas molecules with a surface, which results in momentum and energy transfer. These interactions are specified by momentum and energy accommodation coefficients, indicating the fraction of each that is lost in collision with the wall. The evaluation of accurate accommodation coefficients is of particular importance for continuum-transition flows which have been shown to

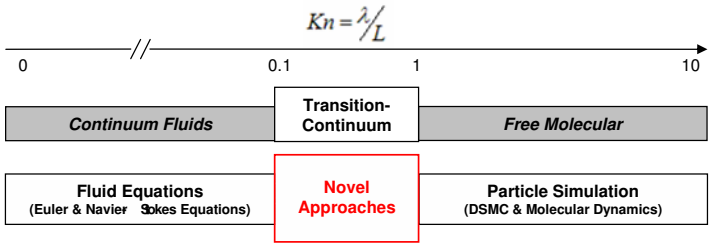

FIGURE 1.4: Outline of rarefied flow regimes and modelling techniques

be heavily dependent upon boundary conditions. In particular, a significant Knudsen sublayer starts to form at wall boundaries between the bulk fluid and the wall surface for even moderate levels of rarefaction, i.e. $Kn > 0.01$. This requires that the standard continuum assumption at the wall surface of stationary flow in thermodynamic equilibriun with the wall fails to adequately capture flow effects. Thus slip boundary conditions are necessary, with some finite velocity and temperature difference observed. For each simulation method, these slip values are heavily dependent upon the tangential momentum and energy accommodation coefficients. However, the evaluation of these coefficients presents a great challenge since they are heavily dependent upon a range of factors including the wall species, the gas species, the temperature of the wall, the surface finish, the cleanliness of the surface and the energy of the incident gas[**?**].

Ideally modelling of this effect would evaluate the accommodation coefficients for each of the incident molecules. Of all the schemes presented thus far, only molecular dynamics offers the means of accurately specifying these molecule-wall interactions, since it allows inclusion of the molecular structure of the wall. However, explicit evaluation of the accommodation of each incident molecule is too computationally expensive for existing technologies and instead each simulated particle represents a number of incident molecules. Providing coefficients for each simulated incident molecule, such MD simulations cannot typically evaluate the bulk flow due to the length scales involved, and instead these coefficients have previously been coupled with bulk continuum simulations in order to evaluate flow systems[**? ?**].

An alternative is to use a probabilistic approach, whereby each incident gas molecule is subject to accommodation determined by a probability distribution. One of several scattering kernels may be applied[**? ?**] and are applicable to either DSMC or direct solutions of the Boltzmann equation.

In the case of continuum models, a macroscopic viewpoint is most often taken and it is deemed

sufficient to utilise averaged accommodation coefficients. Typically specified by experimental research, they are not available for every gas-surface species combination and successive experimentation upon the same combination of materials can often show poor agreement due to the number of factors upon which accommodation may vary. Even so, averaged accommodation coefficients are heavily relied upon and are utilised in continuum slip models that evaluate wall slip velocity and temperature jump with additional dependence upon flow gradients in the vicinity of the wall[**?** **?**]; adoption of these averaged accomommodation models represents the most simplistic yet computationally efficient approach to evaluating slip.

In the simulation of gas neutralisers, the accommodation of incident plasma ions is also necessary. Of particular importance in determining the magnitude of the resultant mass/energy sources provided to the background gas, ideally an MD based simulation specific to the neutraliser plasma ion and wall atom species would be used to truly capture the effects of the molecular structure of the wall along with advanced effects such as adsorption and desorption. In the absence of such work, the use of Monte Carlo simulations validated by selected experimentation have been widely used within the fusion community to provide equivalent number and energy reflection coefficients for a range of gas-surface combinations[**?**]. These studies have also served to provide the isotopic dependence of these coefficients[**?**].

Therefore description of the accommodation of both incident gas and plasma ions can be crudely described by averaged coefficients. However, significant scope for improvement is possible via the use of atomistic schemes to better understand the variation of these coefficients with the myriad of variables upon which they depend.

1.4 Scope and Objectives

The delivery of efficient fusion systems is of paramount importance if fusion energy is to become reality. The efficiency shortfall observed in gas neutralisers is a prime example of how future improvement might be gained by enhanced understanding of existing systems. Therefore this thesis has sought to address the identified gap in existing knowledge of neutraliser gas dynamics via creation of a coupled beam-plasma-gas solver that accurately evaluates each component within the neutraliser.

From the information presented thus far one may identify two key challenges for the creation of such a solver:

1. Development of continuum-transition gas solver capable of accurately simulating both bulk and boundary effects whilst also being computationally efficient

2. Coupling of the beam, plasma and gas models to successfully modify the gas behaviour for the interaction mass/energy sources and sinks

To make use of the computational savings offered by continuum-based approaches, the research sought to apply the Burnett equations to the gas neutraliser and therefore this equation system forms the basis of the developed solver. To be supplemented by accurate gas mass/energy sources

and sinks representing interaction with the beam and plasma, the solver was to be implemeted within HiReCom, an existing in-house modelling framework created at Cranfield University. Note also that detailed modelling of the physics of gas-wall and ion-wall interactions represented a vast task in itself and thus does not form part of this research; averaged accommodation and reflection coefficients were instead deemed adequate for this study of neutraliser gas dynamics.

Thus the aims for this research may be summarised as follows:

- To develop a gas solver to provide accurate modelling of the continuum-transition regime via use of the Burnett equations. Production of this solver was to include the implementation of the necessary fluxes, boundary conditions and computational grid metrics within HiReCom and accuracy was to be ensured via assessment against several test cases.

- To apply the gas solver to the JET neutraliser system in order to assess the accuracy of the adopted modelling method.

- To extend and numerically discretise existing neutraliser beam and plasma models to allow coupling with the gas solver developed in HiReCom. Assessment of the coupled solver was to be undertaken against comparison with the various experimental data obtained at JET.

- To utilise the coupled solver to assess the factors affecting gas heating in neutraliser systems. Examination of future neutraliser systems was desired to predict the possible performance shortfall with a view to improving their design.

1.5 Thesis Structure

This thesis has sought to present the research in a logical and succinct fashion, with the contents of each chapter summarised as follows:

Chapter 2 presents a detailed examination of the JET neutraliser and the development in the understanding of gas heating. The development of the Burnett equations is also presented in considerable detail along with discussions of the slip boundary conditions and model coupling approaches used elsewhere.

Chapter 3 outlines the numerical method utilised in the developed solver. This includes examination of the physics of the neutraliser constituents and their various interactions, formulating a model to couple each of the modelled neutraliser components. The resulting gas governing equations and the computational method utilised within HiReCom are also presented.

Chapter 4 details the development of an accurate continuum-transition gas solver via incremental validation against published test cases. This chapter also seeks to address stability issues concerning the Burnett equations that have been ignored thus far in published works. Assessment of the solver against JET neutraliser experimental data represents the last test case.

Chapter 5 presents results from the finalised coupled solver when applied to two-dimensional and three dimesional neutraliser geometries, both in the presence and absence of beam. This chapter includes validation against experimental data. Several parameter scans are undertaken with a view to better understanding the influence of various model parameters.

Chapter 6 summarises the key findings of the work, assesses the success of the project and suggests suitable areas for future endeavour.

2

The Problem in Detail

Representing a collection of complex physics and engineering ideas, gas neutralisers must be placed in context in order to understand their function and to fully appreciate the principles of their design. A careful examination of the development in understanding of gas neutralisers facilitates the progression towards a logical and suitable model to address the outstanding questions concerning its operation. Therefore presented in this chapter is an overview of neutral beam heating both at JET and beyond, with discussion of the workings of gas neutralisers followed by a detailed presentation of the evolution in understanding of the JET neutraliser. The most appropriate modelling approach for each of the neutraliser constituents is considered. The development of the Burnett equations is further explored as the most appropriate gas modelling method. In closing this chapter, the most suitable means of coupling the models for the beam, plasma and gas is considered.

2.1 Neutral Beam Heating (NBH)

As outlined in Chapter 1, Neutral Beam Heating (NBH) forms the dominant plasma heating mechanism at JET. The system ultimately injects a stream of highly energetic atoms into the reactor vessel. Upon entering the plasma the beam atoms are ionised and thus subject to the intense magnetic field of the tokamak. Heating of the plasma is achieved as the beam particles equilibriate with the plasma, their excess energy is transferred to the other plasma particles via a series of collisions that ultimately provide an increase in the bulk plasma temperature[**?**]. The magnitude of the heating effect observed in the plasma is dependent on both the beam energy and current.

The beam of neutral atoms must be of a sufficiently high energy to allow penetration of the beam particles to the centre of the plasma; insufficient beam energy results in ionisation of the atoms at the plasma edge whereas more effective heating is achieved if ionisation occurs at or near the centre of the plasma. A larger beam current provides a larger number of energetic beam atoms to the plasma and thus a larger heating effect. Therefore the JET NBH operates beams at high energies and current (up to 130keV and 60A)[**?**].

Acceleration of the beam particles to high energies is achieved whilst they are ions. Therefore the neutral beam heating system initially creates large amounts of ions within the beam source, extracting and accelerating them to form a highly energetic ion beam via the use of high-voltage accelerator grids. However, as discussed earlier, the large magnetic field in the vicinity of the tokamak vessel prevents the injection of ions into the plasma. Therefore, this stream of energetic ions passes through a neutraliser with the intention of removing the charge of the beam particles. Within the JET NBH a positive ion beam is initially created and thus neutralisation occurs via the process of charge exchange upon background gas in the neutraliser. Upon emergence from the neutraliser, the beam is a composite of ions and neutral atoms. Therefore, the beam is subjected to the magnetic field of a series of bending magnets to divert the ionic beam component towards an ion dump whilst the neutral component of the beam proceeds unhindered towards the tokamak for injection into the plasma, as shown in figure 2.1.

The entire beamline is kept at near vacuum via substantial pumping infrastructure in the form of turbomolecular pumps and cryopanels, indicated in figure 2.2. Operation at near vacuum is required to minimise the background gas in the beam path beyond the neutraliser and bending magnets. Excess gas in this area results in re-ionisation of the purely neutral beam atoms, with the resulting ions swept onto the walls of the duct and torus port depositing significant heat loads. Note that the presence of duct scrapers in this region also serve to minimise heat loading due to the wings of the more tangential beams.

Upstream of the duct lies the rotary valve that can isolate the neutral injector system from the torus. Beyond this is the fast shutter, the original purpose of which was to minimise the flow of tritium from the torus to the beam injection boxes. When closed it provided a low vacuum conductance and therefore prevented tritium from drifting upstream where it would be condensed upon the cryopumps. Now redundant, this system was of particular importance following plasma disruption events, during which control of the plasma behaviour is lost.

At JET, the beam source, accelerator and neutraliser constitute a Positive Ion Neutral Injector (PINI). JET posesses 16 PINIs in total, sited in two stacks on opposite sides of the machine facilitating a total neutral injected power of up to 23 MW. In the near future, as part of the extensive EP2 upgrade[**?**], the NBH capacity is due to be vastly improved. Upon completion, a total neutral beam heating power of 36 MW will be available with maximum beam duration increased from 10 to 20 seconds.

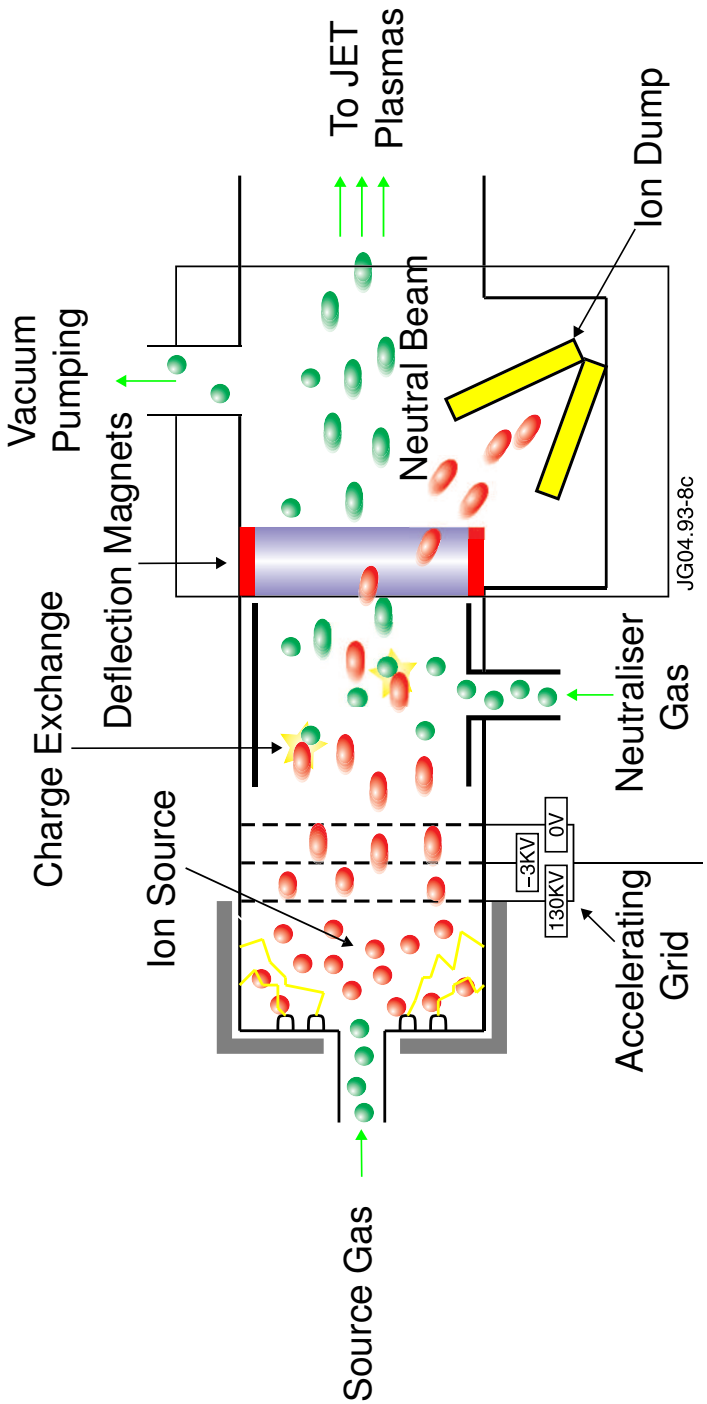

FIGURE 2.1: Progression of beam within the JET beamline

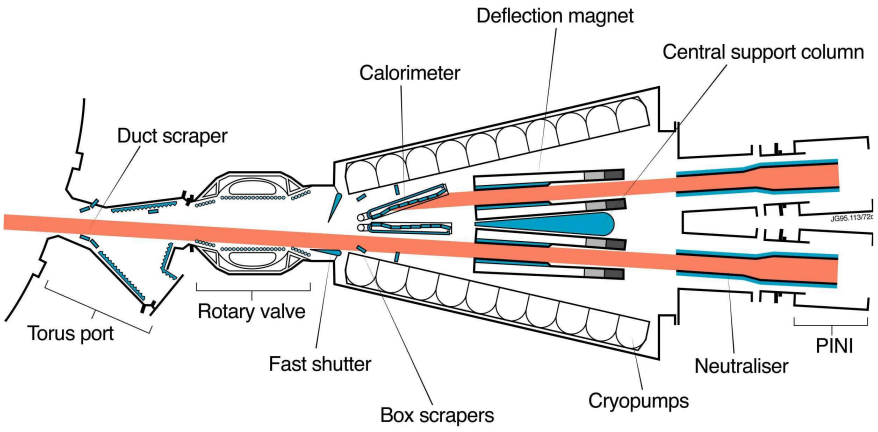

FIGURE 2.2: Plan view of the JET neutral beam injector

The ITER NBH differs in design to the JET system in several ways. Most prominent is that the ITER heating design consists of only two beam injectors each utilising a single beam source producing beams of negative polarity. These two beam injectors, together provide a total neutral power similar to that of the 16 JET PINIs, with the ITER HNB injector designed to produce an ion beam of 40A at an energy of 1MeV and visually summarised in figure 2.3. In addition to the considerably different beam, the ITER beamline will contain a very different gas neutraliser geometry, considerably improved pumping infrastructure and the use of an electric field to remove residual ions from the beam rather than application of a magnetic field, as found within the JET beamline.

Beyond ITER, there is significant conjecture concerning the plasma heating and current drive requirements for DEMO[**?**]. It is widely recognised that each of the present heating and current drive technologies, i.e. neutral beam heating and radio frequency heating, are currently too inefficient to form part of a power plant design. Defining overall efficiency of the NBH system to be the neutral beam power injected into the tokamak as a fraction of utilised electrical power, the efficiency of both the JET and ITER beamline designs is linked to the fraction of beam successfully neutralised within the gas neutraliser. Several technology studies have proposed alternative methods of beam neutralisation such as the use of a highly-ionised plasma or photo-neutralisation[**? ?**]. However, neither proposal has proved successful to date with the former method requiring excessive amounts of electrical power to generate the plasma, whilst the latter posesses significant technical challenges including the lack of reliability, lifetime and large cost associated with existing candidate laser technologies. Therefore whilst these alternative techniques

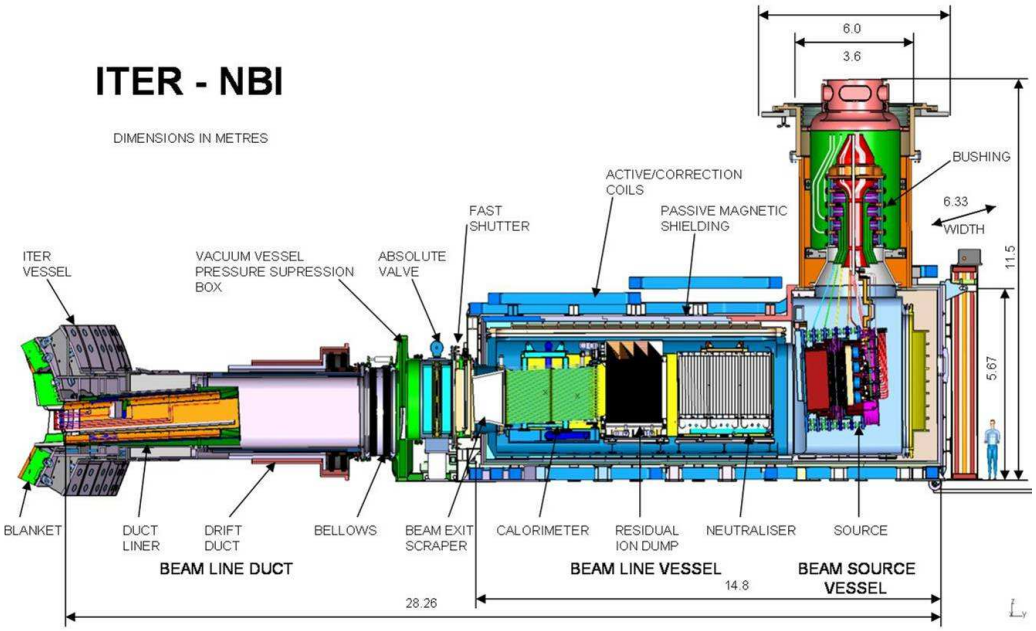

FIGURE 2.3: Plan view of the ITER neutral beam injector

achieve an elevated neutral fraction, they too face inherent drawbacks that have served to thus far prevent their widespread implementation.

2.2 Gas Neutralisers

The JET neutraliser is approximately $1.80m$ long in total and of rectangular race-track cross-section, as shown in figure 2.4. With small amounts of expansion and tapering along its length, this cross section varies from $180mm \times 460mm$ at its narrowest to $220mm \times 460mm$ at its widest. The neutraliser is split into two parts approximately at its longitudinal midpoint, with the resulting parts referred to as the first and second stage neutralisers. The JET beamline has a closely coupled beam source, meaning that upstream of the first stage neutraliser is an attached ion source and series of accelerator grids. Downstream of the second stage neutraliser is the remainder of the beamline including considerable pumping infrastructure to ensure near vacuum conditions in much of the beamline. The two neutraliser stages are separated by a small gap of $60mm$. Therefore, gas may enter the neutraliser via two possible paths; gas may be introduced directly to the

neutraliser via the gap between its two stages, or un-ionised surplus gas may stream into the neutraliser from the coupled beam source.

Alternative neutraliser designs, such as that proposed for the International Thermonuclear Experimental Reactor (ITER)[**?**], are not subject to a closely coupled beam source and the associated streaming of surplus source gas into the neutraliser. The ITER design also offers a significantly different geometry; the ITER design, shown in figure 2.5, at $4m$ is much longer than the JET neutraliser and consists of a number of narrow channels, $\sim 100mm$ in width, through each of which only a fraction of the beam passes.

Essentially gas neutralisers provide a volume of gas through which the beam passes in order to neutralise the ionic contents of the beam. Defining gas target $\int n\, dl_b$ as the gas density n integrated over the beam path through the neutraliser, the over-riding requirement of neutraliser design is to maximise the neutral beam fraction via provision of a gas target whilst minimising the inlet gas flow required to maintain that target. Minimisation of the inlet gas flow reduces the overall resource usage of the system and prevents excessive downtime due to cryopanel regenerations; the pumped gas collects on the surfaces of the cryopumps and must be periodically removed via a process known as regeneration, higher gas flows imply more frequent regenerations and thus reduced operational time.

The neutral fraction that may be realised for a beam of initially positive polarity is limited not only by gas target but also by the equilibrium beam composition. Essentially the neutral beam fraction that results from an infinite gas target, the equilibrium beam composition is dependent upon beam energy, dropping significantly with increasing beam energy for a positive ion beam. The beam composition assymptotically approaches the equilibrium with an increasing gas target, exemplified in figure 2.6 for a 120kV D^+ beam. Therefore in principle for a positive ion beam the larger the gas target, the larger the neutral beam fraction that results from passage of the beam through the neutraliser, though an increasingly small gain in neutral beam fraction is found for an increase in an already large gas target. By contrast, an initially negative ion beam has no equilibrium composition and instead there exists an optimum gas target, specific to each beam energy, at which a maximal neutral fraction might be obtained as demonstrated for a 1MV D^-beam in figure 2.6. Therefore a gas neutraliser associated with a negative polarity beam should aim to provide this optimal gas target to the beam.

With increasing energy, the maximal neutral fraction that may be obtained for a beam of negative polarity is significantly larger than the neutral equilibrium fraction that can be obtained for a beam of positive polarity; therefore at an equivalent beam energy it is possible to provide a larger neutral fraction from a negative polarity beam than one of positive polarity. This observation partially explains the transition to negative polarity for the ITER beamline design. Given the larger size of the ITER plasma, a vastly increased beam energy is required to allow penetration of the injected neutral beam atoms into the centre of the plasma, where they perform optimum plasma heating. Use of a negative beam will thus provide a much larger injected neutral power at the desired beam energy and more effective plasma heating than would be possible for a positive ion system.

At JET, the neutraliser gas target achieved has been well below that expected and thus the

injected neutral beam fractions during experimental operations have consistently fallen well below the equilibrium fractions for a positive polarity beam. Original predictions for the expected injected neutral beam power were made upon the neutraliser gas target in the absence of beam. However, these predictions proved erroneous upon introduction of the beam and measurement of the resulting neutral beam fraction; the presence of the beam served to introduce additional gas effects that surpressed the neutraliser gas target and reduced the resulting neutral beam fraction. Current understanding of this gas target depletion suggests that this is due to gas heating effects which serve to reduce the gas density in the neutraliser, providing two very different scenarios in the absence and presence of beam as summarised in figure 2.7. The following examination of the evolution of this understanding serves to place the project in context and better outlines the issues that this thesis aims to address.

2.3 Evolution of JET Neutraliser Understanding

Given the importance of the neutral beam heating system in providing heating power and fuel for the JET tokamak, significant endeavour was undertaken in formulating and detailing the JET neutraliser design to provide a maximal gas target for neutralisation of the beam. Study of the JET Design Notes reveals the attention given to gas flow within the neutraliser from early stages of the design; analytical flow models were derived by *Hemsworth and Boschi*, and investigated to optimise both the neutraliser system dimensions and the gas inlet placement[**? ?**]. Upon finalisation of the neutraliser design, further conductance analysis identified[**?**] that in the absence of beam much of the neutraliser fell within the continuum-transition regime; an intermediate gas flow regime between continuum and molecular flow wherein both traditional Computational Fluid Dynamics (CFD) and pseude-particle simulation methods both encounter difficulties. Thus, the performance of the neutraliser in the absence of beam was well understood whilst, by contrast, the influence of the beam upon gas target had been little considered until work using the prototype 6MW deuterium line built at Fontenauy-aux-Roses[**?**] indicated much lower gas targets in the presence of beam. Similar tests at JET confirmed poor agreement between measured and predicted neutralisation efficiencies, implying a significant reduction in the gas target[**? ?**].

Though the gas pressure profile throughout the neutraliser has been measured experimentally in the absence of beam via drawing of an ion gauge through the system[**? ?**], such a technique could not be applied in the presence of beam; given a lack of knowledge of the pressure and gas density profiles in the presence of the beam much conjecture followed over the cause of the shortfall. The agreed most likely explanation was that the reduced line density was due to significant heating of the background gas, for which *Pamela* proposed an analytical model[**? ?**]. The model was based upon a gas energy balance between losses at the walls and energy gained from the beam and the background plasma. The model considers momentum to be provided to

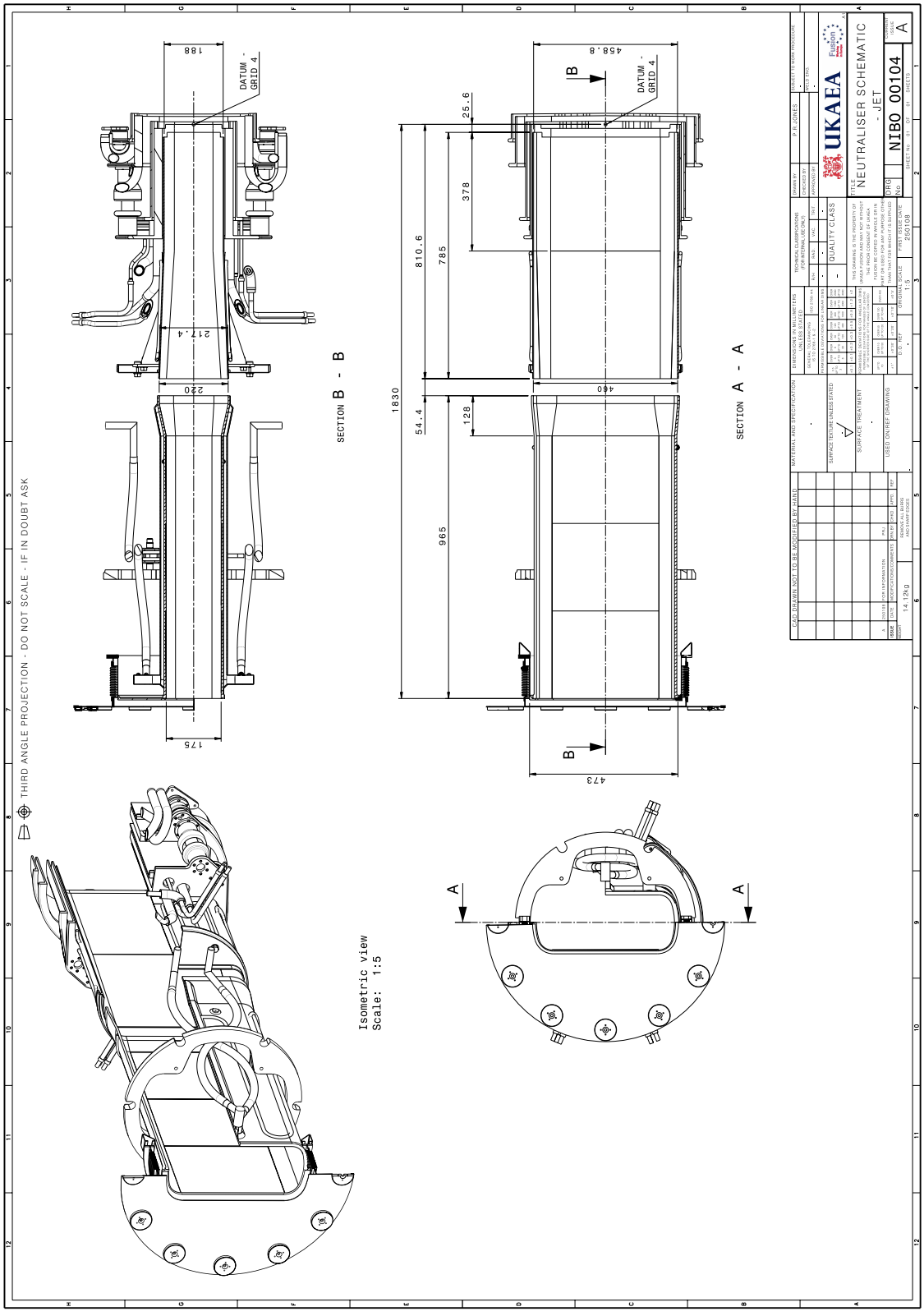

FIGURE 2.4: JET neutraliser geometry

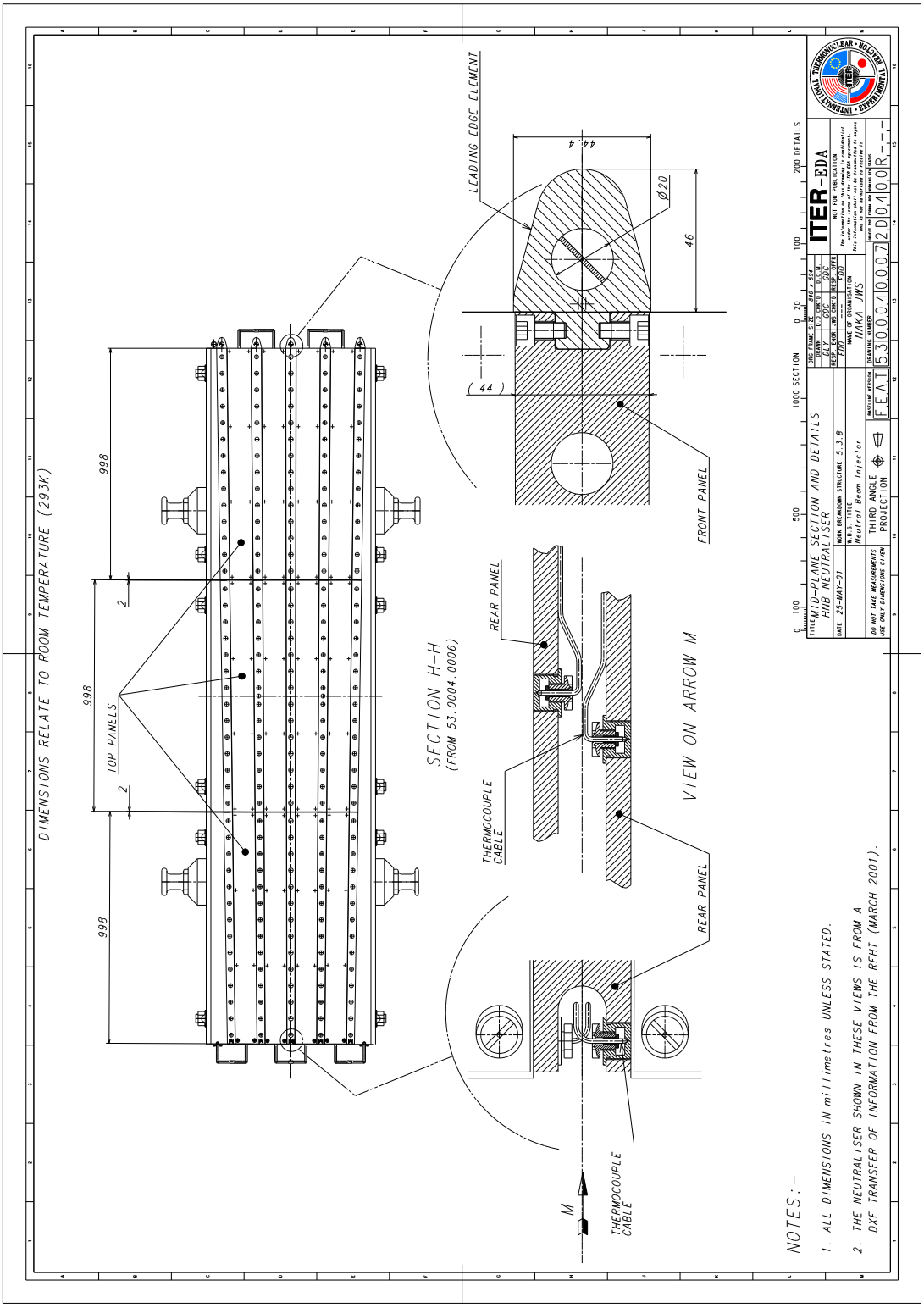

FIGURE 2.5: Longitudinal section of ITER neutraliser geometry[**?**]

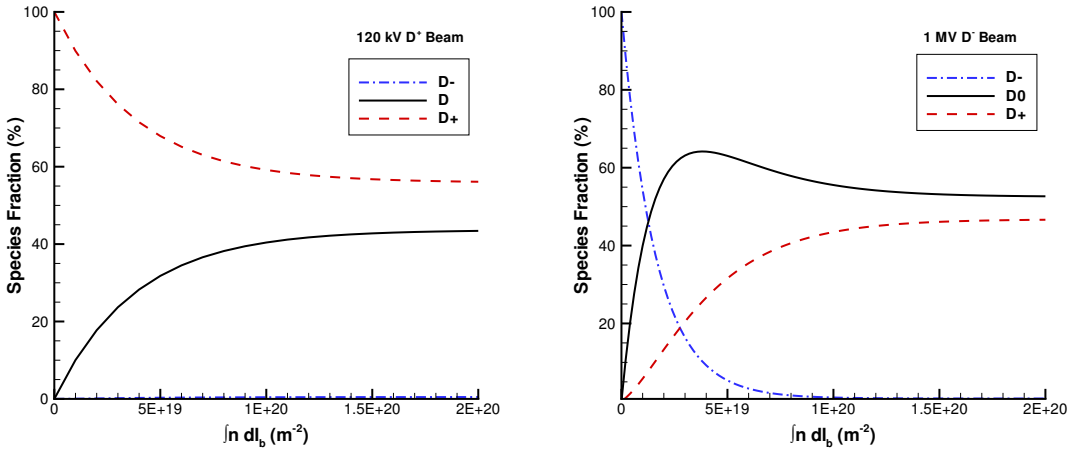

FIGURE 2.6: Equilibrium species fractions for initially positive and negative polarity beams

the gas solely via fast neutral and ionic products resulting from dissociation of the background gas molecules by beam ions and plasma electrons, and plasma ions neutralised and reflected at the wall (detailed discussion of the interaction of the various neutraliser constituents follows in Chapter 3).

Though this model omitted several collisional processes that may serve to further add to gas heating, the model was successfully validated experimentally at JET; the spectroscopic data of *Surrey and Crowley*[**?**] identified neutraliser gas temperatures up to 1200K, whilst electron density and temperature measurements confirmed the presence of a background plasma in the system[**? ?**]. Application of this experimental work to form parameters for substituition into *Pamela*'s model[**? ?**] identified the plasma ions neutralised and reflected at the wall as the dominant heating effect[**?**].

Subsequent attempts to modify the neutraliser walls to reduce the gas heating effect via minimisation of the energy of the reflected plasma ions proved unsuccessful. Another innovation was the inclusion of a septum plate, which effectively split the first stage neutraliser in two for much of its length, in accordance with predictions of much reduced gas heating effects from the heating model of *Pamela*[**?**] following reduction of the neutraliser dimensions. The gas temperature was duly reduced but the neutralisation efficiency observed on JET remained largely unchanged[**?**]. Therefore, though experimentation confirms significant gas heating effects within the JET neutraliser, the model of *Pamela*[**?**] appears unable to fully describe this effect.

In summary, the presence of the beam results in significant perturbation of the gas distribution in the JET neutraliser serving to produce a background plasma in the system, significantly heat the gas and reduce the gas target presented to the beam. However, examination of the work previously undertaken reveals a distinct lack of knowledge of the exact behaviour of the gas within the JET neutraliser system in the presence of beam. To improve this understanding via modelling represents a significant challenge since the complex web of interaction of the background gas

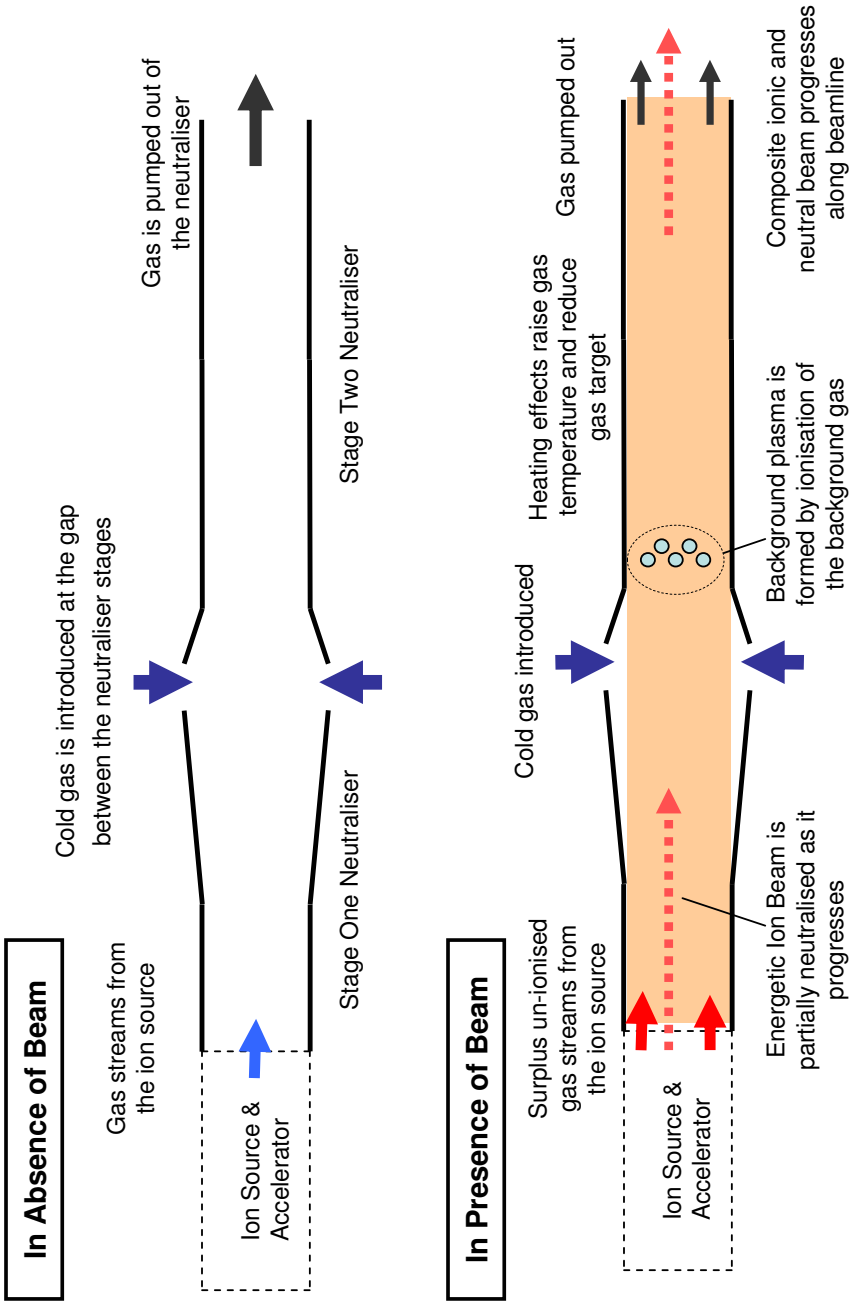

FIGURE 2.7: The JET neutraliser in the absence and presence of beam

with the beam and plasma must be carefully considered. This task is further compounded by the observation that the gas falls within the continuum-transition regime.

Considering work elsewhere within the fusion community, the application of Computational Fluid Dynamics to gas neutraliser systems is detailed in only a single publication; Los Alamos used a Navier-Stokes code[**?**] to model flows within a gas neutraliser system but failed to consider gas flow in the presence of the beam. Similarly, there is evidence of application of Monte-Carlo codes in several instances to neutraliser design, all in the absence of the beam[**?**]; one such example is the body of design work for the ITER neutraliser, produced with the aid of a 3D Monte-Carlo code[**?**]. In addition, since gas neutralisers represent a very unusual unification of ion beam, neutral gas and plasma, the author has been unable to find models of any alternative systems that are directly applicable for use; though some work on ion thrusters seeks to couple neutral and ionic fields in self-consistent simulations and thus presents similar challenges (see [**?**] and [**?**]). In short, there is miminal evidence of neutraliser gas modelling endeavour in the presence of an ion beam. Indeed, with the exception of the work of *Pamela*[**?**] and *Surrey*[**?**], the bulk of neutraliser modelling endeavour has instead been focussed upon the transport of the beam and interaction with the developing background plasma as exemplified by the work of *Duré et al.*[**?**].

2.4 Modelling of the Neutraliser Constituents

This thesis seeks to address the lack of knowledge of neutraliser gas behaviour in the presence of beam. This may only be achieved if one effectively and accurately models all three of the primary neutraliser constituents, namely the beam, plasma and gas. Though one cannot find a previous published modelling framework that may be directly applied to provide a complete model of the neutraliser contents, several techniques are available that would provide adequate models of each individual neutraliser component. The following examines each of the neutraliser contents in turn:

2.4.1 Beam Modelling

Much of the work in modelling ion beams is achieved via the use of Particle-in-Cell (PIC) Codes[**? ? ?**]. The primary concern of much of this work is the effect of space-charge neutralisation, a subject currently very applicable to the development of heavy ion inertial confinement fusion. However, a far simpler, computationally inexpensive method is available.

The work of *Nediakov*[**?**] has experimentally validated a 1D differential equation system to model beam neutralisation and spatial evolution. This system evaluates beam composition as a function of longitudinal distance. Parametric dependence upon reaction cross-sections and background gas density are also introduced. A very similar system has successfully been used by *Surrey*[**?**] to assess the ITER neutral beam system and forms beam prediction software currently in use at JET[**?**].

Given the focus of the thesis upon the gas dynamics within the JET neutraliser, evaluation of

beam composition is the main requirement of any beam model in order to correctly calculate the rates of beam-gas interaction and plasma production. Therefore the modelling of complex beam transport effects via PIC codes is unneccesary. Thus the beam model utilised in this thesis is based upon the far simpler work of *Nediakov*[**?**] and *Surrey*[**?**] as outlined in Chapter 3 wherein the physics of the neutraliser constituents and their interactions are discussed in detail.

2.4.2 Plasma Modelling

Fluid equations and particulate simulation are widely applied in plasma modelling[**? ? ? ?**]. However, in the case of the JET neutraliser, an analytical 1-D diffusion model has been derived by *Surrey*[**?**] to provide estimates of plasma density and temperature. Successfully validated via experimentation at JET[**?**], this model has also been extended and successfully applied to the ITER neutraliser[**?**]. Given its apparent accuracy and computational simplicity in comparison to alternative plasma simulation approaches, this model has been adapted and extended for use in this thesis. This model is the subject of extensive discussion in Chapter 3.

2.4.3 Gas Modelling in the Continuum-Transition Regime

Whilst the most appropriate choice of modelling approach for the beam and plasma within the neutraliser appears straightforward, this is in stark contrast to the neutraliser gas. Since much of the gas flow in the JET neutraliser falls within the continuum-transition regime, the system offers an interesting modelling challenge; typical continuum modelling techniques such as the Navier-Stokes equations are inadequate at these high levels of rarefaction, whilst the gas is insufficiently rarefied to readily apply molecular flow techniques. As discussed in Chapter 1, the latter would require excessively large numbers of simulation particles to provide accurate solutions thus proving prohibitively expensive in both computational time and memory requirments. Thus much published academic endeavour has served to develop several novel higher-order extended or generalized hydrodynamic equations that extend the accuracy of a fluid-based approach into the transitional regime.

One such approach is to extend the constitutive relations for stress and heat flux via the Chapman-Enskog series expansion to include additional higher-order terms beyond Navier-Stokes, which represents the first order solution with respect to Knudsen. Inclusion of these additional higher order terms allows more accurate approximation of the Boltzmann equation for increasing departure from thermodynamic equilibrium, as encountered with increasing rarefaction. As shown in (2.1) -(2.4), the second order solution provides the so-called Burnett Equations. Previous applications of the Burnett Equations, in their several forms, have demonstrated an improved ability to accurately simulate flows in the transitional regime[**? ?**]. Therefore this system represents an approach accurate within the continuum-transition regime, whilst retaining the computational efficiency of a fluid approach.

$$\begin{cases} \sigma_{ij} \approx \sigma_{ij}^{(1)} + ... + \sigma_{ij}^{(n)} \\ q_i \approx q_i^{(1)} + ... + q_i^{(n)} \end{cases} \tag{2.1}$$

$$Navier - Stokes : \begin{cases} \sigma_{ij} = \sigma_{ij}^{(1)} + O(Kn^2) \\ q_i = q_i^{(1)} + O(Kn^2) \end{cases} \tag{2.2}$$

$$Burnett : \begin{cases} \sigma_{ij} = \sigma_{ij}^{(1)} + \sigma_{ij}^{(2)} + O(Kn^3) \\ q_i = q_i^{(1)} + q_i^{(2)} + O(Kn^3) \end{cases} \tag{2.3}$$

$$Super - Burnett : \begin{cases} \sigma_{ij} = \sigma_{ij}^{(1)} + \sigma_{ij}^{(2)} + \sigma_{ij}^{(3)} + O(Kn^4) \\ q_i = q_i^{(1)} + q_i^{(2)} + q_i^{(3)} + O(Kn^4) \end{cases} \tag{2.4}$$

At the early developmental stages of this thesis, the Burnett Equations represented the most straight-forwardly applicable of the generalised hydrodynamic equation systems, with published three-dimensional derivations and well-established test cases. Therefore the Burnett Equations form the basis of the gas solver presented in this thesis. However, this system of equations is not without complications, as highlighted via examination of its development and many variations. The Conventional Burnett Equations, as proposed by *Chapman and Cowling*[**?**], are most often used system for study. Unfortunately, extensive analytical and computational work has demonstrated that, due to small wavelength disturbances, the system experiences instability with increasing grid refinement[**?**]. One amongst several amelioration strategies was that proposed by *Zhong*[**? ?**]: unconditional stability could be provided by the addition of several ad-hoc Super-Burnett terms (i.e. third order terms with respect to Knudsen) to create the Augmented Burnett equations, which were demonstrated to obtain the same results as the Conventional system. Recent work by *Turrilhon and Struchtrup*[**?**] has called into question the form of the ad-hoc terms and their associated coefficients, and also claimed that though *Zhong*'s equations[**?**] demonstrate temporal stability they exhibit spatial instability. However, the Augmented Burnett Equations have been successfully applied in up to three dimensions with no previous instability issues acknowledged by other authors[**? ? ? ? ? ? ?**].

An alternative, avoiding the ad-hoc application of additional terms, are the BGK Burnett Equations derived by *Agrawal et al.*[**?**] via consideration of an alternative collision integral in the Boltzmann Equation; assumption of the Bhatnagar-Gross-Krook (BGK) form of the collision integral and evaluation of moments of the second order Chapman-Enskog expansion provided the conservative form of the equation system. However, there are significant issues concerning the themodynamic validity of these equations[**?**]and additional questions concerning the selection of Prandtl number in their original derivation.The onset of instability also hinders the application of the use of the alternative ES-BGK Burnett equations, which are based upon the ellipsoidal-statistical BGK collisional model[**?**].

Ultimately, of the various Burnett Equation variants summarised in figure 2.8, none have proved obviously superior to the Augmented Burnett Equations. Effectively a higher-order correction of the Conventional Burnett Equations, a three dimensional variation of the equation system is readily available from published material along with various subsidiary test cases that facilitate the accurate development of a solver. Additionally, given the scatter-gun academic interest in the various versions of the Burnett Equations there has not been a huge amount of depth

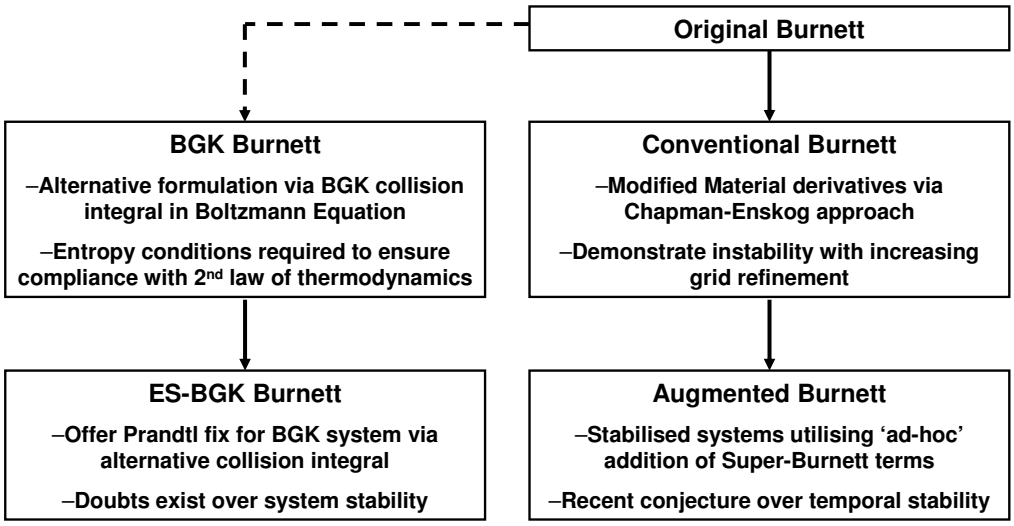

FIGURE 2.8: Outline of development of the Burnett Equations

to previous academic work upon the Augmented Burnett Equations, offering scope for original work to better understand their underlying performance. As such, the Augmented Burnett Equations have been selected for application within this thesis and form the basis of the gas simulation within the neutraliser models. Their implementation is discussed in Chapter 3, whilst the test cases to ensure accuracy of the various facets of the gas model are presented in Chapter 4. Also within Chapter 4 are original investigations of the Burnett Equations and Augmented Burnett Equations to assess previously unaddressed questions concerning their numerical stability and the effect of variable reconstruction schemes.

2.4.4 Coupling Modelling Systems

From the models selected for each of the neutraliser constituents, it is obvious that only the gas flow field need be subject to detailed evolution as both the beam and plasma are subject to fully analytical steady-state solution. Instead the beam and plasma will be evaluated from the knowledge of the gas distribution and not themselves explicitly evolved. This is reasonable given the much faster characteristic time of the beam and plasma, as well as the desire to focus the work upon better understanding the gas distribution. Therefore, having established the modelling techniques for application to each of the neutraliser contents, it is necessary to address how to most effectively couple the additional models to the CFD gas model in order to ensure a consistent model of the beam-gas-plasma system.

Examining published works one notes a common theme in the treatment of CFD models subject to chemical reactions; the fluid of interest in each case is subject to the inclusion of source and

sink terms for density, momentum and energy to model the effects of interaction with the additional species. For chemically reacting flows, these source/sink terms are based upon chemical reaction rates as exemplified by [**?**] and [**?**]. The only point of difference in the published works is how exactly these reaction rates are evaluated. Most typical is the approach of [**?**], where reaction rates are evaluated by consideration of experimental cross sections with reactant energies and densities extracted from the flow field.

By contrast, a far more complex means of modelling interaction is offered by use of a Monte-Carlo (MC) statistical approach exemplified by *de Jong et al.*[**?**]. This technique utilises CFD to evaluate gas evolution but couples this to MC methods that provide probabilistic simulation of local interaction in the flow field; at each local site of interest the MC model evaluates the interaction of multiple pseudo-particles defined by knowledge of the flow field, utilising sampling to ultimately provide the local reaction rate. Obviously this technique is much more computationally intensive but may offer more accurate evaluation of the reactions.

Given the overwhelming consensus in published works, this thesis also seeks to couple the models via source/sink terms within the gas governing equations. However, the much greater computational requirements of the Monte-Carlo reaction evaluation approach is to be avoided with simplistic calcualtion of reaction rates from flow field properties and experimental cross-sections preferred instead. One must note that the neutraliser offers a much more complicated system than the reacting flows typically simulated and therefore great care is necessary to ensure the formulation of the correct source/sink terms with deviation from their typical reaction rate forms. Fully explained and discussed in Chapter 3, their final form is achieved via detailed consideration of the physics of the system to better understand each of the interaction mechanisms between the three model components, namely the background gas, plasma and incident ion beam.

2.5 Wall Interaction

Near walls, there is a region of gas that is out of equilbrium due to the interaction of incident gas molecules with the wall surface; known as the Knudsen layer, its thickness is typically of the order of a mean free path. For continuum flows, at minimal rarefaction ($Kn < 0.01$) this layer is of negligible effect and one can readily ignore its effect. However, as rarefaction increases it is necessary that some finite slip velocity and temperature jump is used to describe the local thermodynamic inequilibrium. These slip values are provided by the use of models dependent upon local flow gradients and properties, with reliance upon the tangential momentum and energy accommodation co-efficients adopted for the wall interactions.

The most widely applied velocity slip condition is the first order model developed by Maxwell [**?**]. Treating the wall surface as an imperfect reflector, the assumption that some fraction σ of the molecules is absorbed by the surface and reemmited with velocities corresponding to stationary gas at the wall temperature is complemented by the assumption the the remaining fraction $1 - \sigma$ is perfectly reflected with no change in velocity. The fraction of absorbed and reemitted molecules corresponds to the tangential momentum accommodation coefficient, which is specific to the gas

species and wall material of interest. Use of a momentum balance ultimately provides the widely quoted version as in (2.5) wherein the exemplar slip velocity u_s is evaluated. The first term of this model is dependent upon the velocity gradient normal to the wall $\left(\frac{\partial u}{\partial \tilde{n}}\right)_s$, the local mean free path λ and the tangential momentum accommodation coefficient σ. The second term is introduced to account for the effects of thermal creep - a phenomena that results in the flow of rarefied gas from cold to hot regions of the wall - and is therefore dependent upon the temperature gradient parallel to the wall $\left(\frac{\partial T}{\partial \tilde{p}}\right)_s$. A consistent temperature jump model is offered by (2.6), which is dependent upon the temperature gradient normal to the wall $\left(\frac{\partial T}{\partial \tilde{n}}\right)_s$ and the energy accommodation coefficient α.

$$u_s = \frac{2-\sigma}{\sigma}\lambda\left(\frac{\partial u}{\partial \tilde{n}}\right)_s + \frac{3}{4}\frac{\mu}{\rho T}\left(\frac{\partial T}{\partial \tilde{p}}\right)_s \tag{2.5}$$

$$T_s = T_w + \frac{2-\alpha}{\alpha}\frac{2\gamma}{\gamma+1}\left(\frac{\partial T}{\partial \tilde{n}}\right)_s \tag{2.6}$$

Recent academic endeavour to establish which slip models offer greatest accuracy at continuum-transition levels of rarefaction has suggested that the Maxwell slip condition becomes inadequate with increasing rarefaction. Various studies have demonstrated that with increasing rarefaction the selection of slip boundary conditions has an increasing effect upon the evolved flow, with the enlargened Knudsen layer dominating the developed flow[**?** **?**]. These works have suggested that extension to second order slip models improves agreement with experimental data, with good accuracy offered up to molecular levels of rarefaction according to the work of *Maurer et al.*[**?**].

However, given the dominant interest of most authors in isothermal flows, few of the proposed second order velocity slip models are complemented by consistent temperature jump models. Of these few self-consistent model pairs, the Deissler second order boundary conditions have recently been shown to provide good comparison with experimental flow fields for $Kn \sim 0.25$[**?**]. Presented in (2.7)-(2.8), these conditions are derived via the adoption of the Navier-Stokes constitutive relations at the boundary, introducing additional terms dependent upon second order derivatives of the flow parallel to the wall $\left(\frac{\partial^2 T}{\partial \tilde{p}^2}\right)_s$, $\left(\frac{\partial^2 u}{\partial \tilde{p}^2}\right)_s$.

$$u_s = \frac{2-\sigma}{\sigma}\lambda\left(\frac{\partial u}{\partial \tilde{n}}\right)_s - \frac{9}{8}\lambda^2\left[\left(\frac{\partial^2 u}{\partial \tilde{n}^2}\right)_s + \frac{1}{2}\left(\frac{\partial^2 u}{\partial \tilde{p}^2}\right)_s\right] + \frac{3}{4}\frac{\mu}{\rho T}\left(\frac{\partial T}{\partial \tilde{p}}\right)_s \tag{2.7}$$

$$T_s = T_w + \frac{2-\alpha}{\alpha}\frac{2\gamma}{\gamma+1}\left(\frac{\partial T}{\partial \tilde{n}}\right)_s - \frac{9}{128}\lambda^2\left(\frac{177\gamma-145}{\gamma+1}\right)\left[\left(\frac{\partial^2 T}{\partial \tilde{n}^2}\right)_s + \frac{1}{2}\left(\frac{\partial^2 T}{\partial \tilde{p}^2}\right)_s\right] \tag{2.8}$$

There exist a set of boundary conditions that are derived from the Burnett constitutive relations, the linearised Maxwell-Burnett boundary condition. However, at the outset of this project minimal published test cases existed and the equations had only been presented in two-dimensions. Therefore this thesis has sought to apply the second order Deissler boundary conditions to gas neutraliser systems.

As outlined in Chapter 1, the adoption of constant coefficients to describe accommodation and reflection is typical for CFD models where coupling to alternative pseudo-particle treatment of wall interactions is deemed unsuitable. The experimental evaluation of these quantities for differing gas species is notoriously difficult and dependent upon an array of factors including the energy of the incident particle. In the neutraliser there are several distinct particle types that are subject to interaction with the wall: e.g. the bulk gas molecules, the fast neutral particles resultant from reactions, the fast ions resultant from reactions and the background plasma ions. For the gas populations this requires the provision of tangential momentum and energy accommodation coefficients, whilst for the ion populations number and energy reflection coefficents are necessary to describe the fraction successfully neutralised at the wall and refected back into the bulk flow. The parameters applicable to each particle type are treated distinctly with the use of experimental coefficients where possible. The selection of these parameters and detailed discussions of the origins of these alternative particle types, their origins and evolution in the neutraliser are discussed in detail in Chapter 3.

2.6 Summary

The evolution of neutraliser understanding highlights the continuing lack of knowledge of neutraliser gas dynamics. Consideration of emerging alternative technologies demonstrates the need to enhance existing gas neutralisers as no definitive alternative has been identified to date. The constituent models of the envisaged coupled beam-plasma-gas solver have each been considered in turn, with justification for the resultant CFD gas model coupled with analytical steady state beam and plasma profiles. The Burnett equations have been examined, with the Augmented Burnett equations deemed most appropriate to form the basis of the gas solver accurate within the continuum-transition regime. Following consultation of published techniques, coupling with the pre-existing beam and plasma models was to be achieved via their various interactions.

3

Modelling Approach

The numerical framework for this thesis is provided by a three-dimensional, unsteady, compressible solver permitting the evaluation of viscous fluxes up to Super-Burnett Order. A block-structured finite volume approach is adopted with solution utilising a generalised curvilinear coordinate system. A central difference scheme is employed for the viscous terms and a Godunov-type method solves for the inviscid fluxes. Both utilise variable reconstruction at the computational cell boundaries. For application to gas neutraliser systems, a detailed model has been developed of the various neutraliser species and their interaction. This model facilitates the formulation of the gas source/sinks provided by the beam and background neutraliser plasma. The resultant plasma model is also used to account for the effects of plasma pressure upon inviscid flux evaluation. Several of these components are newly implemented extensions to the HiReCom modelling framework, a code developed in-house at Cranfield, and the application of a domain decomposition approach has allowed each to be fully parallelised. This chapter presents an outline of the numerical framework for the thesis, with supporting materials provided in Appendices **??**-**??**.

3.1 Outline of the Governing Equations

The Navier-Stokes equations describe the physics of Newtonian fluid flow and represent an extremely useful system of equations. Derived from application of Newton's second law to fluid motion[**?**], they assume that the fluid stress is the sum of a diffusing viscous term and the thermodynamic pressure. As discussed previously, it is extension of this viscous term to higher orders of

approximation that provides the Conventional Burnett and Augmented Burnett equations. Therefore each of these equation systems is closely related, and each may be solved by consideration of a system of coupled generalised conservation laws. Consisting of the continuity, momentum and energy conservation equations (3.1)-(3.3), the fluid is described by its density ρ, cartesian velocity components emodied by $\boldsymbol{u}$ and total energy per unit volume e. Presented here in the absence of external fluid sources or sinks, the system of conservation equations encorporates viscous stresses $\boldsymbol{\sigma}$ and heat flux $\boldsymbol{q}$.

$$\frac{\partial \rho}{\partial t} + \nabla.(\rho \boldsymbol{u}) = 0 \tag{3.1}$$

$$\frac{\partial \rho \boldsymbol{u}}{\partial t} + \rho \boldsymbol{u}.\nabla \boldsymbol{u} + \nabla p - \nabla.\boldsymbol{\sigma} = 0 \tag{3.2}$$

$$\frac{\partial e}{\partial t} + \nabla.(e\boldsymbol{u}) + \nabla.(\boldsymbol{\sigma}.\boldsymbol{u}) + \nabla.\boldsymbol{q} = 0 \tag{3.3}$$

Assuming a perfect gas with negligible inter-molecular forces, the system of continuity equations is complemented by an equation of state (3.4) providing pressure p. This equation of state requires temperature T and gas constant R, the latter of which is is dependent upon the species for consideration. This, together with the assumption of constant specific heat capacities provides total energy e defined as in (3.5) where γ represents the ratio of specific heats and u, v and w are the three-dimensional cartesian velocities; this ratio takes a constant value, $\gamma = \frac{5}{3}$ for monatomic and $\gamma = \frac{7}{5}$ for diatomic gas molecules.

$$p = \rho R T \tag{3.4}$$

$$e = \rho \left(c_v T + \frac{u^2 + v^2 + w^2}{2} \right) \tag{3.5}$$

Given (3.1)-(3.5), it is therefore the description of the viscous stresses and heat fluxes that serves to close the system. Often referred to collectively as the constitutive relations, it is via differing definitions of viscous stress and heat flux that the Navier-Stokes, Conventional Burnett and Augmented Burnett equations may be modelled; assymptotic approximation of the heat flux and stress tensor with respect to Kn as in (3.6), implies that higher order approximation is offered by the inclusion of increasing numbers of terms. As outlined previously, the Navier-Stokes descriptions represent the first order approximation of the viscous stress and heat flux with respect to Knudsen. The Navier-Stokes viscous stress is defined as in (3.7), wherein $\boldsymbol{I}$ represents the identity tensor, μ the dynamic viscosity coefficient and λ_b the bulk viscosity coefficient. The bulk viscosity coefficient is defined by the Stokes hypothesis as in (3.8). Dependent upon the dynamic viscosity

	Maxwellian	Real Gas	Hard-Sphere
ω	1.0	~0.7	0.5

TABLE 3.1: Molecular interaction force models for differing viscosity interaction model exponents

coefficient, it allows for the dilation of the fluid. Within this thesis, the variation of dymanic viscosity co-efficient with temperature is provided by either Sutherland's law (3.9) or an interaction model (3.10) as specified for each flow case. Both require specification of the known viscosity μ_0 at absolute temperature T_0. Sutherland's law also requires parameter T_s from fitting to experimental data, whilst the viscosity interaction law instead necessitates specification of the molecular interaction model via parameter ω. Values of ω correspond to differing models as outlined in Table 3.1.

$$\begin{cases} \sigma_{ij} = \sigma_{ij}^{(1)} + \sigma_{ij}^{(2)} + ... \\ q_i = q_i^{(1)} + q_i^{(2)} + ... \end{cases} \tag{3.6}$$

$$\boldsymbol{\sigma} = -\lambda_b \left(\nabla . \boldsymbol{u}\right) \boldsymbol{I} - \mu \left(\nabla \boldsymbol{u} + \left(\nabla \boldsymbol{u}\right)^T\right) \tag{3.7}$$

$$\lambda_b = -\frac{2}{3}\mu \tag{3.8}$$

$$\mu = \mu_0 \left(\frac{T_0 + T_s}{T + T_s}\right) \left(\frac{T}{T_0}\right)^{\frac{3}{2}} \tag{3.9}$$

$$\mu = \mu_0 \left(\frac{T}{T_0}\right)^{\omega} \tag{3.10}$$

Ultimately, with the application of tensor notation (3.11)-(3.12), the Navier-Stokes stress tensor takes the form (3.14). The associated heat flux follows from Fourier's heat conduction law and is described by (3.15) where κ is the thermal conductivity coefficient specific to the modelled species. The Conventional Burnett equations and Augmented Burnett equations follow from inclusion of additional terms in the constitutive relations as presented in (3.16)-(3.21). Providing accuracy to the second order with respect to Kn, these additional terms present significantly complex and highly nonlinear viscous stresses $\boldsymbol{\sigma}$ and heat fluxes $\boldsymbol{q}$ when compared to their Navier-Stokes counterparts. Co-efficients ω_i and θ_i follow from the Chapman-Enskog method with application of a gas interaction force model. Thus differing co-efficient sets exist for differing assumed models. To date full derivations exist solely for the Maxwellian and hard-sphere models as provided in Appendix **??**. The interaction force model for a real gas falls somewhere between the Maxwellian and hard-sphere models as can be seen by the force model exponents given in Table 3.1. It has been proposed that via linear interpolation in the interaction model exponent ω, a suitable coefficient set for real gases might be provided from the two known coefficient sets[**?**]. However, this has proved inconclusive with studies suggesting that application of the hard-sphere coefficients show better agreement with experimental data [**?**]. In line with these findings, and the lack of a

derivation applicable to typical real gas interaction exponents, the hard-sphere coefficients have been applied throughout this thesis.

$$\overline{A_{ij}} = \begin{cases} \frac{A_{ij}+A_{ji}}{2} - \frac{1}{3}A_{kk} & if\ i = j \\ \frac{A_{ij}+A_{ji}}{2} & if\ i \neq j \end{cases} \tag{3.11}$$

$$A_{kk} = A_{11} + A_{22} + A_{33} \tag{3.12}$$

Navier-Stokes.

$$\begin{cases} \boldsymbol{\sigma^{(NS)}} = \sigma_{ij}^{(NS)} = \sigma_{ij}^{(1)} \\ \boldsymbol{q^{(NS)}} = q_i^{(NS)} = q_i^{(1)} \end{cases} \tag{3.13}$$

$$\sigma_{ij}^{(1)} = -2\mu\overline{\frac{\partial u_i}{\partial x_j}} \tag{3.14}$$

$$q_i^{(1)} = -\kappa\frac{\partial T}{\partial x_i} \tag{3.15}$$

Conventional Burnett Equations.

$$\begin{cases} \boldsymbol{\sigma^{(Burnett)}} = \sigma_{ij}^{(Burnett)} = \sigma_{ij}^{(1)} + \sigma_{ij}^{(2)} \\ \boldsymbol{q^{(Burnett)}} = q_i^{(Burnett)} = q_i^{(1)} + q_i^{(2)} \end{cases} \tag{3.16}$$

$$\begin{aligned} \sigma_{ij}^{(2)} = \frac{\mu^2}{p}\Bigg\{ & \omega_1 \frac{\partial u_k}{\partial x_k}\overline{\frac{\partial u_i}{\partial x_j}} + \omega_2\left[-\overline{\frac{\partial}{\partial x_j}\left(\frac{1}{\rho}\frac{\partial p}{\partial x_j}\right)} - \overline{\frac{\partial u_k}{\partial x_i}\frac{\partial u_j}{\partial x_k}} - 2\overline{\overline{\frac{\partial u_i}{\partial x_k}}\overline{\frac{\partial u_k}{\partial x_j}}}\right] + \\ & \omega_3 R\overline{\frac{\partial^2 T}{\partial x_i \partial x_j}} + \omega_4 \frac{1}{\rho T}\overline{\frac{\partial p}{\partial x_i}\frac{\partial T}{\partial x_k}} + \omega_5 \frac{R}{T}\overline{\frac{\partial T}{\partial x_i}\frac{\partial T}{\partial x_j}} + \omega_6\overline{\overline{\frac{\partial u_i}{\partial x_k}}\overline{\frac{\partial u_k}{\partial x_j}}}\Bigg\} \end{aligned} \tag{3.17}$$

$$\begin{aligned} q_i^{(2)} = \frac{\mu^2}{p}\Bigg\{ & \theta_1 \frac{1}{T}\frac{\partial u_k}{\partial x_k}\frac{\partial T}{\partial x_i} + \theta_2 \frac{1}{T}\left[\frac{2}{3}\frac{\partial}{\partial x_i}\left(T\frac{\partial u_k}{\partial x_k}\right)p + 2\frac{\partial u_k}{\partial x_i}\frac{\partial T}{\partial x_k}\right] + \\ & \theta_3 \frac{1}{\rho}\frac{\partial p}{\partial x_k}\overline{\frac{\partial u_k}{\partial x_i}} + \theta_4 \frac{\partial}{\partial x_k}\left(\overline{\frac{\partial u_k}{\partial x_i}}\right) + \theta_5 \frac{1}{T}\frac{\partial T}{\partial x_k}\overline{\frac{\partial u_k}{\partial x_i}}\Bigg\} \end{aligned} \tag{3.18}$$

Augmented Burnett Equations.

$$\begin{cases} \boldsymbol{\sigma^{(Aug.Burnett)}} = \sigma_{ij}^{(Aug.Burnett)} = \sigma_{ij}^{(1)} + \sigma_{ij}^{(2)} + \sigma_{ij}^{(A)} \\ \boldsymbol{q^{(Aug.Burnett)}} = q_i^{(Aug.Burnett)} = q_i^{(1)} + q_i^{(2)} + q_i^{(A)} \end{cases} \tag{3.19}$$

$$\sigma_{ij}^{(A)} = \frac{\mu^3}{p^2}\left\{\frac{3}{2}\omega_7 RT\overline{\frac{\partial}{\partial x_j}\left(\frac{\partial^2 u_i}{\partial x_k \partial x_k}\right)}\right\} \tag{3.20}$$

$$q_i^{(A)} = \frac{\mu^3}{p\rho}\left\{\theta_7 R\frac{\partial}{\partial x_i}\left(\frac{\partial^2 T}{\partial x_k \partial x_k}\right) + \theta_6\frac{RT}{\rho}\frac{\partial}{\partial x_i}\left(\frac{\partial^2 \rho}{\partial x_k \partial x_k}\right)\right\} \tag{3.21}$$

The initially presented (3.1)-(3.3) represent the equations that may be used to simulate gas flow in the absence of external sources and sinks. Whilst this is adequate to model the neutraliser in the absence of beam, this is not the case in the presence of beam; external gas sources and

sinks, such as those found in the neutraliser in the presence of beam due to interaction of the gas with both the beam and developed plasma, result in modification of the generalised conservation equations. Generally, in the presence of some external mass loss mechanism L_ρ, mass source mechanism S_ρ and additional energy source mechanism S_e one obtains the modified conservation equations (3.22)-(3.24). It is ultimately these equations that are solved within this thesis, with a modified equation of state; the pressure of the plasma p_p presents an additional external force upon the background gas and thus modifies the equation of state from (3.4) to some modified pressure $\widehat{p}$ (3.25). The challenge therefore in the presence of the beam, is to accurately model and quantify both the source/sink mechanisms and the plasma pressure. To achieve this a detailed model of the beam-gas-plasma interactions is necessary, with the interactions serving to couple the developed beam, plasma and gas models.

$$\frac{\partial \rho}{\partial t} + \nabla.(\rho \boldsymbol{u}) = S_\rho - L_\rho \tag{3.22}$$

$$\frac{\partial \rho \boldsymbol{u}}{\partial t} + \rho \boldsymbol{u}.\nabla \boldsymbol{u} + \nabla p - \nabla.\boldsymbol{\sigma} = \left(S_\rho - L_\rho\right)\boldsymbol{u} \tag{3.23}$$

$$\frac{\partial e}{\partial t} + \nabla.(e\boldsymbol{u}) + \nabla.(\boldsymbol{\sigma}.\boldsymbol{u}) + \nabla.\boldsymbol{q} = e\frac{\left(S_\rho - L_\rho\right)}{\rho} + S_e \tag{3.24}$$

$$\widehat{p} = p + p_p \tag{3.25}$$

3.2 Neutraliser Physics Summary & Interaction Model

Within this subsection, the neutraliser contents and their interaction with one another are considered in detail. Assumptions are then proposed to facilitate the modelling of each component within a consistent system that ultimately provides suitable sink and source terms for inclusion in the gas governing equations. Extension of the existing beam and plasma models allows their steady state description for any given gas density profile. This approach may be readily applied to either positive ion or negative ion neutral injection systems. The text assumes a deuterium beam and neutraliser gas but the modelling framework could also be utilised for modelling a hydrogen beam and gas. With appropriate species specific extensions, this framework could be extended to any beam-gas species combination subject to the availability of the relevant cross-sections.

The finalised interaction model consists of three main components - the beam, the plasma and the background gas. The item of most interest is the background gas, with gas source/sink terms offered by the interactions between the model components as summarised in figure 3.1. To provide these source/sink terms the physics of the interactions within the neutraliser must be carefully examined, with the particles of interest defined as follows:

I. Beam The beam is considered to consist of ions and neutrals with beam composition varying as it progresses along the neutraliser in accordance with the background gas density. Reactions of

the beam with the background gas produce various products, which are duly considered in the model: (1) charge exchange reactions form plasma ions, (2) ionisation reactions produce plasma ions and primary electrons, (3) projectile loss reactions produce stripped electrons, (4) dissociation reactions produce primary electrons as well as neutral and ionic dissociation products.

II. Plasma Ions Created by ionisation and charge exchange reactions within the beam path, work outlined in this chapter allows the steady state plasma ion distribution, sheath electron temperature and sheath ion potential to be determined along the neutraliser for a given background gas density profile.

III. Primary Electrons The electrons of significant energy born via ionisation and dissociation reactions at the beam, that lose energy to thermalise and form the background plasma electrons in the neutraliser. Their initial energies are well known from various analytical and experimental work as detailed in this chapter.

IV. Stripped Electrons Are heavily forward projected electrons that travel in the beam path having been created by projectile loss reactions of beam ions or neutrals.

In summary, the gas suffers gas density, momentum and energy losses due to:

I. Interaction with the beam

- Charge exchange by positive ions
- Ionisation of the gas by each of the beam species
- Dissociation reactions due to positive beam ions

II. Interaction with electrons

- Dissociation reactions due to primary electrons
- Dissociation reactions due to stripped electrons

Several of these interactions provide energetic products, which will deposit some fraction of their energy into the gas. Upon reaching equilibrium with the background gas, these reaction products provide an additional mass and momentum source for the gas. Therefore gas mass, momentum and energy sources are provided by:

I. Dissociation by beam positive ions

- Neutral energetic products resulting from dissociation reactions
- Ionic products resulting from dissociation reactions are subject to acceleration, neutralisation and reflection upon initial contact with wall, reflecting as neutral energetic products.

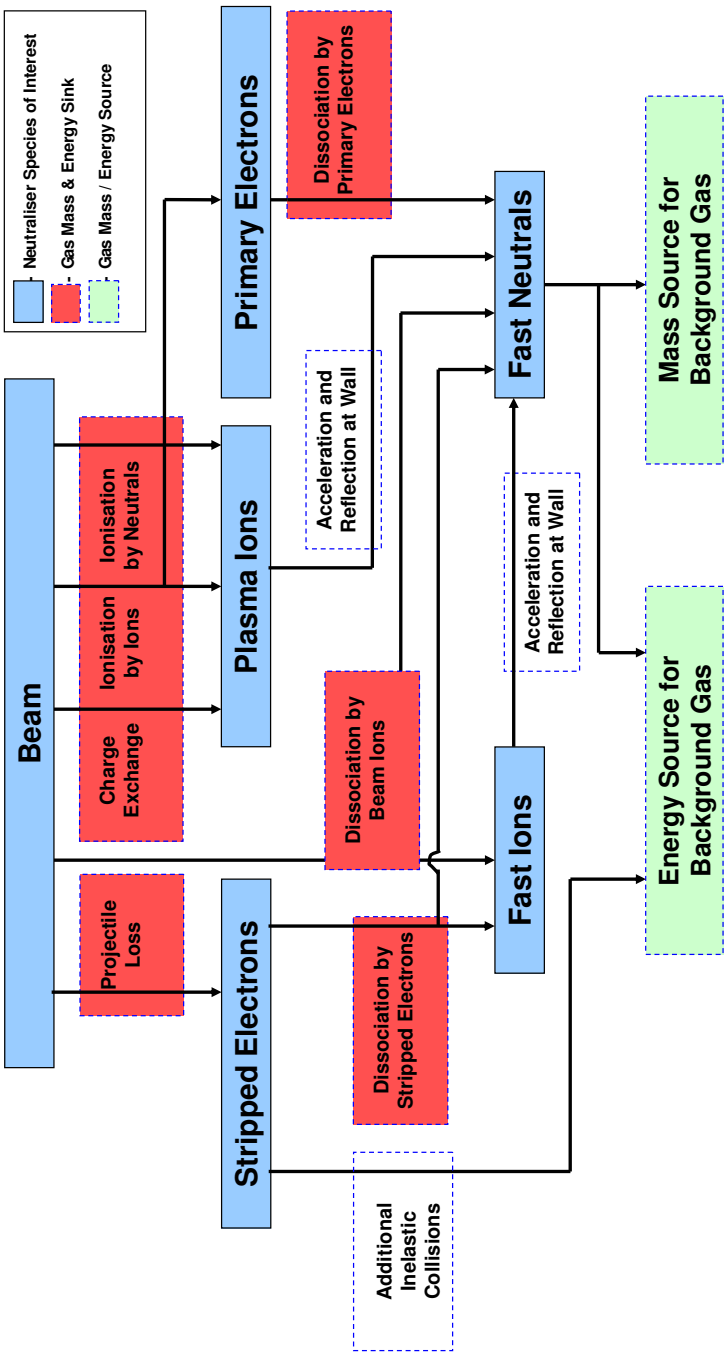

FIGURE 3.1: Summary of gas sources and sinks as described by the interaction model

II. Dissociation by primary electrons

- Neutral energetic products resulting from dissociation reactions

III. Dissociation by stripped electrons

- Neutral energetic products resulting from dissociation reactions
- Ionic products resulting from dissociation reactions are subject to acceleration, neutralisation and reflection upon initial contact with wall, reflecting as neutral energetic products.

IV. Plasma ions

- Plasma ions are subject to acceleration, neutralisation and reflection at the wall, reflecting as neutral energetic products.

Note that within the remainder of this chapter $\boldsymbol{r} = (x, y, z)$ refers to some general position in the neutraliser; x refers to the longitudinal distance of that point from the upstream neutraliser boundary, y refers to height relative to the beam centre and z refers to the depth relative to the beam centre. Obviously it follows that x is always positive, whilst y and z may be either positive or negative. The model ultimately considers the system as a series of infinitesimal slices along the x axis, each of thickness δx. The infinitesimal slice about $\boldsymbol{r}$ defined by $\boldsymbol{r} \pm \frac{\delta x}{2}$ as in (3.26) where $y\epsilon\,(y_{min}, y_{max})$ and $z\epsilon\,(z_{min}, z_{max})$ represent the extent of the neutraliser at longitudinal position x. An infinitesimal volume about $\boldsymbol{r}$, is denoted by $\boldsymbol{r} \pm \frac{\delta r}{2}$ and defined by (3.27) wherein δy and δz represnt the thickness about y and z respectively. A simple visual representation of the infinitesimal neutraliser slice concept is provided in figure 3.2.

$$\boldsymbol{r} \pm \frac{\boldsymbol{\delta x}}{\mathbf{2}} = \left(x \pm \frac{\delta x}{2}, y, z\right) \quad \text{where } y\epsilon\,(y_{min}, y_{max}) \;\&\; z\epsilon\,(z_{min}, z_{max}) \tag{3.26}$$

$$\boldsymbol{r} \pm \frac{\boldsymbol{\delta r}}{\mathbf{2}} = \left(x \pm \frac{\delta x}{2}, y \pm \frac{\delta y}{2}, z \pm \frac{\delta z}{2}\right) \tag{3.27}$$

3.2.1 Beam

During experimental operations, the beam required by the system operator is specified using several parameters. Typically, a particular injected neutral power is required. At JET, to minimise the heat loading on certain components in the beam line, it is also desired that the beam width be minimised and this is achieved by ensuring the beam is at optimum perveance. This optimum perveance is achieved during operation via careful selection of the extracted beam energy and current. Perveance, defined in (3.28), is a collective parameter utilised to indicate the significance of the effect of space-charge upon the trajectory of the individual beam ions. The optimum perveance with respect to beam width is an intrinsic property of each positive ion injector that varies with beam power, as shown in figure 3.3 for a typical JET PINI, and is fully characterised during their conditioning.

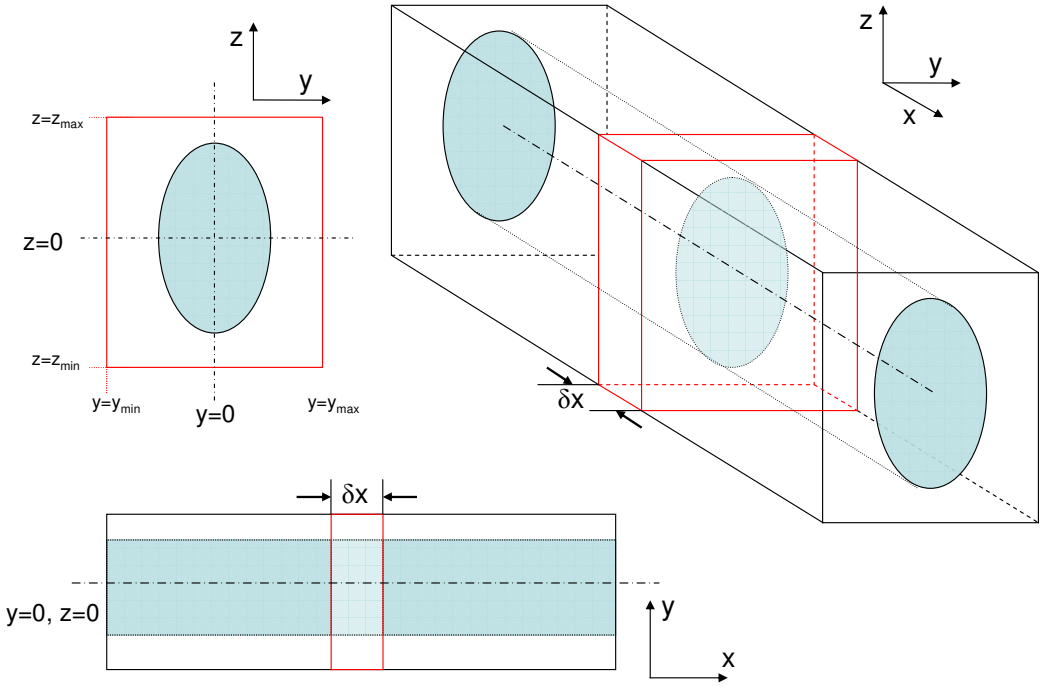

FIGURE 3.2: Outline of the infinitesimal neutraliser slice concept

$$Perv = \frac{I_b}{V_b^{1.5}} \tag{3.28}$$

It is ultimately the extracted beam energy V_b and current I_b that dictate the initial energy in keV per atomic mass unit U_b, velocity v_b and density of the beam n_b entering the neutraliser. For positive ion neutral injection systems such as that at JET, this extracted beam is dominated by D^+ particles with a small portion of D_2^+ and D_3^+ ions. Possessing reduced energy and differing reaction cross-sections, one notes from Table 3.2 that these heavier beam ions present only a small fraction of the beam ion flux. The fraction of the beam flux presented by each beam species is dependent upon several beam parameters - arc current, pressure and magnetic field. For negative ion neutral injection systems such as the ITER beamline, it is the instability of the heavier molecular ion D_2^- that results in a singular extracted beam species of D^-.

To ease simulation, it is reasonable to assume for both positive and negative ion based systems that the beam is mono-energetic and consists solely of a single beam species upon extraction from the source. Therefore within this thesis, PINIs (Positive Ion Neutral Injectors) are assumed to inject only D^+ to the neutraliser, whilst NINIs (Negative Ion Neutral Injectors) inject only D^- particles. However, as it passes through the neutraliser the composition of either beam type changes

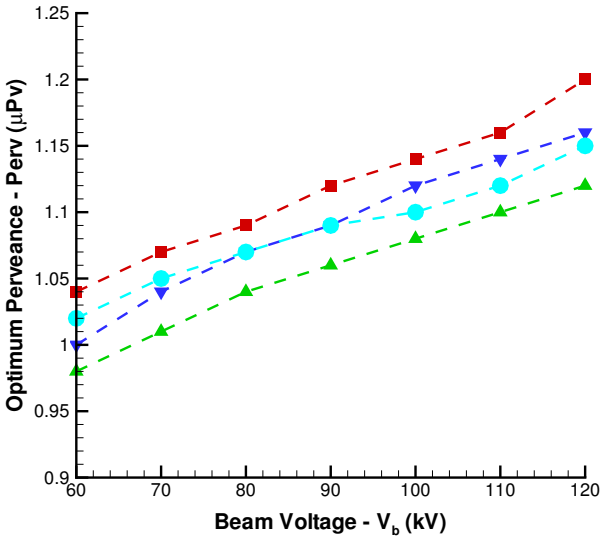

FIGURE 3.3: Optimum perveance versus power for several exemplar JET PINIs

	Supercusp Source		
PINI Voltage/Current	80kV/52A	80kV/60A	130kV/60A
D^+ flux fraction	87.0	89.0	90.0
D_2^+ flux fraction	9.0	8.0	7.0
D_3^+ flux fraction	4.0	3.0	3.0

TABLE 3.2: Ion beam species fractions for JET beam source

due to interaction with the background gas. The assumption of a single beam ionic species implies that the beam composition can be described according to a system of 1D species equations, essentially taken from *Surrey*[**?**] and presented in (3.29). This formulation considers the neutral beam density $\overline{n_b^0}$ and ionic beam density $\overline{n_b^+}$ and $\overline{n_b^-}$ to be uniform across its width. Thus the beam composition is dependent upon the average gas density within its path $\overline{n}$, defined at some longitudinal location as in (3.30) where A_b denotes the beam cross-sectional area. To provide the reaction cross-sections for this description of the beam it is necessary that the processes occurring in the beam are examined in detail.

$$\begin{cases} \frac{d\overline{n_b^0}}{dx} = \overline{n}\left(\overline{n_b^+}\sigma_{10} + \overline{n_b^-}\sigma_{\bar{1}0} - \overline{n_b^0}\left(\sigma_{01} + \sigma_{0\bar{1}}\right)\right) \\ \frac{d\overline{n_b^+}}{dx} = \overline{n}\left(\overline{n_b^-}\sigma_{\bar{1}1} + \overline{n_b^0}\sigma_{01} - \overline{n_b^+}\left(\sigma_{10} + \sigma_{1\bar{1}}\right)\right) \\ \frac{d\overline{n_b^-}}{dx} = \overline{n}\left(\overline{n_b^0}\sigma_{0\bar{1}} + \overline{n_b^+}\sigma_{1\bar{1}} - \overline{n_b^-}\left(\sigma_{\bar{1}0} + \sigma_{\bar{1}1}\right)\right) \end{cases} \tag{3.29}$$

$$\overline{n}\left(x\right) = \frac{\int_{A_b} n\left(x,y,z\right) dA}{A_b} \tag{3.30}$$

Beam Processes Positive ions in the beam may become either neutral or negative via charge exchange with the background gas. Also referred to as electron capture, these processes form a sink for the background gas molecules as can be seen in $(R1)$-$(R4)$:

- Charge Exchange on molecules (σ_{CE}): $D^+ + D_2 \rightarrow D^0 + D_2^+$ $(R1)$
- Dissociative Charge exchange (σ_{BD1}): $D^+ + D_2 \rightarrow D^0 + D + D^+$ $(R2)$
- Charge Exchange on atoms $\left(\sigma_{\widetilde{CE}}\right)$: $D^+ + D \rightarrow D^0 + D^+$ $(R3)$
- Double electron capture(σ_{DCE}): $D^+ + D_2 \rightarrow D^- + 2D^+$ $(R4)$

It is possible that neutrals present in the beam may also return to an ionic state. Negative ions are formed from beam neutrals via electron capture as in $(R5)$-$(R6)$ whilst positive ions results from projectile electon loss as in $(R7)$-$(R8)$:

- Beam neutral electron capture (σ_{EC}): $D^0 + D_2 \rightarrow D^- + D_2^+$ $(R5)$
- Electron capture with ionisation: $D^0 + D_2 \rightarrow D^- + 2D^+ + e$ $(R6)$
- Single neutral projectile electron loss $\left(\sigma_{PL_0}\right)$: $D^0 + D_2 \rightarrow D^+ + D_2 + e$ $(R7)$
- Projectile electron loss with double ionisation: $D^0 + D_2 \rightarrow D^+ + 2D^+ + 3e$ $(R8)$

An electron from each of these projectile electron loss mechanisms possesses significant energy and is capable of themselves inducing further reactions as well as providing energy to the background gas via thermalisation. These stripped electrons are discussed in greater detail in 3.2.2 and are also provided by reactions that serve to form beam neutrals and positive ions from negative ions in the beam as outlined in $(R9)$-$(R10)$:

- Single negative projectile electron loss $\left(\sigma_{PL_-^1}\right)$: $D^- + D_2 \rightarrow D^0 + D_2 + e$ $(R9)$
- Double negative projectile electron loss $\left(\sigma_{PL_-^2}\right)$: $D^- + D_2 \rightarrow D^+ + D_2 + 2e$ $(R10)$

Summing the cross sections of the reactions outlined above, ignoring those of sufficiently small cross-section, one can produce suitable values for σ_{10}, $\sigma_{1\bar{1}}$, σ_{01}, $\sigma_{0\bar{1}}$, $\sigma_{\bar{1}1}$ and $\sigma_{\bar{1}0}$. For simplification of each of the model components (namely the beam, plasma and background gas) it is assumed that the atomic deuterium presence in the neutraliser is minimal when compared to the level of molecular deuterium. Thus, the contribution of $\sigma_{\widetilde{CE}}$ can be ignored within the beam. As such, the cross-sections for the spatial evolution of the beam composition may be taken as in (3.31)-(3.36) with exemplar cross sections given in Table 3.3:

$$\sigma_{10} = \sigma_{CE} + \sigma_{BD1} \tag{3.31}$$

$$\sigma_{1\bar{1}} = \sigma_{DCE} \tag{3.32}$$

$$\sigma_{01} = \sigma_{PL_0} \tag{3.33}$$

	Equation	Cross Section m^2 $(10^{-20}m^2)$ (D)			Reference
		$80keV$	$100keV$	$120keV$	
$\sigma_{CE}(R1)$	$D^+ + D_2 \rightarrow D^0 + D_2^+$	2.50	1.93	1.35	ORNL[**?**]
$\sigma_{BD1}(R2)$	$D^+ + D_2 \rightarrow D^0 + D + D^+$	0.476	0.367	0.283	Crowley[**?**]
$\sigma_{DCE}(R4)$	$D^+ + D_2 \rightarrow D^- + 2D^+$	0.0242	0.0228	0.0235	ORNL[**?**]
$\sigma_{EC}(R5)$	$D^0 + D_2 \rightarrow D^- + D_2^+$	0.0993	0.0798	0.0602	ORNL[**?**]
$\sigma_{PL_0}(R8)$	$D^0 + D_2 \rightarrow D^+ + D_2 + e$	1.54	1.48	1.42	ORNL[**?**]
$\sigma_{PL_-^1}(R9)$	$D^- + D_2 \rightarrow D^0 + D_2 + e$	6.33	1.97	2.05	ORNL[**?**]
$\sigma_{PL_-^2}(R10)$	$D^- + D_2 \rightarrow D^+ + D_2 + 2e$	0.397	0.377	0.356	ORNL[**?**]
$\sigma_+(R11)$	$D^+ + D_2 \rightarrow D^+ + D_2^+ + e$	1.83	1.95	2.20	ORNL[**?**]
$\sigma_0(R12)$	$D^0 + D_2 \rightarrow D^0 + D_2^+ + e$	1.46	1.38	1.31	ORNL[**?**]

TABLE 3.3: Exemplar beam projectiles cross-section table for 80,100,120 keV

$$\sigma_{0\bar{1}} = \sigma_{EC} \tag{3.34}$$

$$\sigma_{\bar{1}1} = \sigma_{PL_-^2} \tag{3.35}$$

$$\sigma_{\bar{1}0} = \sigma_{PL_-^1} \tag{3.36}$$

In addition to those processes which affect beam composition, the beam components can induce additional gas processes which leave the beam composition unaffected, but serve to provide an additional gas sink:

- Single ionisation by positive ion (σ_+):$D^+ + D_2 \rightarrow D^+ + D_2^+ + e$ $(R11)$
- Single ionisation by beam neutral (σ_0):$D^0 + D_2 \rightarrow D^0 + D_2^+ + e$ $(R12)$
- Dissociative ionisation (σ_{BD2}):$D^+ + D_2 \rightarrow D^+ + D^+ + D + e$ $(R13)$
- Double ionisation (σ_{BD3}):$D^+ + D_2 \rightarrow D^+ + 2D^+ + 2e$ $(R14)$
- Simple dissociation (σ_{BD4}):$D^+ + D_2 \rightarrow D^+ + 2D$ $(R15)$

The most appropiate cross-section to describe the ionisation of gas by negative ions is the subject of some academic debate. The plane-wave Born approximation predicts the same cross section for ionisation by either positive or negative ions of the same mass [**?**]. However, this approximation is only valid at high energies, in particular above $\backsim 3.6MeV$ for deuterium [**?**]. Instead, the neutral ionisation cross-sections have been proposed as an alternative for projectile energies typically experienced in neutralisers [**?**]. It is this latter approach that has been applied in this thesis for each of the systems considered; though not ideal for the $1MeV$ beam projectiles of the ITER beamline the author considers this common approach across each of the systems to be most prudent for the research undertaken.

With regards to calculation of relevant cross-sections, the variation of σ_{10}, $\sigma_{1\bar{1}}$, σ_{01}, $\sigma_{0\bar{1}}$, $\sigma_{\bar{1}1}$, $\sigma_{\bar{1}0}$, σ_+ and σ_0 with energy is provided by use of the Chebyschev polynomials. A sequence of orthogonal polynomials defined in (3.37), they provide cross-sections at a given U_b, the projectile energy in keV per atomic mass unit, following normalisation to the valid energy range (E_{min}, E_{max}). Evaluation requires multiplication of each orthogonal polynomial by its corresponding constant,

from $A(0) - A(8)$, with subsequent summation as exemplified in (3.38). The constants required for several relevant cross-sections are presented within the widely used ORNL 'Red books'[**?**] and summarised in Table 3.4. Since each of these reactions occurs with a background molecule, altering its state to provide differing products, one should note that this collection of reactions represents a significant gas density, momentum and energy sink as will be discussed further in section 3.2.5.

$$\begin{cases} C_0(x) = 1 \\ C_1(x) = x \\ C_{n+1}(x) = 2xC_n(x) - C_{n-1}(x) \\ x = \frac{2ln(U_b) - ln(E_{min}) - ln(E_{max}))}{ln(E_{max}) - ln(E_{min})} \end{cases} \tag{3.37}$$

$$\sigma(x) = \sum_{i=0}^{8} A(i) C_i(x) \tag{3.38}$$

Several of the remaining beam cross-sections are provided by alternative function forms. For example, the beam dissociation cross-sections are given by *Crowley*[**?**] as presented in (3.39)-(3.42). These too offer a significant gas sink, as discussed further in 3.2.2 and formulated in 3.2.5.

$$\sigma_{BD1} = exp\left(2.6\left(1 - \frac{U_b}{100}\right)\right).10^{-21} \tag{3.39}$$

$$\sigma_{BD2} = (0.7 + (U_b - 40)/100).10^{-21} \tag{3.40}$$

$$\sigma_{BD3} = exp\left(0.79\left(1 - \frac{U_b}{121}\right)\right).10^{-21} \tag{3.41}$$

$$\sigma_{BD4} = \frac{9.7exp\left(-3.4\left(1 - \frac{64.4}{U_b}\right)^2\right).10^{-21}}{1 + 10^5\left(\frac{U_b}{39}\right)^6} \tag{3.42}$$

Beam Power Loss The energy loss of the beam along the neutraliser is governed by the stopping power. The stopping power model created by *Surrey*[**?**], which is based upon the work of *Ziegler*[**?**] and *Allison et al.*[**?**], describes the power imparted by the beam as it traverses the neutraliser. The model, presented in (3.43), is dependent upon the beam composition, area A_b, velocity and energy, the background gas density and the length of neutraliser traversed $\triangle x$. Stopping power H_{Stop} consists of two components H_{low} and H_{high} dependent upon beam energy as shown in (3.44), combining to provide the energy deposited per unit length at a reference gas number density, defined by Loschmidt's number N_0. The ratio of atomic to total stopping power χ may be estimated from the experimental data provided by *Allison et al.*[**?**] and is tabulated in Table 3.5. Given the treatment of negative ions as neutrals for the purposes of ionisation, χ is taken to descibe the ratio of neutral and negative ion to total stopping power within this thesis.

	$A(0)$	$A(1)$	$A(2)$	$A(3)$	$A(4)$	$A(5)$	$A(6)$	$A(7)$	$A(8)$	E_{min}	E_{max}
σ_{10}	-82.5164	-6.70755	-6.10977	-2.6281	0.709759	0.639033	0.10298	0.26124	-0.263817	2.6	4E6
$\sigma_{1\bar{1}}$	-95.8165	-7.17049	-7.48288	-1.93034	0.761153	0.556689	-0.0542859	-0.270184	-0.0147551	200	1E6
σ_{01}	-79.0892	0.34603	-3.04496	0.50849	-0.075866	0.108006	0.0059345	0	0	60	2E7
$\sigma_{0\bar{1}}$	-82.8333	-1.65457	-2.060408	-1.5387	-0.368649	-0.41362	-0.165702	-0.127116	-0.256041	40	4.6E5
$\sigma_{\bar{1}0}$	-73.1506	-1.75695	-2.00168	-0.19028	0.0171353	0.127083	-0.152314	0	0	2.3	1.7E7
$\sigma_{\bar{1}1}$	-79.0159	-2.10252	-1.24073	0.174799	0.106249	-0.000434273	-0.0465674	0	0	1000	1E7
σ_i	-75.4752	-0.100192	-1.35816	0.230586	0.187780	-0.157087	0.102380	0	0	5000	3.8E6
σ_n	-77.1205	2.47663	-1.43551	-0.126243	0.100447	0.066212	-0.0477593	0	0	200	4E5

TABLE 3.4: Supporting constants for cross-sections evaluation by Chebyschev polynomials[**?**]

Kinetic Energy (eV)	20	50	100	150
χ	0.64	0.42	0.31	0.3

TABLE 3.5: Ratio of atomic to total stopping power for a hydrogen beam [**?**]

Gas	Plasma		Beam	
$n\left(m^{-3}\right)$	$n_p\left(m^{-3}\right)$	$T_e(eV)$	$n_b\left(m^{-3}\right)$	$v_b\left(ms^{-1}\right)$
3×10^{19}	2×10^{16}	15	2×10^{15}	2×10^{6}

TABLE 3.6: Typical experimental values for the JET neutraliser contents subject to 120kv 60A beam

One should also note that the additional stopping power of the beam upon the plasma has been evaluated and considered negligible at the typical plasma densities indicated by experiment and presented in Table 3.6.

$$P_b^{neut} = H_{Stop}\triangle x\left(\overline{n_b^+} + \frac{\chi}{1-\chi}\left(\overline{n_b^0} + \overline{n_b^-}\right)\right)\frac{A_b v_b \overline{n}}{N_0} \tag{3.43}$$

$$H_{Stop} = \begin{cases} \frac{2\times4.272\times10^{-6}}{\frac{1}{H_{high}}+\frac{1}{H_{low}}} & \text{if target is } D_2 \\ H_{low} = 1.45U_b^{0.45} & \\ H_{high} = \frac{242.6}{U_b} ln\left(1+\frac{1.2\times10^4}{U_b}+0.1159U_b\right) & \end{cases} \tag{3.44}$$

Though of significance as an energy source to the neutraliser contents, the energy lost by the beam in traversing the neutraliser is insufficient to significantly reduce the beam velocity at the background gas densities typically observed in gas neutralisers, exemplified in Table 3.6. Thus the beam can be considered to be of constant energy and velocity along its path through the neutraliser.

Beam Profile Entering as an array of beamlets, the beam focuses slightly as it progresses through the neutraliser. This is demonstrated in figure 3.4 using sections of the beam profile provided by *PINI Simulator*[**?**], a beamline simulation software package developed at JET. However, computational constraints in the form of system resources, numerical stability and model complexity imply that the modelling of individual beamlets is impossible at present and therefore does not form part of this thesis.

3.2.2 Energy to the Background Gas

The energy lost by the beam in traversing the neutraliser can be partitioned into differing components, of which *Pamela*[**? ?**] outlines three:

- Molecular ionisation and dissociation
- Excitation of upper atomic and molecular states which is radiatively re-emitted

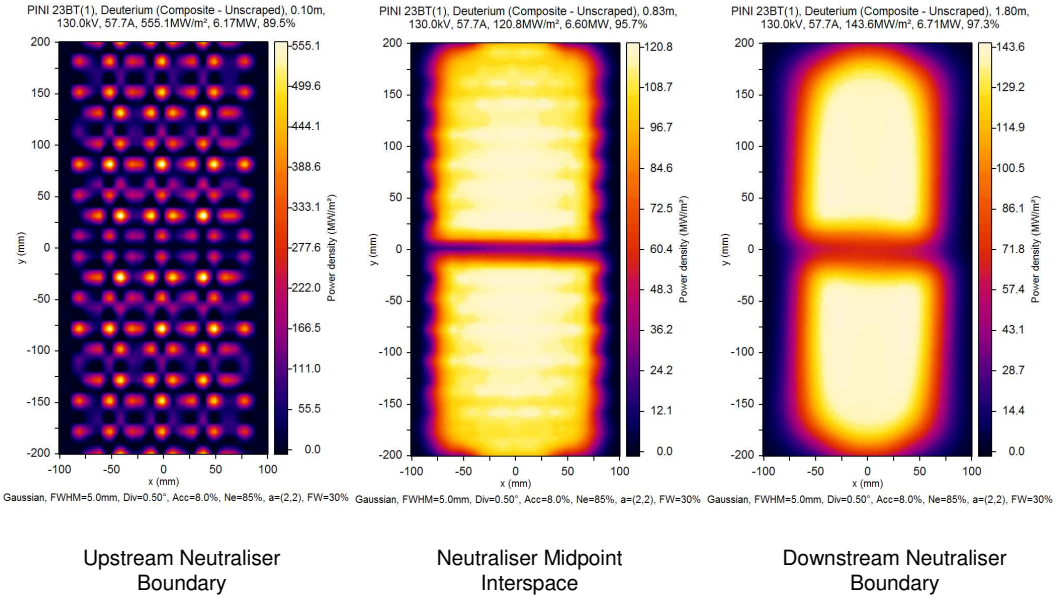

FIGURE 3.4: Beam profile sections along the JET neutraliser from the PINI Simulator[**?**]

- Elastic collision of the beam components with the background gas

The effects of higher vibrational states, in increasing dissociation cross-sections but reducing the energies of the dissociation products, can be assumed to effectively compensate one another with respect to gas heating. Thus excitation of upper atomic and molecular states can be ignored in developing the model. In addition, the elastic collision cross-section, and thus the possibility of direct momentum transfer from the beam to the background gas, is several orders of magnitude less than the molecular ionisation and dissociation processes. Therefore, energy transfer from the beam to the background gas via elastic collision can also be ignored[**?**]. It is concluded that energy transfer from the beam to the background gas occurs indirectly; instead of the beam components, it is the dissociation products and plasma ions that eventually transfer momentum to the background gas via elastic collisions.

Pamela[**?**] proposed two sources of dissociation of the background gas, namely beam ions and background plasma electrons. Re-evaluation of the processes within the neutraliser suggests that this description is incomplete. Instead this thesis proposes three sources of dissociation: (1) beam ions - as per the work of *Pamela*[**?**], (2) primary electrons, i.e. electrons resulting from interactions at the beam and that ultimately thermalise to form the background plasma - these possess greater energy than the thermal plasma electrons and thus greater dissociation cross-sections, (3) stripped electrons, i.e. electrons resulting from beam projectile loss - given their elevated energies these electrons offer significant dissociation cross-section via two possible reactions.

	Equation	Cross-Section $(10^{-20}m^2)$ (D)			Product Energy
		80 keV	100 keV	120 keV	
$\sigma_{BD1}(R16)$	$D^+ + D_2 \rightarrow D^0 + D + D^+$	0.682	0.110	0.0595	$5eV$
$\sigma_{BD2}(R17)$	$D^+ + D_2 \rightarrow D^+ + D^+ + D + e$	0.04	0.06	0.08	$5eV$
$\sigma_{BD3}(R18)$	$D^+ + D_2 \rightarrow D^+ + 2D^+ + e$	0.13069	0.1147	0.10066	$10eV$
$\sigma_{BD4}(R19)$	$D^+ + D_2 \rightarrow D^+ + 2D$	0.85173	0.6286	0.46356	$2.2eV$
$\sigma_{1\bar{1}}$	$D^+ + D_2 \rightarrow D^- + 2D^+$	0.0224	0.0228	0.0235	$10eV$

TABLE 3.7: Table of dissociation by beam ion cross sections[**?** **?**]

In addition to these indirect heating mechanisms, a further energy source for the background gas has recently been identified by *Surrey*[**?**]; stripped electrons in the beam can deposit large fractions of their energy in the background gas via inelastic collisions. In a similar vein, the author proposes that primary electrons also deposit energy in the background gas via inelastic collisions on their path from the beam to the neutraliser wall.

Thus there appears six modes of such 'indirect heating' which serve to transfer momentum to the background gas, and each of the mechanisms for indirect heating is discussed in the following subsections:

- Dissociation by Beam Ions
- Dissociation by Primary Electrons
- Dissociation by Stripped Electrons
- Primary Electron thermalisation via additional inelastic collision
- Stripped Electron thermalisation via additional inelastic collision
- Plasma Ion wall reflection

Dissociation by Positive Beam Ions Molecular dissociation reactions, which serve to split gas molecules into their constituent parts may be induced by several mechanisms within the neutraliser and release significant energy to the dissociation products. Since *Herzberg* suggests that *'The potential energy functions of two isotopic molecules… are identical to a high degree of approximation'*[**?**], the size of this energy release for any hydrogenic molecule can be found via examination of the potential energy curves for the H_2 and H_2^+ electronic states.

From *Massey*[**?**] it is known that several dissociation paths exist for the hydrogen molecule. The appropriate dissociation path for a molecule is determined via the amount of excitation energy supplied, defining which of the dissociative states the molecule ultimately adopts. To allow dissociation to two H atoms, at least $8.8eV$ of excitation energy must be supplied to the initial molecule; this is the minimum interaction energy within the shaded area of figure 3.5 that elevates the molecule from the ground state to the dissociative state $1^3\Sigma_u$. Dissociation then provides each of the product atoms with an energy of $2.2eV$. Similarly, dissociation to an H atom and H^+ ion occurs from the dissociative state $H_2^{+2}\Sigma_u$ following excitation with $28eV$ and ultimately supplies the products with $5eV$ of energy each. Finally, two H^+ ions, each possessing $10eV$ are produced

from the dissociative state H_2^{++} following excitation with $46eV$. Therefore, assuming each of these reaction paths is also valid for deuterium molecules, the energies of the dissociation products are well defined for each.

One of several neutraliser species capable of inducing dissociation of the background gas are beam positive ions. Summarised in Table 3.7, dissociation by beam positive ions may occur via several reaction routes, with dissociation product energies as indicated. Since each dissociation reaction serves to split a background gas molecule, each dissociation reaction represents a gas sink for density, momentum and energy. Presented later, detailed description of this sink is aided by the definition of a total beam dissociation cross-section $\sigma_{b.diss}^{total}$ as in (3.45).

$$\sigma_{b.diss}^{total} = \sigma_{10B} + \sigma_{BD2} + \sigma_{BD3} + \sigma_{BD4} + \sigma_{1\bar{1}} \tag{3.45}$$

For a given beam energy, one can similarly define the total neutral and ionic beam dissociation product cross-sections as $\sigma_{b.diss}^{prod_0}$ (3.46) and $\sigma_{b.diss}^{prod_+}$ (3.48) utilising cross-sections summarised in (3.39)-(3.42). One can also calculate a characteristic ionic product energy $\overline{E_{b.diss}^{+}}$ and neutral product energy $\overline{E_{b.diss}^{0}}$ via (3.47) and (3.49). These properties facilitate the treatment of the various products as singular neutral and ionic populations simplifying the formulation of the gas sources as presented later in this chapter.

$$\sigma_{b.diss}^{prod_0} = \sigma_{BD1} + \sigma_{BD2} + 2\sigma_{BD4} \tag{3.46}$$

$$\overline{E_{b.diss}^{0}} = \frac{\sigma_{BD1}E_{BD1} + \sigma_{BD2}E_{BD2} + 2\sigma_{BD4}E_{BD4}}{\sigma_{bd.diss}^{prod_0}} \tag{3.47}$$

$$\sigma_{b.diss}^{prod_+} = \sigma_{BD1} + \sigma_{BD2} + 2\sigma_{BD3} \tag{3.48}$$

$$\overline{E_{b.diss}^{+}} = \frac{\sigma_{BD1}E_{BD1} + \sigma_{BD2}E_{BD2} + 2\sigma_{BD3}E_{BD3}}{\sigma_{bd.diss}^{prod_+}} \tag{3.49}$$

Primary Electrons The vast majority of electrons formed within the neutraliser are produced by interaction of the background gas molecules with projectiles in the beam. The production cross section and initial energy distribution of these 'primary' electrons can be found from experimental measurements and analytical models published by *Rudd*[**? ?**]. Primary electrons are formed in the beam path and can possess significant initial energy, before undergoing inelastic collisions with the background gas and thermalisation with the background plasma.

The electron temperature utilised in calculating dissociation by electrons is of particular importance. Rather than previous works which have applied the measured background plasma temperature, the author feels that the work of *Rudd* should be applied to instead evaluate dissociation by primary electrons; upon formation these primary electrons possess higher initial energy than that presented by the thermal electron temperature, enhancing the dissociation cross-section.

The analytical models of *Rudd* provide primary electron properties for various target gases subjected to a proton projectile. As isotopic influence is minimal according to *Rudd*, these models

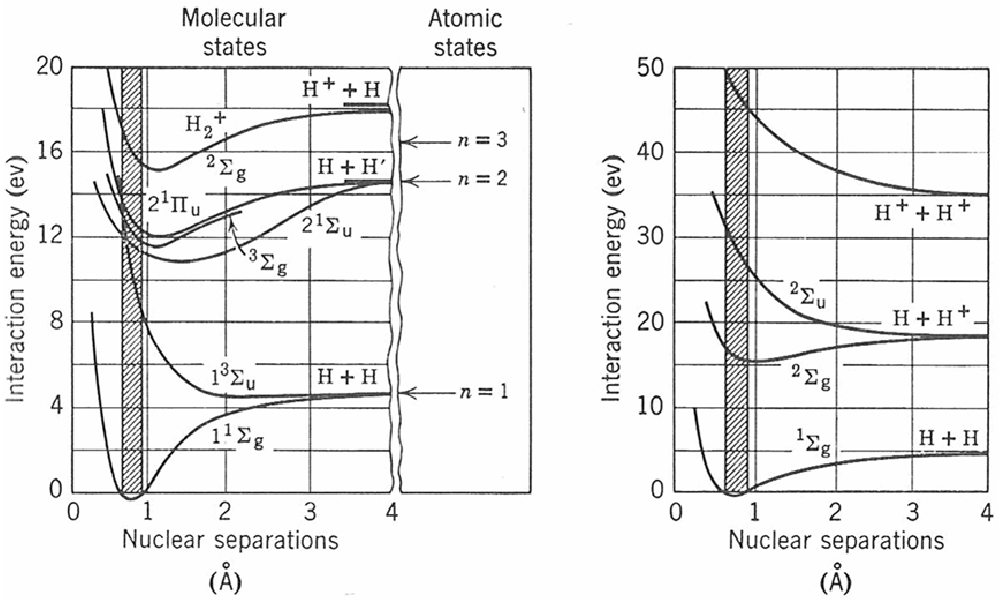

FIGURE 3.5: Potential energy curves for hydrogen[**?**]

therefore offer primary electrons properties for both hydrogen and deuterium positive ion beams. For each gas target species, *Rudd*'s models provide the differential cross-section $\frac{d\sigma_{pe}}{dE_{pe}^{H^+}}$ with respect to resultant primary electron energy $E_{pe}^{H^+}$. This is calculated from a number of expressions, constants and some parameters specific to the gas target of interest. Evaluation of $\frac{d\sigma_{pe}}{dE_{pe}^{H^+}}$ for a series of resultant primary electron energies $E_{pe}^{H^+}(i)$ allows calculation of characteristic primary electron energy and total production cross-section via (3.50) - (3.51)

$$\begin{cases} \sigma_{pe}^{H^+} = \sum_{i=1}^{\infty} \left(E_{pe}^{H^+}(i) - E_{pe}^{H^+}(i-1) \right) \frac{d\sigma_{pe}^{H^+}}{dE_{pe}^{H^+}}(i) \\ E_{pe}^{H^+}(0) = 0 \end{cases} \tag{3.50}$$

$$\begin{cases} \overline{E_{pe}^{H^+}} = \dfrac{\sum_{i=1}^{\infty} E_{pe}^{H^+}(i) \left(E_{pe}^{H^+}(i) - E_{pe}^{H^+}(i-1) \right) \frac{d\sigma_{pe}^{H^+}}{dE_{pe}^{H^+}}(i)}{\sigma_{pe}^{H^+}} \\ E_{pe}^{H^+}(0) = 0 \end{cases} \tag{3.51}$$

It is desirable that these primary electron properties may be evaluated for any combination of beam neutral-ion composition to allow description of the primary electrons at any point along the beam path within the neutraliser. However, the only estimates of the electron energy distribution and production cross-section from neutral hydrogen projectiles result from experimentation

upon a helium target, again produced by *Rudd*. Therefore some manipulation of these existing analytical models and experimental results is required to allow application to the hydrogenic gas target within the neutraliser and permit the evaluation of the total primary electron production cross-section and characterstic primary electron energy for any beam composition.

Rudd's analytical models predict the characteristic primary electron temperature for both hydrogen $\overline{E_{pe}^{H^+}}$ and helium $\overline{E_{pe}^{He^+}}$ to be roughly equal for a given proton projectile energy. Thus the same can be reasonably assumed for a neutral hydrogen projectile implying that the characteristic primary electron energy observed in *Rudd*'s experimental helium data $\overline{E_{pe}^{He^0}}$ can be readily adopted for a hydrogen target to give $\overline{E_{pe}^{H^0}}$ as in (3.52).

$$\overline{E_{pe}^{H^+}} \approx \overline{E_{pe}^{He^+}} \Rightarrow \overline{E_{pe}^{H^0}} = \overline{E_{pe}^{He^0}} \tag{3.52}$$

By contrast, *Rudd*'s analytical model for the total primary electron production cross-section suggests a significant difference in the predicted results for hydrogen and helium targets, i.e. $\sigma_{pe}^{H^+} \neq \sigma_{pe}^{He^+}$. Thus it is proposed that the experimental cross section data for helium subjected to a neutral projectile should be scaled in line with the ratio of these analytical predictions; this proposal provides the total production cross-section for a hydrogenic target subject to a neutral projectile $\sigma_{pe}^{H^0}$, as in (3.53).

$$\sigma_{pe}^{H^0} = \frac{\sigma_{pe}^{H^+}}{\sigma_{pe}^{He^+}} \sigma_{pe}^{He^0} \tag{3.53}$$

One then posesses estimates of the electron energy distribution and production cross-sections for both the neutral and positive ion beam components projected into a hydrogenic target. If one assumes, in tune with previous discussion, that the negative ion beam component creates primary electrons with the same cross-section and characteristic energy as the neutral beam component then for any beam composition one can readily provide an estimate of the primary electron properties via weighting the contribution of each beam component. One therefore obtains total primary electron production cross-section σ_{pe} and characteristic primary electron energy $\overline{E_{pe}}$ at some longitudinal distance x as presented in (3.54)-(3.55).

$$\sigma_{pe}\left(x, U_b, \overline{n}\right) = \frac{\overline{n_b^+}\left(x, U_b, \overline{n}\right)}{n_b^{total}} \sigma_{Rudd}^{H^+}\left(U_b\right) + \frac{\overline{n_b^0}\left(x, U_b, \overline{n}\right) + \overline{n_b^-}\left(x, U_b, \overline{n}\right)}{n_b^{total}} \sigma_{pe}^{H^0}\left(U_b\right) \tag{3.54}$$

$$\overline{E_{pe}}\left(x, U_b, \overline{n}\right) = \frac{\overline{n_b^+}\left(x, U_b, \overline{n}\right)}{n_b^{total}} \overline{E_{pe}^{H^+}}\left(U_b\right) + \frac{\overline{n_b^0}\left(x, U_b, \overline{n}\right) + \overline{n_b^-}\left(x, U_b, \overline{n}\right)}{n_b^{total}} \overline{E_{pe}^{H^0}}\left(U_b\right) \tag{3.55}$$

With regards to the formation of dissociation products by the primary electrons, Pamela highlights a single interaction as the dominant process for dissociation by plasma electrons in his model, namely the dissociation of molecules to form atoms via $(R22)$. At the characteristic primary electron energies predicted for both the JET and ITER neutralisers ($< 30eV$), this reaction

remains the most significant dissociation reaction with variation against energy as shown in figure 3.6. The other reactions listed in Table 3.8 are considered negligible;$(R20)$ provides ionisation of the background gas but is negligible compared to ionisation induced by the beam. Note that the energies provided to the dissociative products, also given in Table 3.8, follow from the potential energy curves and dissociative states discussed in relation to dissociation by positive beam ions. It is noted also that the production of dissociation products presents the dominant inelastic collision mechancism at typical primary electron energies. Therefore one can reasonably ignore the thermalisation of primary electrons by additional inelastic collisions, simplifying the overall complexity of the neutraliser model.

To facilitate modelling, the neutraliser is considered to consist of a series of transverse slices of longitudinal thickness δx with primary electrons unable to move between slices, instead taking a linear path out of the beam and towards a nearby neutraliser wall. It is proposed that the primary electron density $\overline{n_{pe}}$ be considered uniform and at steady state in each of these transverse slices. Given the assumption that all primary electrons created by the beam are successfully thermalised with the background plasma electrons prior to reaching the neutraliser wall, the steady state (3.59) is provided by consideration of a balance equation (3.56) evaluating the total number of primary electrons produced in an infinitesimal transverse slice about some longitudinal location x as in (3.57), and the total number of primary electrons lost to the background plasma in each slice (3.58) where the characteristic primary electron velocity $\overline{v_{pe}}$ follows from the characteristic primary electron energy $\overline{E_{pe}}$ as in (3.72).

$$\frac{d\overline{n_{pe}}}{dt} = Source_{pe} - Sink_{pe} \tag{3.56}$$

$$\begin{aligned} Source_{pe} &= \text{Primary Electrons created by Beam} \\ &= n_b^{total} v_b \sigma_{pe} \int_{A_b} n \, dA \, \delta x \end{aligned} \tag{3.57}$$

$$\begin{aligned} Sink_{pe} &= \text{Primary electrons lost to background plasma following dissociation} \\ &= \overline{n_{pe}} v_{pe} \sigma_{pe.diss}^{total} \int_{A_n} n \, dA \, \delta x \end{aligned} \tag{3.58}$$

$$\frac{d\overline{n_{pe}}}{dt} = 0 \Rightarrow \overline{n_{pe}}(x) = \frac{n_b^{total} v_b \sigma_{pe} \int_{A_b} n \, dA}{\overline{v_{pe}} \sigma_{pe.diss} \int_{A_n} n \, dA} \tag{3.59}$$

$$\overline{v_{pe}}(x) = \sqrt{\frac{2\overline{E_{pe}}}{m_e}} \tag{3.60}$$

As for dissociation by beam ions, each dissocation reaction by primary electrons reduces a background gas molecule to some combination of its constituent parts. This represents a gas sink for density, momentum and energy. Presented later, the description of this sink is aided by the definition of a total beam dissociation cross-section $\sigma_{pe.diss}^{total}$. Given the consideration of only $(R22)$ as a significant dissociation reaction by primary electrons, this implies $\sigma_{pe.diss}^{total}$ may be defined by (3.61). Since this reaction provides two neutral atomic products of the same energy, the energy and production cross-sections for the dissociation products are described via (3.62)-(3.65). Therefore

	Equation	Cross-Section $(10^{-20}m^2)$			Product Energy
		10eV	30eV	50eV	
$(R20)$	$D_2 + e \rightarrow D_2^+ + 2e$	<0.001	0.244	0.0752	-
$\sigma_{ED1}(R21)$	$D_2 + e \rightarrow D^+ + D + 2e$	<0.001	0.00152	0.0269	$5eV$
$\sigma_{ED2}(R22)$	$D_2 + e \rightarrow D + D + e$	0.250	0.380	0.110	$2.25eV$

TABLE 3.8: Cross sections for electron induced processes[**? ?**]

knowledge of the primary electron density, energy, their dissocation cross-sections and associated product energies is available throughout the neutraliser to allow formulation of appropriate gas source/sinks, discussed further in 3.2.5.

$$\sigma_{pe.diss}^{total} = \sigma_{ED2} \tag{3.61}$$

$$\sigma_{pe.diss}^{prod_0} = 2\sigma_{ED2} \tag{3.62}$$

$$\overline{E_{pe.diss}^{0}} = E_{ED2} \tag{3.63}$$

$$\sigma_{pe.diss}^{prod_+} = 0 \tag{3.64}$$

$$\overline{E_{pe.diss}^{+}} = 0 \tag{3.65}$$

Stripped Electrons Stripped electrons are produced via projectile loss reactions within the beam, occurring with cross-section σ_{se_0} for positive beam ions and $\sigma_{se_1^-}$ for negative beam ions as defined in (3.66)-(3.67). These reactions create electrons of significant initial energy E_{se}^0, determined via formula (3.68). These electrons can lose significant energy via inelastic collision with the background gas. It is possible for the stripped electrons to become fully thermalised with the background plasma, but this is extremely unlikely for typical neutraliser gas densities and path lengths, instead reaching the neutraliser outlet with significant additional energy. For simplicity of the plasma model and resulting implementation, the ionisation of the background gas by stripped electrons can be ignored as this is dominated by beam ions and neutrals. However the gas energy source they provide via inelastic collision should be fully evaluated.

$$\sigma_{se_0} = \sigma_{PL_0} \tag{3.66}$$

$$\sigma_{se_1^-} = \sigma_{PL_-^1} + 2\sigma_{PL_-^2} \tag{3.67}$$

$$E_{se}^0 = \frac{m_e}{m_b} E_b \tag{3.68}$$

Unlike the case of the primary electrons, inelastic collisions of stripped electrons with the background gas are not dominated by dissociation alone and therefore energy deposition in the gas is provided via energy deposition rate K_{in}, defined in (3.69) for characteristic stripped electron energy $\overline{E_{se}}$. For stripped electrons, dissociation of the background gas occurs via both $(R21)$ and $(R22)$, whose variation against electron energy is plotted in figure 3.6. $(R21)$, though of small

cross-section, produces an ionic product that is subject to acceleration, neutralisation and reflection as it approaches the neutraliser wall providing the dissociation product with significant energy that is ultimately deposited in the background gas. By comparison, though ($R22$) is of greater cross-section, it creates neutral dissociation products that are not subject to acceleration across the plasma sheath and thus typically provides lesser energy to the background gas per reaction. Thus, it is prudent to consider both dissociation reactions for stripped electrons. This arguably leads to a slight double counting of the energy provided to the background gas by stripped electrons as energy is provided by both the inelastic energy deposition rate and the dissociation mechanisms; this over-estimation should be minimal since the dissociation reactions provide only a small portion of the typical inelastic collision frequency with the background gas but their inclusion is necessary in order to model the gas mass redistribution they provide.

$$K_{in} = 2.4 \times 10^{-12} exp\left(\frac{-28}{\overline{E_{se}}}\right) \tag{3.69}$$

Let stripped electrons pass longitudinally through the neutraliser, and exist only within the beam path. Thus for a given gas density profile and beam composition, the steady state stripped electron density $\overline{n_{se}}$ can be derived at any point along the neutraliser via consideration of balance equations. For ease of modelling, one can assume that the stripped electron density and energy is uniform at given longitudinal point within the beam path of the neutraliser, demonstrating no transverse variation. Therefore, for a sufficiently high beam energy such that stripped electrons do not typically thermalise within the confines of the neutraliser, one can outline the sole stripped electron source at any given point in the beam path as that given in (3.70). Application of the chain rule allows this differential $\frac{d\overline{n_{se}}}{dt}$ to be expressed as a function of distance along the neutraliser $\frac{d\overline{n_{se}}}{dx}$ with a steady state profile then straightforwardly obtained as (3.71), where stripped electron velocity $\overline{v_{se}}$ is defined from the characteristic stripped electron energy $\overline{E_{se}}$ as in (3.72)-(3.73). A similar approach for the total energy of the stripped electrons e_{se}^{Total} provides a balance equation as in (3.74) with source term of the form (3.75) due to the formation of new stripped electrons and sink term (3.76) due to energy loss of the stripped electrons via inelastic collision upon the gas at some longitudinal location x. This outlines a steady state stripped electron energy distribution of the form (3.77).

$$\frac{d\overline{n_{se}}}{dt} = v_b \overline{n}\left(\overline{n_b^0}\sigma_{se_0} + \overline{n_b^-}\sigma_{se_{\bar{1}}}\right) \tag{3.70}$$

$$\frac{d\overline{n_{se}}}{dt} = \frac{d\overline{n_{se}}}{dx}.\frac{dx}{dt} \Rightarrow \frac{d\overline{n_{se}}}{dx} = \frac{v_b}{v_{se_0}}\overline{n}\left(\overline{n_b^0}\sigma_{se_0} + \overline{n_b^-}\sigma_{se_{\bar{1}}}\right) = \overline{n}\left(\overline{n_b^0}\sigma_{se_0} + \overline{n_b^-}\sigma_{se_{\bar{1}}}\right) \tag{3.71}$$

$$\overline{v_{se}} = \sqrt{\frac{2\overline{E_{se}}\,(x)}{m_e}} \tag{3.72}$$

$$\overline{E_{se}} = \frac{e_{se}^{Total}}{\overline{n_{se}}} \tag{3.73}$$

$$\frac{de_{se}^{Total}}{dx} = Source_{se}^{e^{Total}} - Sink_{se}^{e^{Total}} \tag{3.74}$$

$$\begin{aligned} Source_{se}^{e^{Total}} &= \text{Stripped Electrons created by Beam} \\ &= \frac{v_b}{v_{se_0}} \overline{n} E_{se}^0 \left(\overline{n_b^0} \sigma_{se_0} + \overline{n_b^-} \sigma_{se_{\bar{1}}} \right) \end{aligned} \tag{3.75}$$

$$\begin{aligned} Sink_{se}^{e^{Total}} &= \text{Energy Depositon in Gas} \\ &= \overline{n} K_{in} \frac{\overline{n_{se}}}{\overline{v_{se}}} \end{aligned} \tag{3.76}$$

$$\frac{de_{se}^{Total}}{dx} = \overline{n} \left(\overline{n_b^+} \frac{v_b}{v_{se_0}} E_{se}^0 \left(\overline{n_b^0} \sigma_{se_0} + \overline{n_b^-} \sigma_{se_{\bar{1}}} \right) - \frac{\overline{n_{se}} K_{in}}{\overline{v_{se}}} \right) \tag{3.77}$$

Evaluation of (3.70)-(3.77) to provide the stripped electron properties at a given longitudinal distance x within the beam path allows calculation of the induced dissociation effects by stripped electrons. Given the consideration of both $(R21)$ and $(R22)$ as substantial mechanisms for dissociation by stripped electrons, one can describe the resultant neutral and ionic dissociation products via cross-sections $\sigma_{se.diss}^{prod_0}$ and $\sigma_{se.diss}^{prod_+}$ with characteristic energies of $\overline{E_{se.diss}^0}$ and $\overline{E_{se.diss}^+}$ as presented in (3.79)-(3.82). The gas sink offered by these dissociation reactions, is characterised by the total dissociation cross-section (3.78). Therefore, from assumption of sufficient beam energy that stripped electrons do not typically thermalise within the neutraliser, it is possible to describe the stripped electron properties throughout the neutraliser, the energy they deposit in the gas via inelastic collisions and the properties of the dissociation products they create. This faciliates formulation of both gas sources and sinks in section 3.2.5.

$$\sigma_{se.diss}^{total} = \sigma_{ED1} + \sigma_{ED2} \tag{3.78}$$

$$\sigma_{se.diss}^{prod_0} = 2\sigma_{ED2} \tag{3.79}$$

$$\overline{E_{se.diss}^0} = E_{ED1} \tag{3.80}$$

$$\sigma_{se.diss}^{prod_+} = \sigma_{ED1} + \sigma_{ED2} \tag{3.81}$$

$$\overline{E_{se.diss}^+} = \frac{E_{ED1} + E_{ED2}}{\sigma_{se.diss}^{prod_+}} \tag{3.82}$$

Ion Wall Reflection As the beam traverses the neutraliser, ion and electron formation creates a background plasma. Thus, a plasma sheath region exists at the wall, serving to accelerate background ions to the wall at almost normal incidence where they may neutralise and be reflected with some fraction of their incident energy. These energetic neutral gas atoms or molecules then transfer momentum to the background gas via collision. Ion reflection at the wall can be described by two parameters, namely the probability of reflection $N^{Reflect}$ and the fraction of total incident energy $E^{Reflect}$ reflected by the wall.

Simulation studies by *Oen and Robinson*[**?**] as well as the work of *Eckstein and Verbeek*[**?**] have examined the neutralisation and reflection of hydrogenic ions at clean copper walls. These works highlight, perhaps surprisingly, that for the same total incident ion energy the reflection coefficients vary little for the differing hydrogenic isotopes. This is in contrast to relationships observed in reaction cross-sections wherein one often finds near equivalence for differing isotopes

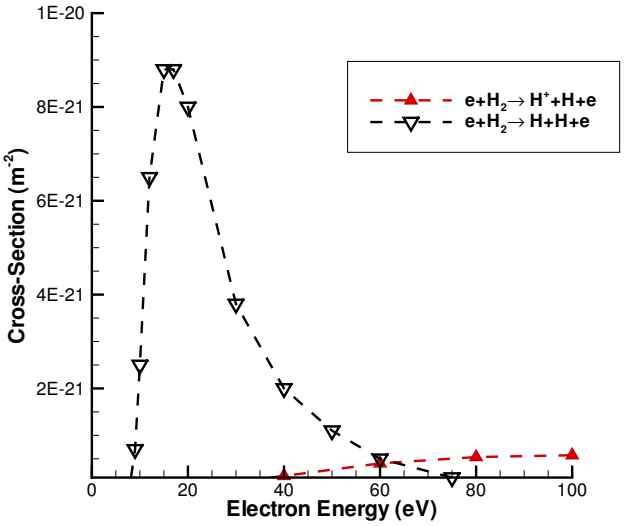

FIGURE 3.6: Dissociation reaction cross-sections for differing projectile electron energies

if one compares at the same energy per unit mass.

The results of *Oen and Robinson*[**?**] for H and T atomic ions at normal incidence are visually summarised in figure 3.7. Though one should note that these are first-order estimates, the data suggests that one might readily assume similar reflection co-efficients for deuterium atomic ions.

There appears a lack of experimental data for the neutralisation and reflection of atomic and molecular ions from copper, which are predicted to be the dominant ionic species in the neutraliser plasma. However, there exists published work considering the reflection of hydrogen atomic and molecular ions from alternative metal surfaces. Work concerning hydrogen molecular ion reflection from aluminium[**?**], identifies no significant difference in the co-efficients if we compare H^+ and H_2^+ ion reflection at the same energy per unit atom. Thus it appears reasonable that the same reflection co-efficients be used for both the atomic and molecular species when considering reflection from the copper neutraliser walls.

Therefore it would appear that the values of *Oen and Robinson*[**?**] could be readily applied for either atomic or molecular ions of deuterium at the same incident energy per atom. A least sqares minimisation fit to their data provides an energy dependent set of reflection parameters for use in the model. For a given incident ion energy per atom E_{ion}, these least squares fits provide reflection coefficients as presented in (3.83)-(3.84) and plotted against the published data in figure 3.7. A note of caution when considering these fits is that these, and the data upon which they depend, have assumed clean reflecting surfaces free from imperfections and debris. These therefore offer extremely idealised systems that may be subject to significant error when compared to less idealised reflecting surfaces.

$$E^{Reflect} = 1.788 E_{ion}^{-0.371} \tag{3.83}$$

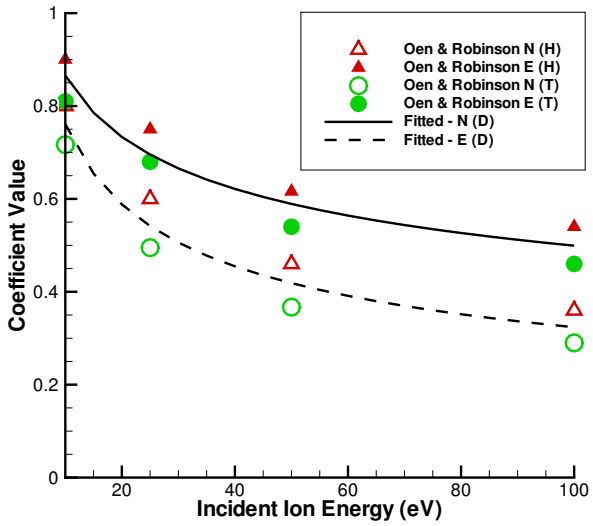

FIGURE 3.7: Published and fitted reflection coefficients for hydrogen on copper[**?**]

$$N^{Reflect} = 1.500 E_{ion}^{-0.239} \tag{3.84}$$

3.2.3 Momentum Transfer Cross-Section

The transfer of momentum from the fast neutrals and ions created via either dissociation and/or ion reflection at the wall, is the dominant mechanism for energy transfer to the background gas. With regards to the rate of this momentum transfer, there is a lack of experimental data for collisions of atomic hydrogenic species with hydrogenic molecules in the range of several eV.

There exist several attempts to produce the momentum transfer cross section via various modelling techniques[**? ? ?**], whilst *Pamela*[**?**] indicated the momentum transfer cross sections for the eV range 'deduced from the relatively well measured interaction potentials' but did not offer any supporting references or supporting calculations to this end. Of all the applicable literature identified, the semi-empirical cross-section of *Phelps*[**?**] appears best suited for use and in fact offers good agreement with the figures originally utilised by *Pamela*[**?**]. This is demonstrated both numerically in Table 3.9 and visually in figure 3.8, where the values of *Phelps*[**?**] are compared with the upper and lower bounds of the momentum cross-section detailed by *Pamela*[**?**].

Exemplar calculation of momentum transfer for typical neutraliser gas densities demonstrates that only a small fraction of the dissociation product energy is transferred before collision with the wall. Examining a neutral product of dissociation by positive beam ions via $(R18)$ implies an initial product energy of $E_{initial} = 10eV$. Assumption of a uniform background gas density similar to that observed in experiment $n = 3 \times 10^{19} m^{-3}$ and application of *Phelps'* model[**?**] of momentum transfer cross-section to provide $\sigma_{mom}\left(E_{initial}\right) = 1.89 \times 10^{-20} m^2$ implies that in

traversing half the JET neutraliser width before collision with a wall $N_{hw} = 0.095m$, the fraction of energy lost by the neutral product to the background gas by momentum transfer is found via (3.85).

$$f_1^{dep_0} = 1 - exp\left(-\sigma_{mom} N_{hw} n\right) = 0.053 \tag{3.85}$$

Thus only a very small fraction of the neutral product energy is lost before reflection at the wall. Thus, even after accommodation and reflection at the wall, the product continues to possess energy well in excess of the background gas equilibrium temperature. Indeed (3.86) reveals that if the accommodation coefficient for energetic particles is similar to that observed for moderate gas temperatures ($i.e. \alpha_{hot} = 0.37$), then upon reflection the neutral product still posesses $\sim 60\%$ of its initial energy. Thus this reflected neutral product is still capable of delivering significant momentum to the background gas.

$$E_{reflected} = \frac{T_w + \left(\left(1 - f_1^{dep_0}\right) 11604.55 E_{initial} - T_w\right)\left(1 - \alpha_{hot}\right)}{11604.55} = 5.98eV \tag{3.86}$$

Therefore, it appears necessary to consider the accommodation of fast product ions and neutrals at the neutraliser walls and multiple passes across the neutraliser to ensure a suitably accurate fraction of their energy is deposited in the background gas. One could reasonably assume that the fast product ions and neutrals travel perpendicular to the beam, repeatedly traversing the neutraliser at a given longitudinal location x depositing energy, undergoing accommodation and reflection at the wall after each traverse until such time as it reaches equilibrium with either the wall or background gas. For initially neutral products from dissociation reactions one envisages some functional dependence as in (3.87), with the amount of energy successfully deposited unique to each energetic source particle population. Considering each of the variables in turn, the energy deposition fraction would be dependent upon the initial characteristic energy of the particle $\overline{E^0_{source}}$, the average background gas temperature in the transverse slice $\overline{T_{neut}}$ as in (3.88), the average gas density in the transverse slice $\overline{n_{neut}}$ from (3.89), the average path length between the neutraliser walls $\overline{d}$, the wall temperature T_w and the accommodation coefficient for energetic particles α_{hot}.

$$E^{dep_0}_{source}(x) = f^{dep_0}_{total}\left(\overline{E^0_{source}}, \overline{T_{neut}}, \overline{n_{neut}}, \overline{d_{neut}}, T_w, \alpha_{hot}\right) \tag{3.87}$$

$$\overline{T_{neut}} = \frac{\int_{A_n} T\, dA}{A_n} \tag{3.88}$$

$$\overline{n_{neut}} = \frac{\int_{A_n} n\, dA}{A_n} \tag{3.89}$$

By contrast, the initially ionic dissociation products deposit some energy in the gas before their

Reactants	Source	Momentum transfer cross-section (eVm^2)			
		0.1eV	1eV	5eV	10eV
$D - D_2$	*Pamela*		$1 - 2 \times 10^{-19}$		
	Phelps	1.51×10^{-20}	6.6×10^{-20}	1.46×10^{-19}	1.87×10^{-19}
$D^+ - D_2$	*Pamela*		$2 - 5 \times 10^{-15}$		
	Phelps	9.00×10^{-20}	2.68×10^{-19}	4.47×10^{-19}	4.90×10^{-19}

TABLE 3.9: Comparison of momentum transfer cross-sections of *Pamela*[**?**] and *Phelps*[**?**]

first interaction with wall, where they are subject to acceleration by the plasma sheath, with neutralisation and reflection determined by probabilities from (3.83)-(3.84). Thus the energy deposition for each ionic particle from a given dissociation mechanism possesses functional dependence as in (3.90), i.e. essentially the same as for the neutral products supplemented by the plasma potential at the sheath. To succesfully evaluate the reflection coefficients for each source mechanism it is necessary to quantify the energy deposited in the gas from initial formation to reaching the plasma sheath. Denoted $f_1^{dep_+}\left(\overline{E^+_{source}}\right)$ for some generic source mechanism, this may be found via (3.91); similar to (3.85), the energy deposited is some fraction of the excess energy above the background gas energy with the assumption of a typical path length in the neutraliser of $\overline{N_{hw}}$.

$$E^{dep_+}_{source}(x) = f^{dep_+}_{total}\left(\phi, \overline{E^+_{source}}, \overline{T_{neut}}, \overline{n_{neut}}, \overline{d_{neut}}, T_w, \alpha_{hot}\right) \tag{3.90}$$

$$f_1^{dep_+} = \left(\overline{E^+_{source}} - \frac{\overline{T_{neut}}}{11604.55}\right)\left(1 - exp\left(-\sigma_{mom}\left(\overline{E^+_{source}}\right)\overline{n_{neut}}|_I \overline{N_{hw}}|_I\right)\right) \tag{3.91}$$

Finally, the calculation of the energy deposition by reflected plasma ions differs from the form of that for the ionic dissociation products. Unlike the ionic dissociation products, no energy deposition in the gas occurs for the bulk plasma ions. A source is instead only offered following acceleration at the plasma sheath and successful reflection at the walls. Thus the functional dependence of energy deposition in the gas is as in (3.92).

$$E^{dep_+}_{plasma}(x) = f^{dep_p}_{total}\left(\phi, \overline{T_{neut}}, \overline{n_{neut}}, \overline{d_{neut}}, T_w, \alpha_{hot}\right) \tag{3.92}$$

The implementation of these functions to evaluate the energy deposition in the gas by each source mechanism is discussed further in Appendix **??**.

3.2.4 Plasma

From the discussions above, it is obvious that determination of the potential and ion flux at the plasma sheath is of considerable importance in calculation of the mass and energy source terms presented by reflection from the wall. This is achieved by building on the work of *Surrey*[**?**].

Sheath plasma potential and electron temperature follow from a system energy balance, knowledge of the plasma ion flux at the wall and the assumption of steady state. Plasma flux may be considered to be produced solely by charge exchange and ionisation reactions at the beam, effectively ignoring additional atomic and molecular ions produced by other reactions. This is

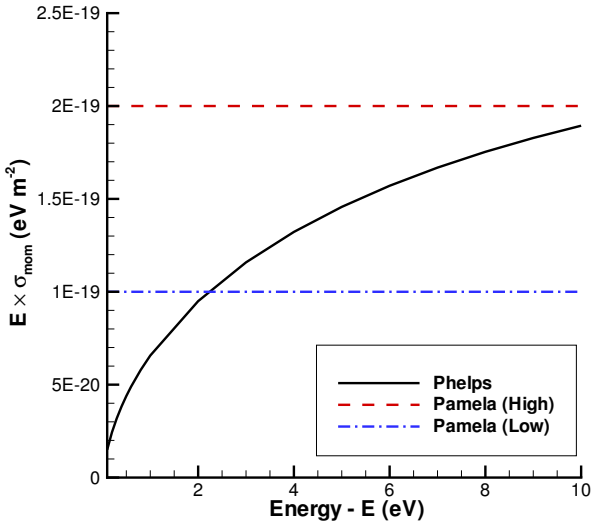

FIGURE 3.8: Comparison of momentum transfer cross-sections of *Pamela*[**?**] and *Phelps*[**?**]

a reasonable assumption in providing an estimate of the plasma parameters and plasma density distribution; additional plasma production can result from the various dissociation reactions discussed in this chapter, however, charge exchange and ionisation represent the dominant ion formation mechanism in the neutraliser. Additional motivation for the restriction of the plasma production methods in this fashion is that the consideration of production mechanisms outside of the beam path, such as primary electron dissociation, would prevent application of this model. In the absence of another suitable analytical model, the application of a particulate or fluid-based plasma model would be required and utilise much greater computational resources.

The plasma model, derived in full in Appendix **??**, assumes that the plasma is unable to flow along the length of the neutraliser and instead remains solely within some infinitesimal transverse slice of the neutraliser at x. All energy deposited by the beam in that neutraliser slice is assumed to ultimately be transferred to the walls of the neutraliser by the plasma with the exception of the energy imparted in newly created stripped electrons, which stream out of the transverse slice taking some fraction of the total deposited beam energy as summarised in figure 3.9. The energy deposited in the slice is P_b^p as in (3.93) whilst the energy carried to the wall by the plasma is P_p^{wall} of (3.95) and energy carried away by newly created stripped electrons is P_b^{se} from (3.94). These three quantities form an energy balance (3.96) from which the electron temperature at the sheath T_e may be found. Therefore calculation of the electron temperature also requires evaluation of the number of plasma ions produced in the slice per second N_p^+ (3.97), the ratio of the plasma potential to the electron temperature η (3.99), surplus ion flux to the wall ψ (3.98). The plasma potential ϕ follows from (3.100).

$$P_b^p = H_{Stop}\left(\overline{n_b^+} + \frac{\chi}{1-\chi}\overline{n_b^0}\right)\frac{A_b v_b \overline{n}\delta x}{N_0} \tag{3.93}$$

$$P_b^{se} = \overline{n}v_b E_{se}^0 \left(\overline{n_b^0}\sigma_{se_0} + \overline{n_b^-}\sigma_{se_{\bar{1}}} \right) A_b \delta x \tag{3.94}$$

$$P_p^{wall} = N_p^+ \left(\eta + 1 - \psi \right) T_e \tag{3.95}$$

$$\begin{array}{rcl} \text{Energy to Wall from Plasma} & = & \text{Energy Lost by Beam} - \text{Energy to Stripped Electrons} \\ P_p^{wall} & = & P_b^p - P_b^{se} \\ & \therefore & \frac{P_b^p(x) - P_b^{se}(x)}{P_p^{wall}} = 1 \end{array} \tag{3.96}$$

$$N_p^+ = \overline{n}v_b \left(\overline{n_b^+} \left(\sigma_+ + \sigma_{10} \right) + \overline{n_b^0} \left(\sigma_n + \sigma_{0\bar{1}} \right) + \overline{n_b^-}\sigma_n \right) A_b \delta x \tag{3.97}$$

$$\psi = \frac{\overline{n_b^+}\sigma_{CE} + \overline{n_b^0}\sigma_{0\bar{1}}}{\overline{n_b^+} \left(\sigma_+ + \sigma_{CE} \right) + \overline{n_b^0} \left(\sigma_n + \sigma_{0\bar{1}} \right) + \overline{n_b^-}\sigma_n} \tag{3.98}$$

$$\eta = ln \left[\left(\frac{m_D}{0.72\pi m_e} \right)^{\frac{1}{2}} \frac{1}{1-\psi} \right] \tag{3.99}$$

$$\phi = \eta T_e \tag{3.100}$$

Given the assumptions in formulating the plasma model, one can classify the the ions within the neutraliser model into two groups: (1) ions produced by charge exchange and ionisation reactions at the beam, (2) ions produced via dissociation. The former provide the plasma density distribution and temperature, whilst the latter are not considered part of the background plasma and not within calculation of the background plasma properties, instead forming an additional secondary ion population. However, both are accelerated via the plasma potential at the neutraliser wall, from which they may be reflected as fast neutrals and thus both groups represent significant possible energy sources for the background gas.

The plasma potential calculated from the model facilitates calculation of ion energies as they strike the wall, their reflection from the wall and ultimately the source terms entering the gas governing equations. From the assumption that all ionic dissociation products and plasma ions travel perpendicular to the beam path and strike the wall at approximately normal incidence, one can provide the number and energy reflection probabilities for each of the differing ion populations outlined thus far. If one assumes the plasma potential ϕ exists at the wall at a given longitudinal neutraliser position x, then the plasma ion number reflection coefficient $N_p^{Reflect}$ and energy coefficient $E_p^{Reflect}$ are calculated as in (3.101) where $\frac{\phi}{2}$ represents the wall incident ion energy per atom. By contrast, ionic dissociation products possess some initial energy before they experience acceleration by the plasma potential. Therefore the reflection coefficients for the ionic dissociation products due to beam positive ions and stripped electrons are provided by the slightly differing forms of (3.102)-(3.103) where correction for product energy deposition in the gas before reaching the plasma sheath is also included.

$$\begin{cases} E_p^{Reflect} = 1.788 \left(\frac{\phi}{2} \right)^{-0.371} \\ N_p^{Reflect} = 1.500 \left(\frac{\phi}{2} \right)^{-0.239} \end{cases} \tag{3.101}$$

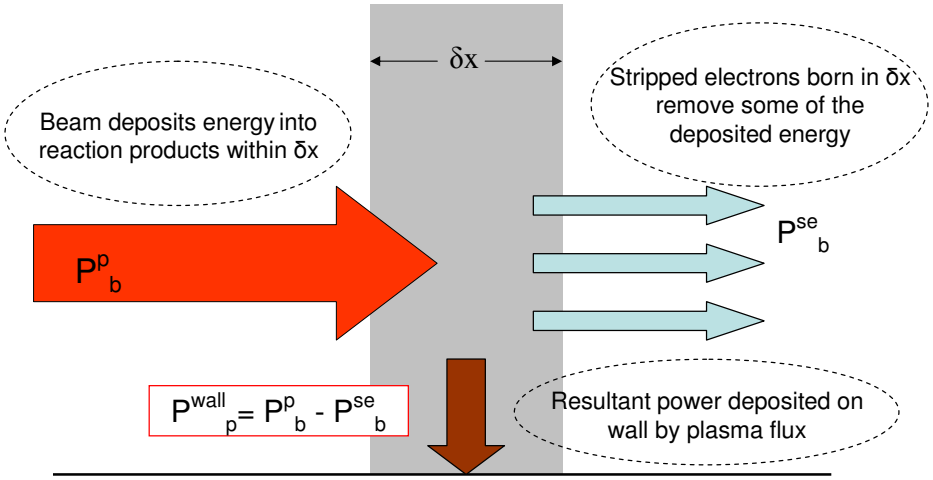

FIGURE 3.9: Beam deposited power balance

$$\begin{cases} E_{b.diss}^{Reflect} = 1.788\left(\phi + \left(1 - f_1^{dep+}\left(\overline{E_{b.diss}^{+}}\right)\right)\overline{E_{b.diss}^{+}}\right)^{-0.371} \\ N_{b.diss}^{Reflect} = 1.500\left(\phi + \left(1 - f_1^{dep+}\left(\overline{E_{b.diss}^{+}}\right)\right)\overline{E_{b.diss}^{+}}\right)^{-0.239} \end{cases} \tag{3.102}$$

$$\begin{cases} E_{se.diss}^{Reflect} = 1.788\left(\phi + \left(1 - f_1^{dep+}\left(\overline{E_{se.diss}^{+}}\right)\right)\overline{E_{se.diss}^{+}}\right)^{-0.371} \\ N_{se.diss}^{Reflect} = 1.500\left(\phi + \left(1 - f_1^{dep+}\left(\overline{E_{se.diss}^{+}}\right)\right)\overline{E_{se.diss}^{+}}\right)^{-0.239} \end{cases} \tag{3.103}$$

To determine the effects of plasma pressure, which experiments and simulation indicate can produce significant gas depletion, it is necessary to determine the distribution of plasma density within each transverse slice. To avoid the need for numerical modelling, an analytical steady-state model of the plasma profile within each infinitesimal neutraliser slice has been developed that is directly dependent upon the neutraliser gas density profile. Based upon the model originally developed by Surrey, the use of the one dimensional diffusion equations for the plasma inside and outside the beam is extended to allow the use of a neutral gas profile rather than uniform gas distribution assumed by Surrey. Generalised distributions are derived for the plasma interior and exterior of the beam with continuity assumed at the beam boundary. These generalised distributions are scaled to allow evaluation of the plasma density at any point within each infinitesimal transverse slice $\widetilde{n_p}$. Evaluation of plasma pressure p_p throughout the neutraliser therefore follows from (3.104).

$$p_p = \widetilde{n_p} k T_e \tag{3.104}$$

3.2.5 Gas Sources & Sinks

From the provision of a steady state beam and plasma for a given gas distribution as discussed above, generalised gas sources and sinks can be formulated for the various interactions of the beam-gas-plasma system. Let us condsider each of the neutraliser species in turn to provide first the sink and then the source mechanisms for each at some generalised location in the neutraliser $\boldsymbol{r}$.

Beam Amongst other reactions, the beam provides a gas sink due to charge exchange and ionisation. These serve to remove background gas molecules in the beam path, and result in a loss of gas density L_b^ρ as described by (3.105). This loss of density produces an associated loss of momentum and energy. The momentum sinks for two-dimensional flow are $L_b^{\rho\boldsymbol{u}}$ presented in (3.106), with energy sink L_b^e as in (3.107). In each case, if $\boldsymbol{r}$ lies outside the beam path the sink due to the beam is obviously zero.

$$L_b^\rho = \rho v_b \left(\left(\sigma_+ + \sigma_{CE} + \sigma_{1\bar{1}} \right) \overline{n_b^+} + \left(\sigma_0 + \sigma_{0\bar{1}} \right) \overline{n_b^0} + \sigma_0 \overline{n_b^-} \right) \tag{3.105}$$

$$L_b^{\rho\boldsymbol{u}} = \boldsymbol{u} L_b^\rho \tag{3.106}$$

$$L_b^e = e \frac{L_b^\rho}{\rho} \tag{3.107}$$

Dissociation by Beam Ions Dissociation by beam ions represents an additional gas sink beyond straightforward ionisation and charge exchange. The density, momentum and energy sinks due to dissociation occur only in the beam path and are provided by $L_{b.diss}^\rho$, $L_{b.diss}^{\rho\boldsymbol{u}}$ and $L_{b.diss}^e$ as per (3.108)-(3.110).

$$L_{b.diss}^\rho = \rho v_b \sigma_{b.diss}^{total} \overline{n_b^+} \tag{3.108}$$

$$L_{b.diss}^{\rho\boldsymbol{u}} = \boldsymbol{u} L_{b.diss}^\rho \tag{3.109}$$

$$L_{b.diss}^e = e \frac{L_{b.diss}^\rho}{\rho} \tag{3.110}$$

As discussed previously, dissociation reactions due to beam ions produce energetic neutral and ionic products. The total number of energetic ionic products produced with an infinitesimally thick transverse slice per unit time $N_{b.diss}^+$ is calculated by (3.111) . Possessing initial characteristic energies $\overline{E_{b.diss}^+}$ from (3.49), the energetic ionic products are subject to accelaration by the plasma potential, neutralisation and possible reflection at the wall. With reflected number fraction $N_{b.diss}^{Reflect}$ from (3.102) a returning flow of particles $\widetilde{N_{b.diss}^+}$ (3.112) is defined.

Description of the neutral products is somewhat simpler since they are not subject to acceleration by the plasma potential nor some probabilistic chance of reflection; the neutral products are assumed to always be successfully reflected until reaching thermal equilibrium and thus the possible effects of absorption and desorption are ignored at the wall. The total number of energetic

neutral dissociation products produced in a slice of thickness δx per unit time is (3.126) with the neutral products possessing an initial characteristic energy $\overline{E^{+0}_{b.diss}}$ as defined in (3.47).

$$N^{+}_{b.diss} = \overline{n^{+}_{b}} v_b \sigma^{prod_+}_{b.diss} \int_{A_b} n \, dA \, \delta x = \overline{n^{+}_{b}} v_b \sigma^{prod_+}_{b.diss} \overline{n} A_b \delta x \tag{3.111}$$

$$\widetilde{N^{+}_{b.diss}} = N^{Reflect}_{b.diss} \overline{n^{+}_{b}} v_b \sigma^{prod_+}_{b.diss} \overline{n} A_b \delta x \tag{3.112}$$

$$\widetilde{E^{+}_{b.diss}} = \frac{E^{Reflect}_{b.diss}}{N^{Reflect}_{b.diss}} \left(\phi + \left(1 - f_1^{dep_+} \left(\overline{E^{+}_{b.diss}} \right) \right) \overline{E^{+}_{b.diss}} \right) \tag{3.113}$$

$$N^{0}_{b.diss} = \overline{n^{+}_{b}} v_b \sigma^{prod_0}_{b.diss} \int_{A_b} n \, dA \, \delta x = \overline{n^{+}_{b}} v_b \sigma^{prod_0}_{b.diss} \overline{n} A_b \delta x \tag{3.114}$$

The energetic particles constituing $N^{0}_{b.diss}$ and $\widetilde{N^{+}_{b.diss}}$ undergo collisions with the background gas to eventually thermalise and replenish the gas density, each depositing energy $E^{dep_0}_{b.diss}$ and $E^{dep_+}_{b.diss}$ respectively. This thermalisation serves to provide the background gas with a source of density, momentum and energy. It is as atoms that the energetic particles ultimately thermalise, therefore the assumption that two atoms immediately recombine upon thermalisation to form a molecule allows one to express the total density source to the transverse slice from beam dissociation products $s^{\rho}_{b.diss}$ via (3.116). A similar energy deposition to the slice $s^{e}_{b.diss}$ is provided via (3.117). One can reasonably assume that the deposition of mass and energy within the transverse slice is greatest at points of highest density within the slice, since the greatest number of collisions occur at these points. Thus one can define the fraction of the total source deposited within the infinitesimal volume $\boldsymbol{r} \pm \frac{\delta \boldsymbol{r}}{2}$ within the slice via D_{source}, as outlined in (3.118). Essentially D_{source} deposits a fraction of the total source to the slice dictated by the ratio of the number of gas molecules in the infinitesimal volume as a fraction of the total number of gas molecules within the entire slice.

It then follows that the density source for the background gas $S^{\rho}_{b.diss}$ due to beam dissociation is given by (3.119), with momentum sources $S^{\rho \boldsymbol{u}}_{b.diss}$ (3.120). The energy source $S^{e}_{b.diss}$ contains two components, the first due to the deposition of mass and the second due to an additional deposition of energy, thus taking the form (3.121).

$$\begin{cases} E^{dep_0}_{b.diss} = f^{dep_0}_{total} \left(\overline{E^{0}_{b.diss}}, \overline{T_{neut}}, \overline{n_{neut}}, \overline{d_{neut}}, T_w, \alpha_{hot} \right) \\ E^{dep_+}_{b.diss} = f^{dep_+}_{total} \left(\phi, \overline{E^{+}_{b.diss}}, \overline{T_{neut}}, \overline{n_{neut}}, \overline{d_{neut}}, T_w, \alpha_{hot} \right) \end{cases} \tag{3.115}$$

$$\begin{aligned} s^{\rho}_{b.diss} = \int_{A_n} S^{\rho}_{b.diss} dA \quad \delta x &= m_D \left(\widetilde{N^{+}_{b.diss}} + N^{0}_{b.diss} \right) \\ &= m_D \overline{n^{+}_{b}} v_b \overline{n} A_b \delta x \left(N^{Reflect}_{b.diss} \sigma^{prod_+}_{b.diss} + \sigma^{prod_0}_{b.diss} \right) \end{aligned} \tag{3.116}$$

$$\begin{aligned} s^{e}_{b.diss} = \int_{A_n} S^{e}_{b.diss} dA \quad \delta x &= E^{dep_+}_{b.diss} \widetilde{N^{+}_{b.diss}} + E^{dep_0}_{b.diss} N^{0}_{b.diss} \\ &= \overline{n^{+}_{b}} v_b \overline{n} A_b \delta x \left(E^{dep_+}_{b.diss} N^{Reflect}_{b.diss} \sigma^{prod_+}_{b.diss} + E^{dep_0}_{b.diss} N^{0}_{b.diss} \sigma^{prod_0}_{b.diss} \right) \end{aligned} \tag{3.117}$$

$$D_{source} = \frac{n \delta x \delta y \delta z}{\int_{A_n} n \, dA \, \delta x} \tag{3.118}$$

$$S^{\rho}_{b.diss} = \frac{D_{source}}{\delta x \delta y \delta z} s^{\rho}_{b.diss} \tag{3.119}$$

$$S^{\rho \boldsymbol{u}}_{b.diss} = \boldsymbol{u} S^{\rho}_{b.diss} \tag{3.120}$$

$$S^{e}_{b.diss} = e\frac{S^{\rho}_{b.diss}}{\rho} + \frac{D_{source}}{\delta x \delta y \delta z} s^{e}_{b.diss} \tag{3.121}$$

Dissociation by Primary Electrons Primary electron density and properties at a given point in the neutraliser follow from the work presented earlier in the chapter. The dissociation reactions induced by primary electrons represents an additional gas sink, outlined by (3.122)-(3.124). Note their similar form to the formulae describing dissociation reactions resulting from beam ions. However, given that the primary electron density is assumed uniform in a given transverse slice, the density sink $L^{\rho}_{pe.diss}$, momentum sinks $L^{\rho \boldsymbol{u}}_{pe.diss}$ and energy sink $L^{e}_{pe.diss}$ provide gas losses throughout the slice and not just in the beam path.

$$L^{\rho}_{pe.diss} = \rho \overline{v_{pe}} \sigma^{total}_{pe.diss} \overline{n_{pe}} \tag{3.122}$$

$$L^{\rho \boldsymbol{u}}_{pe.diss} = \boldsymbol{u} L^{\rho}_{pe.diss} \tag{3.123}$$

$$L^{e}_{pe.diss} = e\frac{L^{\rho}_{pe.diss}}{\rho} \tag{3.124}$$

The major difference to the previous discussion of the source provided by dissociation products is that the dissociation reactions considered for primary electrons produce no ionic products within a given transverse slice as in (3.125). Therefore, only the number of neutral products produced per unit time $N^{0}_{pe.diss}$, as in (3.126), need be considered in the formulation sources due to primary electron dissociation. Mass source to a transverse slice $s^{\rho}_{pe.diss}$ at some longitudinal position is provided by (3.128), with a similar energy source $s^{e}_{pe.diss}$ outlined by (3.129) where the energy successfully deposited in the gas by each product is $E^{dep_0}_{pe.diss}$ from (3.127).

Therefore, the density source for the background gas $S^{\rho}_{pe.diss}$ due to primary electron dissociation is given by (3.130), with momentum sources $S^{\rho \boldsymbol{u}}_{pe.diss}$ (3.131). The energy source $S^{e}_{pe.diss}$ contains two components, the first due to the deposition of mass and the second due to an additional deposition of energy, thus taking the form (3.132).

$$N^{+}_{pe.diss} = 0 \tag{3.125}$$

$$N^{0}_{pe.diss} = \overline{n_{pe} v_{pe}} \sigma^{prod_0}_{pe.diss} \int_{A_n} n \, dA \, \delta x = \overline{n_{pe} v_{pe}} \sigma^{prod_0}_{pe.diss} \overline{n_{neut}} A_n \delta x \tag{3.126}$$

$$E^{dep_0}_{pe.diss} = f^{dep_0}_{total}\left(\overline{E^{0}_{b.diss}}, \overline{T_{neut}}, \overline{n_{neut}}, \overline{d_{neut}}, T_w, \alpha_{hot}\right) \tag{3.127}$$

$$\begin{aligned} s^{\rho}_{pe.diss} = \int_{A_n} S^{\rho}_{pe.diss} dA \quad \delta x &= m_D N^{0}_{pe.diss} \\ &= m_D \overline{n_{pe} v_{pe}} \sigma^{prod_0}_{pe.diss} \overline{n_{neut}} A_n \delta x \end{aligned} \tag{3.128}$$

$$\begin{aligned} s^{e}_{pe.diss}(x) = \int_{A_n} S^{e}_{pe.diss} dA \quad \delta x &= E^{dep_0}_{pe.diss} N^{0}_{pe.diss} \\ &= E^{dep_0}_{pe.diss} \overline{n_{pe} v_{pe}} \sigma^{prod_0}_{pe.diss} \overline{n_{neut}} A_n \delta x \end{aligned} \tag{3.129}$$

$$S^{\rho}_{pe.diss} = \frac{D_{source}}{\delta x \delta y \delta z} s^{\rho}_{pe.diss} \tag{3.130}$$

$$S^{\rho \boldsymbol{u}}_{pe.diss} = \boldsymbol{u} S^{\rho}_{pe.diss} \tag{3.131}$$

$$S^{e}_{pe.diss} = e\frac{S^{\rho}_{pe.diss}}{\rho} + \frac{D_{source}}{\delta x \delta y \delta z} s^{e}_{pe.diss} \tag{3.132}$$

Stripped Electrons Dissociation of the background gas by stripped electrons provides density, momentum and energy sinks in the beam path notated by $L^{\rho}_{se.diss}$, $L^{\rho \boldsymbol{u}}_{se.diss}$ and $L^{e}_{se.diss}$ respectively. These sinks are defined in (3.133)-(3.135):

$$L^{\rho}_{se.diss} = \rho \overline{v_{se}} \sigma^{total}_{se.diss} \overline{n_{se}} \tag{3.133}$$

$$L^{\rho \boldsymbol{u}}_{se.diss} = \boldsymbol{u} L^{\rho}_{se.diss} \tag{3.134}$$

$$L^{e}_{se.diss} = e\frac{L^{\rho}_{se.diss}}{\rho} \tag{3.135}$$

Similar to the case of dissociation by beam ions, the rate of energetic ionic product formation from stripped electron dissociation within each transverse slice of the neutraliser $N^{+}_{se.diss}$ is calculated by (3.137) . Following acceleration by the plasma potential in the vicinity of the wall, the energetic ionic products can undergo neutralisation and reflection at the wall with reflected number and energy fractions $N^{Reflect}_{se.diss}$ and $E^{Reflect}_{se.diss}$ from (3.103). The returning rate of reflected products $\widetilde{N^{+}_{se.diss}}$ is found from (3.138) where (3.139) includes correction for energy deposition in the gas before acceleration of the ionic products at the sheath. The number of energetic neutral dissociation products produced per unit time is provided by (3.136) with the neutral products possessing an initial characteristic energy $\overline{E^{0}_{se.diss}}$ as defined in (3.80).

$$N^{0}_{se.diss} = \overline{n_{se} v_{se}} \sigma^{prod_0}_{se.diss} \int_{A_b} n \, dA \, \delta x = \overline{n_{se} v_{se}} \sigma^{prod_0}_{se.diss} \overline{n} A_b \delta x \tag{3.136}$$

$$N^{+}_{se.diss} = \overline{n_{se} v_{se}} \sigma^{prod_+}_{se.diss} \int_{A_b} n \, dA \, \delta x = \overline{n_{se} v_{se}} \sigma^{prod_+}_{se.diss} \overline{n} A_b \delta x \tag{3.137}$$

$$\widetilde{N^{+}_{se.diss}} = N^{Reflect}_{se.diss} \overline{n^{+}_{b}} v_b \sigma^{prod_+}_{se.diss} \overline{n} A_b \delta x \tag{3.138}$$

$$\widetilde{E^{+}_{se.diss}} = \frac{E^{Reflect}_{se.diss}}{N^{Reflect}_{se.diss}} \left(\phi + \left(1 - f_1^{dep_+} \left(\overline{E^{+}_{de.diss}} \right) \right) \overline{E^{+}_{se.diss}} \right) \tag{3.139}$$

The energetic products eventually thermalise with the background gas. This thermalisation serves to provide the background gas with a source of density, momentum and energy. Following the assumption of atomic recombination upon thermalisation, the total density source to the transverse slice from stripped electron dissociation products $s^{\rho}_{se.diss}$ is provided by (3.141). A similar energy deposition to the slice $s^{e}_{se.diss}$ is provided via (3.142) with energies $E^{dep_+}_{se.diss}$ and $E^{dep_0}_{se.diss}$ deposited the gas of the transverse slice by each ionic and neutral product respectively, and defined in (3.140).

Source distribution via factor D_{source} thus allows formulation of the density source for the

background gas $S^{\rho}_{se.diss}$ due to beam dissociation as in (3.143), with dependent momentum source $S^{\rho u}_{se.diss}$ given in (3.144). The energy source $S^{e}_{se.diss}$ accounts for both the deposition of mass and additional energy, and is defined in (3.145).

$$\begin{cases} E^{dep_0}_{se.diss} = f^{dep_0}_{total}\left(\overline{E^{0}_{se.diss}}, \overline{T_{neut}}, \overline{n_{neut}}, \overline{d_{neut}}, T_w, \alpha_{hot}\right) \\ E^{dep_+}_{se.diss} = f^{dep_+}_{total}\left(\phi, \overline{E^{+}_{se.diss}}, \overline{T_{neut}}, \overline{n_{neut}}, \overline{d_{neut}}, T_w, \alpha_{hot}\right) \end{cases} \tag{3.140}$$

$$\begin{aligned} s^{\rho}_{se.diss} = \int_{A_n} S^{\rho}_{se.diss} dA \quad \delta x = & \quad m_D\left(\widetilde{N^{+}_{se.diss}} + N^{0}_{se.diss}(x)\right) \\ = & \quad m_D \overline{n^{+}_b} v_b \overline{n} A_b \delta x \left(N^{Reflect}_{se.diss}\sigma^{prod_+}_{se.diss} + \sigma^{prod_0}_{se.diss}\right) \end{aligned} \tag{3.141}$$

$$\begin{aligned} s^{e}_{se.diss} = \int_{A_n} S^{\rho}_{se.diss} dA \quad \delta x = & \quad E^{dep_+}_{se.diss}\widetilde{N^{+}_{se.diss}} + E^{dep_0}_{se.diss}N^{0}_{se.diss} \\ = & \quad \overline{n^{+}_b} v_b \overline{n} A_b \delta x \left(E^{dep_+}_{se.diss}N^{Reflect}_{b.diss}\sigma^{prod_+}_{se.diss} + E^{dep_0}_{se.diss}\sigma^{prod_0}_{se.diss}\right) \end{aligned} \tag{3.142}$$

$$S^{\rho}_{se.diss} = \tfrac{D_{source}}{\delta x \delta y \delta z} s^{\rho}_{se.diss} \tag{3.143}$$

$$S^{\rho \boldsymbol{u}}_{se.diss} = \boldsymbol{u} S^{\rho}_{se.diss} \tag{3.144}$$

$$S^{e}_{se.diss} = e^{\frac{S^{\rho}_{se.diss}}{\rho}} + \tfrac{D_{source}}{\delta x \delta y \delta z} s^{e}_{se.diss} \tag{3.145}$$

Other inelastic collision mechanisms serve to provide a further energy source to the background gas. The energy provided to the slice via all inelastic collision mechanisms is outlined by (3.146), wherein one notes that evaluation of the energy successfully deposited is not necessary; one can readily assume that all of the energy lost by the stripped electrons according to K_{in} is successfully deposited in the background gas. It is reasonable to assume that this energy source is only deposited within the beam path, since the stripped electrons have been assumed to be of sufficient energy that full thermalisation is unlikely. In a similar fashion to the factor D_{Source}, D^{Beam}_{Source} from (3.147) distributes the source $S^{e}_{se.inelastic}$ solely within the beam path to give energy deposition of $S^{e}_{se.inelastic}$ to infinitesimal volume $\boldsymbol{r} \pm \boldsymbol{\delta r}$ within the slice, as presented in (3.148).

$$s^{e}_{se.inelastic} = \int_{A_n} S^{e}_{se.inelastic} dA \delta x = \overline{n n_{se}} K_{in} A_b \delta x \tag{3.146}$$

$$D^{beam}_{source} = \begin{cases} \frac{n \delta x \delta y \delta z}{\int_{A_b} n \, dA \, \delta x} & \boldsymbol{r} \epsilon Beam \\ 0 & else \end{cases} \tag{3.147}$$

$$S^{e}_{se.inelastic} = s^{e}_{se.inelastic} \frac{D^{beam}_{source}}{\delta x \delta y \delta z} \tag{3.148}$$

Plasma Each of the plasma ions incident upon the neutraliser wall, quantified per unit time for an infinitesimal transverse slice as N_p, undergoes acceleration by the plasma potential before some fraction is neutralised and reflected back into the neutraliser. This returning flux $\widetilde{N_p}$ is defined by (3.149) and contains neutral molecules of energy $\widetilde{E^{+}_{p}}$ as per (3.150). Following multiple traverses of the neutraliser, each of these energetic molecules provides energy E^{dep}_{p} to the background gas before eventually thermalising, indicated by (3.151). Therefore upon thermalisation,

the gas will have provided both a density source s_p^ρ and an energy source s_p^e to the transverse slice of the neutraliser. These two quantities are distributed across the transverse slice to form density source S_p^ρ as per (3.154), momentum sources $S_p^{\rho \boldsymbol{u}}$ as in (3.155), and an energy source S_p^e of the form (3.156).

$$\widetilde{N_p} = N_p^{Reflect} N_p = N_p^{Reflect} \int_{A_b} n \, dA \, \delta x \, v_b \left(\overline{n_b^+} \left(\sigma_+ + \sigma_{10} \right) + \overline{n_b^0} \left(\sigma_0 + \sigma_{0\bar{1}} \right) + \overline{n_b^-} \sigma_0 \right) \tag{3.149}$$

$$\widetilde{E_p^+} = \frac{E_p^{Reflect}}{N_p^{Reflect}} \phi \tag{3.150}$$

$$E_p^{dep} = f_{total}^{dep_p} \left(\phi, \overline{T_{neut}}, \overline{n_{neut}}, \overline{d_{neut}}, T_w, \alpha_{hot} \right) \tag{3.151}$$

$$\begin{aligned} s_p^\rho = \int_{A_n} S_p^\rho dA \quad \delta x = & \quad m_{D_2} \widetilde{N_p^+}(x) \\ = & \quad m_{D_2} N_p^{Reflect} \overline{n} A_b \delta x \, v_b \left(\overline{n_b^+} \left(\sigma_+ + \sigma_{10} \right) + \overline{n_b^0} \left(\sigma_0 + \sigma_{0\bar{1}} \right) + \overline{n_b^-} \sigma_0 \right) \end{aligned} \tag{3.152}$$

$$\begin{aligned} s_p^e = \int_{A_n} S_p^e dA \quad \delta x = & \quad E_p^{dep} \widetilde{N_p^+} \\ = & \quad E_p^{dep} \overline{n} A_b \delta x \, v_b \left(\overline{n_b^+} \left(\sigma_+ + \sigma_{10} \right) + \overline{n_b^0} \left(\sigma_0 + \sigma_{0\bar{1}} \right) + \overline{n_b^-} \sigma_0 \right) \end{aligned} \tag{3.153}$$

$$S_p^\rho = \frac{D_{source}}{\delta x \delta y \delta z} s_p^\rho \tag{3.154}$$

$$S_p^{\rho \boldsymbol{u}} = \boldsymbol{u} S_p^\rho \tag{3.155}$$

$$S_p^e = e \frac{S_p^\rho}{\rho} + \frac{D_{source}}{\delta x \delta y \delta z} s_p^e \tag{3.156}$$

3.3 Finalised Governing Equations

From the outline of the gas governing equations in 3.1 and the provision of gas sources and sinks from the detailed physics examination of 3.2, the finalised governing equations take the form (3.157). It is this system that is applied to model gas neutralisers for the remainder of this thesis. Essentially the same as the outline of the gas governing equations (3.22)-(3.24), but presented in matrix form for three dimensions, flow variables $\boldsymbol{U}$ (3.158) are found via evaluation of inviscid fluxes $\boldsymbol{E}$, $\boldsymbol{F}$ and $\boldsymbol{G}$ (3.159) and viscous fluxes $\boldsymbol{E}_v$, $\boldsymbol{F}_v$ and $\boldsymbol{G}_v$ (3.160) with gas sources $\boldsymbol{S}$ and sinks $\boldsymbol{L}$ provided by (3.161)-(3.164). In the absence of the beam, and the plasma it generates, $\boldsymbol{S}$ and $\boldsymbol{L}$ return to zero and the system reduces to the basic gas governing equations outlined in (3.1)-(3.3). Note also that the system utilises the modified equation of state $\widehat{p}$ (3.25) to account for the effect of plasma pressure in the presence of beam; this too reduces to the original form (3.4) in the absence of beam since there is then no plasma in the system and thus no additional contribution to pressure. Apart from these modifications, the system retains the original definition of total gas energy equation (3.5), with viscosity provided by either (3.9) or (3.10) as discussed, and the viscous stress and heat flux provided by either the Navier-Stokes, Burnett or Augmented Burnett definitions from (3.13)-(3.21).

$$\frac{\partial}{\partial x}(\boldsymbol{E}-\boldsymbol{E}_v)+\frac{\partial}{\partial y}(\boldsymbol{F}-\boldsymbol{F}_v)+\frac{\partial}{\partial z}(\boldsymbol{G}-\boldsymbol{G}_v)+\frac{\partial}{\partial t}\boldsymbol{U}=\boldsymbol{S}-\boldsymbol{L} \tag{3.157}$$

$$\boldsymbol{U}=\begin{bmatrix}\rho\\ \rho u\\ \rho v\\ \rho w\\ e\end{bmatrix} \tag{3.158}$$

$$\begin{cases}\boldsymbol{E}=\begin{bmatrix}\rho u\\ \rho u^2+\widehat{p}\\ \rho uv\\ \rho uw\\ (e+\widehat{p})\,u\end{bmatrix}, \quad \boldsymbol{F}=\begin{bmatrix}\rho v\\ \rho uv\\ \rho v^2+\widehat{p}\\ \rho uw\\ (e+\widehat{p})\,v\end{bmatrix}, \quad \boldsymbol{G}=\begin{bmatrix}\rho w\\ \rho uw\\ \rho vw\\ \rho w^2+\widehat{p}\\ (e+\widehat{p})\,v\end{bmatrix}\end{cases} \tag{3.159}$$

$$\begin{cases}\boldsymbol{E}_v=\begin{bmatrix}0\\ \sigma_{11}\\ \sigma_{12}\\ \sigma_{13}\\ u\sigma_{11}+v\sigma_{12}+w\sigma_{13}+q_1\end{bmatrix}\\ \boldsymbol{F}_v=\begin{bmatrix}0\\ \sigma_{21}\\ \sigma_{22}\\ \sigma_{23}\\ u\sigma_{21}+v\sigma_{22}+w\sigma_{23}+q_2\end{bmatrix}\\ \boldsymbol{G}_v=\begin{bmatrix}0\\ \sigma_{31}\\ \sigma_{32}\\ \sigma_{33}\\ u\sigma_{31}+v\sigma_{32}+w\sigma_{33}+q_3\end{bmatrix}\end{cases} \tag{3.160}$$

$$\boldsymbol{L}=\boldsymbol{L}_{beam}+\boldsymbol{L}_{b.diss}+\boldsymbol{L}_{pe.diss}+\boldsymbol{L}_{se.diss} \tag{3.161}$$

$$
\begin{cases}
\boldsymbol{L}_b = \begin{bmatrix} L_b^{\rho} \\ L_b^{\rho u} \\ L_b^{\rho v} \\ L_b^{\rho w} \\ L_b^{e} \end{bmatrix} \\
\boldsymbol{L}_{b.diss} = \begin{bmatrix} L_{b.diss}^{\rho} \\ L_{b.diss}^{\rho u} \\ L_{b.diss}^{\rho v} \\ L_{b.diss}^{\rho w} \\ L_{b.diss}^{e} \end{bmatrix} \\
\boldsymbol{L}_{pe.diss} = \begin{bmatrix} L_{pe.diss}^{\rho} \\ L_{pe.diss}^{\rho u} \\ L_{pe.diss}^{\rho v} \\ L_{pe.diss}^{\rho w} \\ L_{pe.diss}^{e} \end{bmatrix} \\
\boldsymbol{L}_{se.diss} = \begin{bmatrix} L_{se.diss}^{\rho} \\ L_{se.diss}^{\rho u} \\ L_{se.diss}^{\rho v} \\ L_{se.diss}^{\rho w} \\ L_{se.diss}^{e} \end{bmatrix}
\end{cases}
\tag{3.162}
$$

$$
\boldsymbol{S} = \boldsymbol{S}_{b.diss} + \boldsymbol{S}_{pe.diss} + \boldsymbol{S}_{se.diss} + \boldsymbol{S}_{se.inelastic} + \boldsymbol{S}_p \tag{3.163}
$$

$$
\begin{cases}
\boldsymbol{S}_{b.diss} = \begin{bmatrix} S^{\rho}_{b.diss} \\ S^{\rho u}_{b.diss} \\ S^{\rho v}_{b.diss} \\ S^{\rho w}_{b.diss} \\ S^{e}_{b.diss} \end{bmatrix} \\
\boldsymbol{S}_{pe.diss} = \begin{bmatrix} S^{\rho}_{pe.diss} \\ S^{\rho u}_{pe.diss} \\ S^{\rho v}_{pe.diss} \\ S^{\rho w}_{pe.diss} \\ S^{e}_{pe.diss} \end{bmatrix} \\
\boldsymbol{S}_{se.diss} = \begin{bmatrix} S^{\rho}_{se.diss} \\ S^{\rho u}_{se.diss} \\ S^{\rho v}_{se.diss} \\ S^{\rho w}_{se.diss} \\ S^{e}_{se.diss} \end{bmatrix} \\
\boldsymbol{S}_{se.inelastic} = \begin{bmatrix} 0 \\ 0 \\ 0 \\ 0 \\ S^{e}_{se.inelastic} \end{bmatrix} \\
\boldsymbol{S}_{p} = \begin{bmatrix} S^{\rho}_{p} \\ S^{\rho u}_{p} \\ S^{\rho v}_{p} \\ S^{\rho w}_{p} \\ S^{e}_{p} \end{bmatrix}
\end{cases}
\tag{3.164}
$$

3.4 Numerical Framework

Within this thesis the gas governing equations have been solved for each of the flow cases by application of a finite volume method. Forming part of HiReCom, a numerical modelling framework developed in-house at Cranfield, the method has sought to solve the presented equation system via third order Runge-Kutta time integration with inviscid fluxes computed by an Eberle Characteristics-Based scheme and viscous fluxes via second order accurate central differences. To facilitate the accurate modelling of rarefied flow, care has been taken to accurately extend HiReCom to evaluate slip boundary conditions and the higher order viscous terms up to Super Burnett order. Considerable effort has also been necessary to implement the neutraliser source and sink terms of the neutraliser interaction model within the discrete computational environment. The code has been fully parallelised via domain decomposition to facilitate faster results. Each of these items is presented and discussed, with additional supporting material provided in Appendices **??**, **??** and **??**. An outline of the HiReCom code structure and the various modifications necessary to facilitate the work of this thesis is also given in Appendix **??**.

3.4.1 Finite Volume Method

Essentially dividing a domain of interest into a series of finite volumes, this method has been applied extensively within fluid dynamics as it facilitates the approximation of flow conservation laws[**?**]. Each of the created finite volumes is commonly referred to as a cell. A block-structured scheme is implemented within HiReCom and thus requires computational domains of quadrilateral or hexagonal cells. As summarised in figure 3.10, for two-dimensional domains each cell is thus outlined by four grid lines whilst for three-dimensional domains each cell is outlined by six faces. In each case, these cell boundaries serve to frame a computational node. One should note that the flow variables are reduced to volumetric averages over the computational cell.

3.4.2 Generalised Curvilinear Co-ordinates

To allow application of the developed solver to non-simple geometries such as the JET neutraliser geometry, each equation system has in fact been solved within a generalised curvilinear coordinate system. Described via variables $\xi = \xi(x,y,z,t)$, $\eta = \eta(x,y,z,t)$, and $\zeta = \zeta(x,y,z,t)$, this alternative coordinate system allows evaluation of irregularly spaced grids and curved geometries.

Conversion of the Cartesian form of (3.157) to a generalized curvilinear coordinate system is achieved by multiplication with the Jacobian determinant $|\boldsymbol{J}|$ of the co-ordinate transformation, as in (3.165), and substitution of the partial derivatives, exemplified in (3.166). Ultimately, one obtains the curvilinear form (3.167) where the curvilinear equivalents of the flow variables and fluxes are defined as in (3.168). The complete list of the grid metrics and partial derivatives required to convert the terms up to Super Burnett order to and from a curvilinear system are detailed in Appendix **??**.

$$|\boldsymbol{J}| = \frac{\partial x}{\partial \xi}\left(\frac{\partial y}{\partial \eta}\frac{\partial z}{\partial \zeta} - \frac{\partial y}{\partial \zeta}\frac{\partial z}{\partial \eta}\right) + \frac{\partial y}{\partial \xi}\left(\frac{\partial z}{\partial \eta}\frac{\partial x}{\partial \zeta} - \frac{\partial z}{\partial \zeta}\frac{\partial x}{\partial \eta}\right) + \frac{\partial z}{\partial \xi}\left(\frac{\partial x}{\partial \eta}\frac{\partial y}{\partial \zeta} - \frac{\partial x}{\partial \zeta}\frac{\partial y}{\partial \eta}\right) \tag{3.165}$$

$$
\begin{cases}
\frac{\partial}{\partial x} &= \frac{\partial \xi}{\partial x}\frac{\partial}{\partial \xi} + \frac{\partial \eta}{\partial x}\frac{\partial}{\partial \eta} + \frac{\partial \zeta}{\partial x}\frac{\partial}{\partial \zeta} \\
\frac{\partial^2}{\partial x^2} &= \left(\frac{\partial \xi}{\partial x}\right)^2 \frac{\partial^2}{\partial \xi^2} + \left(\frac{\partial \eta}{\partial x}\right)^2 \frac{\partial^2}{\partial \eta^2} + \left(\frac{\partial \zeta}{\partial x}\right)^2 \frac{\partial^2}{\partial \zeta^2} + \\
& 2\frac{\partial \xi}{\partial x}\frac{\partial \eta}{\partial x}\frac{\partial^2}{\partial \xi \partial \eta} + 2\frac{\partial \xi}{\partial x}\frac{\partial \zeta}{\partial x}\frac{\partial^2}{\partial \xi \partial \zeta} + 2\frac{\partial \eta}{\partial x}\frac{\partial \zeta}{\partial x}\frac{\partial^2}{\partial \eta \partial \zeta} + \\
& \frac{\partial^2 \xi}{\partial x^2}\frac{\partial}{\partial \xi} + \frac{\partial^2 \eta}{\partial x^2}\frac{\partial}{\partial \eta} + \frac{\partial^2 \zeta}{\partial x^2}\frac{\partial}{\partial \zeta} \\
\frac{\partial^3}{\partial x^3} &= \left(\frac{\partial \xi}{\partial x}\right)^3 \frac{\partial^3}{\partial \xi^3} + \left(\frac{\partial \eta}{\partial x}\right)^3 \frac{\partial^3}{\partial \eta^3} + \left(\frac{\partial \zeta}{\partial x}\right)^3 \frac{\partial^3}{\partial \zeta^3} + 6\frac{\partial \xi}{\partial x}\frac{\partial \eta}{\partial x}\frac{\partial \zeta}{\partial x}\frac{\partial^3}{\partial \xi \partial \eta \partial \zeta} + \\
& 3\left(\frac{\partial \xi}{\partial x}\right)^2 \frac{\partial \eta}{\partial x}\frac{\partial^3}{\partial \xi^2 \partial \eta} + 3\left(\frac{\partial \xi}{\partial x}\right)^2 \frac{\partial \zeta}{\partial x}\frac{\partial^3}{\partial \xi^2 \partial \zeta} + 3\left(\frac{\partial \eta}{\partial x}\right)^2 \frac{\partial \xi}{\partial x}\frac{\partial^3}{\partial \eta^2 \partial \xi} + \\
& 3\left(\frac{\partial \eta}{\partial x}\right)^2 \frac{\partial \zeta}{\partial x}\frac{\partial^3}{\partial \eta^2 \partial \zeta} + 3\left(\frac{\partial \zeta}{\partial x}\right)^2 \frac{\partial \xi}{\partial x}\frac{\partial^3}{\partial \zeta^2 \partial \xi} + 3\left(\frac{\partial \zeta}{\partial x}\right)^2 \frac{\partial \eta}{\partial x}\frac{\partial^3}{\partial \zeta^2 \partial \eta} + \\
& 3\frac{\partial \xi}{\partial x}\frac{\partial^2 \xi}{\partial x^2}\frac{\partial^2}{\partial \xi^2} + 3\frac{\partial \eta}{\partial x}\frac{\partial^2 \eta}{\partial x^2}\frac{\partial^2}{\partial \eta^2} + 3\frac{\partial \zeta}{\partial x}\frac{\partial^2 \zeta}{\partial x^2}\frac{\partial^2}{\partial \zeta^2} + \\
& 3\left(\frac{\partial \xi}{\partial x}\frac{\partial^2 \eta}{\partial x^2} + \frac{\partial \eta}{\partial x}\frac{\partial^2 \xi}{\partial x^2}\right)\frac{\partial^2}{\partial \xi \partial \eta} + 3\left(\frac{\partial \xi}{\partial x}\frac{\partial^2 \zeta}{\partial x^2} + \frac{\partial \zeta}{\partial x}\frac{\partial^2 \xi}{\partial x^2}\right)\frac{\partial^2}{\partial \xi \partial \zeta} + 3\left(\frac{\partial \eta}{\partial x}\frac{\partial^2 \zeta}{\partial x^2} + \frac{\partial \zeta}{\partial x}\frac{\partial^2 \eta}{\partial x^2}\right)\frac{\partial^2}{\partial \eta \partial \zeta} + \\
& \frac{\partial^3 \xi}{\partial x^3}\frac{\partial}{\partial \xi} + \frac{\partial^3 \eta}{\partial x^3}\frac{\partial}{\partial \eta} + \frac{\partial^3 \zeta}{\partial x^3}\frac{\partial}{\partial \zeta} \\
\frac{\partial}{\partial t} &= \frac{\partial}{\partial \tau}
\end{cases}
\tag{3.166}
$$

$$
\frac{\partial}{\partial \xi}\left(\tilde{\boldsymbol{E}} - \tilde{\boldsymbol{E}_v}\right) + \frac{\partial}{\partial \eta}\left(\tilde{\boldsymbol{F}} - \tilde{\boldsymbol{F}_v}\right) + \frac{\partial}{\partial \zeta}\left(\boldsymbol{G} - \tilde{\boldsymbol{G}_v}\right) + \frac{\partial}{\partial t}\tilde{\boldsymbol{U}} = 0 \tag{3.167}
$$

$$
\begin{cases}
\tilde{\boldsymbol{U}} = |\boldsymbol{J}|\boldsymbol{U} \\
\tilde{\boldsymbol{E}} = |\boldsymbol{J}|\left(\boldsymbol{E}\xi_x + \boldsymbol{F}\xi_y + \boldsymbol{G}\xi_z\right) \\
\tilde{\boldsymbol{F}} = |\boldsymbol{J}|\left(\boldsymbol{E}\eta_x + \boldsymbol{F}\eta_y + \boldsymbol{G}\eta_z\right) \\
\tilde{\boldsymbol{G}} = |\boldsymbol{J}|\left(\boldsymbol{E}\zeta_x + \boldsymbol{F}\zeta_y + \boldsymbol{G}\zeta_z\right) \\
\tilde{\boldsymbol{E}_v} = |\boldsymbol{J}|\left(\boldsymbol{E}_v\xi_x + \boldsymbol{F}_v\xi_y + \boldsymbol{G}_v\xi_z\right) \\
\tilde{\boldsymbol{F}_v} = |\boldsymbol{J}|\left(\boldsymbol{E}_v\eta_x + \boldsymbol{F}_v\eta_y + \boldsymbol{G}_v\eta_z\right) \\
\tilde{\boldsymbol{G}_v} = |\boldsymbol{J}|\left(\boldsymbol{E}_v\zeta_x + \boldsymbol{F}_v\zeta_y + \boldsymbol{G}_v\zeta_z\right)
\end{cases}
\tag{3.168}
$$

3.4.3 Spatial discretisation

A spatially semi-discretised form (3.169) of the governing equations (3.167) has been solved in order to allow stepping of the solution with time. This form results from discretisation of each finite volume via inter-cell flux values at the cell faces.

$$
\begin{aligned}
\frac{\partial \boldsymbol{U}_{I,J,K}}{\partial t} = & -\frac{\tilde{\boldsymbol{E}}_{I+\frac{1}{2},J,K} - \tilde{\boldsymbol{E}}_{I-\frac{1}{2},J,K}}{\triangle \xi} - \frac{\tilde{\boldsymbol{F}}_{I,J+\frac{1}{2},K} - \tilde{\boldsymbol{F}}_{I,J-\frac{1}{2},K}}{\triangle \eta} - \frac{\tilde{\boldsymbol{G}}_{I,J,K+\frac{1}{2}} - \tilde{\boldsymbol{G}}_{I,J,K-\frac{1}{2}}}{\triangle \zeta} \\
& + \frac{\tilde{\boldsymbol{E}}_{v,I+\frac{1}{2},J,K} - \tilde{\boldsymbol{E}}_{v,I-\frac{1}{2},J,K}}{\triangle \xi} + \frac{\tilde{\boldsymbol{F}}_{v,I,J+\frac{1}{2},K} - \tilde{\boldsymbol{F}}_{v,I,J-\frac{1}{2},K}}{\triangle \eta} + \frac{\tilde{\boldsymbol{G}}_{v,I,J,K+\frac{1}{2}} - \tilde{\boldsymbol{G}}_{v,I,J,K-\frac{1}{2}}}{\triangle \zeta}
\end{aligned}
\tag{3.169}
$$

It follows that the rate of change of the flow variable volumetric averages in each finite volume is defined by the net fluxes into the cell across corresponding boundaries. Corresponding boundaries are formed by opposite grid lines or faces, in two or three dimensional domains respectively. Note that since each bounding face of the cell is common to it and the adjacent cell, the flux entering a cell at a particular boundary should be identical to that leaving the adjacent cell via that common boundary.

The piecewise-constant distribution offered by the set of volumetric cell averages leads to discontinuity at the cell interfaces. At each cell interface, this discontinuity offers a Riemann

problem and thus evaluation of the inter-cell fluxes is achieved via application of an approximate Riemann solver, which utilises knowledge of the left and right flow variable states at the cell interface. These left and right states can follow from the piecewise-constant distribution offered by the cell averages, as in (3.170). However, the accuracy of these states and thus the resultant inter-cell fluxes can be enhanced by a process known as variable reconstruction which seeks to reproduce knowledge of spatial variation within the cells.

$$\begin{aligned} \boldsymbol{U}_{L,I+\frac{1}{2}} &= \boldsymbol{U}_I \\ \boldsymbol{U}_{R,I+\frac{1}{2}} &= \boldsymbol{U}_{I+1} \end{aligned} \tag{3.170}$$

Within this thesis, the non-linear inviscid fluxes are solved via a Godunov-type characteristics based method first presented for the compressible Euler equations by *Eberle*[**?**], later extended by *Drikakis*[**?**] and *Drikakis et al*[**?**], and furthered by the characteristics-based scheme of *Shapiro*[**?** **?**]. By contrast, the linear viscous fluxes are provided by a second-order accurate central difference scheme. Whilst the majority of the work presented in the thesis utilises the Monotonic Upwind Scheme for Scalar Conservation Laws (MUSCL)[**?**] to provide variable reconstruction, additional schemes and their influence upon the Burnett Equations are evaluated; utilisation of the piecewise-constant distribution provided by the cell averages, uniformly second order reconstruction and the Weighted Essentially Non-Oscillatory (WENO)[**?**] scheme are all also examined.

Uniformly second order reconstruction is discussed in detail by *Drikakis*[**?**]. It utilises Taylor series expansion of the volumetric averages at the cells neighbouring the cell interface, accuracy of their derivatives is ensured to the desired order of accuracy. The second order scheme thus results in formula (3.171) to provide the left and right states.

$$\begin{aligned} \boldsymbol{U}_{L,I+\frac{1}{2}} &= \tfrac{3}{2}\boldsymbol{U}_I - \tfrac{1}{2}\boldsymbol{U}_{I-1} \\ \boldsymbol{U}_{R,I+\frac{1}{2}} &= \tfrac{3}{2}\boldsymbol{U}_{I+1} - \tfrac{1}{2}\boldsymbol{U}_{I+2} \end{aligned} \tag{3.171}$$

Within the MUSCL scheme left and right states of the conservative variables at some generalised cell interface $I+\frac{1}{2}$ are provided by the formulae (3.172) of e.g. *Toro*[**?**]. In the work presented in this thesis, the free parameter k has been set to $k=-1$. Utilising the volume averaged values in neighbouring cells, the scheme constructs piecewise linear approximations of the variable values in each cell, whose slopes are limited by a prescribed function ϕ. The limiter function serves to avoid spurious oscillations that can occur due to shock structures or sharp changes in the solution domain. Wherever the MUSCL scheme is applied within this thesis the second order MinMod limiter function $\widetilde{\phi}$ [**?**] has been used (3.173), where the ratio of the slopes $\widetilde{r}$ corresponds to (3.174).

$$\begin{aligned} \boldsymbol{U}_{L,I+\frac{1}{2}} &= \boldsymbol{U}_I + \tfrac{1}{4}\left|(1-k)\,\widetilde{\phi}_L\left(\boldsymbol{U}_I - \boldsymbol{U}_{I-1}\right) + (1+k)\,\widetilde{\phi}_L\left(\boldsymbol{U}_{I+1} - \boldsymbol{U}_I\right)\right| \\ \boldsymbol{U}_{R,I+\frac{1}{2}} &= \boldsymbol{U}_I - \tfrac{1}{4}\left|(1-k)\,\widetilde{\phi}_R\left(\boldsymbol{U}_{I+2} - \boldsymbol{U}_{I+1}\right) + (1+k)\,\widetilde{\phi}_R\left(\boldsymbol{U}_{I+1} - \boldsymbol{U}_I\right)\right| \end{aligned} \tag{3.172}$$

$$\widetilde{\phi}_{L,R} = \begin{cases} 0 & \text{if } \widetilde{r}_{L,R} \leq 0 \\ \widetilde{r}_{L,R} & \text{if } \widetilde{r}_{L,R} > 0 \end{cases} \tag{3.173}$$

$$\left\{ \begin{array}{c} \widetilde{r}_L = \frac{\boldsymbol{u}_{I+1} - \boldsymbol{u}_I}{\boldsymbol{u}_I - \boldsymbol{u}_{I-1}} \\ \widetilde{r}_R = \frac{\boldsymbol{u}_{I+1} - \boldsymbol{u}_I}{\boldsymbol{u}_{I+2} - \boldsymbol{u}_{I+1}} \end{array} \right\} \tag{3.174}$$

WENO schemes are an extension of the Essentially Non-Oscillatory (ENO) schemes, which were developed to smooth the oscillations that often occur from reconstruction utilising higher-order polynomial interpolation. Rather than the application of a variable limiter as in MUSCL schemes, the ENO and WENO schemes produce several polynomial candidates for the reconstruction, which are then subject to selection criterion or weighting; ENO schemes produce several stencils, essentially data samples about the cell interface, of which the smoothest is used to provide polynomial interpolation to the desired left or right state[**?**], whilst the WENO method seeks to use all of these stencils and weight them by their smoothness[**?**].

Only the WENO method is applied in this thesis, and it utilises three cell values either side of the cell boundary of interest to provides a fifth-order accurate variable reconstruction. Exemplified for reconstruction of the left and right states at some generalised cell boundary at $I + \frac{1}{2}$, three stencils are produced for each of the states $\boldsymbol{U}_R$ and $\boldsymbol{U}_L$ via sampling of the cell values near the cell boundary of interest as in (3.175)-(3.176). Each stencil provides a polynomial interpolation of the states at the cell boundary p_n from a generic function as in (3.177). The differing polynomials applicable to each state are then combined via (3.178) in accordance with their multipliers c_n to provide either $\boldsymbol{U}_R$ or $\boldsymbol{U}_L$. The multipliers for each state are determined via (3.179), and consists of optimised weighting factors α_n, a small positive number $\widetilde{\delta}$ to avoid division by zero, and the smoothness indicator I_n. Specific to the stencil sets for each state, the smoothness indicator is evaluated by a generic function of the stencil set (3.180). Note that higher-order accuracy beyond fifth order demands increasing numbers of local cells to provide larger stencils, and in turn more complex polynomial candidates and smoothness indicators.

$$\left\{ \begin{array}{c} S_{1,L} = (\boldsymbol{U}_I, \boldsymbol{U}_{I+1}, \boldsymbol{U}_{I+2}) \\ S_{2,L} = (\boldsymbol{U}_{I-1}, \boldsymbol{U}_I, \boldsymbol{U}_{I+1}) \\ S_{3,L} = (\boldsymbol{U}_{I-2}, \boldsymbol{U}_{I-1}, \boldsymbol{U}_I) \end{array} \right. \tag{3.175}$$

$$\left\{ \begin{array}{c} S_{1,R} = (\boldsymbol{U}_{I-1}, \boldsymbol{U}_I, \boldsymbol{U}_{I+1}) \\ S_{2,R} = (\boldsymbol{U}_I, \boldsymbol{U}_{I+1}, \boldsymbol{U}_{I+2}) \\ S_{3,R} = (\boldsymbol{U}_{I+1}, \boldsymbol{U}_{I+2}, \boldsymbol{U}_{I+3}) \end{array} \right. \tag{3.176}$$

$$\left\{ \begin{array}{c} p_{n,*}(x) = f(S_{n,*}, x) \\ *\epsilon \{L, R\} \\ n\epsilon \{1, 2, 3\} \end{array} \right. \tag{3.177}$$

$$\left\{ \begin{array}{c} \boldsymbol{U}_{*,I+\frac{1}{2}} = \frac{p_{1,*}\left(x_{I+\frac{1}{2}}\right)c_{1,*} + p_{2,*}\left(x_{I+\frac{1}{2}}\right)c_{2,*} + p_{3,*}\left(x_{I+\frac{1}{2}}\right)c_{3,*}}{c_1 + c_2 + c_3} \\ *\epsilon (L, R) \end{array} \right. \tag{3.178}$$

$$\begin{cases} c_{n,*} = \frac{\alpha_n}{\left(\tilde{\delta}+I_{n,*}\right)^2} \\ *\epsilon \{L,R\} \\ n\epsilon \{1,2,3\} \end{cases} \tag{3.179}$$

$$\begin{cases} I_{n,*} = g\left(S_{n,*},x\right) \\ *\epsilon \{L,R\} \\ n\epsilon \{1,2,3\} \end{cases} \tag{3.180}$$

3.4.4 Time Integration

In general, there are two distinct approaches to provide solutions of time-dependent partial differential equations. Explicit methods seek to step the solution to some future time via knowledge of only the system at the current time, as in (3.181). By contrast implicit methods seek to provide the state of the system at some future time by solution of an equation involving both that future state and the current state, as in (3.182). The latter are generally difficult to implement and require greater computation to achieve a single timestep. However, in the event of stiff problems that serve to surpress the stable explicit timestep, implicit methods typically offer significantly larger stable timesteps and thus may offer an overall reduction in the computational effort required to provide a solution over a large time interval.

$$\boldsymbol{U}\left(t+\triangle t\right) = G_E\left(\boldsymbol{U}\left(t\right)\right) \tag{3.181}$$

$$G_I\left(\boldsymbol{U}\left(t\right),\boldsymbol{U}\left(t+\triangle t\right)\right) = 0 \tag{3.182}$$

As time-resolved experimental measurements indicate that the neutraliser gas flow quickly reaches a steady state both in the absence and presence of beam [**?**], a steady state solution is sought for each of the simulations presented in this thesis. Thus, a solution is obtained via a time-marching algorithm that assymptotically approaches the required solution. Though an implicit scheme might prove advantageous in speeding up overall convergence of the system, the algebraic complexity of the beam and plasma models, and that of their coupling to the gas model, imply the derivation of an implicit formulation would prove impractical. Whilst these gas source/sink terms could be treated explicitly and the stiff viscous terms subjected to implicit solution via the use of an Implicit-Explicit (IMEX) scheme [**?**], this would have presented a significant project risk given the desire for simulations in up to three-dimensions; in-house development of an IMEX scheme at Cranfield University applicable to solid mechanics has demonstrated significant difficulties in application to multiple spatial dimensions[**?**]. Instead, a fully explicit Runge-Kutta time integration method has been implemented for the model developed in HiReCom in order to minimise the project risk of over-run. A third-order accurate TVD scheme[**?**] has been utilised, as summarised in (3.183).

Given the application of a fully explicit time-dependent scheme, time marching is achieved via a global timestep over the computational domain applied to each cell at every solution step. It is typical to evaluate this global timestep $\triangle t$ via calculation of the eigenvalues of the jacobians of the inviscid fluxes $\boldsymbol{E},\boldsymbol{F},\boldsymbol{G}$ within each cell of the domain as in (3.184). It is the minimum value over

the domain that forms the theoretical timestep limit, with additional restriction often necessary to provide the applied timestep. This additional restriction is achieved via selection of the Courant-Friedrichs-Lewy (CFL) number. For stiff systems, such as the Burnett and Augmented Burnett equations increasing restriction of the global timestep is required to ensure a stable solution is obtained, and achieved via lowering the CFL. Indeed, though the theoretically stable limit of the forward Euler method is $CFL \leq 1$, previous applications of the Augmented Burnett equations with an eigenalue based timestep limit have required a CFL value several orders of magnitude lower in order to provide stable, accurate simulations[**?**] . Thus, within this thesis an alternative timestep limit is formulated that seeks to avoid the exhaustive search for a suitably low CFL. This alternative formulation is derived in Appendix **??** and further discussed in chapter 4. Presented in (3.185) for the Navier-Stokes equations and (3.186) for the Augmented Burnett equations, these formulae consider each interior cell of the computational domain and denote δ to be the minimum distance between corresponding boundaries for each cell, i.e. $\delta = min\left(\Delta x, \Delta y, \Delta z\right)$.

$$\begin{aligned} \frac{\boldsymbol{u}^1 - \boldsymbol{u}^n}{\triangle t} &= f\left(\boldsymbol{U}^n, t^n\right) \\ \frac{\boldsymbol{u}^2 - \boldsymbol{u}^n}{\triangle t} &= \frac{1}{4}\left[f\left(\boldsymbol{U}^n, t^n\right) + f\left(\boldsymbol{U}^1, t^{n+\frac{1}{3}}\right)\right] \\ \frac{\boldsymbol{u}^{n+1} - \boldsymbol{u}^n}{\triangle t} &= \frac{1}{6}\left[f\left(\boldsymbol{U}^n, t^n\right) + 4f\left(\boldsymbol{U}^2, t^{n+\frac{2}{3}}\right) + f\left(\boldsymbol{U}^1, t^{n+\frac{1}{3}}\right)\right] \end{aligned} \tag{3.183}$$

$$\triangle t = min\left(|\boldsymbol{J}| \frac{CFL}{max\left(\left|\lambda_0^\xi\right|, \left|\lambda_+^\xi\right|, \left|\lambda_-^\xi\right|, \left|\lambda_0^\eta\right|, \left|\lambda_+^\eta\right|, \left|\lambda_-^\eta\right|, \left|\lambda_0^\zeta\right|, \left|\lambda_+^\zeta\right|, \left|\lambda_-^\zeta\right|\right)}\right) \tag{3.184}$$

$$\triangle t = min\left(\frac{CFL.3\rho\delta^2}{8\mu}, |\boldsymbol{J}| \frac{CFL.\delta}{max_{\alpha\epsilon\xi,\eta,\zeta}\left(\left|\lambda_0^\alpha\right|, \left|\lambda_+^\alpha\right|, \left|\lambda_-^\alpha\right|\right)}\right) \tag{3.185}$$

$$\triangle t = min\left(\frac{CFL.9\delta^4\rho^2 p}{16\mu^3}, \frac{CFL.3\delta^2\rho}{8\mu}, |\boldsymbol{J}| \frac{CFL.\delta}{max_{\alpha\epsilon\xi,\eta,\zeta}\left(\left|\lambda_0^\alpha\right|, \left|\lambda_+^\alpha\right| \left|\lambda_-^\alpha\right|,\right)}\right) \tag{3.186}$$

3.4.5 Boundary Conditions

The implemented scheme within HiReCom is such that the computational domain consists of interior cells and fictitious boundary cells. The flow governing equations are evaluated solely for the interior cells. By contrast, the fictitious boundary cells lie beyond some associated boundary and their variable values are specified from both the conditions required at the boundary and the nearby interior flow cells. The values at the fictitious cells are used to evaluate differentials and variable reconstruction, thus influencing the fluxes calculated for the interior cells at and near the boundary. Evaluation of most CFD equation systems requires only two fictitious cells, but evaluation of the viscous terms up to Super Burnett order requires three fictitious cells because the higher order derivatives draw on variable values from a larger number of local cells.

Within this thesis symmetry, inlet/outlet flow and wall conditions have all been applied. Each is outlined briefly in the summary paragraphs below, wherein a generalised variable is denoted by $*$, values at the boundary possess subscript $bdry$, interior cells of the computational domain are denoted by a subscript i that describes the cell's location and fictitious cells are denoted by

subscript $F(i)$. Note that fictitious cell $F(i)$ can be considered to correspond to interior cell i via symmetry at the boundary, simplifiying the formulae presented below. This nomenclature is visually summarised in figure 3.12.

Symmetry Symmetry boundary conditions require variable derivatives normal to the boundary to equal zero at the boundary, as in (3.187). One exception is the treatment of the velocity normal to the boundary, denoted by $*_{\tilde{n}}$ in (3.188), which must equal zero at the boundary. Within the HiReCom framework this boundary condition results in the equating of all fictitious cell variables to corresponding internal cells, with the exception of the velocity normal to the boundary which instead takes on the negated value of the corresponding fictitious cell. This fictitious cell specification can therefore be summarised by (3.189)-(3.190).

$$\frac{\partial *}{\partial \tilde{n}}|_{bdry} = 0 \tag{3.187}$$

$$*_{\tilde{n}}|_{bdry} = 0 \tag{3.188}$$

$$*|_{F(i)} = *|_i \tag{3.189}$$

$$*_{\tilde{n}}|_{F(i)} = -*|_i \tag{3.190}$$

Inlet/Outlet Inlet and outlet flow boundary conditions typically involve simple extrapolation of variable values across the boundary to the fictitious cells as exemplified in (3.191). Some inlet and outlet flow cases also require the fixing of one or more variables to a set value at the boundary as provided by (3.192).

$$*|_{F(i)} = \begin{cases} 2*|_1 - *|_2 & i = 1 \\ 2*|_{F(1)} - *|_1 & i = 2 \\ 2*|_{F(i-1)} - *|_{F(i-2)} & i > 2 \end{cases} \tag{3.191}$$

$$*|_{F(i)} = 2*|_{bdry} - *|_i \tag{3.192}$$

Wall The implementation of wall boundary conditions requires both symmetry and extrapolation formulae. It is necessary to ensure no mass flow over the boundary via the stipulation of a zero density gradient at the wall, in similar fashion to (3.187). This is typically achieved in HiReCom via equality of the density within the fictitious cells to their corresponding interior cells, as exemplified by (3.189). Specification of the temperature and velocity in the fictitious cells results from (3.191), with the value at the boundary equal to the evaluated slip values. Note that velocity normal to the boundary is equated to zero at the boundary and thus its value at the fictitious cells is typically evaluated via negation of the value corresponding to the interior cells, as in (3.190), in order to imply no flow across the boundary, as in (3.188).

As discussed in Chapter 2, the implementation of wall boundary conditions is of great importance in the simulation of rarefied gas flows. Therefore, the production of this thesis has included

great endeavour to ensure their accurate implementation within HiReCom. Accurate slip evaluation is not straightforward for finite volume solvers due to the discretisation of the domain; velocity and temperature slip evaluation require calculation of derivatives both normal and perpendicular to the wall and thus care is necessary to maintain precision in their evaluation. To implement wall conditions at the boundary one must find the wall slip velocity and temperature values for each cell of the boundary face. The boundary condition extensions implemented within HiReCom allow application of the no-slip, first order Maxwell-Smoluchowski and second order Deissler conditions. Whilst their full implementation is presented in significant detail in Appendix **??**, the rationale of these implementations is given briefly in the following paragraph.

To provide the slip temperature and velocities it is necessary to numerically evaluate each of the terms in the slip model formulae (2.5)-(2.6) or (2.7)-(2.8), and then subject these formulae to algebraic manipulation to provide the desired slip quantities as resultants. In order to evaluate each term of the slip model formulae, it is necessary to evaluate first order and second order derivates normal and parallel to the boundary, as well as the mean free path, density, temperature and velocity, all at the wall. Of these items, the most obvious are the latter collection of variables, which may be provided at the wall for each cell of the boundary face via second order extrapolation from interior cells as exemplified by (3.193) for some generalised variable $*$ and the set of cells normal to our boundary cell of interest in figure 3.13. With regards to the derivatives, it is necessary to evaluate both temperature and velocity derivatives; the author advocates the evaluation of derivatives of curvilinear velocities as its components are assured to be normal and parallel to the boundary, something which cannot be guaranteed for Cartesian velocity components in the case of an irregular wall boundary. It is also beneficial to treat the normal and parallel derivatives separately; forward derivatives are necessary to evaluate the normal derivatives at the wall whilst central differencing is applicable to the parallel derivatives. It follows that the first order and second order normal derivatives are therefore provided by use of the interior cells (3.194)-(3.195), with nomenclature as indicated in figure 3.13. Indirect use of the interior cells is also required for the parallel derivatives, which should be evaluated from the values of temperature and curvilinear velocity extrapolated to the wall as in (3.196)-(3.197); if the slip values at neighbouring cells were instead used, a sytem of simultaneous equations for all the cells at the boundary would develop and require excessive and unnecessary computational effort to solve. Thus from each of these numerical terms it is possible to provide resultant slip quantities for slip (3.198)-(3.199) for the two-dimensional system represented in figure 3.13. Since the wall may be irregular in shape, it is the curvilinear velocities that together with temperature extrapolated to the fictitious cells. These fictitious cell velocities are then transformed back into Cartesian components for use in the remainder of the solver. This outline is provided in greater detail with further discussion and formulae for a generalised three-dimenensional domain in Appendix **??**.

$$*|_0 = \frac{15*|_1 - 10*|_2 + 3*|_3}{8} \tag{3.193}$$

$$\frac{\partial *}{\partial n}|_s = \frac{*|_1 - *|_s}{\frac{\triangle_1}{2}} \tag{3.194}$$

$$\frac{\partial^2 *}{\partial n^2}|_s = \frac{*|_2 \frac{\triangle_1}{2} - *|_1 \left(\triangle_1 + \frac{\triangle_2}{2}\right) + *|_s \left(\frac{\triangle_1}{2} + \frac{\triangle_2}{2}\right)}{\left(\frac{\triangle_1}{2}\right)^2 \left(\frac{\triangle_1}{2} + \frac{\triangle_2}{2}\right)} \tag{3.195}$$

$$\frac{d*}{dp}|_s = \frac{\widetilde{*}|_{+1} - \widetilde{*}|_{-1}}{\triangle_{p_+} + \triangle_{p_-}} \tag{3.196}$$

$$\frac{d^2 *}{dp^2}|_s = \frac{\triangle_{p_-} \widetilde{*}|_{+1} - \left(\triangle_{p_-} + \triangle_{p_+}\right) \widetilde{*}|_0 + \triangle_{p_+} \widetilde{*}|_{-1}}{\triangle_{p_+} \triangle_{p_0} \triangle_{p_-}} \tag{3.197}$$

$$T_s|_0 = \begin{cases} T_w & \text{No-Slip} \\ \frac{\triangle_1 T_w + 2c_T \widetilde{\lambda}|_0 T|_1}{\Delta_1 + 2c_T \widetilde{\lambda}|_0} & \text{if Maxwell First Order Slip} \\ \frac{1}{\left(\frac{\triangle_1}{2}\right)^2 \left(\frac{\triangle_1}{2} + \frac{\triangle_2}{2}\right) + c_{T_1} \widetilde{\lambda}|_0 \frac{\triangle_1}{2} \left(\frac{\triangle_1}{2} + \frac{\triangle_2}{2}\right) + c_{T_2} \widetilde{\lambda}|_0^2 \left(\frac{\triangle_1}{2} + \frac{\triangle_2}{2}\right)} \times & \\ \left(\left(\frac{\triangle_1}{2}\right)^2 \left(\frac{\triangle_1}{2} + \frac{\triangle_2}{2}\right) T_w + \left(c_{T_1} \widetilde{\lambda}|_0 \frac{\triangle_1}{2} \left(\frac{\triangle_1}{2} + \frac{\triangle_2}{2}\right)\right.\right. & \text{if Deissler Second Order Slip} \\ \left.\left. - c_{T_2} \widetilde{\lambda}|_0^2 \frac{\triangle_1}{2} T|_2\right) T|_1 - c_{T_2} \frac{\widetilde{\lambda}|_0^2}{2} \left(\frac{\triangle_1}{2}\right)^2 \left(\frac{\triangle_1}{2} + \frac{\triangle_2}{2}\right) \left(\sum_{i=1}^{2} \left(\frac{d^2 T}{dp_i^2}\right)_s\right) \end{cases} \tag{3.198}$$

$$u_s^p|_0 = \begin{cases} 0 & \text{if No-Slip} \\ \frac{2c_u \widetilde{\lambda}|_0 u^p|_{\pm,1} + \Delta_1 c_{creep} \left(\frac{dT}{dy}\right)_{s,\pm}}{\Delta_1 + 2c_u \widetilde{\lambda}|_0} & \text{if Maxwell First Order Slip} \\ \frac{1}{\left(\frac{\triangle_1}{2}\right)^2 \left(\frac{\triangle_1}{2} + \frac{\triangle_2}{2}\right) + c_{T_1} \widetilde{\lambda}|_0 \frac{\triangle_1}{2} \left(\frac{\triangle_1}{2} + \frac{\triangle_2}{2}\right) + c_{T_2} \widetilde{\lambda}|_0^2 \left(\frac{\triangle_1}{2} + \frac{\triangle_2}{2}\right)} \times & \\ \left(\left(c_{u_1} \widetilde{\lambda}|_0 \frac{\triangle_1}{2} \left(\frac{\triangle_1}{2} + \frac{\triangle_2}{2}\right) + c_{u_2} \widetilde{\lambda}|_0^2 \left(\frac{\triangle_1}{2}\right)^2 \left(\triangle_1 + \frac{\triangle_2}{2}\right)\right) u^p|_{\pm,1}\right. & \text{if Deissler Second Order Slip} \\ - c_{u_2} \widetilde{\lambda}|_0^2 \frac{\triangle_1}{2} v^\eta|_{\pm,2} - c_{u_2} \frac{\widetilde{\lambda}|_0^2}{2} \left(\frac{\triangle_1}{2}\right)^2 \left(\frac{\triangle_1}{2} + \frac{\triangle_2}{2}\right) \frac{d^2 u^p}{dp^2}|_s & \\ \left. + c_{creep} \left(\frac{\triangle_1}{2}\right)^2 \left(\frac{\triangle_1}{2} + \frac{\triangle_2}{2}\right) \frac{du}{dp}|_s\right) & \end{cases} \tag{3.199}$$

3.4.6 Neutraliser Source/Sink & Pressure Evaluation

The model to provide gas sources and sinks due to the beam and plasma has already been presented in great detail. Obviously implementation within HiReCom of the steady state beam and plasma models throughout the neutraliser domain and the evaluation of the gas sources and sinks within each cell has required signifiant numerical interperation and coding effort. The finalised discretisation and implementation allows application to various computational geometries in both two and three dimensions, and may be applied to domains both with and without transverse symmetry conditions. The implementation for each computational domain type essentially adapts the neutraliser slice modelling approach, with the slices corresponding to each longitudinal plane of cells in the computational grid. A detailed presentation of the implemented interaction, beam and plasma model may be found in Appendix **??**.

As well as the evaluation of gas source/sinks, these neutraliser specific model components include the evaluation of the steady state plasma density distribution in the neutraliser. This quantity facilitates the evaluation of the modified equation of state (3.25) in the presence of beam and serves to impact on the calculation of inviscid fluxes; in a style typical of turbulence models[**?**], plasma pressure may be evaluated at each cell boundary via treatment as some additional external force. Plasma pressure at each cell boundary may be determined for any position in the neutraliser from the plasma density distribution and electron temperature profile, as discussed in Appendix **??**, and thus reconstruction at cell boundaries is not necessary for plasma pressure

within the inviscid flux routines.

3.4.7 Domain Decomposition

The surpression of the stable timestep limit due to the very stiff viscous terms leads to long simulation run-times. To facilitate reduced run times parallel processing techniques have been applied; domain decomposition has been undertaken and the computational geometries split into several sub-grids. Though simplistic in that it outlines the transfer of only one layer of process boundary cells yet the transfer of three layers is necessary for solution of the Augmented Burnett equations, figure 3.14 straightforwardly visualises this decomposition. The solution of each sub-grid constitutes a process, and the processes are distributed over several computational processors in order to split the computational load. This splitting of computational load results in a reduction of the overall real-time required for completion of the simulation, with each processor effectively solving its own smaller problem. Partitioning in this fashion also facilitates the solution of computationally irregular geometries as shall be presented and discussed later in the thesis.

At various locations within each computational step, the processes pass information to one another to facilitate solution; for example, flow field details near the boundary of each sub-grid are required. The requirement for this particular information is analogous to the provision of flow field data from fictitious cells at the edge of the domain, which is required to properly characterise flow near boundaries of the domain. Within the developed code, this exchange of information is undertaken via the standard message-passing specification MPI [**?**]. As such, all data to be transferred is initially copied into buffer arrays and sent to the appropriate process which then receives and unscrambles the data, storing it as appropriate. This process is essentially the same for the transfer of both local boundary details and macroscopic comparison of quantities over the computational domain, which is required to establish items such as the applied global timestep.

3.5 Summary

In this chapter, the flow governing equations in the absence and presence of beam have been presented along with the numerical methods employed in this thesis to provide their solution. Facilitated by the development of a model of the neutraliser species and their interaction, the system in the presence of beam includes various sources and sinks due to the beam and the development of the neutraliser plasma. The various extensions necessary to accurately model rarefied gas flow, namely the evaluation of higher order viscous terms and slip boundary conditions, have also been outlined. Details of their implementation, the basics of parallel computing and the logic of the solver all point to the complexity of the code developed for this thesis.

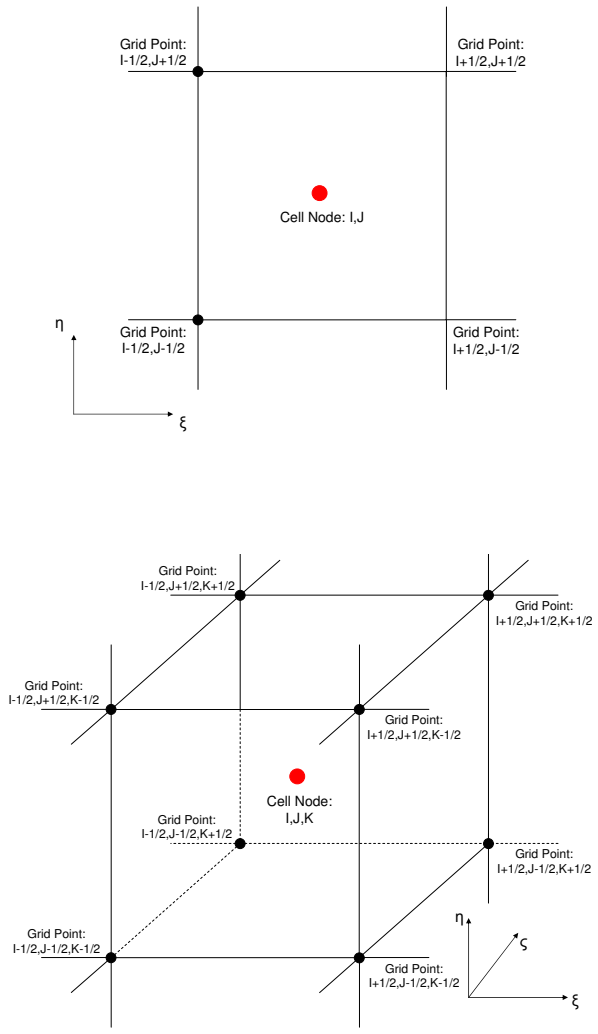

FIGURE 3.10: Exemplar finite volume method 2D and 3D computational cells

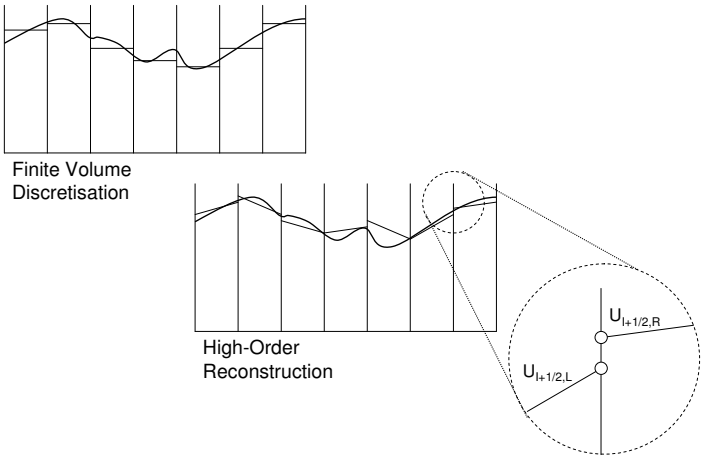

FIGURE 3.11: Visual outline of the discretisation and reconstruction process

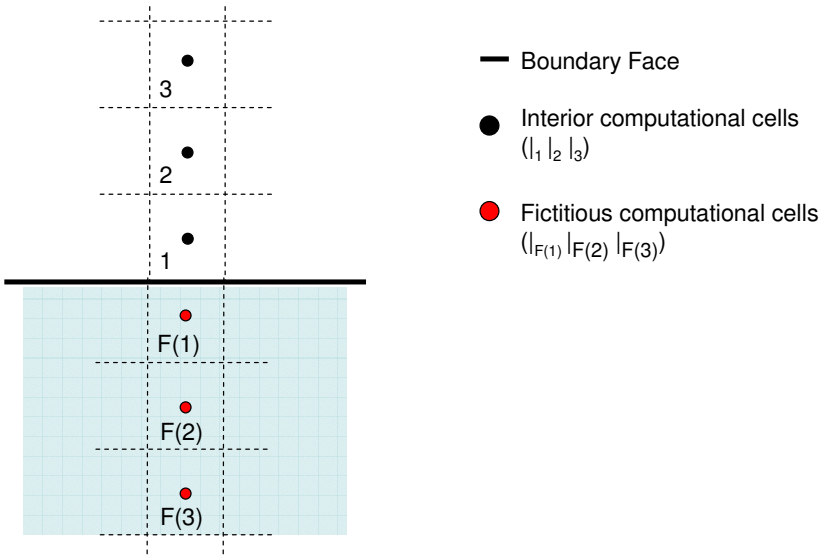

FIGURE 3.12: Visual summary of notation for demonstration of boundary conditions

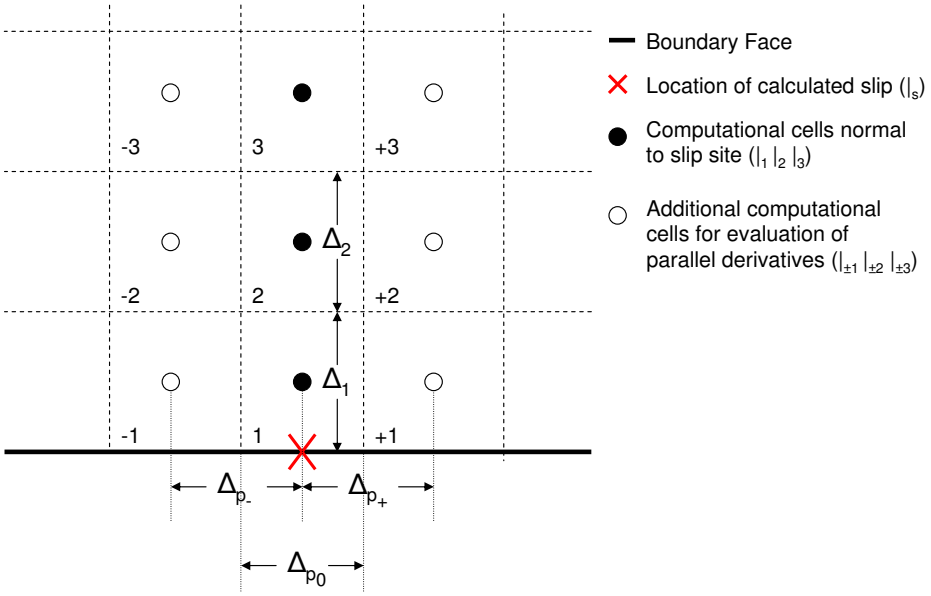

FIGURE 3.13: Visual summary of notation for demonstration of slip condition evaluation

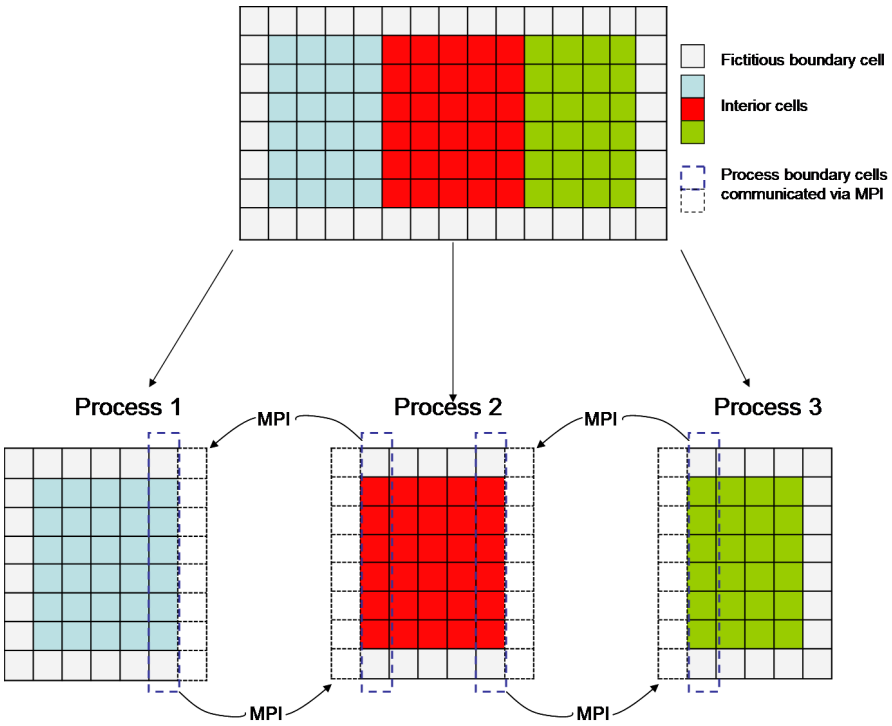

FIGURE 3.14: Exemplar partitioning of simulation amongst several MPI processes

4

Development of Continuum-Transition Solver

Given the number of extensions to the HiReCom framework required to allow application to the continuum-transition regime, it has been necessary to utilise a number of incremental validation cases. This incremental approach commenced with validation of fluxes for the Navier-Stokes, Burnett and Augmented Burnett models via application to a 1D hypersonic shock, a test case selected for its minimal boundary complexity. Consideration of a 2D hypersonic shock about a blunt body then confirmed the applicability of the system to non-simple grids. These hypersonic shock cases also allowed the effects of both variable reconstruction and the newly derived timestep criterion to be investigated in detail. Variable reconstruction has been examined for its impact upon the onset of instability in the Conventional Burnett equations due to increasing grid refinement. The newly derived timestep limit has been assessed for both the Navier-Stokes and Augmented Burnett equations, to ensure its advantage over traditional time-stepping approaches in bypassing the exhaustive search for a suitably low CFL when modelling rarefied flows.

Validation of the newly implemented slip boundary conditions follows, with the accuracy of each of the wall slip conditions ensured via comparison of microchannel simulations with analytical models and published works. Quantitative agreement of the Navier-Stokes simulations is demonstrated for both 2D and 3D microchannels against analytical models, whilst qualitative agreement with published works was also sought.

Following this development and validation, the solver has examined the JET neutraliser in the absence of beam. Two-dimensional simulations, representing the first application of the Navier-Stokes and Augmented Burnett equations to this system, are compared to an experimental pressure profile in the absence of beam in order to assess the suitability of the solver. Given the high

level of rarefaction near the neutraliser outlet, this work also offers means of understanding the behaviour of the equation systems at near molecular flow.

4.1 1D Hypersonic Shock

The strong thermodynamic nonequilibrium in a shock structure cannot be fully captured by the Navier Stokes equations, justifying the use of the higher order Burnett Equations. Though the evaulation of such a shock with the assumption of constant γ represents a simplistic flow case, it has been considered extensively elsewhere and therefore permits comparison with published works. It has been demonstrated by *Fiscko et al.*[**?**] that the Burnett Equations offer an enhanced description of the shock structure in much closer agreement to DSMC and experimental data. Such strong shock structures have also provided means for demonstrating the enhanced stability of the Augmented Burnett Equations following the breakdown of the Burnett Equations on refined grids[**? ?**]. Investigation of a 1D hypersonic shock structure also avoids any issues resulting from the selection of wall boundary conditions, a much debated issue in the application of the Burnett Equations[**?**].

Following an initial convergence study, validation of the utilised solver against published works is presented for both a Maxwellian and argon gas shock. These published works encompass the fluid simulation work of both *Fiscko et al.*[**?**] and *Zhong*[**?**], and comparison with the experimental work of *Alsmeyer*[**?**]. A Maxwellian shock also forms the basis of the computational investigation of the influence of variable reconstruction upon the onset of instability in the Conventional Burnett Equations, as well as an assessment of the validity of the derived timestep criteria (3.185) and (3.186) discussed in (3). The inverse shock thickness $\frac{\lambda_{in}}{t_p}$ is the means of comparison used both here and in the referenced works, and follows from the shock thickness density t_p as defined in (4.1).

$$t_p = \frac{\rho_{out} - \rho_{in}}{\left(\frac{\partial \rho}{\partial x}\right)_{max}} \tag{4.1}$$

4.1.1 Boundary Conditions and Flow Parameters

The initial flow conditions at the start of each simulation offered a discontinuity at the centre-point of the domain. All upstream cell values were set equal to the inlet conditions, whilst all downstream cell values were set equal to the outlet conditions. Inlet temperature T_{in} and pressure p_{in} were identical across all of the shocks considered, with inlet velocity u_{in} set according to the desired Mach number M for each shock. The outlet boundary conditions were specified using the Rankine-Hugoniot conditions (4.2)-(4.4)[**?**]. One should note that though the boundaries were thus over-specified, the conditions were deemed suitable in light of the successful validation against published works.

As highlighted earlier, a constant gas parameter γ has been implemented throughout each shock as given in Table 4.1, a simplifying assumption utilised throughout the published works

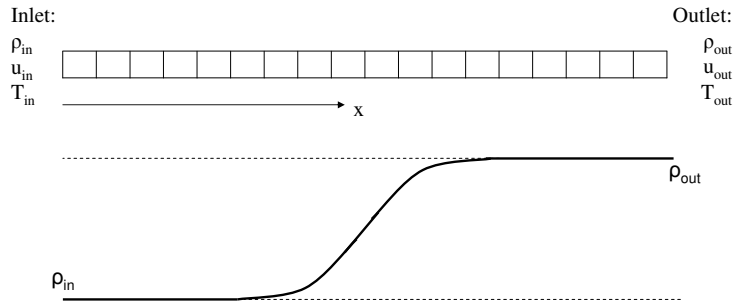

FIGURE 4.1: Schematic of 1D hypersonic shock test case

T_{in} (K)	p_{in} (atm)	γ	ω		Pr	μ_0 $(kg\,m^{-1}s^{-1})$	T_0 (K)
			ω_{Max}	ω_{Arg}			
300	1	$\frac{5}{3}$	1	0.7222	$\frac{2}{3}$	0.00002272	300

TABLE 4.1: Gas parameters utilised in 1D hypersonic shock simulation

for comparison. A viscosity interaction model of (3.10) was used with the component ω as in Table 4.1 from the assumption of a molecular interaction force applicable to either a Maxwellian or argon gas. In accordance with the published works for comparison, a monatomic gas with the molecular weight of argon was simulated in both cases.

For each simulated shock, steady state profiles are presented. Each profile was deemed converged upon reduction of the rate of change of shock thickness $\frac{dt_p}{dt}$ to less than 10^{-5} of that evaluated at the initial timestep.

$$\rho_{out} = \rho_{in}\frac{\gamma+1}{\gamma-1+2M^2} \tag{4.2}$$

$$T_{out} = T_{in}\frac{\left(2\gamma M^2-(\gamma-1)\right)\left(2+(\gamma-1)M^2\right)}{(\gamma+1)^2 M^2} \tag{4.3}$$

$$u_{out} = \frac{u_{in}}{(\gamma+1)\left((\gamma-1)+2M^2\right)} \tag{4.4}$$

4.1.2 Convergence Study & Comparison with Published Works

A simulation domain of $80\lambda_{in}^{Max}$ was utilised for each shock, where $\lambda_{in}^{Max} = 7.15\times10^{-8}m$ represents the inlet mean free path resultant from use of a Maxwellian viscosity interaction model.

Grid Resolution	Shock Thickness	
	Mach 2	Mach 20
100	0.224	0.0806
200	0.244	0.0815
400	0.244	0.0810
800	0.243	0.0811

TABLE 4.2: Convergence study for Navier-Stokes argon 1D shocks

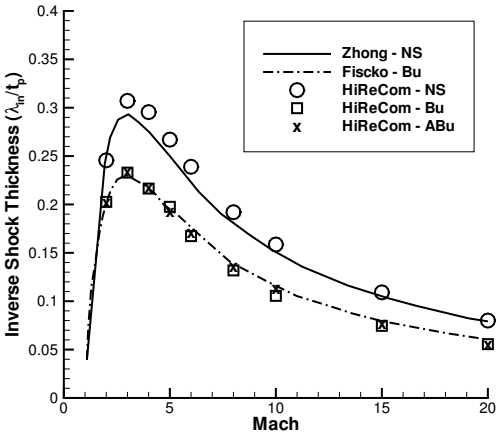

FIGURE 4.2: Results of Maxwellian 1D hypersonic shock study

Doubling of grid resolution from that used for each shock was found to offer only a small difference in the steady state shock thickness; as detailed in Table 4.2, shock thicknesses from application of the Navier Stokes equations to a Maxwellian shock of Mach 2 or Mach 20 both differ by $< 1\%$ if grid resolution is increased from 400 to 800 cells. Thus, all results of the Navier Stokes and Augmented Burnett equations presented in this thesis were produced using the 400 cell grid. By contrast, this grid is excessively fine to provide stable solutions of the Conventional Burnett Equations for the range of shocks considered. Instead, results are presented upon the most refined grid upon which spatial stability is encountered.

The resulting Maxwellian shock simulation results for the MUSCL variable reconstruction scheme with Minmod limiter over the range of Mach 2 - Mach 20 are presented in figure 4.2. All three equation sets show good agreement with published works. Use of the same grids and reconstruction scheme for argon gas also provides good agreement with relevant experimental data as shown in figure 4.3. Therefore these sets of results demonstrate the accuracy of the developed fluxes for each of the viscous systems considered.

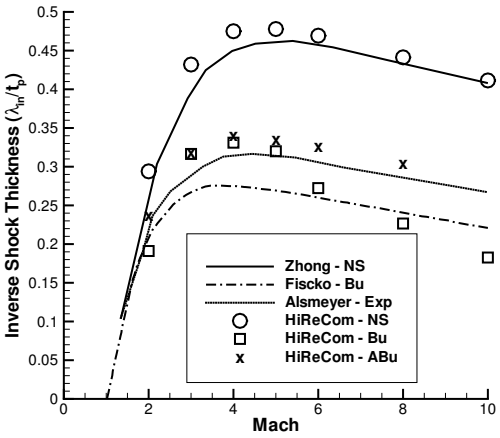

FIGURE 4.3: Results of argon 1D hypersonic shock study

4.1.3 Instability of the Conventional Burnett Equations

Comparison with Published Works In his PhD dissertation, *Zhong*[**?**] derived a theoretical estimate for the minimum grid spacing upon which stability should be observed for 1D hypersonic shocks evaluated via the Conventional Burnett Eqauations (4.5). Within the same work, computational investigation of this theoretical limit for a Mach 20 Maxwellian shock provided a computational stability limit permitting smaller grid spacing (4.6).

Investigated over a series of successively refined grids, with an initial shock structure provided by the converged Navier Stokes shock profile, the onset of instability observed within HiReCom for Conventional Burnett simulations is summarised in Table 4.3. This data suggests that the HiReCom implementation is capable of providing stability well beyond the theoretical limit of *Zhong*. Within the PhD dissertation, *Zhong* suggested that the introduction of numerical viscosity might explain the discrepancy between theory and computational experiment. The significant difference between that computational testing and the results from HiReCom further suggest that effects specific to each compuational approach result in vast differences in the observed grid spacing limit. As such, an investigation of the effect due solely to variable reconstruction was sought, to exemplify the variation observed for differing computational methods.

$$\left[\left(\frac{\Delta x}{\lambda}\right)^{Zhong}_{min}\right]^{M=20}_{Theory} = 1.02 \tag{4.5}$$

$$\left[\left(\frac{\Delta x}{\lambda}\right)^{Zhong}_{min}\right]^{M=20}_{Comp} = 0.8265 \tag{4.6}$$

Variable Reconstruction Investigation A one-dimensional Maxwellian Mach 20 shock was simulated by the Conventional Burnett Equations for a series of successively refined grids until the

Mach	Grid Cell Limit	$\left[\left(\frac{\Delta x}{\lambda}\right)_{min}^{HiReCom}\right]_{Comp}^{M=20}$
2	260	0.24
3	265	0.19
4	125	0.34
6	90	0.34
8	65	0.36
10	45	0.43
15	30	0.44
20	21	0.45

TABLE 4.3: Onset of instability for Conventional Burnett Equations due to increasing grid refinement

onset of instability was identified. The onset of instability was taken to indicate that the previous, slightly coarser grid represented the minimum grid spacing for application of the Conventional Burnett Equations. In all, three variable reconstruction schemes were considered: first order interpolation, MUSCL scheme with MinMod limiter and fifth-order WENO. Results revealed that variation of the variable reconstruction scheme significantly alters the onset of instability, with the grid spacing limit varying by as much as 25% over the schemes considered (Table 4.4).

Explanation of the discrepancies between the onset of instability for the differing schemes is necessary, and springs from knowledge that instability develops when the mean free path reaches some critical value, and that the Maxwellian shock posesses a mean free path proportional to $\frac{\sqrt{T}}{\rho}$ due to the viscosity model utilised. The developed shock posesses a temperature discontinuity at the shock interface, increasing from upstream to downstream. Whilst the density also increases from upstream to downstream, crucially it lags behind the temperature distribution, which serves to produce a peak in mean free path at approximately the centre of the shock with respect to temperature (see figure 4.4). One might conjecture for large shocks, that this peak is elevated for higher resolution reconstruction schemes as the temperature gradient is larger, and therefore increases the likelihood that an unstable mode develops as the mean free path exceeds some critical value. This would explain why it is the higher resolution WENO scheme that requires a larger grid spacing to provide a stable solution, and is further supported by the observation that first order interpolation provides the largest stable grid spacing of the observed methods.

This conjecture appears further substantiated if one examines in detail a Mach shock upon a grid of $N = 20$. Considering application of the Conventional Burnett Equations upon the converged Navier-Stokes profile provided by first order interpolation. Application of first order interpolation implies the grid is suitably coarse to allow a stable solution, however, application of the WENO fifth-order reconstruction scheme produces instability. Figure 4.5 shows the peak mean free path in the domain as the Conventional Burnettt Equation simulations progress and demonstrates that the higher-order WENO scheme does indeed provide a larger mean free path, peaking at approximately timestep 400 for $CFL = 0.1$, apparently enters an unstable mode and eventually terminates the run unsuccessfully after $\sim$ 800 timesteps. Overall one concludes that the selection of variable reconstruction has a substantial effect upon the onset of instabilty in the Conventional Burnett Equations.

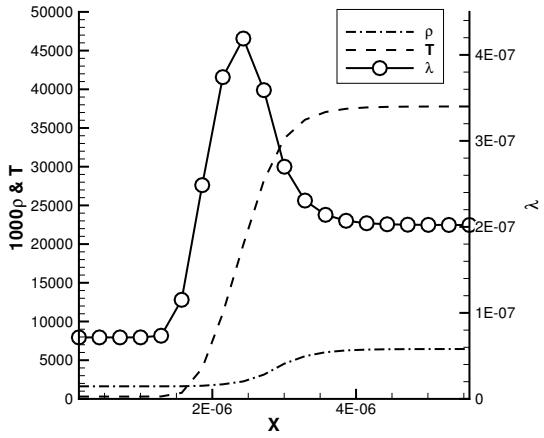

FIGURE 4.4: Navier-Stokes Mach 20 Maxwellian 1D shock profiles near shock interface

Mach	First Order Interpolation	MUSCL-1	WENO
N_{max}	22	21	18
$\left[\left(\frac{\Delta x}{\lambda}\right)_{min}\right]_{Comp}$	0.45	0.47	0.55

TABLE 4.4: Onset of instability in 1D shock for differing variable reconstruction schemes

4.1.4 Assessment of Novel Timestep Limits

The timestep limit criteria derived in (3.185) and (3.186) were compared against the observed computational timestep limit for the 1D hypersonic shock structure, a fully compressible flow with temperature gradient. To facilitate comparison, the timestep for the solver was specified in HiReCom via (**??**); the global timestep at each solution step was determined as the minimum timestep limit provided by application of (3.185) and/or (3.186) over each of the cells within the computational domain, subject to a multiplicative user-specified CFL factor. Note that, though consideration of all the applicable timestep limits undertaken at each solution step within HiReCom, the Navier Stokes simulations were restricted most heavily via the derived Navier-Stokes timestep limit (3.185) and the Augmented Burnett simulations by the derived Augmented Burnett timestep limit (3.186).

Factor CFL was varied over successive simulations to determine the maximal value at which a stable computational solution could be found. The value of CFL offered an indication of the suitability of the derived limits (3.186) and (3.185); the closer the value of CFL to unity the closer the agreement of the derived timestep criteria with the computationally observed limit.

Over the Mach range examined there was substantial variation of the CFL factor for which stability was observed, as demonstrated in Table 4.5. For both the Augmented Burnett Equations

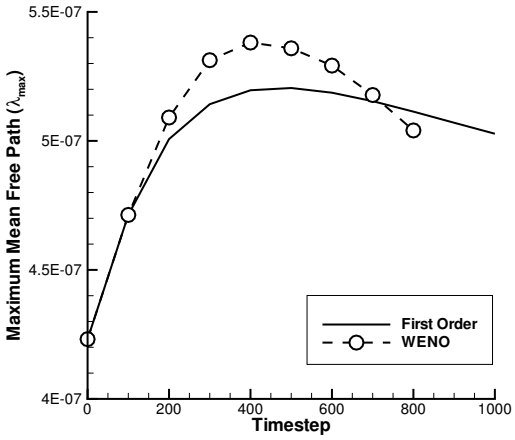

FIGURE 4.5: Maximum mean free path as a function of timestep for Conventional Burnett Mach 20 Maxwellian 1D shock

criterion derived in this study and the Navier Stokes Equations criterion, CFL remains very close to or above 0.1 for all of the simulated shock structures and thus the timestep criteria agree with the observed computational limits to within an order of magnitude. This is particularly suprising given the simplifying assumptions made in their derivation; unlike the assumptions of weak compressibility and the absence of temperature gradients, the initial shockwave profiles are subject to significant temperature and density gradients about the shock front. Given these simplifying assumptions, the derived timestep limits obviously do not capture all flow criteria that limit the stable timestep, with the restriction of the stable Augmented Burnett timestep judged to be much greater due to these additional factors than that for the Navier Stokes equations from the observed CFL presented in Table 4.5. However, the timestep limit does appear suitable and does imply significantly less endeavour is necessary to obtain a suitable CFL. One should note that no 'late onset' instability, i.e. instability developing after significant numbers of computational timesteps, was observed for any of the Augmented Burnett shocks examined, which is a vast improvement over initial testing with the traditional eigenvalue based approach; late onset instability blighted initial solver development as instability would develop well into the flow development.

One might even conjecture the form of the additional components to the timestep limit resulting from the density and temperature gradients. For example from figure 4.6, one can observe that the the observed CFL profile for the Augmented Burnett equations would appear to be described by the reciprocal of the gradient of either temperature or density, with the upturn in observed CFL at high Mach due to some additional component provided by the un-reciprocated gradient of the other variable.

The identification of un-reciprocated temperature or density gradient as a significant contributor to the restriction of the timestep limit is further corroborated via examination of the effect of variable reconstruction upon the observed CFL limit; first order interpolation, the MUSCL scheme and WENO reconstruction have all been investigated, as detailed in Table 4.5. It is the

Mach	2	3	4	5	6	8	10	15	20
First Order Interpolation									
CFL^{NS}	0.925	0.631	0.548	0.509	0.488	0.467	0.457	0.448	0.444
CFL^{ABu}	0.632	0.240	0.109	0.095	0.097	0.106	0.116	0.141	0.161
MUSCL Scheme - Minmod Limiter									
CFL^{NS}	0.931	0.629	0.554	0.514	0.494	0.473	0.464	0.454	0.451
CFL^{ABu}	0.632	0.245	0.115	0.101	0.104	0.112	0.123	0.147	0.166
WENO									
CFL^{NS}	0.965	0.665	0.609	0.587	0.576	0.561	0.553	0.544	0.541
CFL^{ABu}	0.659	0.284	0.138	0.123	0.126	0.138	0.151	0.181	0.204

TABLE 4.5: Comparison of the computational stability limits for 1D shock subject to differing variable reconstruction schemes

WENO scheme that permits the largest stable timesteps, followed by the MUSCL scheme, with the smallest stable timesteps provided by first order interpolation; from this data one deduces that increasing the order of variable reconstruction provides an increasing CFL limit. Since increasing the order of variable reconstruction increases the calculated temperature and density gradient at the shock interface, and that the presented data suggests that the permissible timestep also increases, this appears to support the conclusion that density or temperature gradient form a significant contibutor to the timestep limit.

4.2 2D Hypersonic Flow about Blunt Body

Hypersonic flow about a 2D blunt body offers further demonstration of the enhanced capability of the Burnett Equations to simulate transitional flows; comparison with DSMC elsewhere confirms that the thicker bow-shock predicted by the Augmented Burnett Equations offers better agreement than the narrower shock predicted by the Navier Stokes equations[**?** **?**]. The highly non-uniform grid required to simulate the development of such a bow-shock profile offers a means of validating the implemented metrics and curvilinear transformations, as well as further validation of the implemented fluxes. This also offers an interesting case upon which to extend the application of the derived timestep limits to 2D and further assess their suitability.

Following an initial convergence study, validation of the implemented solver against published works is presented for hypersonic flow about a 2D blunt body for both the Navier Stokes and Augmented Burnett Equations; a Mach 10 shock wave was examined and simulated until a steady-state profile was reached. The means of comparison with published results are the density, temperature and velocity profiles provided along the stagnation streamline, i.e. the symmetry boundary of the computational domain. Following validation, computational timestep limits were assessed for shockwaves over the range Mach 2- Mach 20 and compared with the derived limits.

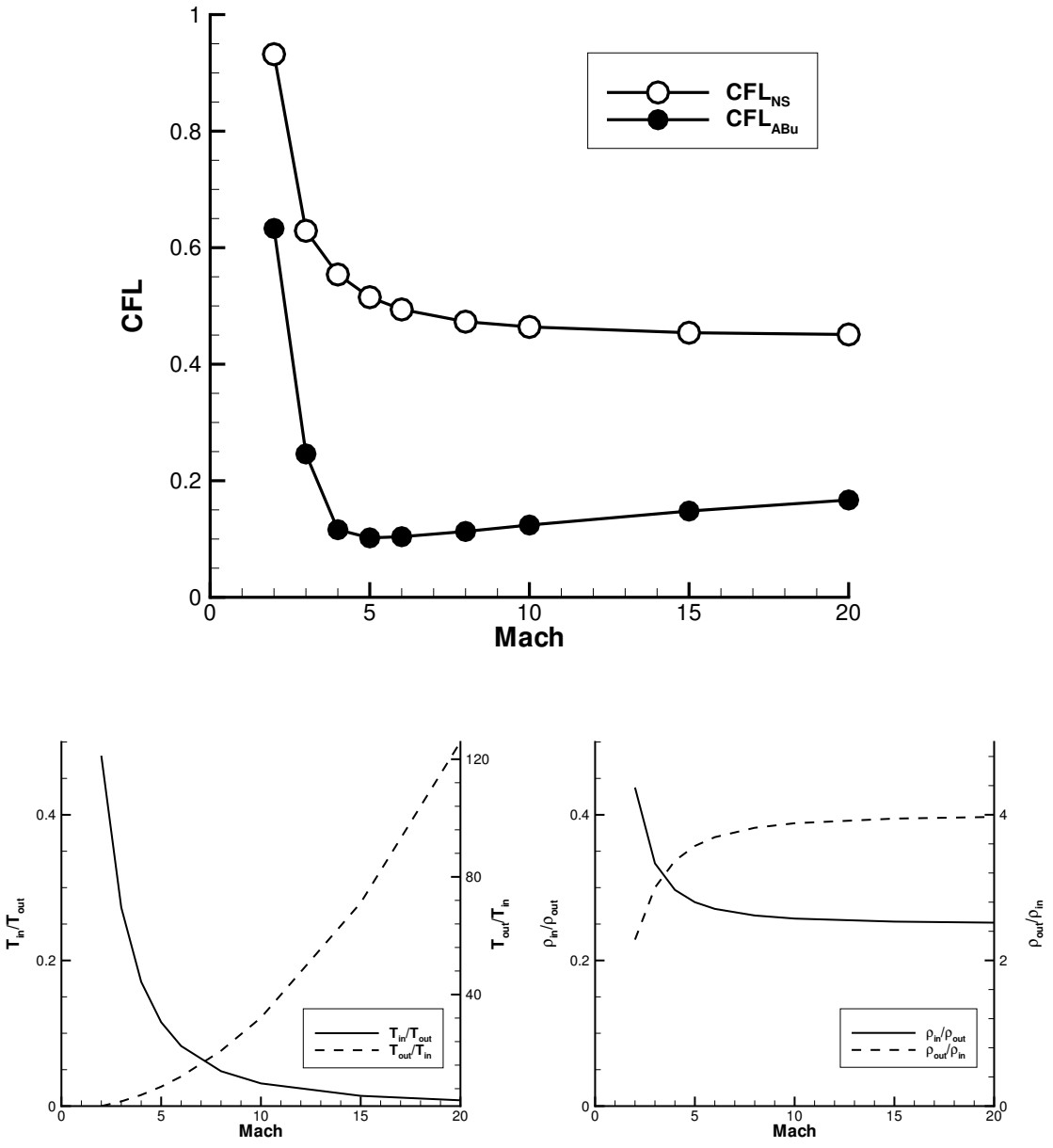

FIGURE 4.6: Observed limits for 1D shock and conjectured additional *CFL* factors

r (m)	M_∞	Kn_∞	Re_∞	p_∞ (Pa)	T_∞ (K)
$0.02m$	$2-20$	0.102	167.9	2.3881	208.399

TABLE 4.6: Freestream boundary conditions utilised in 2D bow shock simulation

T_w (K)	T_s (K)	T_0 (K)	μ_0 $(kg\,m^{-1}s^{-1})$
1100	110.33	288.0	1.7894×10^{-5}

TABLE 4.7: Gas parameters utilised in 2D bow shock simulation

4.2.1 Boundary Conditions and Flow Parameters

In accordance with the published works for comparison, the freestream conditions, wall temperature and blunt body radius given in Table 4.6 were utilised. Free-stream flow conditions were specified at the boundary opposite the blunt body with the cell variables throughout the domain also initially set to these values at the commencement of a simulation. For the purposes of comparison with the work of *Zhong*, the Maxwellian-Schmolukowski slip boundary conditions with creep were adopted at the blunt-body wall. For the purpose of reducing computational effort, only the upper half of the flow system was simulated with a symmetric boundary condition implemented along the stagnation streamline. Note that first order extrapolation of all flow variables was implemented at the outflow boundary.

The gas viscosity was provided by Sutherland's Law, as provided in (3.9). Constants were set to allow the simulation of air, as used in the published works for comparison (see Table 4.7).

As for the previous test cases, steady state progiles were found and are presented here. For 2D hypersonic shock about a blunt body, the flow was deemed converged when the peak rate of change of temperature along the stagnation streamline was reduced to less than 10^{-5} of that at the initial timestep.

4.2.2 Convergence Study & Comparison with Published Works

Three grids were created from a purpose-built grid generator, discussed and detailed in Appendix **??**. Grid 1 (120×80) approximately corresponded to that utilised by *Zhong*[**?** **?**] and has been used to provide the results presented in this thesis. Examining the peak temperature observed along the stagnation streamline, one notes that halving the grid resolution to Grid 0 (60×40) produces a difference of $\tilde{1}$% for both the Navier-Stokes and Augmented Burnett equation solutions when compared to that obtained with grid 1. By contrast, doubling the grid resolution to Grid 2 (240×160) provides differences $\ll 1$%, see figure 4.7. This suggests that the results upon Grid 1 are suitably converged.

As can be seen from figure 4.8, HiReCom compares very favourably with the published results of *Zhong*[**?**] for both the Navier Stokes and Augmented Burnett equations. As expected, the Augmented Burnett Equations provide a much thicker shock than that produced by the Navier Stokes Equations. This is most notable in the temperature and velocity profiles where the region

of transition from the free stream conditions to the cylinder body is much greater than that of the Navier Stokes equations.

4.2.3 Assessment of Novel Timestep Limits

The timestep limit criteria derived in (3.185) and (3.186) were compared against the observed computational timestep limit for 2D hypersonic flow about a blunt body to extend the work of Section 4.1.4 into an additional dimension. To facilitate comparison, the timestep for the solver was specified in HiReCom via (**??**); note the similar form to the implementation in 1D (**??**) but that the distance calculation is modified to account for an additional dimension, effectively taking the minimum length of the four sides of each cell to calculate its stable timestep limit, before once again taking the minimum evaluated timestep over every cell in the computational domain as the implemented global timestep. As in Section 4.1.4, the Navier Stokes simulations were restricted most heavily via the dervied Navier-Stokes timestep limit (3.185) and the Augmented Burnett simulations by the derived Augmented Burnett timestep limit (3.186).

As before, the factor CFL was varied over successive simulations to determine the maximal value at which a stable computational solution could be found with the proximity of CFL to unity demonstrating the validity of the agreement between the derived timestep limit criteria with the computationally observed limit.

The maximal values providing stability for Mach 2 - Mach 20 freestream conditions are presented in Table 4.8. For much of this range, the stable computational timestep limit observed agrees to within an order of magnitude with the derived timestep limit, i.e. $CFL \geq 0.1$. However, for the Augmented Burnett Equations at high Mach flows, the computational timestep limit shows poorer agreement than that observed in 1D. The disagreement in the shape of the CFL profiles for the 1D and 2D against increasing Mach number (exemplified in figure 4.10 for the Augmented Burnett equations subject to MUSCL variable reconstruction) may be explained by the differing magnitudes and locations of the initial temperature and density gradients encountered in the two flow cases; the 1D shock case results in peak temperature and density gradients near the shock interface, determined by input Mach and the Rankine-Hugoniot equations, whereas the 2D flow about a blunt body experiences an initial temperature gradient at the wall determined by the freestream and the wall temperatures, with a density gradient developing at the wall over time from an initial zero gradient. Thus the differing CFL profiles against Mach for the 1D and 2D cases follow from the conjecture that some combination of temperature and density gradient influence CFL profile given their absence from the derivation of the timestep stability limits.

With regards to the influence of the variable reconstruction scheme, the WENO scheme once again offers the largest stable computational timestep. However, in the 2D case there is minimal difference between the stable computational timesteps observed for first order interpolation and MUSCL reconstruction schemes. This could be due to the MUSCL reconstruction scheme reducing to first order interpolation in the region near the wall, where the instabilities are found to develop for this flow case.

Overall, the results of this 2D investigation provides good agreement with the tests upon the

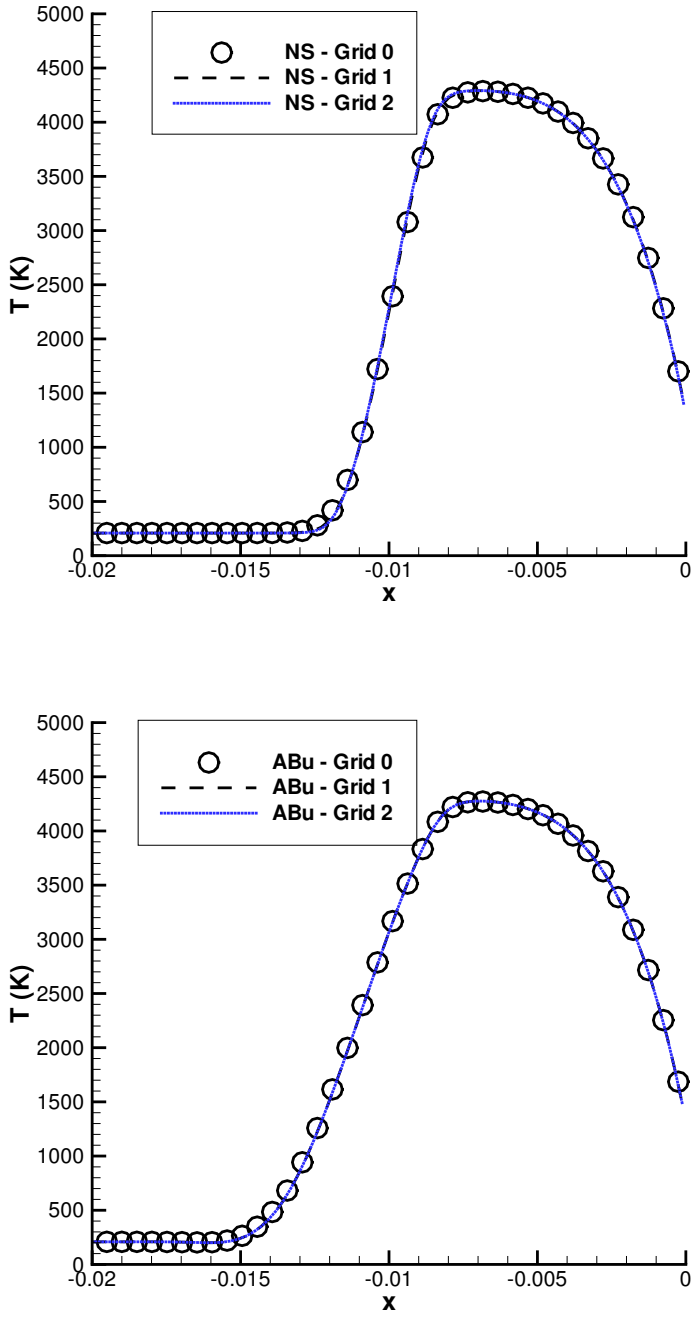

FIGURE 4.7: 2D bow shock grid convergence study - temperature along the stagnation streamline

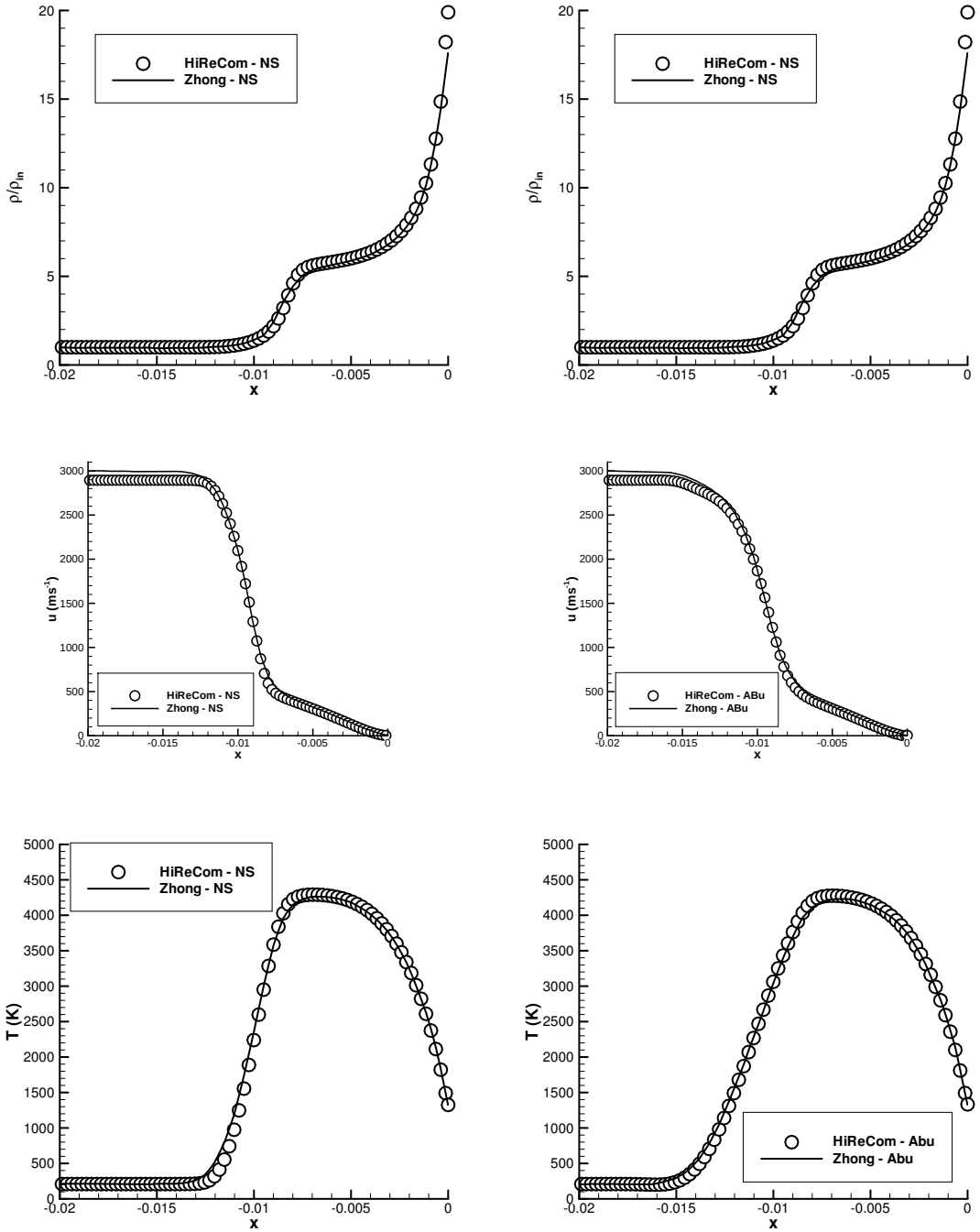

FIGURE 4.8: Comparison of 2D bow shock results with published data along the stagnation streamline

Mach	2	3	4	5	6	8	10	15	20
First Order Interpolation									
CFL^{NS}	0.813	0.664	0.486	0.382	0.312	0.226	0.178	0.116	0.086
CFL^{ABu}	0.447	0.247	0.160	0.117	0.091	0.063	0.049	0.031	0.023
MUSCL Scheme - Minmod Limiter									
CFL^{NS}	0.812	0.666	0.486	0.382	0.312	0.226	0.178	0.116	0.086
CFL^{ABu}	0.447	0.247	0.160	0.117	0.091	0.063	0.049	0.031	0.023
WENO									
CFL^{NS}	0.812	0.666	0.486	0.382	0.312	0.226	0.178	0.116	0.086
CFL^{ABu}	0.521	0.299	0.188	0.133	0.102	0.070	0.053	0.034	0.023

TABLE 4.8: Comparison of the computational stability limits for differing variable reconstruction schemes

1D shock structure, implying that the derived stability criteria are equally valid when applied to two dimensions. This is particularly suprising given the simplifying assumptions and consideration of only a single dimension in their derivation.

4.3 2D Microchannel

As discussed in Chapter 1, the implementation of suitable wall boundary conditions in an important issue in the modelling of rarefied gases. In particular, the no slip conditions fail to capture the effect of the Knudsen sublayer which develops between the wall and the bulk fluid for $Kn > 0.01$. Therefore the application of flow slip velocity at wall boundaries becomes a necessity when modelling flows in the transition regime. Analogous to slip velocity, is the implementation of a temperature jump at the wall which is determined via an energy balance at the wall.

To ensure the accurate implementation of such wall boundary conditions within HiReCom, a two dimensional microchannel geometry is examined for Poiseuille pressure driven flows and compared against published analytical models for the continuum-transition regime. In all, results are obtained from the no-slip, Maxwell first order and Deissler second order models. The Maxwell slip model is the most widely studied published model, whilst the Deissler slip model results from semi-analytical analysis utilising Navier-Stokes constitutive relations in the vicinity of the wall. Both models provide self-consistent velocity slip and temperature jump conditions.

Results obtained within the HiReCom framework with the Navier-Stokes equations demonstrate good agreement with analytical models. In addition, qualitative differences observed between results for the Navier-Stokes equations and the Burnett equations are demonstrated to agree with those found in published literature.

4.3.1 Boundary Conditions and Flow Parameters.

The pressure driven flow of nitrogen through a long microchannel was examined, with geometry and gas parameters as summarised in Table 4.9. Given $h \gg w$, the depth may be effectively ignored and the microchannel treated as a two dimensional domain.

Inlet pressure p_{in} and outlet pressure p_{out} were specified via (4.7)-(4.8) to correspond to Knudsen values (Kn_{in}, Kn_{out}) as in (4.9). Inlet temperature T_{in} was fixed as in (4.10), with zero transverse velocity v_{in} was also assumed as given in (4.11). Other flow variables at the inlet and outlet were obtained via extrapolation from the internal flow variables. Gas viscosity was simulated via Suthlerland's Law of viscosity (3.9) with parameters as detailed in Table 4.9. For the purposes of confirming that the solver and boundary condition implementation were free from any erroneous assymetrical effects, the entire width of the channel was examined with two wall boundary and no centreline symmetry thus applied.

$$p_{in} = \frac{16}{5\sqrt{2\pi}} \frac{\mu\left(T_{in}\right)\sqrt{RT_{in}}}{Kn_{in}h} \tag{4.7}$$

$$p_{out} = \frac{16}{5\sqrt{2\pi}} \frac{\mu\left(T_{out}\right)\sqrt{RT_{out}}}{Kn_{out}h} \tag{4.8}$$

$$(Kn_{in}, Kn_{out}) = (0.05, 0.1) \tag{4.9}$$

$$T_{in} = 300K \tag{4.10}$$

$$v_{in} = 0 \tag{4.11}$$

Results have been obtained for three differing wall boundary conditions each outlined in Chapter 3 and Appendix **??**. The most simplistic of these conditions are the no-slip conditions, which assume stationary flow in thermal equilibrium with the wall. The second model considered is the most widely studied of the slip models and results from the pioneering work of *Maxwell*[**?**], who demonstrated that fluids experience slip at wall surfaces, via consideration of a momentum balance for gas in contact with a solid body. The final model considered is a consistent second order slip velocity and temperature jump model provided by the work of *Deissler*[**?**] resulting in (2.7)-(2.8). Derived via the assumption of Navier Stokes constitutive relations at the wall boundary, this model has been shown to offer good agreement with experiment well into the continuum-transition regime[**? ?**]. For both the Maxwell and Deissler velocity conditions, the final term represents an additional term to allow for thermal creep; also known as the transpiration effect, thermal creep results in gas flow from colder to hotter regions which provides an additonal contribution to slip velocity. As discussed in Chapter 3 the slip velocity and temperature are evaluated for each cell of the wall boundary planes and values of the fictitious cells beyond those planes found via extrapolation of the internal flow variables utilising these established slip values at the boundary. For all of the simulations presented in this subsection, perfect momentum accommodation σ and thermal accomodation α was assumed with a fixed wall temperature T_w as given in Table 4.9.

In each case steady state profiles were sought, and determined to have occurred upon the rate of change of density at the microchannel outlet reducing to less than 10^{-5} of that at the

l (μm)	w (μm)	d (m)	T_0 (K)	T_1 (K)	μ_0 ($kg\,m^{-1}s^{-1}$)	σ	α	T_w (K)	R ($J\,kg^{-1}K^{-1}$)	γ
20	1	1	107	297	1.66×10^{-5}	1	1	300	297	1.4

TABLE 4.9: 2D microchannel geometry and gas parameters

initial simulation step. The resultant converged steady state profiles are presented in this section. Note that, as for the two-dimensional mircochannel test case, the MUSCL variable reconstruction scheme with MinMod limiter was utilised throughout this work.

4.3.2 Analytical Models

To ensure the accuracy of the slip model implementations in HiReCom, comparison has been underaken with a published analytical model of pressure driven microchannel flow. This model assumes application of the Navier-Stokes equations and that the developed flow is isothermal. Though not ideal for validation of the results in HiReCom, the assumption of isothermal flow is not unreasonable for long microchannels subject to low Mach flows.

The model considered is that of *Beskok*[**?** **?**]. Similar to the work of *Arkilic et al.*[**?**], this model allows the establishment of pressure p, which in turn provides volumetric flow rate $\dot{Q}$ and longitudinal velocity u throughout the microchannel for any velocity slip condition of the general form (4.12) with typical parameters C_1 and C_2 given in (4.13).

$$u_s = C_1 \lambda \frac{2-\sigma}{\sigma} \left(\frac{\partial u}{\partial n}\right)_s - C_2 \frac{\lambda^2}{2} \left(\frac{\partial^2 u}{\partial n^2}\right)_s \tag{4.12}$$

$$(C_1, C_2) = \begin{cases} (0,0) & \text{No-Slip} \\ (1,0) & \text{Maxwell-Shmoluckowski first order Slip} \\ (1, \frac{9}{8}) & \text{Deissler second order Slip} \end{cases} \tag{4.13}$$

The HiReCom Navier-Stokes solutions for the no-slip, Maxwell-Schmoluckowski first order and Deissler second order have all been compared against the following formulae to determine the accuracy of the implemented slip boundary conditions, wherein x denotes the longitudinal distance along the channel measured from the inlet and y denotes the transverse distance to the channel centreline.

Pressure The longitudinal pressure profile is found from equation (4.14); note that the transverse pressure profile is considered uniform at a given longitudinal point in the channel. For the first order velocity slip conditions such as the Maxwell boundary condition, this explicitly provides pressure via (4.15). However, for second order conditions, (4.14) presents an implicit relation.

	$\dot{Q}_{mid}$ $(m^3.s^{-1})$
200×11	3.672×10^{-5}
400×21	3.697×10^{-5}

TABLE 4.10: Grid convergence study results for the 2D microchannel test case

$$\begin{cases} \left(\frac{p(x)}{p_{out}}\right)^2 + 12\frac{2-\sigma}{\sigma}C_1 Kn_{out}\left(\frac{p(x)}{p_{out}} - 1\right) - \\ \qquad 12\frac{2-\sigma}{\sigma}C_2 Kn_{out}^2 ln\left(\frac{p(x)}{p_{out}}\right) + B\,(l-x) - 1 = 0 \\ B = \frac{1}{l}\left(1 - \left(\frac{p_{in}}{p_{out}}\right)^2 + 12\frac{2-\sigma}{\sigma}C_1 Kn_{out}\left(1 - \frac{p_{in}}{p_{out}}\right)\right. \\ \qquad \left. +12\frac{2-\sigma}{\sigma}C_2 Kn_{out}^2 ln\left(\frac{p_{in}}{p_{out}}\right)\right) \end{cases} \tag{4.14}$$

$$\begin{aligned} p\,(x) \quad = \quad & -6\frac{2-\sigma}{\sigma}C_1 Kn_{out} + \left[\left(6\frac{2-\sigma}{\sigma}C_1 Kn_{out}\right)^2 + \left(1 + 12\frac{2-\sigma}{\sigma}C_1 Kn_{out}\right)\frac{x}{l} + \right. \\ & \left. \left(\frac{p_{in}}{p_{out}} + 12\frac{2-\sigma}{\sigma}C_1 Kn_{out}\frac{p_{in}}{p_{out}}\right)\left(1 - \frac{x}{l}\right)\right]^{\frac{1}{2}} \end{aligned} \tag{4.15}$$

Volumetric Flow Assuming the depth of the channel $w = 1$, the local volumetric flow at any longitudinal point along the neutraliser follows from the pressure distribution via equation (4.16).

$$\dot{Q}\,(x) = -\frac{w^3}{2\mu}\frac{dp}{dx}\left(\frac{1}{6} + C_1 Kn + 2C_2 Kn^2\right) \tag{4.16}$$

Longitudinal Velocity From the momentum equation, the analytical solution of the longitudinal velocity distribution across a transverse section of the channel is offered by (4.17).

$$u\,(x,y) = -\frac{w^3}{2\mu}\frac{dp}{dx}\left(-\left(\frac{y}{w}\right)^2 + \left(\frac{y}{w}\right) + C_1 Kn + 2C_2 Kn^2\right) \tag{4.17}$$

4.3.3 Results

Approximately doubling the grid resolution from 200×11 to 400×21 provides a minimal difference in the presented flows for the Navier-Stokes HiReCom. This is exemplified via comparison of the volumetric flow at the channel midpoint as in Table 4.10, which differs by less than 1% for the two grids upon application of the Deissler boundary conditions. Thus the remainder of the simulations in this section are undertaken upon the coarser 200×11 grid.

The pressure profiles provided by HiReCom for Navier-Stokes simulations agree well with the analytical models (4.14)-(4.15). This agreement is easily summarised via consideration of the Root Mean Square (RMS) error of the profiles to the analytical models as in Table 4.11. The obtained profile shape is exemplified in figure 4.11.

	$\dot{Q}_{mid}$ $(m^3.s^{-1})$		RMS Error (p)
	HiReCom	Beskok	Error to (4.14)-(4.15)
No Slip	1.523×10^{-5}	1.512×10^{-5}	0.030%
Maxwell Slip	2.138×10^{-5}	2.146×10^{-5}	0.073%
Deissler Slip	2.376×10^{-5}	2.312×10^{-5}	0.748%

TABLE 4.11: Comparison of Navier-Stokes 2D microchannel simulations with an analytical model

As for pressure, the volumetric flow rates obtained from all three slip models in HiReCom correspond well to the analytical model of Beskok. Examination of the outlet volumetric flow rates demonstrates this, and is presented in Table 4.11. Note also, the enhanced volumetric flow for the second order Deissler conditions, an effect noted by *Colin et al.*[**?**] and obviously due to the selection of slip coefficients C_1 and C_2 of generalised form (4.12). The larger error between HiReCom and the analytical model in the case of the Deissler slip is due in part to the increased temperature jump experienced at the wall for this slip model, as will be detailed later in this section; this effect highlights the increased inadequacy of the isothermal flow assumption. The relative volumetric flows from the three slip models are visually demonstrated via consideration of the centreline velocities for each, as given in figure 4.12.

The velocity distribution also shows good agreement with the analytical models. Typified by sections taken at the channel outlet and presented in figure 4.13, the largest error in the longitudinal velocity is observed at the wall of the channel but in each case is less than 5%. This error may result from the analytical model's assumption of isothermal flow, which is not the case in the HiReCom simulations as demonstrated by examination of the centreline temperature profiles in figure 4.12.

The significant differences in the finalised flow are obvious from the figures presented thus far, and further underline the importance of slip model selection when evaluating rarefied flow; it is the interplay of the slip model and the interior flow that determines the converged profiles. The slip velocity and temperature from HiReCom are presented for the Navier-Stokes simulations of the microchannel in figure 4.14.

As observed in HiReCom and given in figure 4.15, *Xu*[**?**] found that the Burnett equations demonstrate a pressure minimum at the centre of the channel, whilst the Navier Stokes equations identify a flat pressure profile across the channel. *Xu*[**?**] compared these effects to DSMC results, which confirmed that the Burnett equations capture the correct effect. Thus one can conclude that, in addition to the quantitative microchannel validation fo the Navier-Stokes simulations offered by the analytical model of *Beskok*, the work of *Xu*[**?**] provides qualitative microchannel validation for the Burnett and Augmented Burnett equations in HiReCom.

4.4 3D Microchannel

To ensure the accurate implementation of the slip wall conditions in three dimensions, a three dimensional microchannel geometry subject for Poiseuille pressure driven flows has also been

l (μm)	w (μm)	h (μm)	T_0 (K)	T_1 (K)	μ_0 $\left(kg\,m^{-1}s^{-1}\right)$	σ	α	T_w (K)	R $\left(J\,kg^{-1}K^{-1}\right)$	γ
20	1	$w \times AR$	107	297	1.66×10^{-5}	1	1	300	297	1.4

TABLE 4.12: 3D microchannel geometry and gas parameters

evaluated. As for the two-dimensional case, comparison is made with published analytical models applicable to each of the implemented slip models. Once again, results obtained within the HiReCom framework with the Navier-Stokes equations demonstrate good agreement with analytical models.

4.4.1 Boundary Conditions and Flow Parameters.

As for section 4.3 the pressure driven flow of nitrogen through a long microchannel was examined. With geometry and gas parameters as summarised in Table 4.12, a three-dimensional domain was considered since $h \sim w$. Note that several channels of differing aspect ratio $AR = \frac{h}{w}$ have been considered.

Inlet and outlet boundary conditions were specified as discussed in section 4.3. However, given the demonstration of adequate solution symmetry in the results for the two-dimensional domain, centreline symmetry conditions have been implemented in both the transerse dimensions of the three-dimensional channel in order to minimise the required computational effort.

All three of the implemented slip models - the no-slip, Maxwell and Deissler conditions - have been evaluated for the three-dimensional microchannel with the assumption of perfect accommodation with a fixed wall temperature T_w as given in Table 4.12. As per the work of section 4.3, steady state profiles were sought for each simulation and was determined to have occurred upon the rate of change of density at the microchannel outlet reducing to less than 10^{-5} of that at the initial simulation step. The resultant converged steady state profiles are presented in this section.

4.4.2 Analytical Models

Extensions of the published analytical models discussed in 4.3, facilitate the description of pressure driven microchannel flow in three dimensions. These models once again assume the application of the Navier-Stokes equations and that the developed flow is isothermal.

The three-dimensional model of microchannel flow is an extension of the analytical model presented in **4.3**. The pressure can be evaluated by the work of *Jang and Wereley*[**?**], from which one obtains pressure normalised to the outlet pressure p_{out} as in (4.18), with parameters $CP1$ and $CP2$ defined by (4.19) and thus dependent upon the channel dimensions. Whilst this pressure model is only applicable to the first order Maxwell slip model, the works of *Beskok and Karniadakis*[**? ?**] may be applied to any slip model and facilitate the evaluation of volumetric flow rate $\dot{Q}$ via (4.20). Their model allows for any channel aspect ratio, and any slip model of the form (4.12); the former enters via corrective coefficient $C\left(AR\right)$ from (4.21) and the latter via model coefficients C_1 and C_2 as defined in (4.13) of 4.3. The HiReCom Navier-Stokes solutions for the no-slip, Maxwell-Schmoluckowski first order and Deissler second order have all been compared

	$\dot{Q}_{mid}$ $(m^3.s^{-1})$
$200 \times 6 \times 6$	1.144×10^{-11}
$400 \times 11 \times 11$	1.112×10^{-11}

TABLE 4.13: Grid convergence study results for the 3D microchannel test case

against these formulae to determine the accuracy of the implemented slip boundary conditions in three dimesnions.

$$p(x) = -Kn_{out}\left(\frac{CP2}{CP1}\right) + \left[\left(Kn_{out}\left(\frac{CP2}{CP1}\right)\right)^2 + 1 + 2Kn_{out}\left(\frac{CP2}{CP1}\right) + \left(1 - \frac{x}{l}\right) \times \left(\left(\frac{p_{in}}{p_{out}}\right)^2 - 1 + 2Kn_{out}\left(\frac{CP2}{CP1}\right)\left(\frac{p_{in}}{p_{out}} - 1\right)\right)\right]^{\frac{1}{2}} \tag{4.18}$$

$$\begin{aligned} CP1 &= -\frac{4}{3}\left(1 - \frac{192}{\pi^5}\left(\frac{w}{h}\right)\sum_{n=1,3,5,\ldots}^{\infty}\frac{1}{n^5}tanh\left(\frac{n\pi}{2}\frac{h}{w}\right)\right) \\ CP2 &= -\frac{32}{3}\left(1 - \frac{192}{\pi^5}\left(\frac{w}{h}\right)\sum_{n=1,3,5,\ldots}^{\infty}\frac{1}{n^5}tanh\left(\frac{n\pi}{2}\frac{h}{w}\right)\right) + \frac{256}{\pi^4}\left(1 - \frac{h}{w}\right)\sum_{n=1,3,5,\ldots}^{\infty}\frac{1}{n^4}tanh\left(\frac{n\pi}{2}\frac{h}{w}\right) \end{aligned} \tag{4.19}$$

$$\dot{Q}(x) = -C(AR)\frac{hw^3}{2\mu}\frac{dp}{dx}\left(\frac{1}{6} + C_1Kn + 2C_2Kn^2\right) \tag{4.20}$$

$$\begin{aligned} C(1) &= 0.4217 \\ C(2) &= 0.6860 \\ C(4) &= 0.8424 \end{aligned} \tag{4.21}$$

4.4.3 Results

Approximately doubling the grid resolution from $200 \times 11 \times 11$ to $400 \times 21 \times 21$ provides a minimal difference in the presented flows for the Navier-Stokes HiReCom results found for $AR = 1$. This is exemplified via comparison of the volumetric flow at the channel midpoint as in Table 4.13, which differs by less than 3% for the two grids upon application of the Deissler boundary conditions. Thus the remainder of the simulations in this section are undertaken upon the coarser $200 \times 11 \times 11$ grid.

The centreline pressure profiles provided by HiReCom for Navier-Stokes simulations agree well with the analytical model (4.18), which assumes the transverse pressure profile to be uniform and thus that the pressure field only varies in the longitudinal dimension. This agreement is easily summarised via consideration of the RMS error of the profiles to the analytical models as in Table 4.14.

The variation of the results from HiReCom in accordance with both aspect ratio and slip model

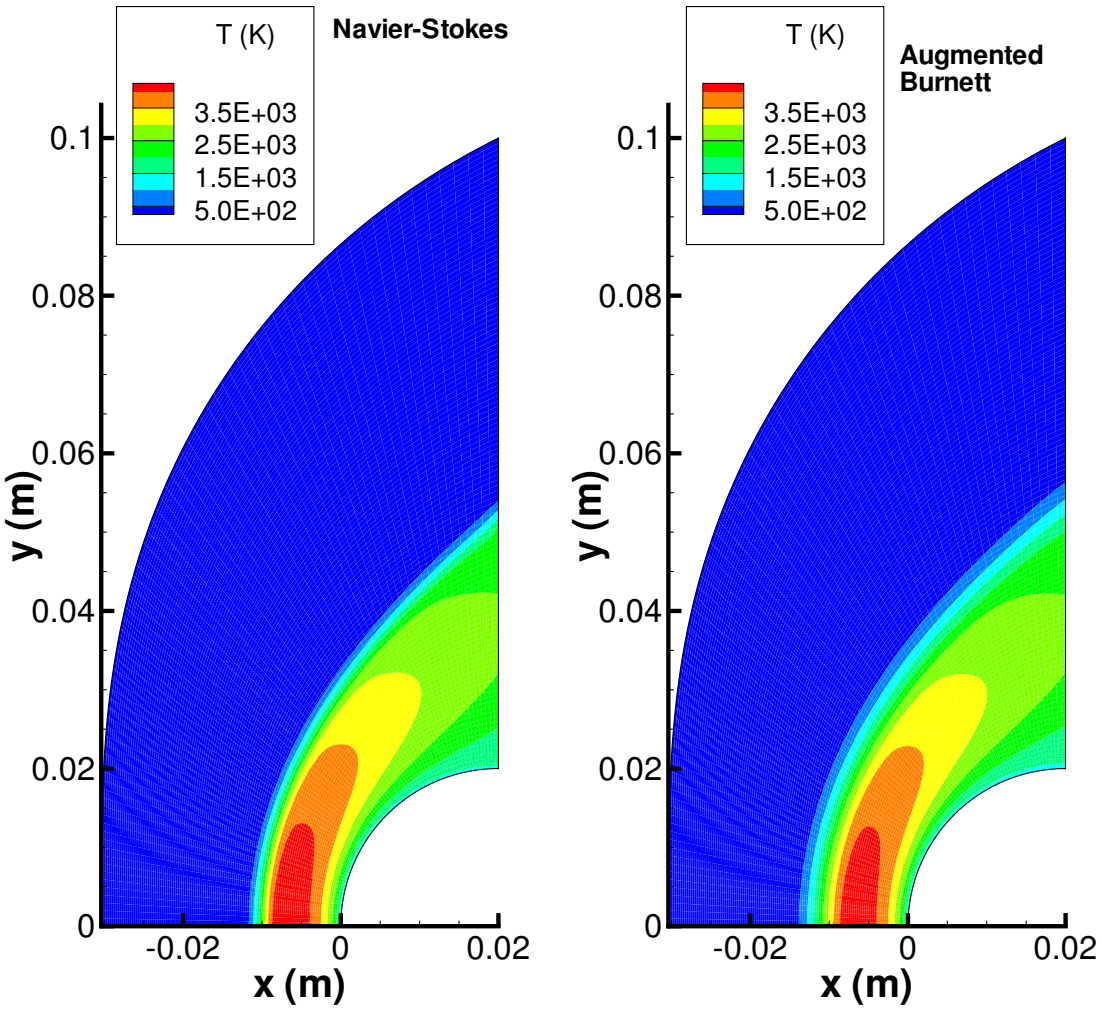

FIGURE 4.9: 2D bow shock temperature contours comparing Navier-Stokes and Augmented Burnett solutions

AR	RMS Error (p) Error to (4.18)
1	0.166%
2	0.152%
4	0.048%

TABLE 4.14: Comparison of HiReCom Navier-Stokes 3D microchannel simulations with an analytical pressure model

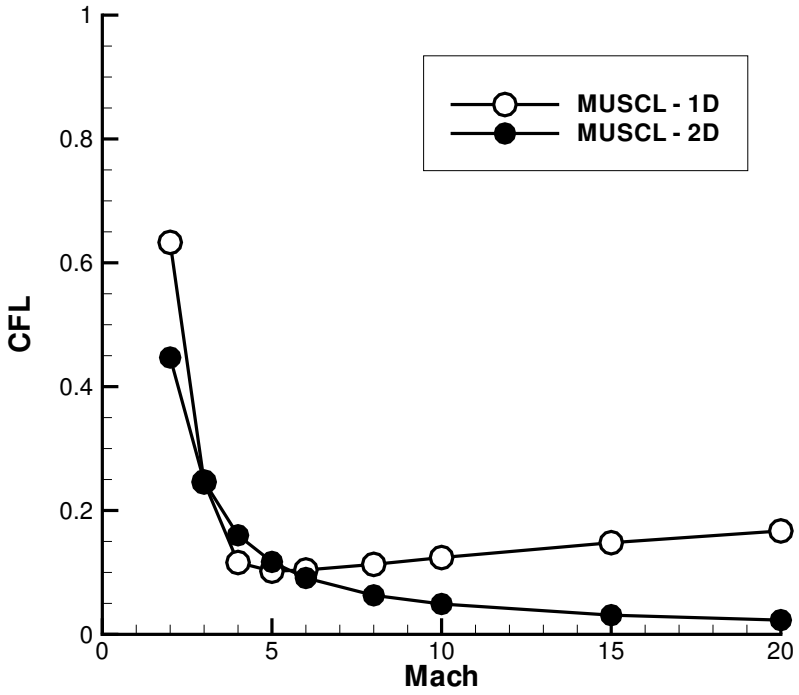

FIGURE 4.10: Comparison of observed 1D shock and 2D bow-shock *CFL* factors

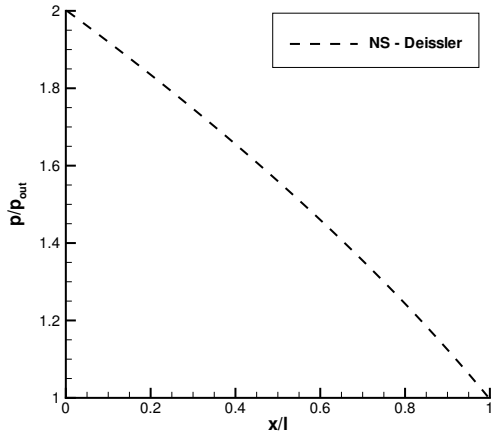

FIGURE 4.11: Exemplar pressure distribution for a Navier-Stokes 2D microchannel simulation

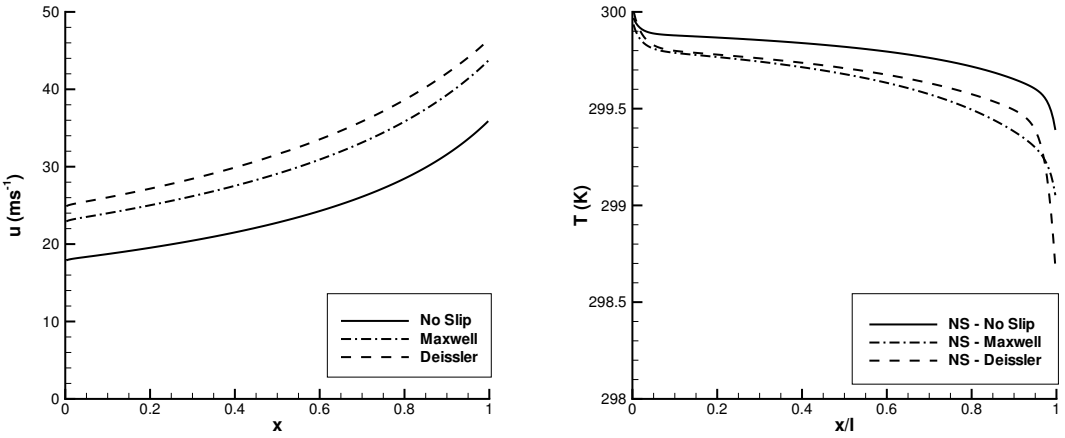

FIGURE 4.12: Centreline velocity and temperature profiles for 2D microchannel simulations with differing slip models

similarly corresponds well with that found in the model of *Beskok and Karniadakis*[**?** **?**]. Highlighted by Table 4.15, examination of the midpoint volumetric flow rates demonstrates this correspondence. Agreement is improved with increasing aspect ratio, and decreasing slip order. The former is perhaps due to the reduction of three-dimensional effects with increasing aspect ratio. The latter may be due to the fact that the temperature minimum at the centre of the channel is more pronounced with increasing slip order as shown in figure 4.16.

4.5 2D JET Neutraliser

To validate the application of the continuum-transition solver to high levels of rarefaction such as that in gas neutraliser systems, the solver developed in HiReCom has been applied to the JET neutraliser to simulate gas flow in the absence of the beam. This work includes, to the author's knowledge, the first application of the Augmented Burnett Equations to a gas neutraliser system and has thus been submitted for publication[**?**]. Several computational versions of the JET neutraliser geometry were examined, with comparisons made against experimental pressure data in the absence of beam. Due to the molecular flow observed at the neutraliser outlet, examination of these differing geometries also facilitates an examination of the effectiveness of the Augmented Burnett Equations approaching the molecular limit of $Kn = 1$, beyond their theoretical domain of applicability.

4.5.1 Boundary Conditions and Flow Parameters

Three computational geometries corresponding to the JET neutraliser have been examined, as described in figure 4.17. Ultimately, two-dimensional simulations were generated for hydrogen

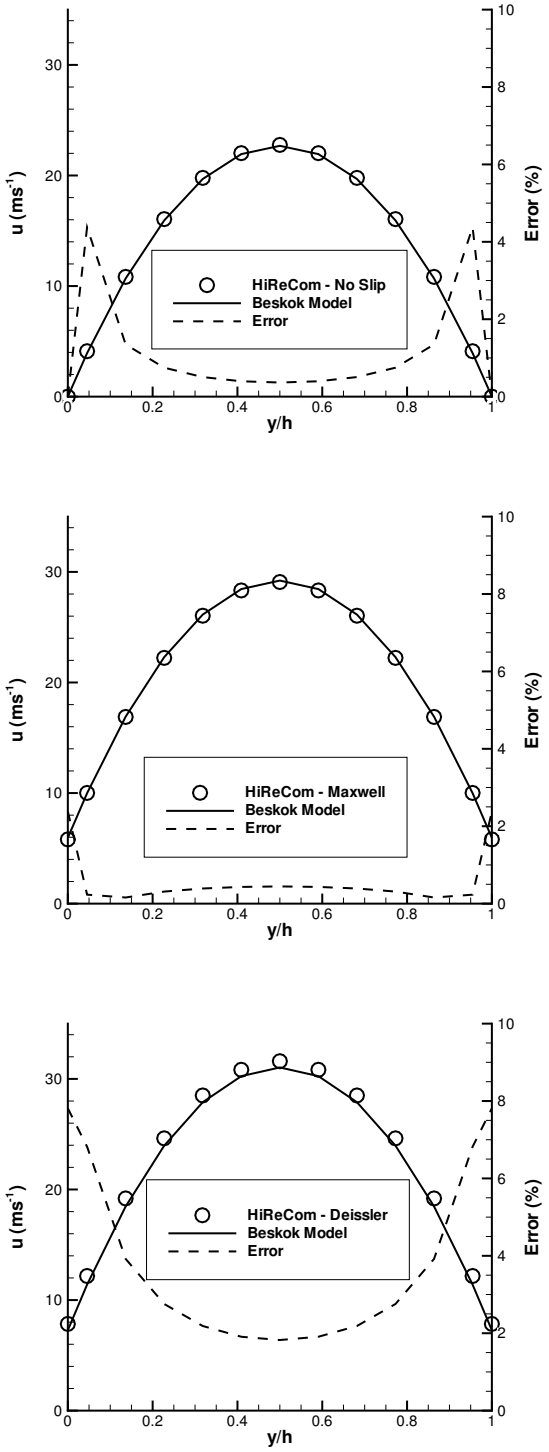

FIGURE 4.13: Sections indicating velocity profiles at 2D microchannel midpoint for differing slip models

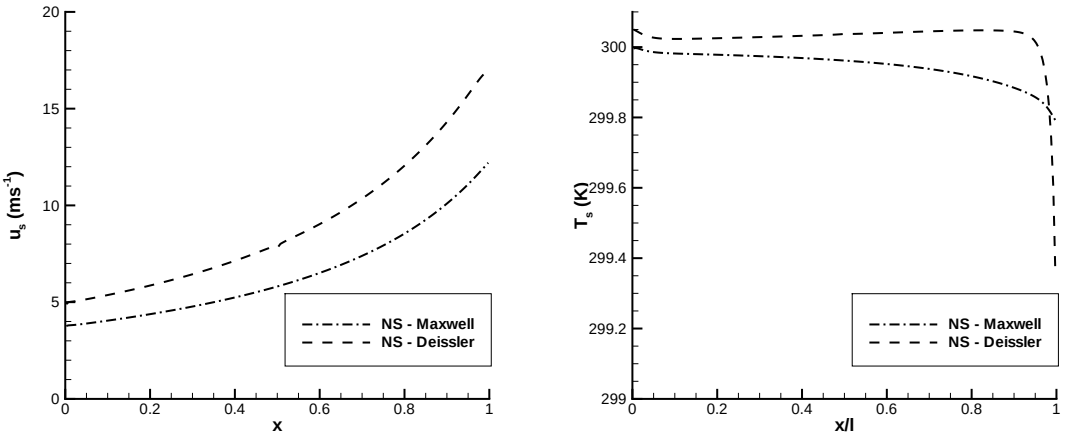

FIGURE 4.14: 2D microchannel wall slip velocity and temperature for differing slip models

with boundary conditions and parameters formulated to facilitate comparison with the experimental pressure profile of *Hemsworth* [**?**]; the only experimental data available in the absence of the beam, this profile includes an estimated error of 10% due to the apparatus utilised. To mimic the experimental set-up, no gas was considered to flow from the beam source into the neutraliser, with the gap between the neutraliser stages the sole gas inlet; the upstream neutraliser boundary was considered to act as an additional neutraliser wall instead of an inlet. The throughput to the neutraliser interspace recorded by *Hemsworth*[**?**] ($Q_{in} = 2.36 Pa.m^3/s$) was utilised to formulate an appropriate velocity boundary condition; note that throughput represents the typical mass flow quantity used in near vacuum applications[**?**]. The inflowing gas at this interspace was assumed to enter normally across the boundary providing $u_{in} = 0$ with a fixed inlet temperature $T_{in} = 300K$. Density at this interspace ρ_{in} was found by extrapolation from interior cells, resulting in an inlet velocity v_{in} across the boundary as in (4.22) where $A_{in} = 0.0552m^2$ represents the total interspace area.

$$v_{in} = \frac{Q_{in}}{A_{in}\rho_{in}RT_{in}} \tag{4.22}$$

The second order Deissler conditions have been applied as given in (2.7)-(2.8), whose implementation in HiReCom was validated in sections 4.3-4.4. Note that due to the second order accuracy of the Augmented Burnett Equations with respect to Kn, the application of this second order boundary condition ensures consistency. The application of first order slip or no-slip boundary conditions is technically unsuitable, and results in an incompletely defined boundary for the Augmented Burnett Equations. The Navier-Stokes equations similarly, should be subject to at least first order wall boundary conditions for flows within the continuum-transition regime. However, for the purposes of demonstrating the marked effect of inconsistent slip models upon flows at elevated Kn, some Navier-Stokes profiles utilising no-slip wall boundary conditions are also presented. Within the slip models, non unity accomodation co-efficients were used to better

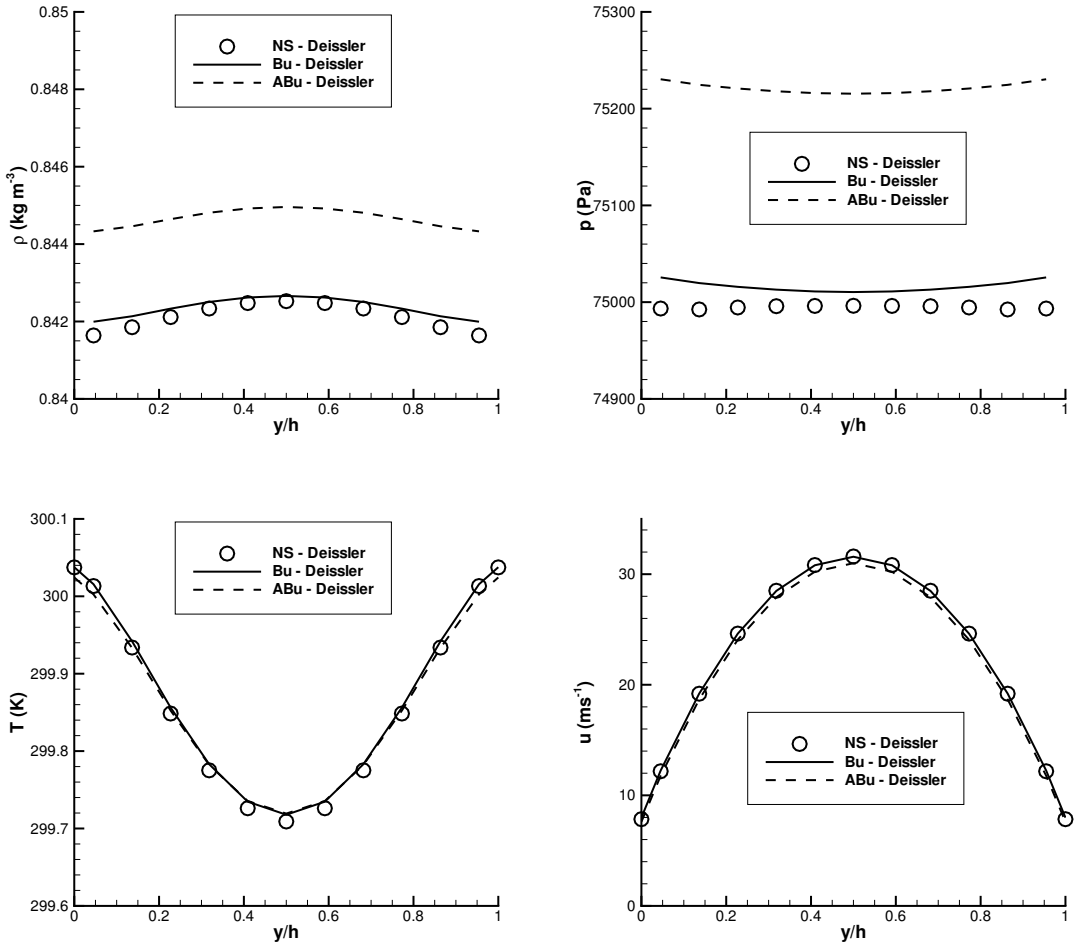

FIGURE 4.15: Sections indicating variable profiles at 2D microchannel midpoint for differing viscous models

simulate the properties of hydrogen; due to a lack of knowledge of the accomodation of hydrogen upon copper surfaces, experimental data for hydrogen upon platinum was utilised[**?**]. These and other gas utilised parameters are summarised in Table 4.16, including values comprising the adopted interaction viscosity model (3.10).

For each computational geometry, the considered length of the neutraliser differed (A: 140cm, B: 160cm, C: 180cm) with the outlet pressure boundary condition for each corresponding to the experimental data of *Hemsworth*[**?**] (A: 0.166Pa, B: 0.116Pa, C: 0.05Pa). Note also that the introduction of a symmetry boundary condition was used to reduce computational effort and exploit the centreline symmetry of the neutraliser, as indicated in figure 4.17.

The results presented wihin this section are steady state solutions; simulations were deemed to have reached steady state upon the time derivative of the area averaged inlet-to-outlet pressure

	$\dot{Q}_{mid}$ $(m^3.s^{-1})$		*Error* (%)
	HiReCom	Beskok	
NO SLIP:			
$AR = 1$	6.589×10^{-12}	6.400×10^{-12}	2.958
$AR = 2$	2.109×10^{-11}	2.077×10^{-11}	1.512
$AR = 4$	5.161×10^{-11}	5.103×10^{-11}	1.133
MAXWELL SLIP:			
$AR = 1$	9.925×10^{-12}	9.076×10^{-12}	9.358
$AR = 2$	3.005×10^{-11}	2.936×10^{-11}	2.349
$AR = 4$	7.294×10^{-11}	7.233×10^{-11}	0.084
DEISSLER SLIP:			
$AR = 1$	1.144×10^{-11}	9.638×10^{-12}	18.726
$AR = 2$	3.343×10^{-11}	3.099×10^{-11}	7.881
$AR = 4$	8.013×10^{-11}	7.627×10^{-11}	5.070

TABLE 4.15: Comparison of HiReCom Navier-Stokes microchannel simulations with an analytical volumetric flow rate model

γ	R $(J\,kg^{-1}K^{-1})$	ω	μ_0 $(kg\,m^{-1}s^{-1})$	T_{ref} (K)	σ	α	T_w (K)
1.4	4124	0.67	0.00000845	273	0.94	0.29	300

TABLE 4.16: Summary of 2D JET neutraliser gas and wall parameters for hydrogen

drop reaching 1×10^{-5} of its value at the initial time step. What follows utilises second order variables interpolation; as an alternative, the second order MUSCL variables reconstruction utilising the MINMOD limiter has also been considered but yielded adifference in the computed centreline pressure distribution of less than 1%.

4.5.2 Results

Initially grid convergence was investigated taking geometry A as a reference case. Doubling of grid resolution from the baseline grid 70×5 used within this thesis was found to offer only a small difference in the inlet-outlet pressure drop. The Navier Stokes pressure drop and the Augmented

Geometry	Length (m)	Equation Set	p_{out} (Pa)	Kn_{out}^{final}	RMS Error (p) Error to [**?**]	Timesteps to Convergence
A	1.4	NS	0.166	0.420	21.86 %	$\sim 5 \times 10^4$
	1.4	Aug. B	0.166	0.422	14.43 %	$\sim 1 \times 10^5$
B	1.6	NS	0.116	0.589	34.62 %	$\sim 1 \times 10^5$
	1.6	Aug. B	0.116	0.581	20.48 %	$\sim 5 \times 10^5$
C	1.8	NS	0.05	1.222	58.43 %	$\sim 2 \times 10^5$
	1.8	Aug. B	0.05	0.775	30.87 %	$\sim 2 \times 10^7$

TABLE 4.17: Summary of 2D JET neutraliser results with Deissler slip boundary conditions

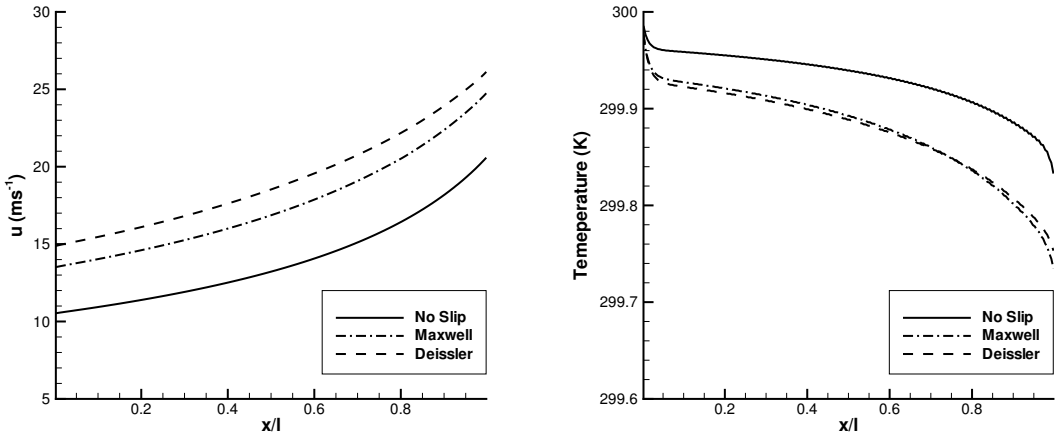

FIGURE 4.16: Centreline velocity and temperature profiles for 3D microchannel simulations with differing slip models at $AR = 1$

Burnett equations pressure drop each differ for the two grids by less than 5% when Deissler boundary conditions are considered. The remainder of the results presented for each geometry were thus produced using grids of the same cell spacing as this baseline grid for geometry A.

Figure 4.18 presents the vector plot for the flow obtained with the Navier Stokes and Augmented Burnett formulations for geometry A. The gas injected through the neutraliser interspace is immediately directed towards the low pressure outlet of the neutraliser. A recirculation is formed in the stagnation zone towards the sealed beam inlet region of the system. The results reveal a significant difference in the size of the recirculation region for the two equation systems; the closer proximity of the recirculation zone boundary to the gas inlet can be attributed to the larger magnitude of stresses in the Augmented Burnett formulation. Note that vectors of uniform length are used in figure 4.18 to better highlight the recirculation zone. Note also that the boundary of the recirculation zone corresponds to extrema in the distribution of flow variables on the centreline of the geometry in figure 4.19.

Considering geometry A, both equation sets demonstrate similar profiles for both centreline temperature and velocity. In the temperature distribution however the boundary of the recirculation zone corresponds to a local minimum in the Augmented Burnett equations and to a local maximum in the Navier Stokes solution. Also, the Augmented Burnett equations offer a much more pronounced temperature drop to the outlet (figure 4.19).

Figure 4.20 shows velocity and temperature profiles in the outlet section from the centreline located at $y = 0$ to the wall located at $y = 0.09m$. Both modified equation sets offer 'flat' outlet profiles across the neutraliser in comparison to the Navier Stokes no-slip equivalent as they are not constrained to a stationary flow at a fixed temperature at the wall. The difference between the Navier Stokes and Augmented Burnett outlet profiles with slip, results from the interplay of the field and boundary conditions in determining the final steady state profile.

One notes the shape of the pressure profile is consistent with the gas inlet and outlet points of

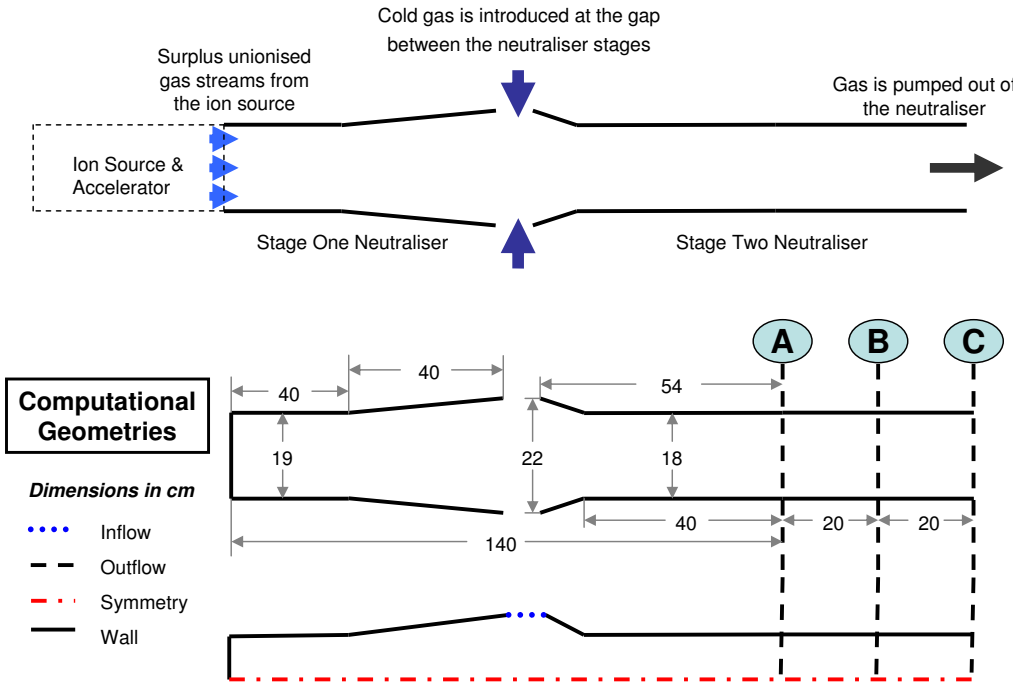

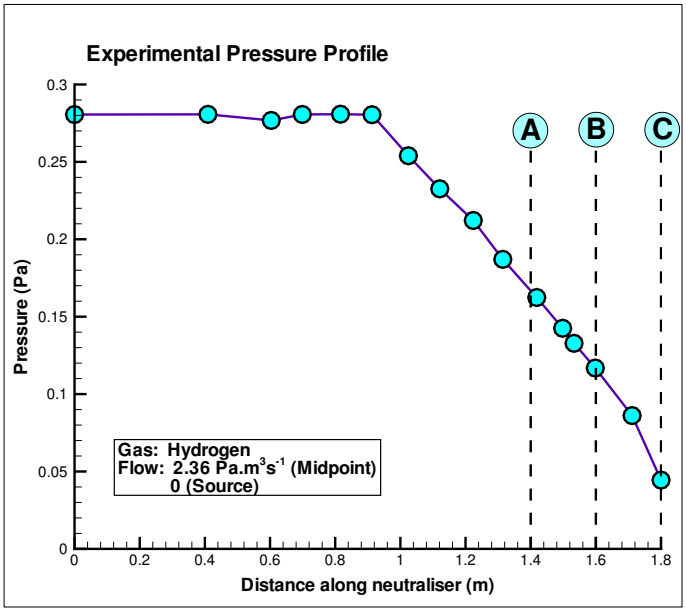

FIGURE 4.17: 2D JET Neutraliser computational geometries (without diagnostic collar)

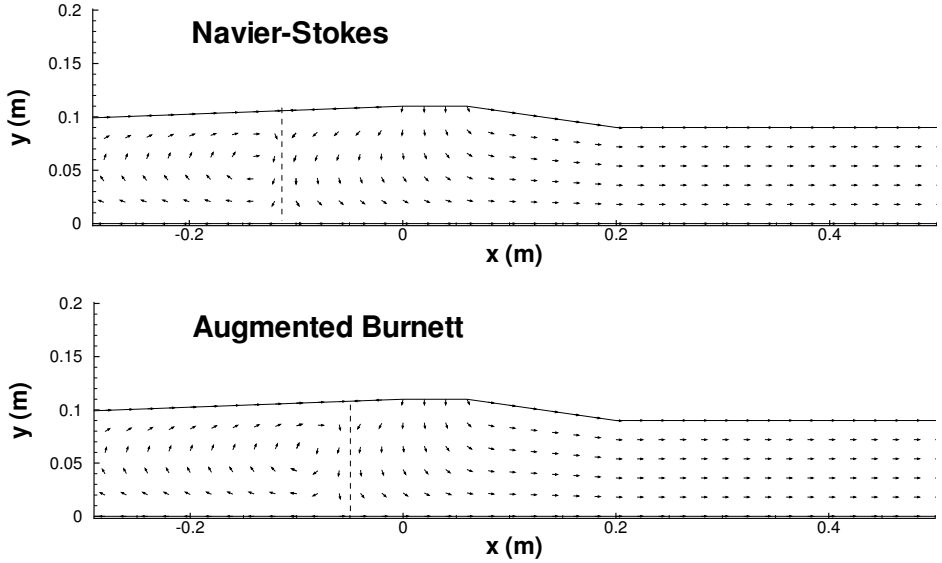

FIGURE 4.18: 2D JET neutraliser flow vector plots (geometry A). Dashed line shows approximate position of the recirculation zone

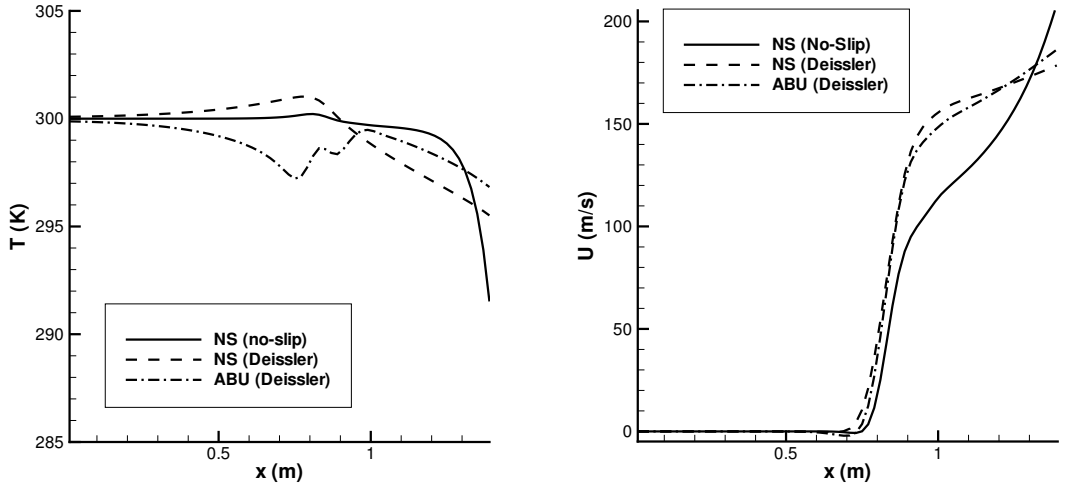

FIGURE 4.19: 2D JET neutraliser centreline velocity and temperature profiles for geometry A

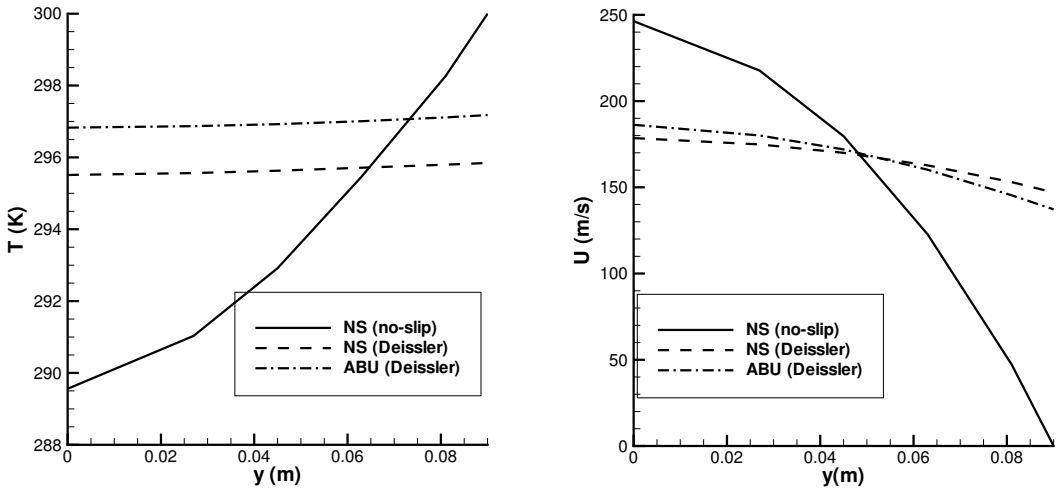

FIGURE 4.20: 2D JET neutraliser transverse outlet velocity and temperature profiles for geometry A

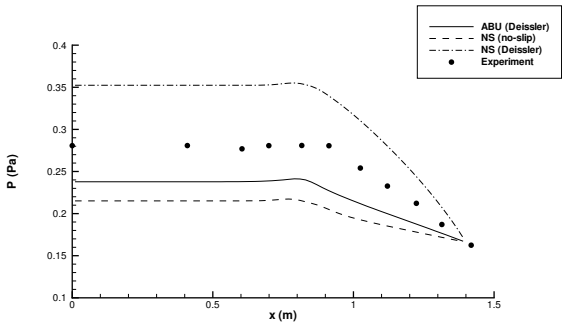

FIGURE 4.21: 2D JET neutraliser centreline pressure for geometry A (Navier-Stokes & Augmented Burnett)

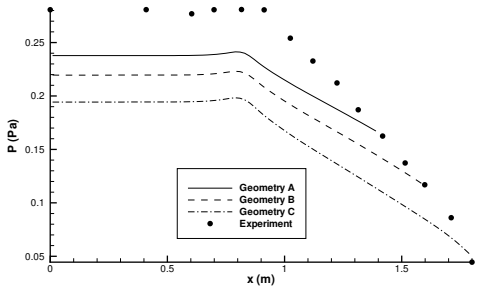

FIGURE 4.22: 2D JET neutraliser centreline pressure profiles for geometries A, B & C (Augmented Burnett)

the geometry (figure 4.21); each profile consists of a flat region within the first stage neutraliser due to the absence of a gas inlet upstream of the neutraliser midpoint, whilst injection of gas at the neutraliser midpoint results in an approximately linear presure profile over the second stage neutraliser to the outlet. With respect to the experimental pressure profile of *Hemsworth*[**?**], the no slip simulation significantly over-estimates the pressure in the neutraliser highlighting the neccessity of velcocity slip and temperature jump wall boundary conditions to successfully undertake modelling in the transitional regime. The source of higher pressure differential stems from higher viscous losses associated with the flow field generated by a no-slip model. As expected, the Augmented Burnett equations more closely capture the experimental pressure profile of *Hemsworth*[**?**] than the Navier Stokes for comparable boundary conditions; the centreline profiles differ by an RMS value of $\sim$ 14% for the Augmented Burnett equations and therefore is comparable to the predicted experimental error of the *Hemsworth* profile[**?**], whilst the Navier Stokes centreline profile differs by an RMS value of $\sim$ 22% and is thus well outside of the predicted experimental error.

The results achieved for the three computational geometries are summarised in Table 4.17. Given that the only difference with respect to the boundary conditions for each geometry is the outlet pressure condition, it seems logical that the differences in the gas profiles for each geometry, as exemplified by figure 4.22, are dictated by the outlet pressure and indirectly the outlet Knudsen. Therefore, comparison of the RMS error of the pressure fields against the experimental work of *Hemsworth*[**?**] reveal the greater performance with increasing outlet rarefaction of the Augmented Burnett Equations against the Navier Stokes Equations; the Augmented Burnett equations produced RMS errors of $\sim$ 14%, $\sim$ 20% and$\sim$ 31% for Geometries A, B and C respectively compared with RMS errors of $\sim$ 22%, $\sim$ 35% and $\sim$ 58% for the Navier-Stokes equations. One also notes that the Augmented Burnett Equations still offer reasonable accuracy as one approaches the molecular limit of $Kn \sim 1$, which would appear to support the applicability of the Augmented Burnett Equations at such high levels of rarefaction.

Closer examination of Geometry C helps reveal the marked differences in the results produced by the Navier Stokes and Augmented Burnett equations for the most rarefied case considered in this study. Aside from the observation that the Augmented Burnett equations reduce the RMS error to the experimental data of *Hemsworth*[**?**] by a factor of two when compared with the results of the Navier Stokes equations, perhaps the most interesting observation to be made from figure 4.23 is the significant difference in the outlet Knudsen values; for the same outlet pressure the Navier Stokes equations exceed the molecular limit of $Kn = 1$ in the vicinity of the outlet, whilst the Augmented Burnett equations do not, remaining more than 20% lower than this limit. Considering the other centreline profiles of figure 4.23, it appears that this surpression of outlet Knudsen occurs via two mechanisms; the outlet centreline temperature is significantly lower and the outlet centreline density is significantly higher for the Augmented Burnett Equations than the Navier Stokes equations.

4.6 3D JET Neutraliser

The investigation of section 4.5 was undertaken in two-dimensions to reduce the computational effort required. Extension of this work to three-dimensions would have proved prohibitively expensive, especially for the Augmented Burnett equations when applied to the most rarefied cases. However, confirmation of the suitability of the three-dimensional solver was desired. Therefore it was deemed necessary only to consider one computational geometry subject to the Navier-Stokes and Augmented Burnett equations, revealing good correlation with the results found in two-dimensions.

4.6.1 Boundary Conditions and Flow Parameters

The computational geometry examined is essentially geometry A of figure 4.17, with flow in the depth dimension fully evaluated. Simulations were generated for hydrogen with boundary conditions and parameters as per that detailed in section 4.5.1. The second order Deissler conditions have been applied for both the Navier-Stokes and Augmented Burnett simulations of this section. Steady state simulations were once again sought.

4.6.2 Results

Results are presented for a grid of $70 \times 5 \times 5$, with a convergence study demonstrating that doubling of this resolution offers minimal difference in the evolved centreline pressure profile. The good agreement of the three-dimensional simulation results with the work in two dimensions is exemplified by comparison of the centreline pressure profiles in figure 4.24. Interestingly, the three-dimensional work does not contain the anomalous local peak near the interspace gas inlet. This may well be because the developed flow differs significantly from that seen in the two-dimensional works. A separate recirculation zone does not develop in the first stage neutraliser for the three-dimensional simulations; the flow in the upper half of the neutraliser is drawn towards the upstream boundary of the neutraliser before being drawn back down the neutraliser near the vertical midplane of the system. This effect in the vertical direction obviously could not be captured within the two-dimensional simulations and further expains the recirculation zones that developed therein. Note also that though the convergence study indicated minimal enhancement in the centreline pressure profile with increased grid resolution, results clearly suggest that evaluation on more refined grids is necessary as some streamtraces escape the system near vertices; a much refined grid would be necessary to capture the vortices that are conjectured to develop near at these vertex locations. Such a very fine grid would prove prohibitively computationally expensive for the present solver due to the surpression of the stable timestep limit with rarefaction and therefore has not been examined within this research.

Note that the elevated centreline pressure for the Augmented Burnett equations may well be due to the reduced Kn encountered at the outlet for the three-dimensional geometry. Demsontrated in figure 4.25, this would concur with the work of section 4.5 wherein reduced outlet Kn was obsered for the most rarefied cases and resulted in improved agreement of the Augmented

Burnett Equations with experiment.

4.7 Summary

Validation of the HiReCom implementation of the Navier-Stokes, Burnett and Augmented Burnett equations has been undertaken for several test cases. Good agreement has been found with experimental data, analytical models and published simulation studies. These test cases have also served to validate the implemented wall slip boundary conditions and grid metrics. The developed continuum-transition solver produced in HiReCom can thus be used with confidence.

Two of the test cases have also facilitated computational investigation of the Conventional and Augmented Burnett Equations. This investigation has demonstrated that the developed solver offers stable solutions of the Conventional Burnett Equations at far greater grid refinements than has been obtained in other published implementations. This is conjectured to be due to the selection of numerical method, and the work in this thesis has demonstrated that variable reconstruction at cell faces has a significant impact upon the onset of instability.

The novel timestep limit derived for the Navier-Stokes and Augmented Burnett equations has also been tested. Though derived via consideration of a one-dimensional system under the assumption of weak compressibility and in the absence of thermal gradients, these limits have been demonstrated to agree to within an order of magnitude with the computational limits observed in both 1D and 2D hypersonic shock systems. This good quality of agreement is surprising given the simplifying assumptions applied to the system in their derivation. These novel timestep limits offer useful tools in the explicit timestepping of the Augmented Burnett Equations since their adoption appears to eradicate late onset instability, which had proved problematic when using traditional eigenvalue based approaches. Therefore the novel timestep avoids the associated exhaustive searches for suitably small numerical CFL. This approach is therefore adopted for the remainder of the thesis.

Finally, the Augmented Burnett Equations have been applied to a gas neutraliser system for the first time via examination of the JET neutraliser system. Noting the variation in pressure profiles for the differing outlet conditions considered in two-dimensions, one concludes that the outlet Knudsen value is a significant parameter with respect to the accuracy of the simulations presented. With increasing Kn, as expected, the accuracy of both the Navier Stokes and Augmented Burnett equations is hampered. However, in this study the Augmented Burnett equations have demonstrated good accuracy when compared against experimental data. Further corroborated by applicaton of the solver to similar three-dimensional geometries, one concludes that the application of continuum methods to investigate gas neutraliser systems is justified.

Also, one notes from Table 4.17, a significant increase in the number of timesteps necessary to ensure a converged solution with increasing rarefaction; in particular the Navier-Stokes equations progress approximately arithmetically, whilst the necessary timesteps for the Augmented Burnett equations appears to grow geometrically. Given the rarefaction is likely to be further enhanced upon the inclusion of the interaction mass/energy source and sinks, based upon experimental

observations, it is concluded that the remainder of the simulations in this thesis should be undertaken upon computational grids curtailed to ensure excessive rarefaction bordering on molecular flow is not encountered; though this Chapter has demonstrated that the developed solver does not produce unacceptable errors for near molecular flows it is necessary to minimise the computational demands of each simulation by reducing the number of timesteps required to provide steady state solutions.

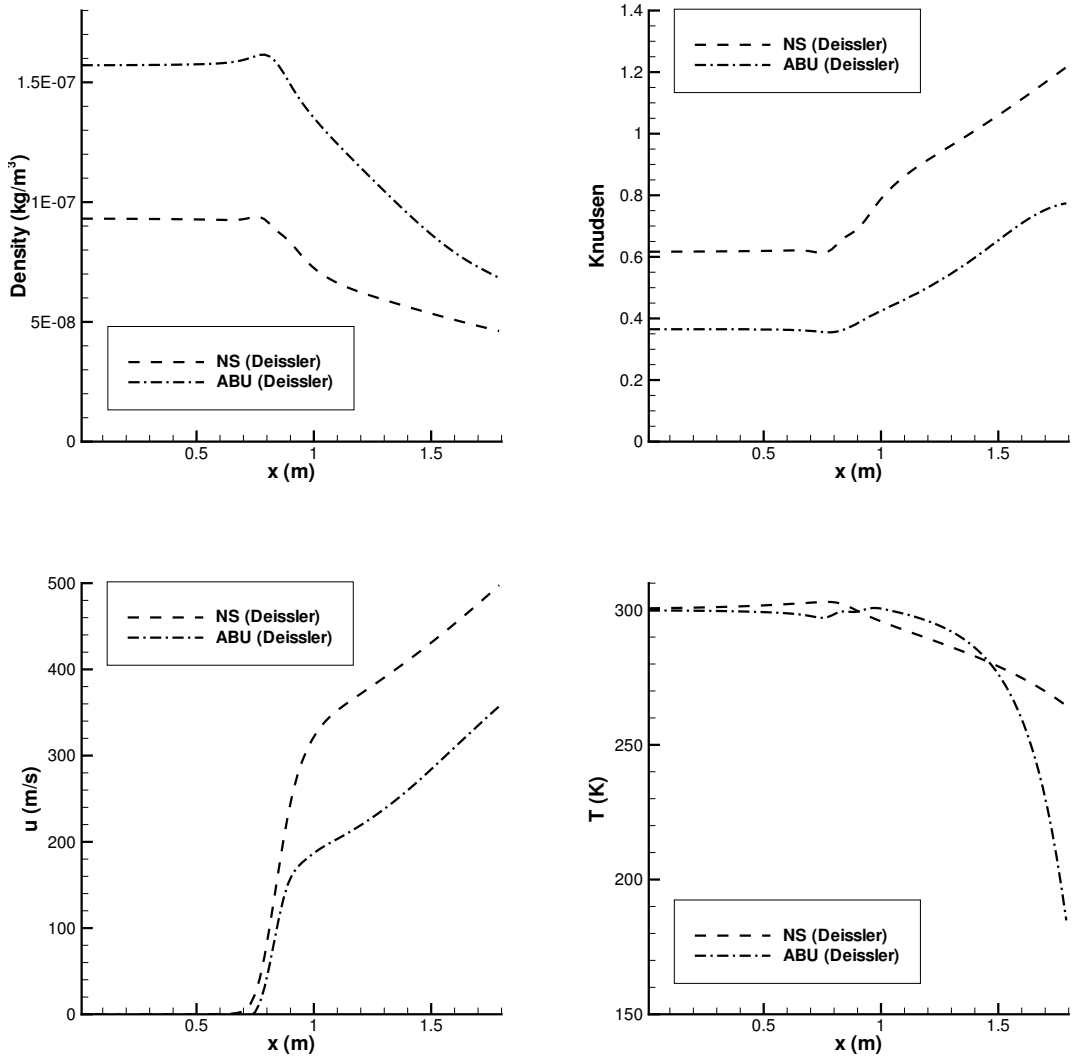

FIGURE 4.23: Various 2D JET neutraliser centreline profiles for geometry C (Navier-Stokes & Augmented Burnett)

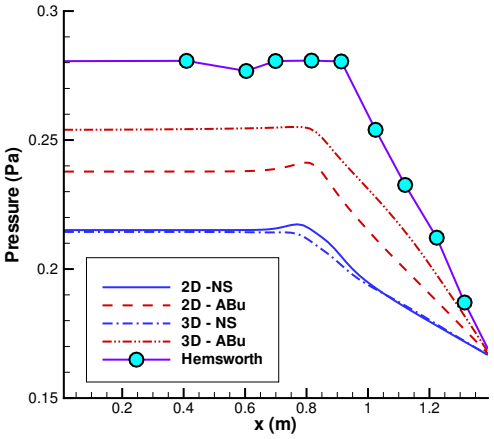

FIGURE 4.24: Comparing 2D and 3D JET neutraliser centreline pressure profiles

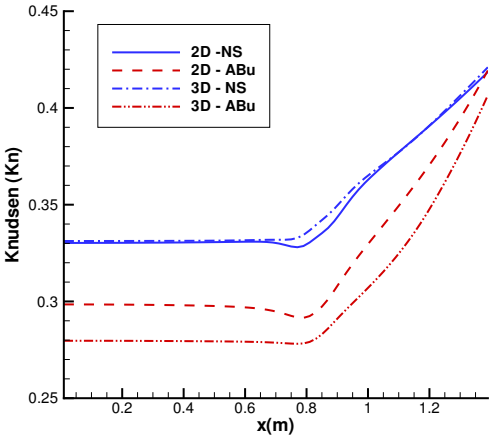

FIGURE 4.25: Comparing 2D and 3D JET neutraliser centreline *Kn* profiles

5

Application of the Coupled Beam-Plasma-Gas Solver

The coupling of the continuum-transition gas solver with the developed interaction model serves to offer a useful investigative tool with which to evaluate gas neutraliser dynamics. Validated in both 2D and 3D by comparison with a range of experimental data for the JET neutraliser, the solver also applied to the ITER neutraliser to establish the effects of gas heating in both current and future neutraliser designs. The influence of the various model parameters is examined via a series of parameter scans, with simulations also investigating the effect of geometry. This Chapter, together with Appendix **??** serves to advance neutraliser understanding, suggesting how their design might be optimised to mitigate the effects of gas heating.

5.1 2D JET Neutraliser

To fully validate the developed interaction model, and the resultant coupled beam-gas-plasma solver, it is necessary to compare against experimental neutraliser data collected at JET in the presence of beam. There exists a significant catalogue of experimental data relevant to the JET neutraliser resulting from the various experimental endeavours pre-dating this thesis. This has recently been supplemented via work specifically aimed at aiding the development of the neutraliser model within HiReCom.

The bulk of the historical experimental data was collected from experiments upon the JET Neutral Beam Test Bed via the use of its diagnostic collar located about the neutraliser interspace

and consisting of a series of diagnostic ports as indicated in figure 5.1. For the purpose of tuning and validating the neutraliser model, one can produce fits to the experimental data for gas temperature $\overline{T_{gas}}$, electron density $\overline{n_e}$, electron temperature $\overline{T_e}$ and the fraction of cold target $\overline{F_c}$. Each of these relationships is provided at a gas flow rate to the beam source of $Q_s = 12mbarl/s$ and a neutraliser gas flow rate at the interspace between the two system stages of $Q_n = 13mbarl/s$. These relationships are summarised in Table 5.1 and demonstrated in figure 5.2; note that they are applicable only in the presence of beam over the limited range of beam powers upon which data was collected, namely $1MW \leq P_b \leq 7MW$, and therefore include the injection of hot surplus gas from the source. The unsuitability of these relationships in the absence of beam can is exemplified by $\overline{T_{gas}} = 682K$ at $P_b = 0$.

From the spectroscopic work of *Surrey & Crowley*[**?**], measurement of the gas temperature across the neutraliser at the diagnostic collar has been achieved for varying beam powers and gas flows. This work utilised the experimental emission spectrum of rotational-vibrational states of the background gas molecules, in particular the Q branch of the Fulcher α spectrum. Gas temperatures were established via comparison of the distribution of emission intensities amongst the rotational-vibrational states with an analytical model. Normalisation of the emission intensities to erradicate noise arguably results in minimal contribution of cold gas to intensity distribution and thus the experimental gas temperatures effectively ignore any cold gas found at the diagnostic collar. Instead, this technique provides a line of sight average temperature $\overline{T_{gas}}$ for the hot gas plateau that is conjectured to develop in the centre of the neutraliser in the presence of beam. It was found that gas temperature increased approximately linearly with beam power, as shown in figure 5.2.

Experimental measurement of the plasma parameters was undertaken via the application of Langmuir probes. Effectively small electrodes inserted into the plasma, Langmuir probes represent one of the fundamental techniques for experimental plasma measurement. Via biasing the probe over a range of voltages both negative and positive to the plasma, several plasma parameters may be determined with application of established theory to the experimental traces that result[**?**]. In the work of *Crowley et al.*[**?**], such experimental work has included the determination of plasma electron density $\overline{n_e}$, electron temperature $\overline{T_e}$ and the electron energy distribution function within the JET neutraliser. Obtained at the diagnostic collar over a range of beam powers, this data is also summarised in figure 5.2.

The reduction of the neutraliser gas target in the presence of beam has also been experimentally determined at JET, via the use of calorimetric measurements as presented by *Surrey et al.*[**?**]. From the temperature rise of the calorimeter, a beam diagnostic tool employed extensively at JET and described previously in Chapter 2, the deflected and undeflected beam powers can be determined. Corresponding to the neutral power and the total extracted power respectively, their ratio provides the neutral fraction of the beam following passage through the neutraliser. Application of the 1D beam model given in (3.29), and knowledge of the beam energy permit evaluation of the hot gas target $\int n_{hot}\, dl_b$ through which the beam has passed in order to provide this beam composition. This target in the presence of beam, referred to as the hot target, may then be expressed as a fraction of the gas target in the absence of beam at the same inlet throughputs, which

is then referred to as the fraction of cold target. Offering a straightforward measure of the gas depletion in the presence of beam, this method is detailed in *Surrey et al.* [**?**], wherein the the data of figure 5.2 is presented. This data highlights the sharp fall in the fraction of cold target against beam power. Though significant experimental errors are found at low powers, experimental accuracy is much improved at higher beam powers and thus offer a useful tool for evaluation of the neutraliser model in HiReCom; the larger error at low beam powers is due to the assymptotic nature of the equilibrium beam composition with gas target, which is reached at much lower gas targets at low energies as indicated in Chapter 2; given the experimental measurement accuracy it is possible that the neutral beam fraction can be matched to a wide range of neutral gas targets since only a small change in beam composition is observed over a larger range of gas target due to near equilibrium conditions being achieved at much lower gas targets.

The most recent experimentation was undertaken in support of this thesis and intended to address the shortfall in knowledge of the gas pressure profile that develops in the JET neutraliser in the presence of beam; as discussed in Chapter 2, the only detailed knowledge of the longitudinal gas profile was obtained solely in the absence of beam. Discussed in greater detail in Appendix **??**, this latest experimentation was to facilitate the formulation of realistic boundary conditions for the neutraliser model in HiReCom. Ultimately a series of three point pressure profiles were obtained on the JET Neutral Beam Test Bed. These profiles consisted of one measure upstream of the neutraliser in the interspace between grids 3 and 4 of the accelerator (referred to as the grid-gas site), another at the neutraliser interspace via use of the Test Bed's diagnostic collar, and a final measure at the neutraliser outlet via gas sampling with a 'sniffer tube'. These measurements were readily applicable to the model in HiReCom in the absence of beam and provided boundary data applicable to the upstream, interspace and outlet boundaries. However, correction of these experimental pressure measurements for transpiration was necessary in the presence of beam due to the elevation of gas temperature. This is further discussed in the formulation of boundary conditions in section 5.1.1.

Overall, the purpose of section 5.1 is two-fold. Firstly, the outlined sets of experimental data sets are used to assess the accuracy of the coupled neutraliser model in HiReCom. Utilising flow conditions and model boundary conditions applicable to these experiments, the model parameter α_{Hot} is tuned to best match the experimental data for a 6MW beam pulse. The simulation with the most suitable value of α_{Hot} is explored in detail to better understand the model. The mass and energy sources within each slice of the computational grid, the developed beam and plasma profiles, and most importantly the gas distribution are all considered. A beam power scan is then used to assess the accuracy of the neutraliser model against experimental data over the typical range of operational beam powers used at JET. The second aspect of this section is to understand how the gas target in the presence of beam is influenced by the various model parameters. As such a series of additional parameter scans are then undertaken to better understand how the gas target might be improved and include variation of wall temperature T_w, inlet throughputs Q_n and Q_s, and finally beam current density via alteration of beam width B_w.

The development of the computational grids has also been the subject of significant attention

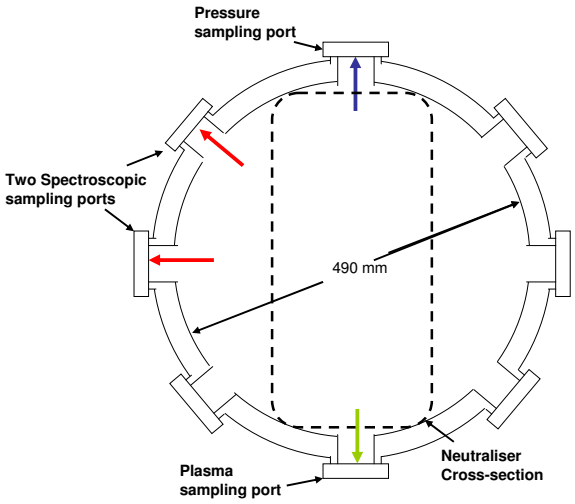

FIGURE 5.1: JET Neutral Beam Test Bed diagnostic collar

$Q_s = 12\,mbar.l.s^{-1}$,$Q_n = 13\,mbar.l.s^{-1}$	Experimental Fit Vs P_b	$\frac{RSS}{dof}$
Gas Temperature Plateau at Diagnostic Collar	$\overline{T_{gas}} = 31.858P_b + 682.39$	0.005
Electron Density at Diagnostic Collar	$\overline{n_e} = 10^{15}\left[-0.51P_b^2 + 6.14P_b + 2.46\right]$	0.037
Electron Temperature at Diagnostic Collar	$\overline{T_e} = 0.045P_b^2 + 2.732P_b + 0.621$	0.008
Fraction of Cold Gas Target	$F_c = 0.8022\,P_b^{-0.5168}$	0.062

TABLE 5.1: Functional fits to JET neutraliser experimental data

due to the unorthodox computational geometry that results from inclusion of the diagnostic collar. The issues are explored in 5.1.2 and mitigation strategies are presented. One such issue arising in simulation of the neutraliser gas in the presence of beam is the significant reduction of the stable timestep limit for the Augmented Burnett equations resulting from elevated gas temperature and reduced density. This supression of the stable timestep limit results in prohibitively long computational runs. Ultimately, qualitatively accurate simulations of the JET neutraliser have only been possible in the presence of beam with the Navier-Stokes simulations. The reasons for this are explored in detail.

5.1.1 Boundary Conditions and Flow Parameters

Within this section two-dimensional simulations have been undertaken and whilst the computational geometry is very similar to that of section 4.5, it has been necessary to add an additional region to simulate the diagnostic collar and the setup of the JET Neutral Beam Test Bed. As in

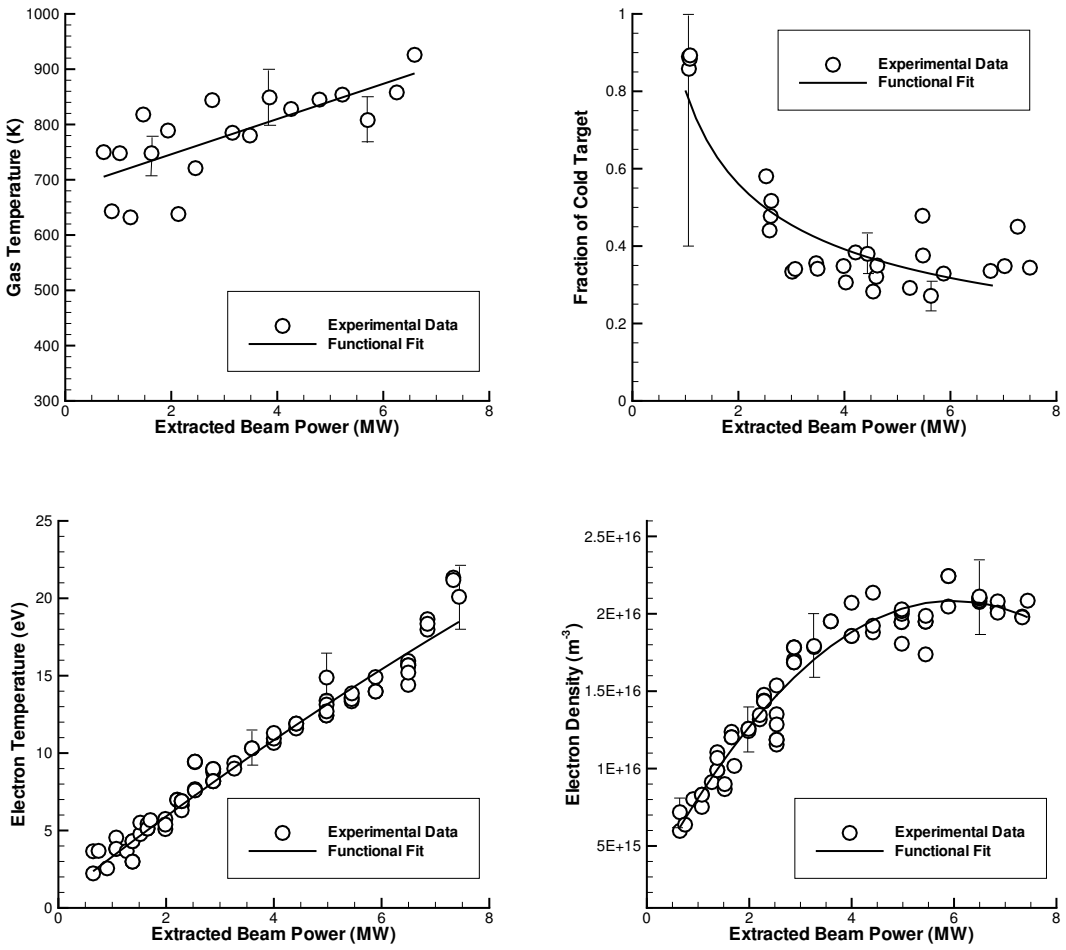

FIGURE 5.2: JET neutraliser experimental data and trends, with exemplar error bars

section 4.5, Deissler second order boundary conditions have been used within the computational geometry along with a symmetry boundary condition along the neutraliser centreline and an outlet at the downstream end of the neutraliser chamber. As per the findings of section 4.5 only $1.4m$ of the JET neutraliser has been simulated in order to enhance system convergence.

Unlike the work of section 4.5, the flow of surplus un-ionised gas from the source has been considered and thus the upstream boundary common with the beam source represents an additional gas inlet, with the assumption of flow entering normal to the boundary, e.g. $v_{in} = 0$, and user specified inlet temperature T_{inj}. The diagnostic collar has been included via extension of the geometry to a new region beyond the interspace, which is bounded by the wall of the collar. Accordingly, the interspace inlet condition of 4.5 has been replaced by implementation of two gas inlet boundaries for this newly extended collar region, with flow assumed to be entering at normal incidence to each boundary, i.e. $v_{in}^{d_1} = v_{in}^{d_2} = 0$, with a fixed temperature of T_{mid} specified

for each simulation by the user. Therefore the computational geometry may be visually summarised as in figure 5.3. The full specification of the inlet and outlet boundary conditions has required particular attention not only to ensure correct interpretation of the recent experimental pressure measurements presented in Appendix **??**, but also to ensure correct functioning of the compressible fluid model in HiReCom.

As touched upon in the introduction to section 5.1, in the presence of beam it is necessary to correct the experimental pressure measurements for the effect of transpiration; referred to as thermal creep elsewhere in this thesis, transpiration results in fluid flow from hot to cold regions. Given that the baratrons used to make the experimental pressure measurements were held at a fixed temperature of $300K$ during their operation, and that the neutraliser gas it measured was subject to significant heating in the presence of beam, the pressure registered by the baratron is supressed by transpiraton. Therefore, it is necessary to correct these experimental pressure measurements via (5.1) to provide exemplar gas pressure $p_{correct}$, where $T_{baratron} = 300K$ and $T_{correct}$ represents the actual gas temperature[**?**].

$$p_{correct} = p_{baratron}\sqrt{\frac{T_{correct}}{T_{baratron}}} \tag{5.1}$$

In order to achieve this correction at each of the pressure measurement sites, knowledge of gas temperature at each site is required. This is possible at both the grid gas and the diagnostic collar interspace locations but not at the neutraliser outlet. At the grid gas measurement site, an adapted version of the source model of *Holmes*[**?**] can be applied in conjunction with estimation of the accommodation upon the accelerator grids to estimate temperature at the experimental measurement site and facilitate transpiration correction; this source model is discussed in greater detail and applied to each of the experimental scenarios in Appendix **??**. By contrast, at the diagnostic collar measurement site the baratron measures the pressure of gas that lies well outside of the beam path, within a region being constantly filled with cold incoming gas from the neutraliser reservoirs. It is therefore reasonable to assume that this gas is at or near $300K$. Unfortunately, no experimental measure, analytical model or simplifying assumption can be provided at the neutraliser outlet and thus an outlet boundary condition does not readily follow from the experimental data in the presence of beam.

The specification of compressible inlet and outlet boundaries is best achieved as in section 4.5 via specification of some but not all variable criteria at both the inlet and outlet of the system; ideally, as in section 4.5 one would specify outlet pressure, inlet temperature and inlet throughput when considering the JET neutraliser either in the presence or absence of beam. This is obviously not possible if accurate knowledge of the outlet pressure is unavailable, as is the case for the neutraliser model in the presence of beam. Indeed, attempts to estimate the temperature at the outlet measurement site in the presence of beam in order to correct the experimentally observed pressure has resulted in numerical failure of model simulations; the author conjectures that such attempts have broken down either to the magnitude of the heating terms or the provision of conflicting boundary pressure and temperature estimates.

An alternative formulation in the presence of beam has sought to specify inlet pressure, temperature and throughput at the upstream neutraliser boundary, with inlet temperature and throughput specified at the interspace inlets and all variables extrapolated at the outlet of the model. Though not ideal as it is does not conform with standard compressible boundary specification, it has to date resulted in no numerical failures due specifically to the inlet/outlet boundary specification. Therefore, the author has utilised differing boundary conditions in the absence and presence of beam:

Absence of beam

- Outlet: user-specified outlet pressure p_{out}, implemented via temperature specification at the outlet and the use of density extrapolated to the boundary.
- Upstream Inlet: user-specified inlet temperature T_{inj} and throughput Q_s. The latter is implemented via the longitudinal velocity at the boundary, with velocity transverse to the boundary set to zero and density extrapolated to the boundary.
- Interspace Inlet: utilises the same method as the upstream inlet, with user-specified inlet temperature T_{mid} and throughput Q_n.

Presence of beam

- Outlet: all variables extrapolated to the boundary
- Upstream Inlet: user-specified inlet temperature T_{inj}, pressure p_{inj} and throughput $Q_s^{'}$. The latter is implemented via the longitudinal velocity at the boundary, with transverse velocity $v_{inj} = 0$ and density resultant from the equation of state and the specified inlet temperature and pressure. $Q_s^{'}$ follows from $Q_s$via (5.2), and represents the surplus source gas that does not form part of the beam, and instead streams into the neutraliser un-ionised.

$$Q_s^{'} = Q_s - 0.145 I_b \tag{5.2}$$

- Interspace Inlet: is unchanged from the approach used in the absence of beam.

As per the available experimental data and typical operational practice at JET, simulations were generated for deuterium with boundary conditions and parameters formulated to facilitate comparison with experiment. Utilising the viscosity interaction model and gas parameters as in Table 5.2, the results in this section represent steady-state solutions. As per the work of section 4.5 the solutions were deemed converged upon the inlet-to-outlet pressure drop reaching 10^{-5} of that encountered at the initial timestep. However, in contrast to that of previously presented work, the inlet pressure was taken from the upstream boundary rather than at the interspace between the neutraliser stages.

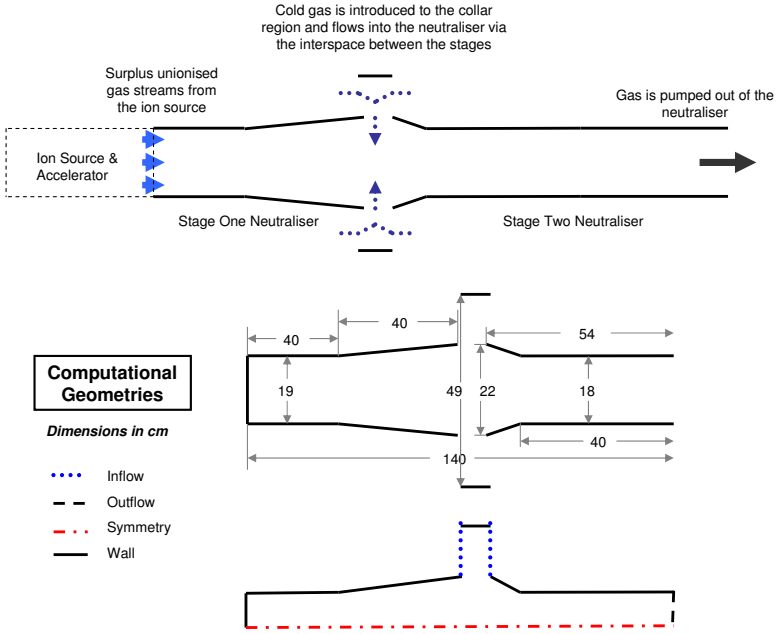

FIGURE 5.3: JET 2D computational geometry including diagnostic collar

γ	R $\left(Jkg^{-1}K^{-1}\right)$	ω	μ_0 $\left(kgm^{-1}s^{-1}\right)$	T_{ref} (K)	σ	α	T_w (K)
1.4	2062	0.67	0.0000126	$300K$	0.94	0.37	$300K$

TABLE 5.2: Gas parameters for deuterium simulations of the JET and ITER neutralisers

5.1.2 Grid Development

Inclusion of the diagnostic collar within the computational geometry was highly desirable to ensure correspondence between the simulations in HiReCom and the experimental data against which they were to be assessed. However, its impact upon the computational geometry is such that extensive investigation was necessary to understand how qualitatively correct, suitably accurate simulation could be achieved in the collar region.

Failures in the Collar Region

It was necessary to split the geometry into three computational blocks with distinct blocks prior to, encompassing and after the neutraliser section containing the diagnostic collar. This was due to the additional transverse cells necessary in the collar region and resulted in dissimilar numbers of transverse cells in each of the three computational blocks. The infrastructure of the HiReCom

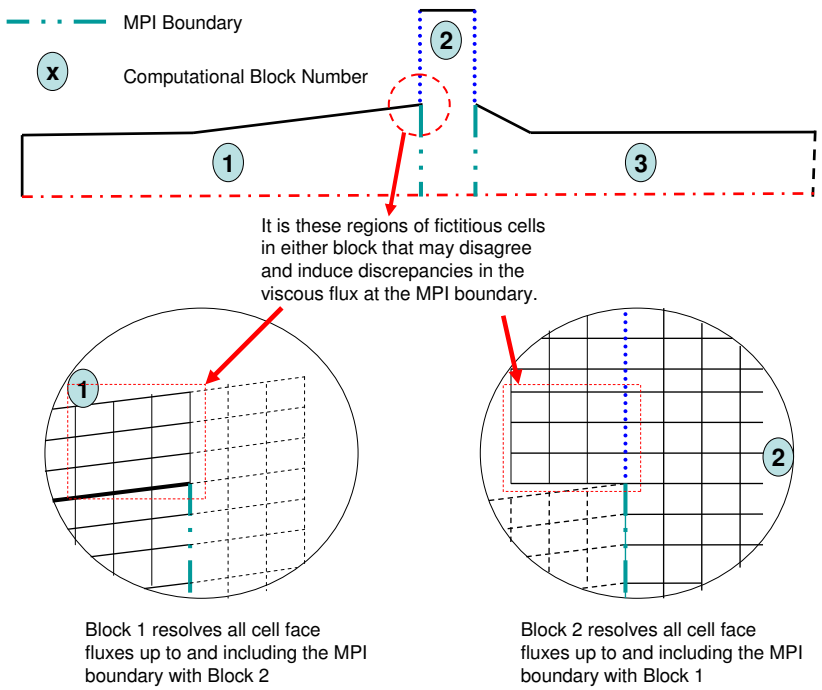

FIGURE 5.4: Fictitious boundary cell issues for the 2D JET neutraliser geometry the including diagnostic collar

Q_s $(Pa.m^3s^{-1})$	Q_n $(Pa.m^3s^{-1})$	T_{inj} (K)	T_{mid} (K)	P_{out} (Pa)
12	13	300	300	0.174

TABLE 5.3: JET 2D neutraliser grid with collar - development study simulation parameters

modelling framework and the computational grid required was such that partitioning of the grid in this fashion was the only means of solution, with each computational block solved via a different process. Investigation was deemed necessary to assess the behaviour of the solver in relation to these dissimilar sized process blocks. For this purpose, a coarse baseline grid was examined in the absence of beam with use of the simulation parameters of Table 5.3. This baseline grid utilised refinement in the collar region and nearby cells to allow better evaluation of gas flow in the collar region and entering the neutraliser via the interspace region.

For the Navier-Stokes equations, evaluation of this baseline grid proceeded without problem, however the Augmented Burnett equations could not be evaluated straightforwardly upon this grid. It was the dissimilar blocks that were ultimately identified as the cause of this failure with the overlap of the computational blocks, the associated passing of solution information near the boundary and duplicate fictitious cells of differing value all contributing. Examining the transition to the collar block from the preceeding computational block, as in figure 5.4, helps detail this

issue. As discussed in Chapter 3 the model developed in HiReCom utilises fictitious cells beyond the boundaries to facilitate the implementation of the correct numerical conditions at the boundary face. Two computational boundaries lay adjacent to one another in this transition region, as highlighted in figure 5.4; since each boundary requires its own set of fictitious cells in order to implement the correct conditions at the boundary face, these cells in fact overlap for the computational geometry. This is alleviated by the handling of each set of fictitious cells by a differing process, with each knowing nothing of the existence of the other set of fictitious cells.

Such an approach is fine for the Navier-Stokes equations but fails to prove sufficient for the Augmented Burnett equations. In fact the breakdown of the Augmented Burnett equations typically occurred at the MPI boundary between the two blocks, identified in figure 5.4. As explained in Chapter 3 the viscous fluxes are evaluated at each cell face to provide the inter-cell fluxes. For the computational geometry indicated, the viscous fluxes are calculated twice for certain interior cell faces, i.e. those that constitute the MPI boundary are subject to evaluation in both blocks to which they belong. Those MPI boundary faces close to the geometric boundaries require the use of the fictitious boundary cell data in order to evaluate viscous fluxes; remember nearby cells are necessary to evaluate derivations at the cell face. Therefore the differing values of these fictitious cells within each block imply the viscous fluxes evaluated at the same cell face may be different for their evaluation in each blocks. This is exacerbated for the Augmented Burnett equations, which heavily rely upon cross derivative terms - i.e. higher order derivatives with respect to more than one direction - and can provide discrepancies of significant magnitude. Therefore in the central refined region of the grid, it is necessary to only evaluate the Navier-Stokes viscous stress term and avoid extension to the Augmented Burnett stresses, thereby avoiding numerical failure of the developing solution. Though not ideal, this reduction in accuracy when calculating only the Navier-Stokes viscous terms in the central computational block does not significantly increase the error of the converged solution; this region does not represent the most rarefied region in the neutraliser, and the work of section 4.5 suggests that it is the treatment of the most rarefied flow that most affects the accuracy of a given solution.

Grid Resolution

Work was undertaken to understand the grid resolution necessary to ensure qualitatively correct, sufficiently accurate flows. Longitudinal grid spacing $\triangle_{x_{col}}$ in the collar computational block and $\triangle_{x_{out}}$ outside of the computational block were each varied, along with the minimum transverse cell size $min\left(\triangle_y\right)$ as summarised in Table 5.4. Each grid was simulated in the presence of beam, with simulation parameters as in Table 5.5.

Flow Behaviour in the Presence of Beam The consideration of the differing grids revealed grid spacing within the diagnostic collar computational block to be of great importance in ensuring evaluation of qualitatively correct fluid flow in this region. Overall, five grids have been considered and the effect of grid resolution within the collar block upon the evaluated fluid flow is best exempified by consideration of the Navier-Stokes solutions in the presence of beam upon grids 1 and 2 of Table 5.4.

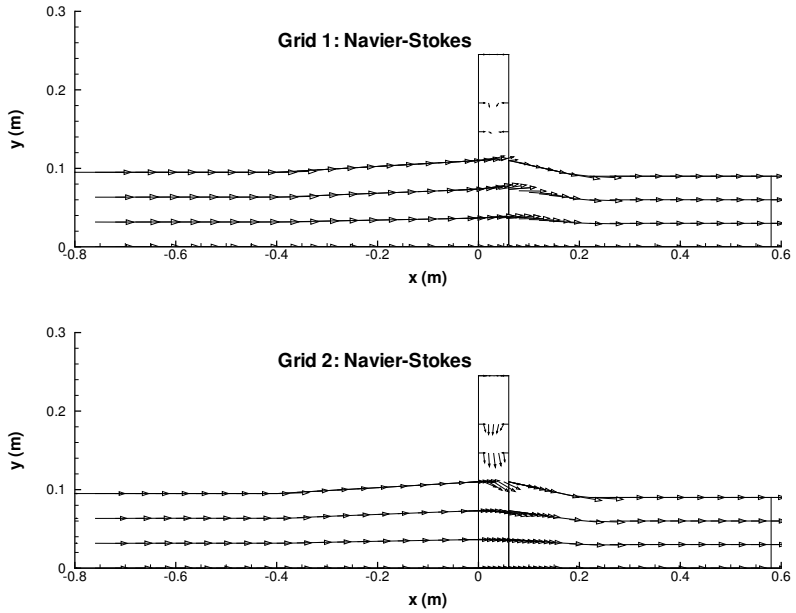

FIGURE 5.5: JET 2D neutraliser with collar - flow vector diagrams for Navier-Stokes simulations upon grids 1 & 2

Gas is introduced to both the upstream boundary with the beam source and to the diagnostic collar region, reesulting in velocity vector patterns presented in figure 5.5. One expects gas to flow from these two inlets to the chamber outlet. However, this apparently logical flow behaviour only occurs for grid 2, whereas for the coarse grid 1 gas is unable to penetrate from introduction at the interspace into the bulk neutraliser region. This failure of flow to enter the neutraliser bulk is easily seen if one examines the average transverse velocity of the gas $\overline{v_{col}}$ along a chord from the collar edge to the neutraliser centreline - for grid 1 this average remains positive, whilst for grid 2 it is negative implying gas intoduced at the collar successfully reaches the bulk of the neutraliser only for the latter grid. Therefore from the grid resolution work undertaken one concludes that a maximum longitudinal grid spacing of $\triangle_{x_{col}} = 0.01m$ must be used in the computational block containing the collar in order to provide qualitatively accurate flow simulations in the presence of beam.

Timestep & Convergence With regards to the restriction of the stable timestep limits, investigation has demonstrated that in the presence of beam the most severe timestep restriction for the Navier-Stokes equations occurs in the collar computational block if this is the subject of local refinement. By contrast it is the neutraliser outlet region that proves most restrictive for simulations with the Augmented Burnett equations; this represents the region of highest mean free path, and given that the refined collar region is only subject to the Navier-Stokes equations, it is increased rarefaction rather than grid resolution that serves to suppress the stable timestep limit.

Grid	Spacings			Equations	Properties at Collar			Gas Target	Timesteps
	$\triangle_{x_{col}}\,(m)$	$\triangle_{x_{out}}\,(m)$	$min\,(\triangle_y)\,(m)$		$\overline{n_e}\,(m^{-3})$	$\overline{v_{col}}\,(ms^{-1})$	$\overline{T}_{gas}\,(K)$	$\int_0^{1.4} n_{hot} dl_b\,(m^{-2})$	
1	0.04	0.02	0.03	NS	4.56×10^{16}	6.48	646	3.96×10^{19}	$\sim 6 \times 10^4$
				ABu	5.16×10^{16}	14.00	641	4.93×10^{19}	$\sim 5 \times 10^5$
2		0.01		NS	5.42×10^{16}	-13.6	688	4.49×10^{19}	$\sim 2 \times 10^5$
				ABu	Unconverged after 1×10^7 timesteps				
3	0.02	0.02	0.018	NS	4.94×10^{16}	6.08	651	4.12×10^{19}	$\sim 1 \times 10^5$
				ABu	Unconverged after 1×10^7 timesteps				
4		0.01		NS	6.00×10^{16}	-3.72	697	4.85×10^{19}	$\sim 2 \times 10^5$
				ABu	Unconverged after 1×10^7 timesteps				
5		0.005		NS	7.14×10^{16}	-20.00	760	5.70×10^{19}	$\sim 8 \times 10^5$
				ABu	Unconverged after 1×10^7 timesteps				

TABLE 5.4: JET 2D neutraliser with collar - grid resolution study results summary

Q_s $(Pa.m^3s^{-1})$	Q_n $(Pa.m^3s^{-1})$	P_b (MW)	T_w (K)	α	α_{Hot}	P_{inj} (Pa)	T_{inj} (K)	T_{mid} (K)
12	13	6	300	0.37	1	0.646	637	300

TABLE 5.5: JET 2D neutraliser with collar - grid resolution study simulation parameters

From Table 5.4 one notes that for grid 1 it was possible to provide converged Augmented Burnett simulations, whilst convergence was not possible within a reasonable number of timesteps for grids 2, 3 and 4. Notably, grid 1 did not provide qualitatively a correct converged Augmented Burnett profile since $\overline{v_{col}} > 0$. Therefore, the production of converged Augmented Burnett simultions has not been possible for the JET neutraliser due largely to the magnitude of gas heating serving to excessively suppress the stable timestep achievable with the presently fully-explicit timestepping approach of the present model.

By contrast, the application of the Navier-Stokes equations to refined grids was solved within a reasonable number of timesteps for each of the grids studied due to the much more lenient timestep restiction (3.185). Application to grids 1-5 suggests that simulations are suitably accurate for the spacing of grid 4 and the Navier-Stokes results presented for the remainder of this Chapter have utilised this grid; doubling the collar resolution to that of grid 5 offers little enhancement of either gas target or plasma density.

Therefore in summary, simulations of the JET neutraliser in the absence of beam have been possible for both the Navier-Stokes and Augmented Burnett equations, with qualitatively correct, suitably converged profiles obtained upon grids 2 and 4 respectively. In the presence of beam, qualitatively correct flow profiles have only been possible within a reasonable number of timesteps for the Navier-Stokes equations.

5.1.3 In the Absence of Beam

Offering a more complete description of the JET neutraliser than section 4.5 due to the inclusion of the diagnostic collar, simulations have been undertaken in the absence of the beam to provide estimates of the gas target offered to the beam at a number of gas flow settings for both the Navier-Stokes and Augmented Burnett equations.

Considering the case of $Q_s = 12mbarl/s$ and $Q_n = 13mbarl/s$ one can outline the typical flow behaviour for each of the flow cases considered, which differs significantly from that of section 4.5 predominantly due to the inclusion of an additional gas inlet at the upstream neutraliser boundary with the beam source. Examination of the flow vectors that develop within the system for the Navier-Stokes and Augmented Burnett equations are presented in figure 5.6. These diagrams demonstrate that the flow from the upstream boundary results in very regular longitudinal flow in the first stage neutraliser. A flow mixing region develops in the collar computational block where flow enters longitudinally from the gas inlets adjacent to the collar before being drawn down transversely into the neutraliser bulk and then proceeding longitudinally along the second stage of the neutraliser towards the outlet of the chamber. The inclusion of the upstream boundary is also evident in the centreline neutraliser pressure profiles that develop, as given in figure

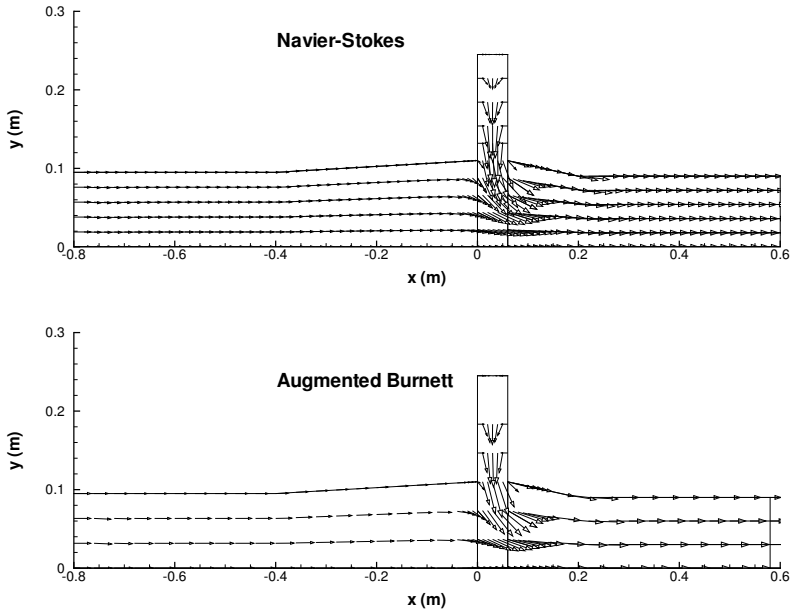

FIGURE 5.6: JET 2D neutraliser grid with collar - Exemplar flow vector diagrams in the absence of beam

5.7; one notes that rather than the flat pressure profile for the first stage neutraliser as noted in figure 4.22 of section 4.5, one obtains a linear profile in the first stage neutraliser. The anomalous local peaks in the Augmented Burnett pressure profile occur at the start and end of the collar computational block and may be induced by the evaluation of only the Navier-Stokes order fluxes within this region. The local pressure profile peaks about the collar computational block correspond to local effects in the density profile, with the temperature profile by contrast appearing smooth. These resultant local effects highlight the significant discrepancies in flow transport that result from inclusion and removal of the higher order viscous terms.

Ultimately, of most interest with regards to neutraliser efficiency is of course the gas target presented to the beam. For each of the flow cases considered in the absence of beam, the cold gas targets have been extracted and are presented in Table 5.6. Heavily dependent upon the outlet pressure boundary conditions formulated from the experimental data of Appendix **??**, the gas targets observe an approximately linear increase with both increasing source and neutraliser gas flow as shown in figure 5.8. In general the Augmented Burnett equations provide a larger estimate of gas target within the neutraliser, in agreement with the elevated pressure observed in figure 5.7 and throughout the work of section 4.5.

5.1.4 In the Presence of Beam

Comparison with experimental data is utilised to first tune the model, then assess its accuracy in application to varying beam powers. A series of parameter scans are then presented in order to outline the effects of the differing model parameters upon the effects of gas heating.

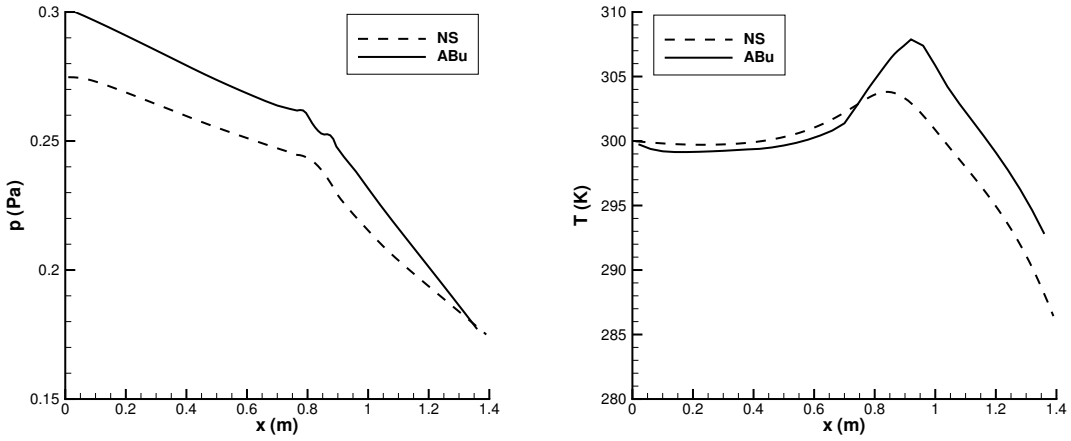

FIGURE 5.7: JET 2D neutraliser grid with collar - exemplar centreline pressure and temperature profiles in the absence of beam

$Q_s\ (mbarls^{-1})$	12	12	12	12	12	9	10	11	13
$Q_n\ (mbarls^{-1})$	5	10	13	18	20	20	20	20	20
NS (Grid 4)									
$\int_0^{1.4} n_{cold} dl_b\ (10^{19} m^{-2})$	5.65	7.19	8.03	9.32	9.77	9.11	9.42	9.60	10.02
ABu (Grid 2)									
$\int_0^{1.4} n_{cold} dl_b\ (10^{19} m^{-2})$	6.97	7.88	8.53	9.66	10.10	9.44	9.74	10.12	10.50

TABLE 5.6: JET 2D neutraliser with collar - gas targets in the absence of beam

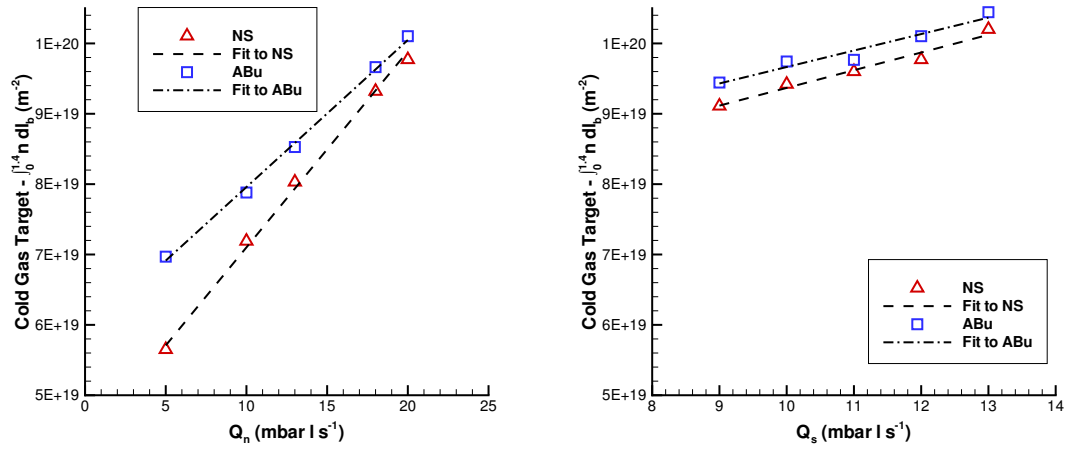

FIGURE 5.8: JET 2D neutraliser grid with collar - neutraliser cold gas targets with varying gas flow

Q_s $(Pa.m^3s^{-1})$	Q_n $(Pa.m^3s^{-1})$	P_b (MW)	T_w (K)	α	α_{Hot}	P_{inj} (Pa)	T_{inj} (K)	T_{mid} (K)
12	13	6	300	0.37	1	0.646	637	300
					0.8			
					0.6			
					0.4			
					0.37			
					0.2			

TABLE 5.7: JET 2D neutraliser with collar - α_{Hot} scan model parameters

α_{hot} Scan - Navier-Stokes

Utilising model parameters and boundary conditions as indicated in Table 5.7, variation of the parameter α_{hot} was undertaken for an extracted beam power of 6MW to ascertain which value demonstrates best agreement with experimental data. This tuned value was then to be used for the remainder of the two-dimensional neutraliser investigation. Simulated via the Navier-Stokes equations, significant variation in gas temperature, electron density and gas target is found, as presented in figure 5.9; note that the indicated experimental values correspond to the fitted experimental relationships of Table 5.1, which are only valid for $1MW \leq P_b \leq 7MW$.

In summary, reduction of α_{Hot} results in an elevated gas temperature plateau $\overline{T_{gas}}$ and reduced electron density $\overline{n_e}$ at the diagnostic collar, whilst the total gas target presented to the beam $\int_0^{1.4} n\, dl_b$ is also reduced and provides an associated reduction in the fraction of cold target $\overline{F_c}$. These effects, all of which may be noted from figure 5.9, appear logical given that reduction of α_{hot} implies reduced accommodation of the fast neutrals upon the neutraliser walls and results in an increased fraction of their initial energy being deposited in the background gas, increasing gas heating and reducing gas density. However, there is anomalous behaviour encountered at values of $\alpha_{hot} \leq 0.2$; the flow simulations appear to enter an unstable regime wherein qualitatively correct flow can no longer be resolved and gas is no longer able to pentrate the neutraliser bulk from introduction in the collar region, behaviour discussed with regards to grid development in 5.1.2. This behaviour results in vastly increased gas temperature, pressure and electron density. One concludes this is qualitatively incorrect since the test statistic $\overline{v_{col}} > 0$. The author conjectures that this is due to the magnitude of the source heating terms resultant from the reduced accommodation of the hot source particles upon the neutraliser walls. One should also note that all simulations for $\alpha_{Hot} \geq 0.35$ were obtainable from converged profiles in the absence of beam with compatible inlet throughputs. By contrast, for $\alpha_{Hot} < 0.35$ it was necessary to utilise a converged profile in the presence of beam, e.g. the converged simulation where $\alpha_{Hot} = 0.35$, else numerical failure of the simulation was encountered.

Examining the error plot figure 5.10 one concludes that the fraction of cold target F_c demonstrates optimum agreement at $\alpha_{hot} \sim 0.4$ for the Navier-Stokes simulations considered. At this value of α_{hot} each of the other comparisons with experimental data (i.e. gas temperature at the plateau $\overline{T_{gas}}$, electron density n_e and gas pressure $\overline{p_{col}}$ measured at the diagnostic collar) agree to within $\sim 40\%$. Agreement for these additional quantities is further improved with reducing α_{hot},

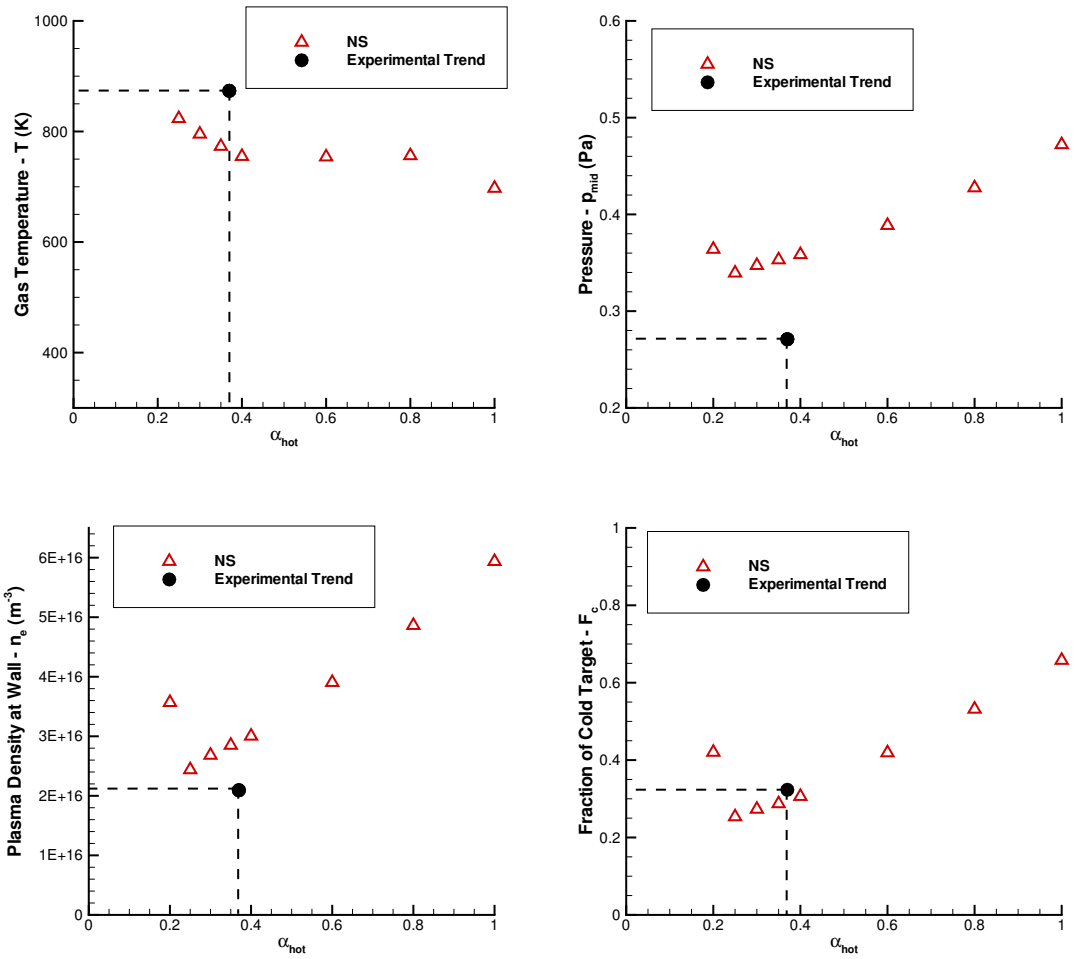

FIGURE 5.9: JET 2D neutraliser with collar - α_{Hot} scan comparison to experimental data (experimental trend is indicated at $\alpha_{hot} = 0.37$)

but is limited to an minimum error of $\sim 25\%$ for both p_{col} and n_e before instability is encountered.

The author considers the loss of gas target due to gas heating as the most important consideration in evaluating the coupled solver. Therefore, a value of $\alpha_{hot} = 0.37$ has been selected for use in the remainder of the 2D simulations since this appears to offer an accurate estimate of F_c and also agrees with the utilised α. Though published experimental data vaguely suggests that the accommodation coefficient may be lower with increasing incident temperature, this observation is far from unanimous (as shown in [**?**]). Therefore, in the absence of definitive knowledge of the behaviour of the thermal accommodation coefficient for fast particles, use of the experimentally determined value for near room temperature projectiles ensures consistency in the treatment of interactions with the wall.

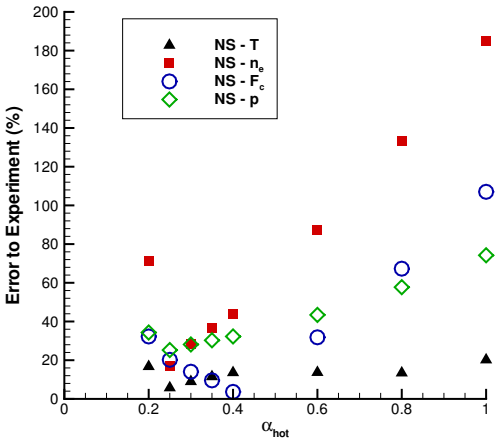

FIGURE 5.10: JET 2D neutraliser with collar - summary of α_{hot} scan error to experimental data

6MW Simulation in Detail - Navier-Stokes

Focusing on the single simulation obtained with $\alpha_{hot} = 0.37$ allows better understanding of the effects of the various model constituents and the resultant gas flow provided. The gas density profile in the presence of beam is significantly different to that in the absence of beam at the same inlet throughput conditions. As can be seen from figure 5.11, the neutral gas density profile in the presence of a 6MW beam is much depleted, with two distinctive peaks at the gas inlets. These peaks correspond to the upstream boundary with the beam source and the interspace between the neutraliser stages. Interestingly, the temperature profile is almost an inverted version of the gas density profile, with gas temperature minima provided at the inlets. This would seem logical for the inlets at the midpoint interspace given the introduction of cold gas at $T_{mid} = 300K$, whilst one must reason that the temperature of the hot surplus source gas streaming into the neutraliser at the upstream boundary $T_{inj} = 637K$ must form a plateau from which additional heating occurs.

Examining the contours of figure 5.12 that develop across the neutraliser, in conjunction with the transverse profiles given in figure 5.13, one notes that neutral gas density peaks at the wall and experiences a minimum in the centre of the beam path. The opposite behaviour is found for temperature, where one notes the plateau in gas temperature within the beam path, i.e where $\frac{y}{B_{hw}} \leq 1$; the gas temperature quoted at the collar for much of this Chapter is the average of the temperature values in the beam path, effectively ignoring the contribution of colder gas in the computational slice, as per the discussion of the experimental method employed by *Surrey and Crowley*[**?**].

The flow of gas resulting within the neutraliser is similar in behaviour to that presented previously in figure 5.5. Heavily forward projected, the gas falls towards the centre of the beam for much of the flow as indicated by a negative transverse velocity. This tendency towards the beam centreline is more pronounced near the gas inlets where the transverse velocity magnitude is found to be larger.

With regards to the beam evolution within the neutraliser for the 6MW beam, the ion-neutral composition is summarised via figure 5.14. In the Navier-Stokes case, an average neutral fraction of 21.4% is found at the modelled neutraliser outlet.The computational geometry does not simulate the entire length of the neutraliser and therefore does not account for all of the gas target through which the beam passes. If one considers the full $1.8m$ of the JET neutraliser rather than the simulated $1.4m$, this neutral fraction can be increased slightly. This is achieved via fitting a quadratic formula to the average neutral beam fraction in the final 10 computational slices, and extrapolation of this quadratic over the additional length that is unaccounted for by the model, namely $0.4m$. As indicated by figure 5.14, extrapolation results in an adjusted neutral fraction of 23.7% for the 6MW Navier Stokes simulation.

As one might expect, the shape of the plasma density profile along the neutraliser mimics the gas density profile, as exemplified by consideration of the plasma electron density at the wall in figure 5.15. By contrast the electron temperature remains fairly flat throughout the model, demonstrating a slightly negative approximately linear relationship, which is also presented in figure 5.15. The transverse plasma density profile also remains flat when examined at any longitudinal location within the neutraliser; peaking for each transverse profile at the beam centre, the reduction in electron density to the wall varies from $\sim 5\%$ at the neutraliser outlet to $\sim 10\%$ at the upstream boundary, with this fall-off most pronounced in the computational grid encompassing the diagnostic collar where the difference in wall and centreline electron density reaches $\sim 20\%$. This small variation in the electron density, combined with the low levels of ionisation and electron temperature in the neutraliser, result in a very small plasma pressure term when compared to the gas pressure; the plasma pressure differential induced by the variation in electron density from the beam centre to the neutraliser wall corresponds to $< 2\%$ of the total gas pressure for much of the neutraliser length. One thus concludes that plasma pressure has minimal impact upon the neutraliser gas distribution.

Closer examination of the 6MW simulations also offers further insight into the distribution of energy and mass sources within the model. Figure 5.16 provides the fraction of the total energy and mass source provided to the background gas by each source type. One notes that the three dominant energy sources for the gas result from plasma ions reflection at the wall, dissociation by beam ions and dissociation by primary electrons. Direct energy transfer from stripped electrons to the gas represents an increasing fraction of the total energy source in each computational slice as one progresses along the neutraliser. Whilst the mass source to each slice is dominated by plasma ion reflection, dissociation products from reactions induced by beam ions and primary electrons play a significant role. By contrast, stripped electrons offer a minimal mass source to the background gas since dissociation by stripped electrons is less prevelant than for the other reactants. Figure 5.17 also reveals that the actual magnitude of the beam dissociation and plasma ion sources closely follow the gas density profile of 5.11.

There is a notable irregularity in the source profiles for $0.8m \leq x \leq 0.86m$. This behaviour is due to the inclusion of the diagnostic collar within the neutraliser computational geometry, which offers a significantly larger local neutraliser width and impacts upon the model in two ways. Firstly, the increased neutraliser width promotes a significant decrease in the primary electron

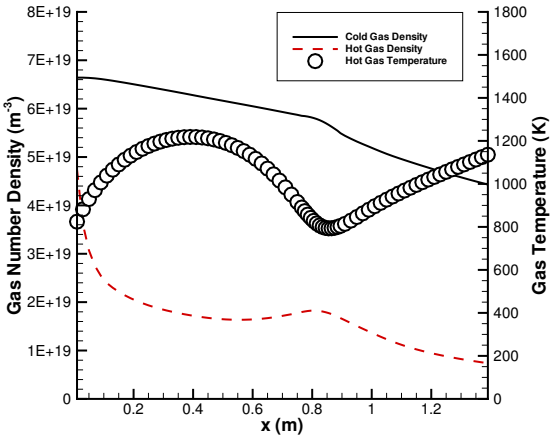

FIGURE 5.11: JET 2D neutraliser grid with collar - centreline gas density and temperature for $P_b = 6MW$

density within the collar due to the form of the primary electron density equation derived in 3.59 and visualised in figure 5.19. This decreased density significantly reduces the contribution of the mass and energy source attributable to primary electron induced dissociation in the collar region. Secondly, the increased local neutraliser width and the dense cold gas exterior to the beam results in a significantly higher gas target within which the fast neutrals of the various source terms might deposit their energy. This provides a significant local elevation in the energy deposited by each source particle as shown in figure 5.18. Therefore, the former effect accounts for the significantly reduced contribution of primary electron dissociation mass and energy source terms within the collar, whilst the latter effect explains the local spike in the magnitude of each of the other energy source terms.

Note that the mass source magnitude curves of beam ion dissociation and plasma ion reflection of figure 5.17 do not exhibit irregularity at the collar since the entirety of each mass source term is assumed to be successfully deposited in the gas of each computational slice. Thus, the magnitude of the mass source terms depends primarily upon conditions within the beam path. Similarly the collar has little effect upon the stripped electron density, since its calculation 3.59 is dependent solely upon beam and gas densities in the beam path, and does not directly interact with gas outside of the beam path. It is therefore, the reducing gas density over the second stage of the neutraliser that, even in spite of an increasing stripped electron density, is responsible for the reduced magnitude of the energy source term due to stripped electrons (see figure 5.19).

P_b Scan- Navier-Stokes & Augmented Burnett

Variation of the beam power P_b within the model in accordance with Table 5.9 allows further assessment of the accuracy of the model in HiReCom against the fits to experimental data provided in Table 5.9. Comparing the model with experiment in Figure 5.20 reveals reasonable overall agreement with experimental data. Consider each of the experimental data sets in turn:

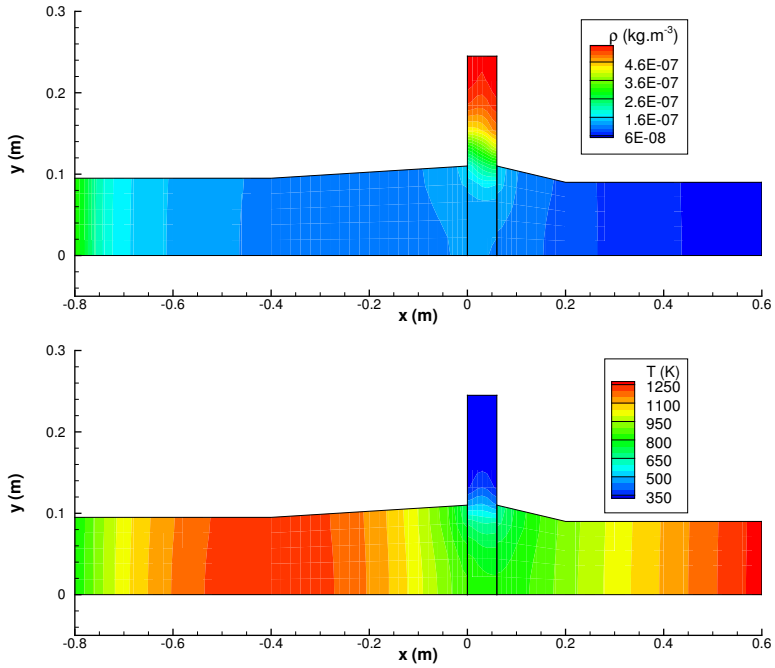

FIGURE 5.12: JET 2D neutraliser grid with collar - gas temperature and density contours for $P_b = 6MW$

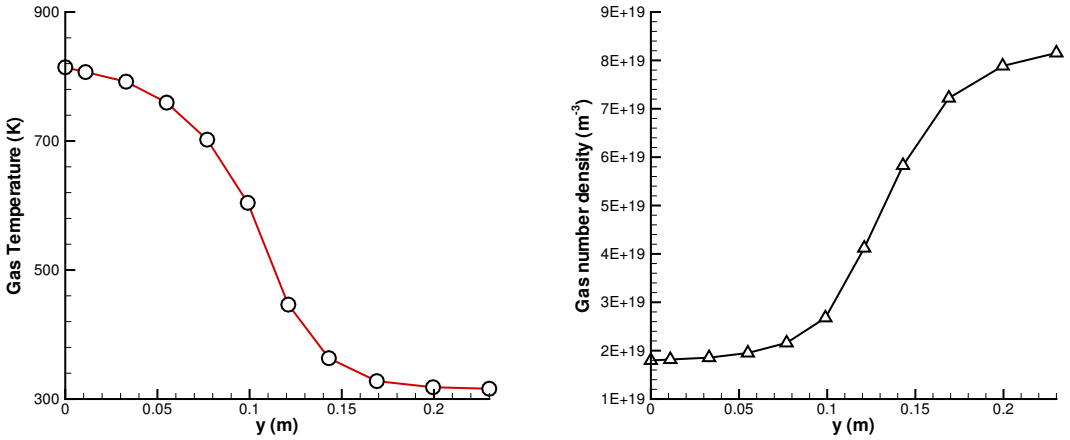

FIGURE 5.13: JET 2D neutraliser grid with collar - gas temperature and density at the diagnostic collar for $P_b = 6MW$

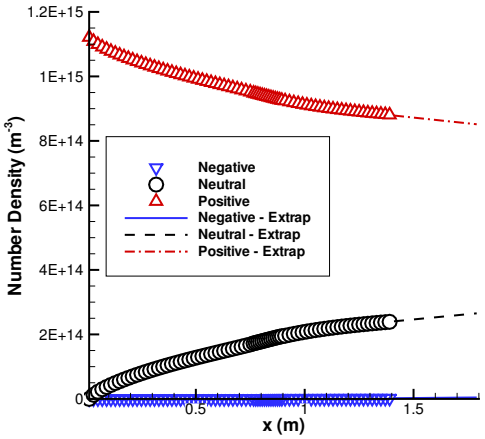

FIGURE 5.14: JET 2D neutraliser grid with collar - beam composition for $P_b = 6MW$

Gas Temperature One notes that experimental data for the gas temperature at the diagnostic collar increases with beam power. Whilst this is correctly captured by the three-dimensional model in HiReCom, as shall be demonstrated later in this Chapter, the temperature provided by the two dimensional model in HiReCom decreases slightly over the range of powers considered. This appears to further justify the extension of the model and demonstrates the truly three dimensional nature of the problem.

Fraction of Cold Target Following tuning of α_{hot} one notes the excellent agreement of the model results with experimental observations of the fraction of cold target. Over the range of powers considered, agreement is found with experiment to within $\sim 10\%$.

Electron Density The plasma developed in the model in HiReCom shows only reasonable agreement with experimental data. For example, the model appears to significantly over-estimate electron density, performing particularly poorly at low powers with slightly better agreement found at higher powers. Since the primary interest of this thesis is in understanding gas neutralisers during typical high power operations this is acceptable, with an error to experiment of $< 40\%$ for $P_b \geq 6MW$.

Electron Temperature The model in HiReCom shows reasonable agreement with experiment for electron temperature taken at the collar. Whilst the sheath electron temperature provided by the model is of the correct order and agrees within a factor of ~ 2 for the range of beam powers considered, it does not show the strong positive linear relationship found in the experimental relations. However, the author feels one should take care when directly comparing the results of the model in HiReCom with the experimental work of *Crowley*[**?**].

The experimental characteristic electron temperature is a singular value evaluated from the electron energy distribution function (EEDF) encountered by the Langmuir probe. This can be

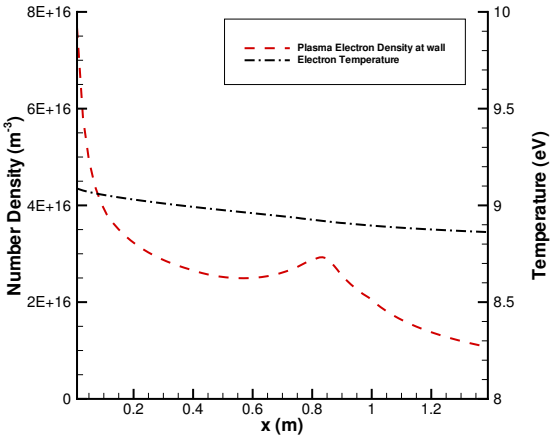

FIGURE 5.15: JET 2D neutraliser grid with collar - plasma electron density and temperature for $P_b = 6MW$

taken to be a good indication of the sheath electron temperature provided that the distribution is fairly mono-energetic. Within the neutraliser the author suggests this is not always the case and thus that the experimental electron temperatures may be misleading.

It is conjectured that the experimental probe encounters three distinct electron types. The first are background plasma electrons, with an inherent energy equal to the sheath electron temperature. The second population are primary electrons born in the beam path and subject to inelastic collision before reaching the probe at the diagnostic collar. Though within the developed neutraliser model it has been assumed that primary electrons are fully thermalised upon reaching the wall; this may not be the case and therefore primary electrons may represent an electron population with a differing typical electron temperature to the incident background plasma electrons. The third possible contributor to the experimental EEDF are stripped electrons subject to inelastic collision and possible thermalisation. Within the model it has been assumed that stripped electrons, though subject to inelastic collision, continue to travel within the beam path. This is obviously highly idealised and instead some portion will in reality be subject to significant deviation of their trajectory and may ultimately encounter a probe placed at the diagnotic collar.

Examination of the collected EEDFs appears to support the possibility of distinct electron populations being incident at the probe. Indeed, it is noted that with increasing beam power, the distribution functions develop peaks at intermediate energies that are distinct from the apparent background plasma population. In summary, the author argues that the experimental electron temperatures provided in figure 5.20 may not adequately describe the sheath electron temperature with increasing beam power; the author contests that these values are artificially high since they do not include contributions to the EEDFs of alternative electron populations with typically higher energies than the background plasma electrons.

Consideration of the converged gas profiles reveals details of how increasing beam power affects neutraliser gas flow. The centreline gas density profile follows a similar shape for each of

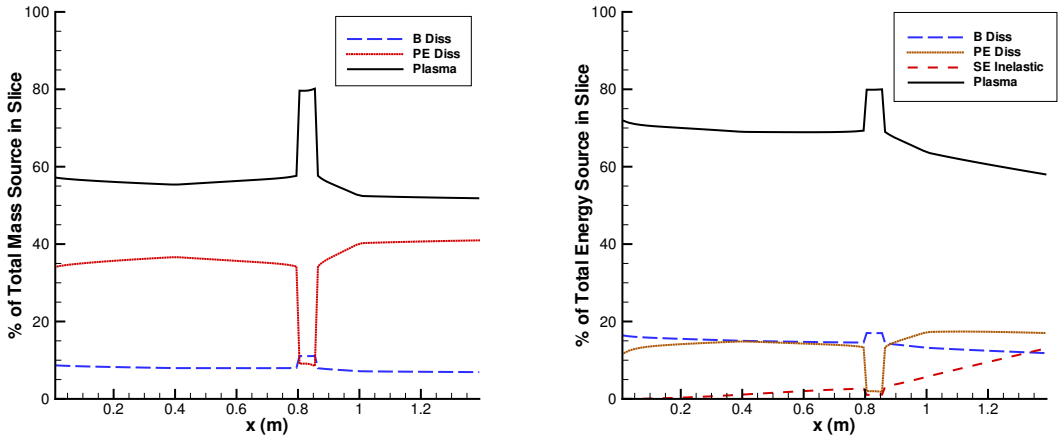

FIGURE 5.16: JET 2D neutraliser grid with collar - fractional contribution of each mass and energy source type for $P_b = 6MW$

the beam powers considered, with local peaks in the region of the two gas inlets. Note that with increasing beam power, one observes enhance gas depletion and therefore reduced gas density, as shown in figure 5.21. As per the observations of 5.1.4 the centreline temperature profile is an approximate inversion of the density profile for each beam power considered. However, one also notes from figure 5.21 that the temperature profile experiences overlap in the first stage neutraliser, before becoming ordered by beam power within the second stage neutraliser. The reason for this overlap is unclear, though it may be due to the developed plasma in the neutraliser since the reflection of plasma ions represents the dominant energy source term to the gas. As can be seen in figure 5.22, the plasma density and electron temperature profiles along the neutraliser overlap more extensively than the centreline gas temperature profiles. Note that the electron density at the wall only achieves successful ordering by beam power near the outlet of the system, whilst the shape of the electron temperature profile differs dramatically with beam power. The latter observes an approximately linear relationship with distance along the neutralier, with a positive gradient for $P_b = 2MW$ with each successive power producing a flatter profile before a slightly negative gradient is found for $P_b = 7MW$. The form of these plasma profiles is largely dictated by the cross sections for plasma ion production, the beam composition and gas density profile. This is obvious from consideration of the electron temperature formulae of 5.1.4, which simplify to (5.3) where f_+, f_0 and f_- represent the positive, neutral and negative fractions of the beam. Denote T_e^+ as the electron temperature resulting from an entirely positive beam, i.e. where $f_+ = 1$ and $f_0 = f_- = 0$, and T_e^0 as that resulting from an entirely neutral beam, i.e. where $f_0 = 1$ and $f_+ = f_- = 0$. Therefore at the upstream boundary, one obtains the electron temperature T_e^+ of Table 5.8. As one proceeds along the neutraliser, the f_- remains negligible within the JET system, but f_0 represents a significant fraction at the expense of f_+. As a result, the electron temperature tends towards T_e^0 of Table 5.8 as one progresses along the neutraliser.

These values of T_e^+ and T_e^0, along with their blending by beam fraction in (5.3) explain the

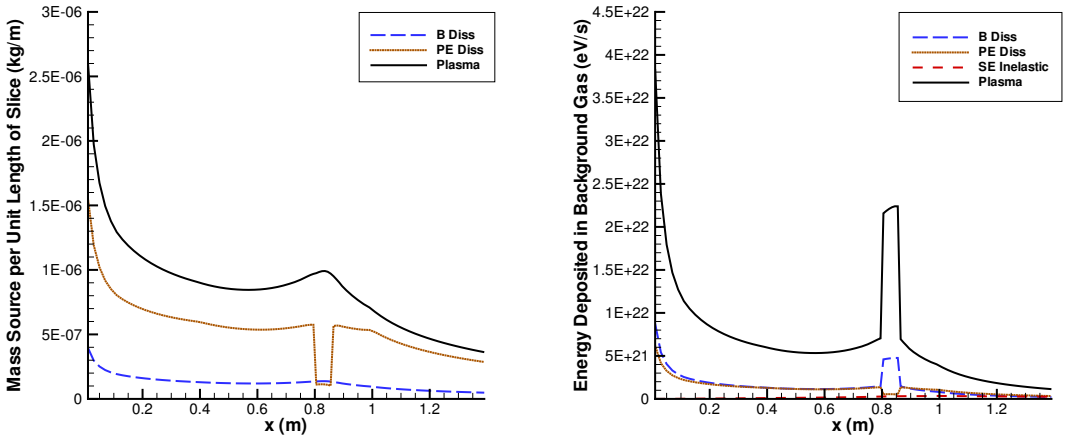

FIGURE 5.17: JET 2D neutraliser grid with collar - magnitude of each mass and energy source type for $P_b = 6MW$

trends observed in figure 5.22. For example, the strong increase of electron temperature for $P_b = 2MW$ is due to the fact $T_e \rightarrow T_e^0$ with increasing neutral fracton and that $T_e^0 > T_e^+$. The flat profile of T_e at $P_b = 4MW$ is similarly due to the fact that $T_e^0 \approx T_e^+$, whilst the reduction of T_e for $P_b = 6MW$ and $P_b = 7MW$ follows from $T_e^0 < T_e^+$. The rate of reduction is lesser for the latter because of the smaller neutral beam fraction that develops.

$$\begin{aligned} T_e &= \frac{2(H_+f_+ + H_{0,-}(f_- + f_0)) - \left(f_0\sigma_{se}^0 + f_-\sigma_{se}^-\right)E_{se}^0}{N_0(\eta+1-\psi)\left(f_+(\sigma_+ + \sigma_{10}) + f_0\left(\sigma_0 + \sigma_{0\bar{1}}\right) + f_-\sigma_0\right)} \\ &\rightarrow \frac{2(H_+f_+ + H_{0,-}f_0) - f_0\sigma_{se}^0 E_{se}^0}{N_0(\eta+1-\psi)\left(f_+(\sigma_+ + \sigma_{10}) + f_0\left(\sigma_0 + \sigma_{0\bar{1}}\right)\right)} \end{aligned} \tag{5.3}$$

T_w Scan - Navier-Stokes

From water calorimetry estimates of deposited power upon the neutraliser walls, it has been conjectured that the walls are subject to significant temperature rise in the presence of beam[**?**]. In order to assess the impact of wall temperature upon the developed flow, variation of T_w was undertaken. Interestingly, variation of the wall temperature in accordance with the model parameters presented in Table 5.10 provides minimal impact upon the gas target as indicated in figure 5.23. Also presented in this figure are the neutral beam fractions achieved at the model outlet of the neutraliser $f_0^{1.4}$ and a second order extrapolation of this to the actual neutraliser outlet $\widetilde{f_0^{1.8}}$; both experience minimal change due to the variation of wall temperature.

One slight note of caution is that this scan has been undertaken with constant α and α_{Hot}. The assumption of constant values is reasonable given the lack of knowledge of their variation with wall temperature and incident gas temperature. If some temperature dependent variation of these quantities was included in the model, the variation of gas target with wall temperature might be more substantial. However, based upon the current results obtained from the neutraliser

P_b (MW)	$2H_+$ $\left(eV.m^{-2}\right)$	$N_0\left(\eta+1-\psi\right)_+\left(\sigma_+ + \sigma_{10}\right)$ $\left(m^{-2}\right)$	T_e^+ (eV)	$2H_0 - \sigma_{se}^0 E_{se}^0$ $\left(eV.m^{-2}\right)$	$N_0\left(\eta+1-\psi\right)_0\left(\sigma_0 + \sigma_{0\bar{1}}\right)$ $\left(m^{-2}\right)$	T_e^0 (eV)
2	5.27×10^{10}	8.32×10^9	6.34	4.32×10^{10}	3.12×10^9	13.80
4	5.45×10^{10}	6.61×10^9	8.25	2.58×10^{10}	2.94×10^9	8.77
6	5.47×10^{10}	6.02×10^9	9.09	2.00×10^{10}	2.78×10^9	7.21
7	5.47×10^{10}	5.85×10^9	9.33	1.79×10^{10}	2.74×10^9	6.54

TABLE 5.8: JET 2D neutraliser grid with collar - values supporting electron temperature evaluation for P_b scan

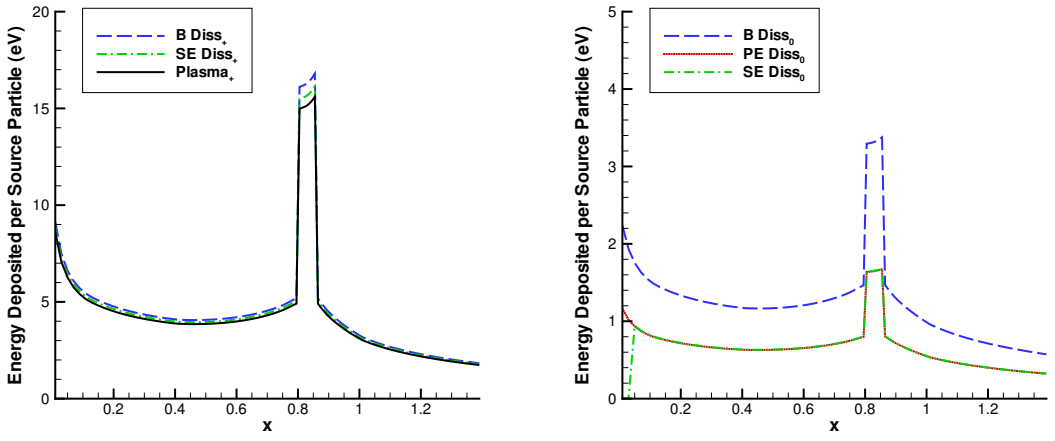

FIGURE 5.18: JET 2D neutraliser grid with collar - energy deposited per source particle for each source type at $P_b = 6MW$

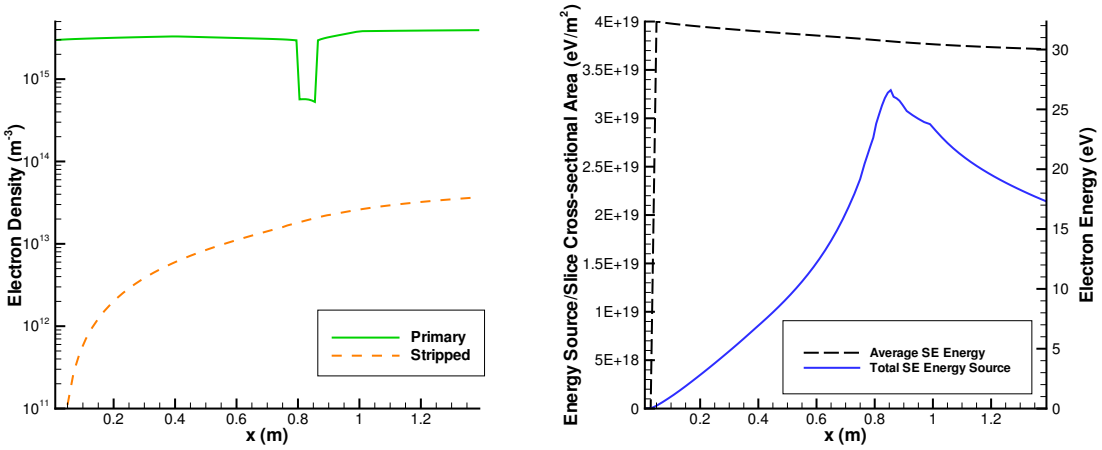

FIGURE 5.19: JET 2D neutraliser grid with collar - primary and stripped electron details for $P_b = 6MW$

Q_s	Q_n	P_b	T_w	α	α_{Hot}	P_{inj}	T_{inj}	T_{mid}
$(Pa.m^3s^{-1})$	$(Pa.m^3s^{-1})$	(MW)	(K)			(Pa)	(K)	(K)
12	13	2	300	0.37	0.37	0.664	637	300
		3						
		4				0.685	722	
		5						
		6				0.646	786	
		7				0.6	802	

TABLE 5.9: JET 2D neutraliser grid with collar - P_b scan model parameters

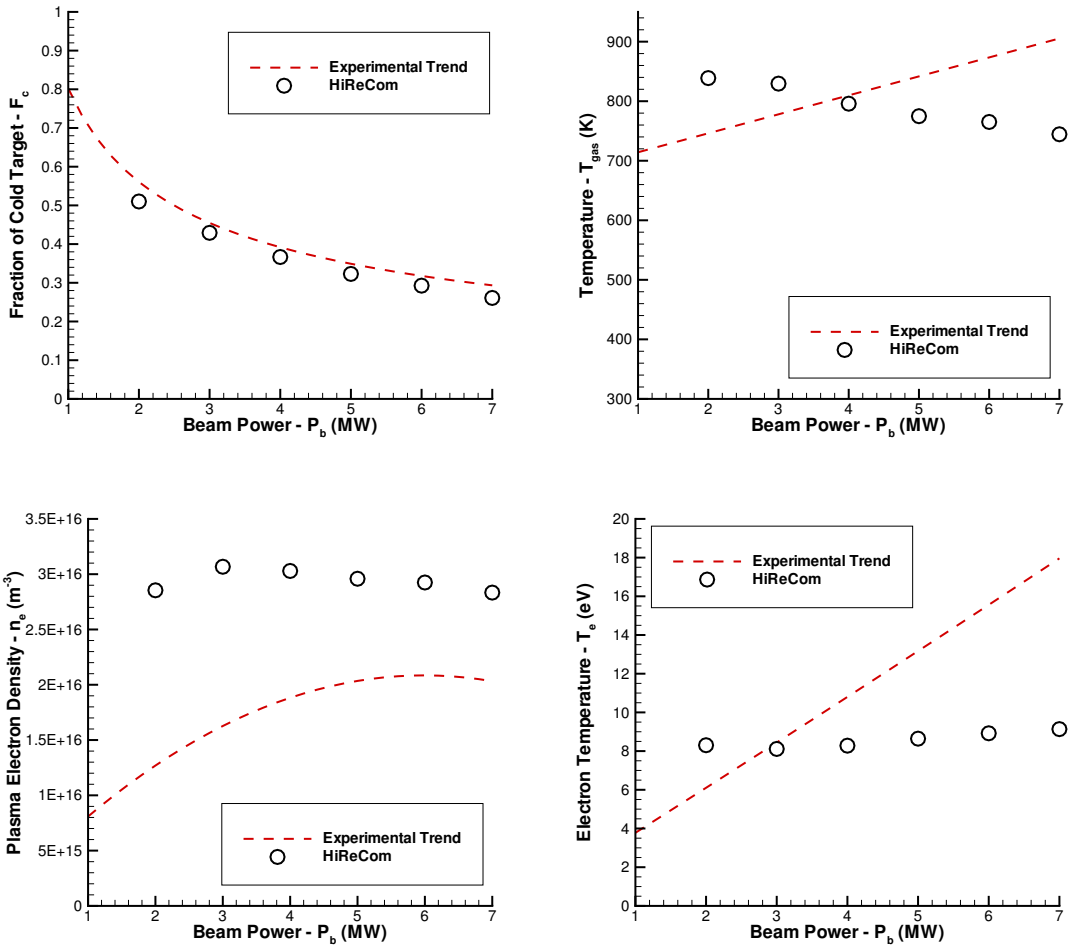

FIGURE 5.20: JET 2D neutraliser grid with collar - comparison of P_b scan to experiment

model in HiReCom, the conjectured temperature rise of the neutraliser walls[**?**] due to deposited power appears of little consequence to the neutraliser gas target. Therefore the omission of this temperature rise from the model results in minimal error, and suggests that previously proposed modification of the neutraliser to include actively cooled neutraliser walls appears of little benefit in improving gas target.

Q_n Scan - Navier-Stokes

Variation of neutraliser gas flow Q_n in the presence of beam was undertaken via model and boundary parameters as in Table 5.11. Introduced at the interspace between the neutraliser stages, increase of this flow reveals that an increasing gas target is offered. Indeed, with increasing Q_n this gas target represents an increasing fraction of the corresponding cold target in the absence of beam as can be seen in figure 5.25; a positive linear relationship between neutraliser gas target in

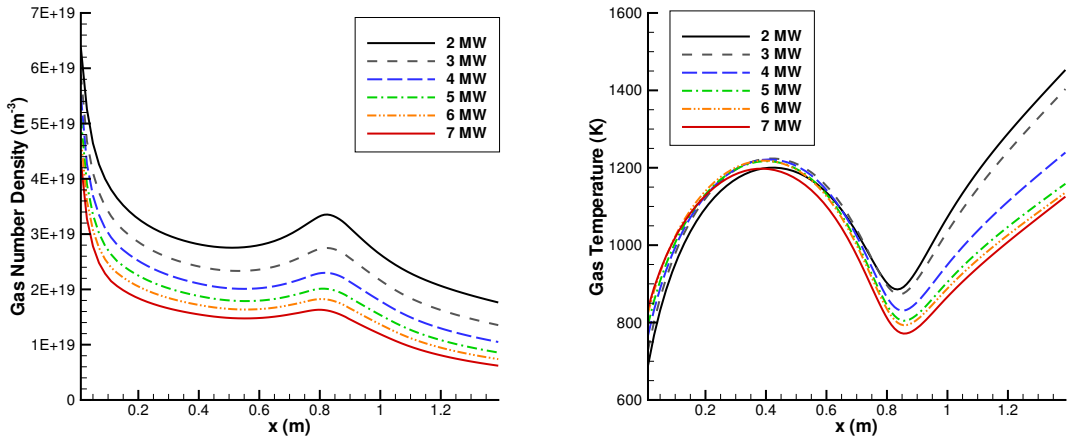

FIGURE 5.21: JET 2D neutraliser grid with collar - P_b scan centreline density and temperature profiles

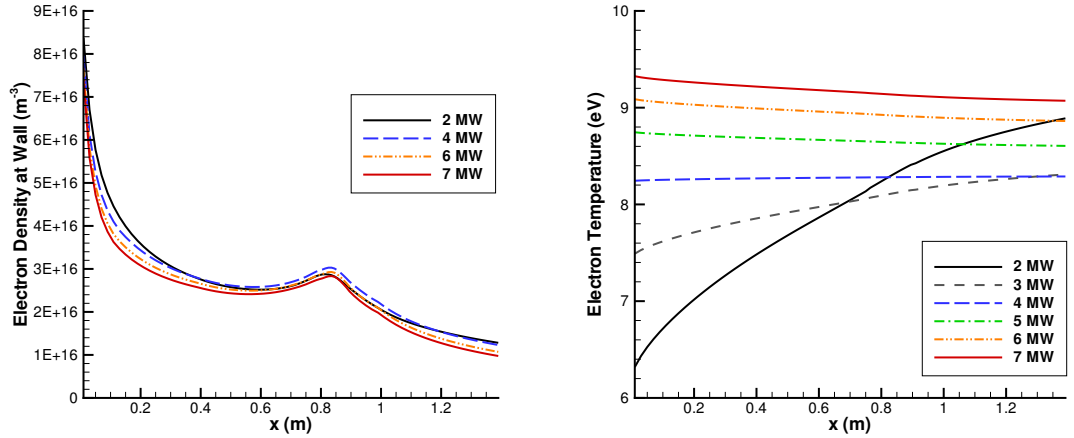

FIGURE 5.22: JET 2D neutraliser grid with collar - P_b scan electron density and temperature longitudinal profiles

Q_s $(Pa.m^3s^{-1})$	Q_n $(Pa.m^3s^{-1})$	P_b (MW)	T_w (K)	α	α_{Hot}	P_{inj} (Pa)	T_{inj} (K)	T_{mid} (K)
12	13	6	200	0.37	0.37	0.646	786	300
			250					
			300					
			400					
			500					

TABLE 5.10: JET 2D neutraliser grid with collar - T_w scan model parameters

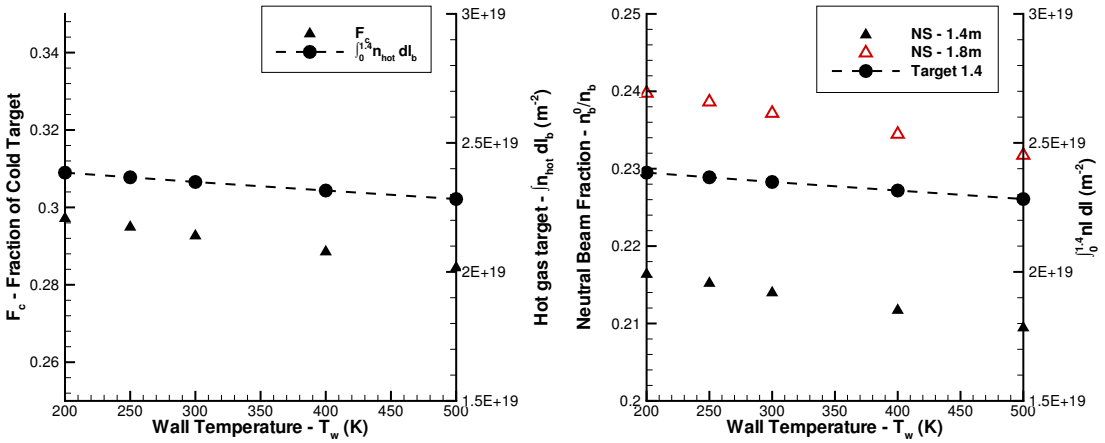

FIGURE 5.23: JET 2D neutraliser grid with collar - T_w scan cold gas target and neutral beam fractions

the presence and absence of beam is observed, with a similar positive linear relationship for the fraction of cold target. These relationships suggest that the beam neutral fraction can be pushed towards optimum by further increase of neutraliser gas flow beyond current operational flows. However, this would lead to complications elsewhere in the neutral beam system due to either the pumping limits of the cryoplant or in excessive high voltage breakdowns in the accelerator due to grid arcing events.

Examining the centreline gas temperature and density profiles in figure 5.24, one notes the elevation of both gas temperature and neutral density with increasing flow. This elevation of temperature agrees with the experimental observations of *Surrey*[**?**]; comparison of the experimental transverse gas temperature plateau measured at the diagnostic collar with that resultant in HiReCom shows a similar positive linear relationship for each, as shown in figure 5.26. This also appears to further validate the model in HiReCom and suggests for parameter scans independent of cross-section variation and error, i.e. at fixed beam power, that one obtains relationships in qualitative agreement with experimental data.

Note also that these results serve to support the previous explanation of T_e variation with P_b. From figure 5.27 one observes that with increasing gas flow, and thus increasing beam neutral fraction, the outlet electron temperature is reduced. This is because increased neutral beam fraction implies $T_e \rightarrow T_e^0$ and that $T_e^0 < T_e^+$ for $P_b = 6MW$, as can be seen in Table 5.8.

Q_s Scan - Navier-Stokes

Assesment of the effect of altering Q_s and therefore the surplus source gas flow into the neutraliser at its upstream boundary was carried out with model and boundary parameters as in Table 5.12. Overall, this variation demonstrated similar findings to the variation of neutraliser gas flow Q_n; with increasing gas flow, one retains an increasing fraction of the cold gas target in the presence of beam. However, the enhancement of cold fraction is much more pronounced for a given increase

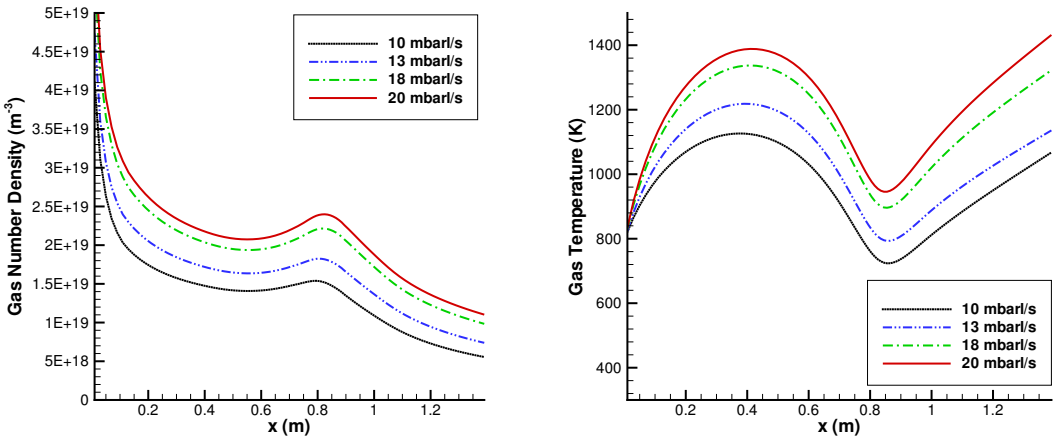

FIGURE 5.24: JET 2D neutraliser grid with collar - Q_n scan longitudinal gas density and temperature profiles

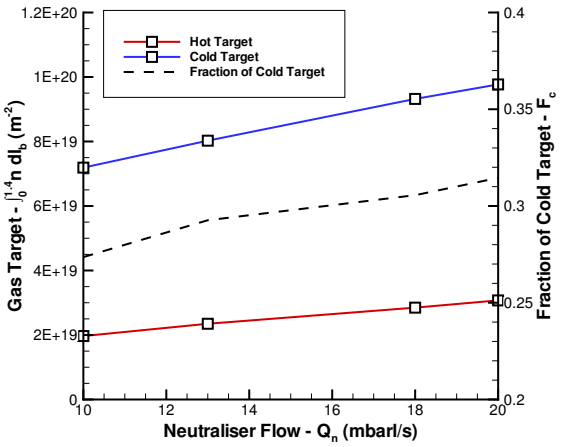

FIGURE 5.25: JET 2D neutraliser grid with collar - Q_n scan gas targets

Q_s	Q_n	P_b	T_w	α	α_{hot}	P_{inj}	T_{inj}	T_{mid}
$(Pa.m^3s^{-1})$	$(Pa.m^3s^{-1})$	(MW)	(K)			(Pa)	(K)	(K)
12	5	6	300	0.37	0.37	0.464	786	300
	10					0.560		
	13					0.646		
	18					0.753		
	20					0.794		

TABLE 5.11: JET 2D neutraliser grid with collar - Q_n scan model parameters

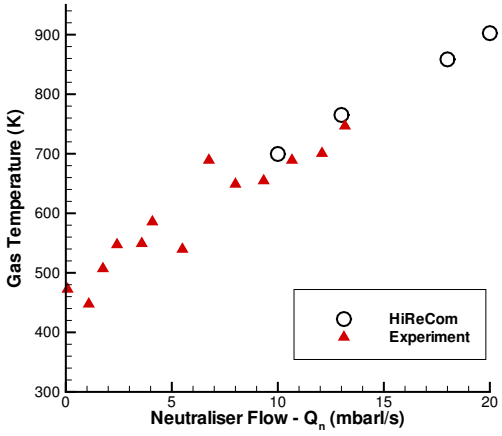

FIGURE 5.26: JET 2D neutraliser grid with collar - Q_n scan comparison of gas temperature at the diagnostic collar with experiment

Q_s	Q_n	P_b	T_w	α	α_{Hot}	P_{inj}	T_{inj}	T_{mid}
$(Pa.m^3s^{-1})$	$(Pa.m^3s^{-1})$	(MW)	(K)			(Pa)	(K)	(K)
9	18	6	300	0.37	0.37	0.581	786	300
10						0.629		
11						0.679		
12						0.753		
13						0.808		

TABLE 5.12: JET 2D neutraliser grid with collar - Q_s scan model parameters

in Q_s than for the same increase in Q_n, as can be seen in comparing figure 5.28 with figure 5.25.

This observation suggests that elevation of Q_s beyond typical operating levels would bring an improved beam neutral fraction. Unfortunately, as well as the pumping issues discussed in relation to any possible increase in neutraliser gas flow, an increase of source gas flow would produce an increase in pressure within the beam source. Such an increase in source pressure, as touched upon for the Q_n scan, reduces the quality and continuity of the extracted beam due to beam breakdowns that result from arcing events within the accelerator. Therefore the potential benefits of increased source gas flow must be balanced against other operational restrictions.

B_w Scan - Navier-Stokes

Variation of the beam width B_w was undertaken, with simulation and beam parameters as indicated in Table 5.12. For each of the simulations constant beam depth B_d, beam power P_b and total beam current I_b were assumed, with variation of beam width from $50mm$ to $180mm$ considered. Note that $B_w = 180mm$ represents the maximum beam width possible for the JET neutraliser design before excessive 'scraping' of the beam by the neutraliser walls is encountered. Also, given the variation of only beam width in isolation of the other beam parameters, reduction of beam

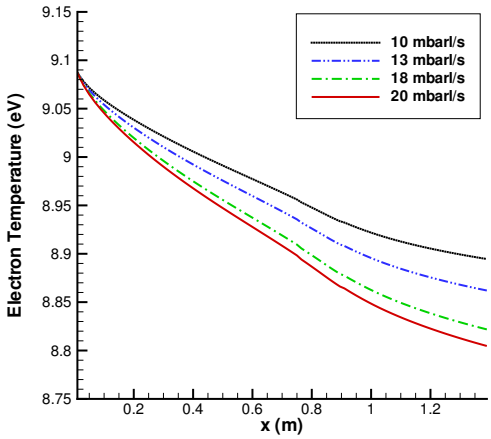

FIGURE 5.27: JET 2D neutraliser grid with collar - Q_n scan electron temperature profiles

P_b	I_b	B_d	B_w
(MW)	(A)	(mm)	(mm)
6	50	460	50
			100
			150
			180

Q_s $(Pa.m^3s^{-1})$	Q_n $(Pa.m^3s^{-1})$	P_b (MW)	T_w (K)	α	α_{Hot}	P_{inj} (Pa)	T_{inj} (K)	T_{mid} (K)
12	13	6	300	0.37	0.37	0.646	637	300

TABLE 5.13: JET 2D neutraliser grid with collar - B_w scan beam parameters

width also implied higher current density.

In short, the simulations revealed that the smaller the beam the more localised were the effects of gas depletion in the beam path, with gas temperature also increased. The more severe depletion obviously provides a smaller gas target to the beam and ultimately a smaller beam neutral fraction. For the 6MW beam examined, comparison of the smallest to larget beam width suggests neutral fraction of the beam may be reduced by ~ 2%. As shown in figure 5.29, the neutral beam fraction was found to reduce approximately linearly with increasing beam current density. For $B_w = 150mm$ and $B_w = 180mm$ the neutral beam fraction and gas target were found to be comparable.

5.2 2D ITER Neutraliser

As discussed previously, the neutraliser model in HiReCom can be applied to both positive and negative ion based systems. This has facilitated evaluation of the ITER neutraliser design, which in contrast to the JET system utilises an initially negative ion beam. When compared to the JET

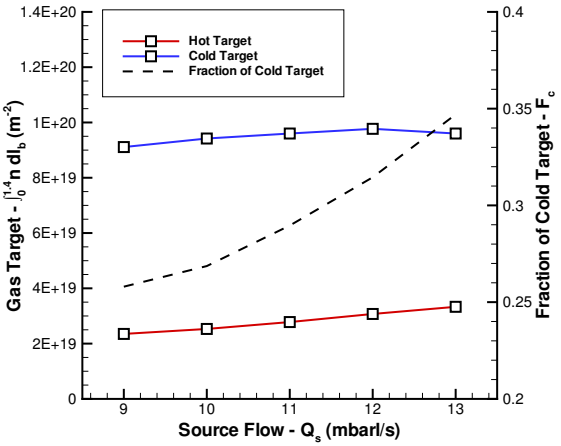

FIGURE 5.28: JET 2D neutraliser grid with collar - Q_s scan gas targets

neutraliser system as in Table 5.14, it is clear that the ITER neutraliser represents a significantly different design. Not a close-coupled system, the ITER neutraliser is detached from the beam source. It consists of four channels with partitioning of the beam resulting in reduced beam current through each. One notes also the difference in size between the JET and ITER neutraliser designs, the ITER neutraliser is significantly longer and thus requires a lower gas density to achieve a given gas target. Given its significantly larger total beam area, the ITER system also provides reduced beam current density when compared to the JET neutraliser.

To date, the only published neutraliser gas simulations of the ITER neutraliser are provided in the absence of beam. Presented in the ITER DDD[**?**], this work was undertaken with a 3D Monte Carlo code, with interest focused upon the presentation of longitudinal gas density profiles along the neutraliser. As discussed in Chapter 2, other ITER neutraliser studies have focussed upon modelling of the system's beam and plasma, with only the work of *Surrey*[**?**] considering the effects observed for the gas during beam operations. However, the model of *Surrey*[**?**] was unable to consider the effects of gas flow. Thus, there is a lack of detailed knowledge of the gas distribution in the presence of beam and the effects this may have upon the ITER neutraliser performance.

Therefore, within this Chapter, Navier-Stokes and Augmented Burnett simulations of the ITER neutraliser geometry are undertaken in the absence and presence of beam. Results in the absence of beam are compared against the gas profiles provided within the ITER DDD, then simulations in the presence of beam are examined to assess the magnitude of gas heating effects. Comparison with the JET system highlight not only the effects of differing geometry but also polarity. Understanding of the effects of total current, the transverse neutraliser dimension and the effects of neutraliser partitioning is enhanced by variation of the model parameters and computational geometry.

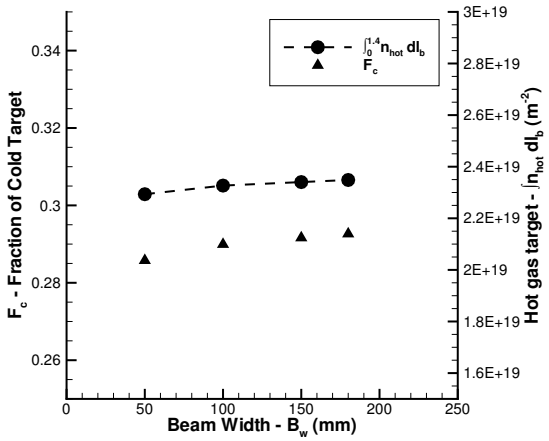

FIGURE 5.29: JET 2D neutraliser grid with collar - B_w scan gas targets

	ITER HNB	*JET*
BEAM PARAMETERS:		
Beam Ion	D^-	D^+
Beam Energy (kV)	1000	$60 - 130$
Current per Neutraliser Channel (A)	10	$17 - 55$
Dimensions in Neutraliser (m)	0.07×1.36	0.2×0.4
NEUTRALISER PARAMETERS:		
Number of Channels	4	1
Channel Dimensions (m)	$0.1 \times 1.7 \times 3.0$	$0.2 \times 0.4 \times 1.8$
Inlet Gas Flow Rate per Channel $\left(Pa.m^{-3}.s^{-1}\right)$	3.725	1.3

TABLE 5.14: Comparison of neutraliser and beam parameters for ITER and JET

5.2.1 Boundary Conditions and Flow Parameters

The ITER neutraliser is partitioned into a series of similar channels and can thus be most efficiently modelled via consideration of just one of these channels. Given that it is not closely coupled to the beam source, the computational geometry applicable to a single neutraliser channel differs significantly from that examined in 5.1. Not subject to the streaming of surplus gas from the beam source, which is instead pumped away from the interspace between the beam source and the neutraliser, the only source of gas for each neutraliser channel is found at its longitudinal midpoint. Gas is introduced to each of the neutraliser channels via a series of circular holes in a vertical column at the longitudinal midpoint of one of its walls; therefore unlike the JET neutraliser the gas introduction to each ITER neutraliser channel is asymmetric, and enters via much smaller inlets. Gas flow out of each ITER neutraliser channel occurs via both of its longitudinal ends, since the upstream boundary and downstream boundary both form outlets. Considering the neutraliser channel in two dimensions, one therefore obtains a computational geometry of type A in figure 5.30, with parameters as in Table 5.15.

From figure 5.30, one notes several simplifications that facilitate two-dimensional simulation via the model in HiReCom. For example, to improve the accuracy of the flow simulations and the speed of numerical convergence, the extreme ends of the neutralizer have been ignored due to the excessive rarefaction in these regions; molecular flow dominates near the neutralizer outlets severely surpressing the numerically stable timestep obtainable in these regions and inclusion would result in excessive run times. Thus, only the innermost $2m$ of the ITER neutralizer have been modeled. Also, given that the geometry is considered only in two-dimensions within this section, the several vertical gas inlets at the neutraliser midpoint have been simplified to a gap in one of the channel walls. Finally, the ITER neutraliser contains no diagnostic collar region, with the gas inlets instead very shallow extrusions cut into the wall of each channel and therefore not requiring modelling since source deposition in the extraneous regions beyond the main neutraliser wall is minimal. Instead, as per the work of section 4.5, gas has been assumed to be directly introduced to the computational geometry at its longitudinal midpoint without need for evaluation of local mixing within the gas inlet extrusions.

In all, four computational geometries have been considered in order to better understand the influence of design and model parameters upon gas heating. The effect of asymmetric and symmetric gas introduction is examined via comparison of simulations upon geometry A with geometry $S1$ of figure 5.30; the latter contains centreline symmetry and therefore presents two gas inlets symmetrically placed about the centreline. Computational geometries $S2$ and $S3$ of figure 5.30 were also considered; of differing widths, $S2$ is akin to partitioning of the ITER neutraliser width into only two channels, whilst $S3$ effectively considers the neutraliser to not be partitioned at all. Ultimately, comparison of results upon $S1$, $S2$ and $S3$ provide understanding of the effects of neutraliser width and neutraliser partitioning.

Given the lack of experimental data due to the developmental nature of the existing ITER design, the formulation of boundary conditions has relied upon the existing analytical work of the ITER DDD. The conditions in the presence and absence of beam are the same:

- Outlet: user-specified outlet pressure P_{out}, implemented via temperature specification at the outlet and the use of density extrapolated to the boundary. Note that P_{out} has been estimated from the ITER DDD gas number density profile.

- Inlet: user-specified inlet temperature T_{in} and throughput Q_n. The latter is implemented via specification of the transerse velocity v_{in} at the boundary with (5.4), with dependency upon inlet area A_{in}. This inlet flow is assumed normal to the boundary $u_{in} = 0$ and density is extrapolated to the boundary.

$$v_{in} = \frac{Q_{in}}{\rho_{in} R T_{in} A_{in}} \tag{5.4}$$

As in the preceeding sections of this Chapter, the gas considered within the neutraliser is deuterium. The viscosity interaction model has been used with parameters μ_0, T_{ref} and ω as given previously in Table 5.2, from which gas parameters R and γ have also been taken.

In order to ensure a suitably accurate grid spacing for each of the computational geometries, a convergence study has been undertaken upon geometry A and is summarised in Table 5.16.

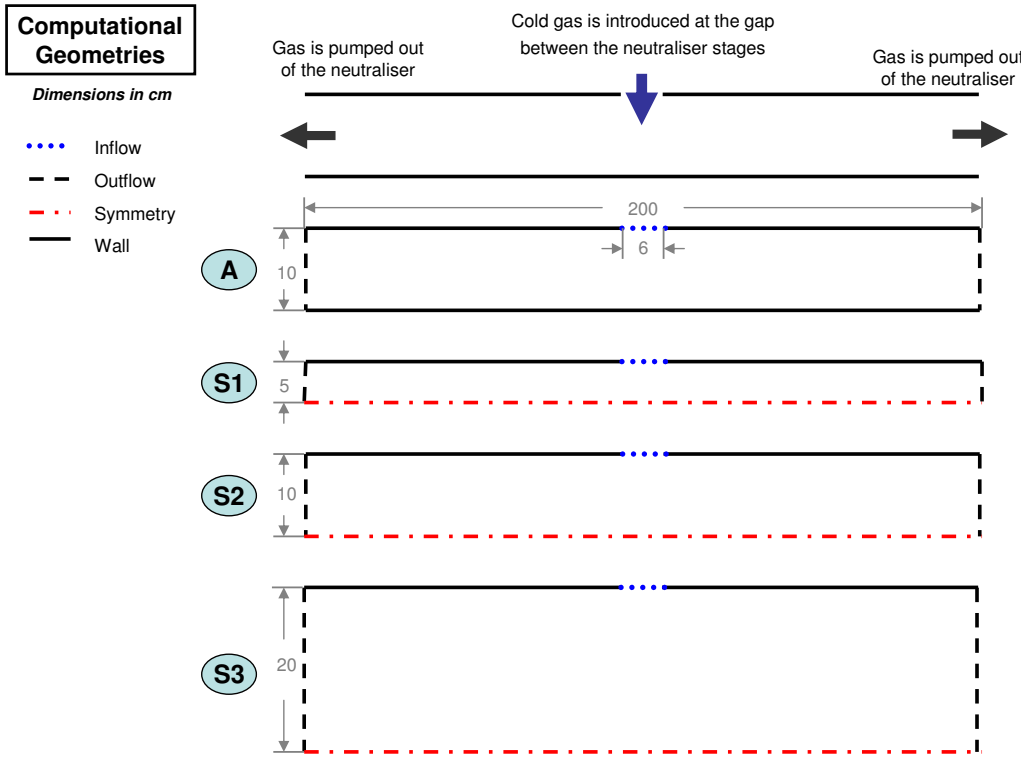

FIGURE 5.30: 2D ITER relevant computational geometries

Doubling of grid resolution from the baseline 100×5 grid has demonstrated that the evolved gas target for the simulated geometry increases by $\sim 5\%$ for the Navier Stokes Equations and $\sim 5\%$ for the Augmented Burnett Equations in the absence or presence of beam. Thus the remainder of results in this section are obtained with the baseline grid spacings for each geometry, i.e. $\triangle x = 0.02m$ and $\triangle y = 0.01m$.

5.2.2 In the Absence of Beam

The model developed in HiReCom shows good agreement with the ITER DDD in the absence of beam for both the Navier Stokes and Augmented Burnett equations. The centreline neutral density profile for both equation systems is presented in figure 5.31. Over the simulated length of the neutraliser the ITER DDD line density of $1.181 \times 10^{20} m^{-2}$ is underestimated by the Navier Stokes equations at $9.08 \times 10^{19} m^{-2}$, with better agreement demonstrated by the Augmented Burnett equations with $1.200 \times 10^{20} m^{-2}$; the two equation sets thus provide errors of 23% and 2%

Geometry	N_w (mm)	Q_{in} $(mbarl/s)$	A_{in} (mm^2)	σ_v	α	T_w (K)	T_{mid} (K)	P_{out} (Pa)
A	100	37.25	0.068	0.94	0.37	300	300	0.16
$S1$	100	37.25	0.136					
$S2$	200	74.5	0.136					
$S3$	400	149	0.136					

TABLE 5.15: Table of 2D ITER model parameters

	$\triangle x$ (m)	$\triangle y$ (m)	$\int_0^2 nl\, dl_b$ (m^{-2})
IN THE ABSENCE OF BEAM:			
Navier-Stokes	0.02	0.01	9.08×10^{19}
	0.01	0.005	9.13×10^{19}
Augmented Burnett	0.02	0.01	1.20×10^{20}
	0.01	0.005	1.25×10^{20}
IN THE PRESENCE OF BEAM:			
Navier-Stokes	0.02	0.01	7.42×10^{19}
	0.01	0.005	7.81×10^{19}
Augmented Burnett	0.02	0.01	1.05×10^{20}
	0.01	0.005	1.11×10^{20}

TABLE 5.16: Table of convergence study upon ITER relevant neutraliser geometry A

respectively. A differing centreline temperature profile is also produced; in line with the observations of section 4.5 the transition area for the flow near the gas inlet corresponds to local minima in the Augmented Burnett profiles whilst the Navier-Stokes equations provide local maxima, as shown in figure 5.31.

The developed gas flow within the ITER neutraliser is best demonstrated via velocity vector plots as provided in figure 5.32. Entering transversely at the longitudinal midpoint, the flow quickly becomes regular and streams towards the outlets provided by the upstream and downstream boundaries. One notes minor differences between the two equation sets for the flow developed in the region near the inlet. For example, the disordered region about the gas inlet before regular longitudinal flow is encountered, is slightly larger for the Navier-Stokes equations.

5.2.3 In the Presence of Beam

Utilising α_{hot} parameters tuned to the JET experimental data and beam parameters applicable to the ITER neutraliser design, as summarised in Table 5.18, the behaviour of the ITER neutraliser gas flow in the presence of beam was simulated. As for the JET system, the effects of gas heating serve to surpress the line density presented to the beam within the ITER neutraliser. As demonstrated in figure 5.33 via a longitudinal plot of the centreline gas number density, reduced line density is encountered for both the Navier Stokes and Augmented Burnett equations. For the Navier Stokes equations, this represents a loss of 18.4% against the simulated cold target, and 12.5% for the Augmented Burnett equations.

The marked differences in the flow simulation offered by the Navier-Stokes and Augmented

	Modelled 2m			Extrapolated to 3m		
	$\int_0^2 n_{hot} dl_b$ $\left(m^{-2}\right)$	$\frac{\int_0^2 n_{hot} dl}{\int_0^2 n_{cold} dl}$	$\frac{\int_0^2 n_{hot} dl}{\int_0^2 n_{DDD} l dl}$	$\frac{\bar{n_b^0}}{\bar{n_b}}$	$\widetilde{\int_0^3 n_{hot} dl}$ $\left(m^{-2}\right)$	$\frac{\widetilde{\int_0^3 n_{hot} dl}}{\widetilde{\int_0^3 n_{cold} dl}}$
DDD	1.181×10^{20}	-	0.572	1.423×10^{20}	-	0.578
Augmented Burnett	1.20×10^{20}	1.016	0.573	1.473×10^{20}	1.035	0.578
Navier-Stokes	9.08×10^{19}	0.757	0.537	1.271×10^{20}	0.863	0.576

TABLE 5.17: 2D ITER neutraliser - gas targets in the absence of beam

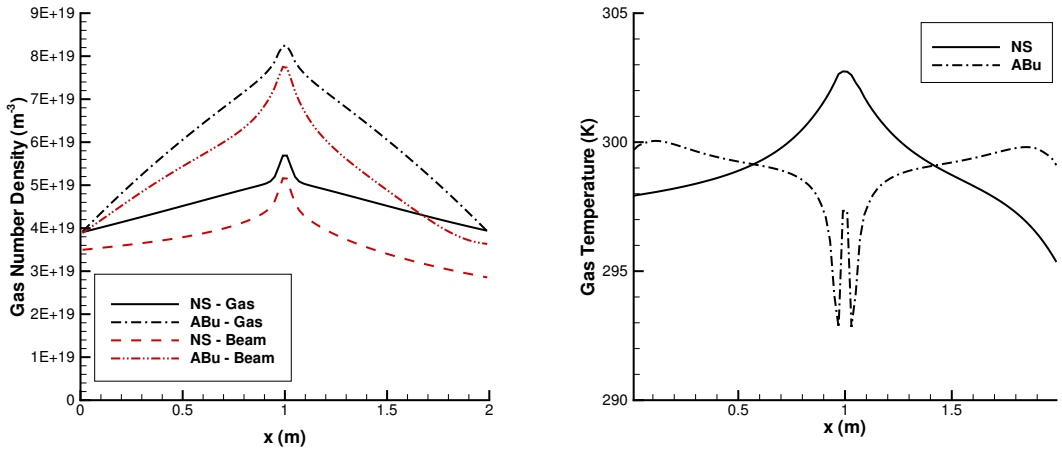

FIGURE 5.31: 2D ITER neutraliser - centreline gas density and temperature in the absence of beam

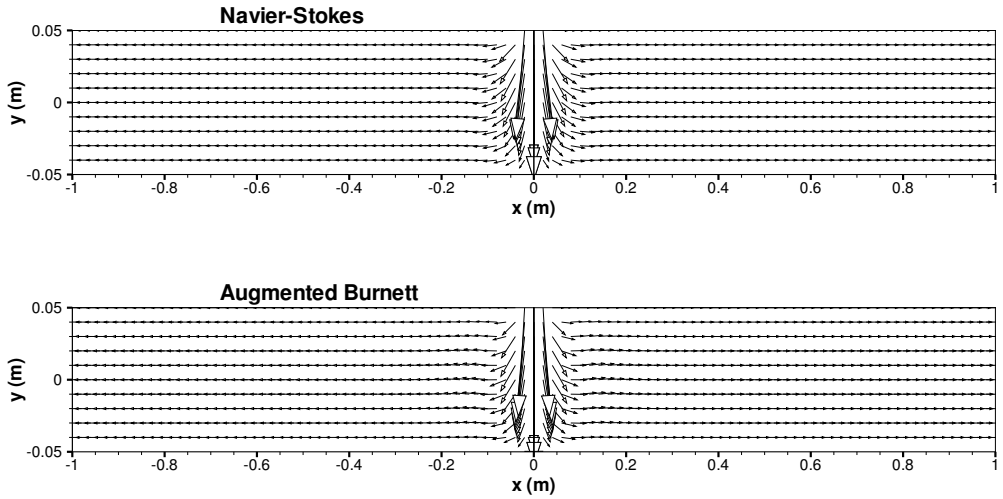

FIGURE 5.32: 2D ITER neutraliser - velocity vector plot in the absence of beam

Geometry	E_b (kV)	I_b (A)	B_h (m)	B_w (m)	α_{hot}
A	1000	10	1.36	0.1	0.37

TABLE 5.18: 2D ITER neutraliser - model parameters in the presence of beam

	ITER HNB $1MV\ D^-$	*JET* $120kV\ D^0$
Energy Deposition:	$(eVatom^{-1}m^{-2})$	
D^-	1.80×10^{10}	1.22×10^{10}
D^0	1.80×10^{10}	1.22×10^{10}
D^+	2.73×10^{10}	8.42×10^{9}
Cross-Section:	(m^2)	
σ_+	6.57×10^{-21}	2.06×10^{-20}
σ_0	4.21×10^{-21}	1.35×10^{-20}
σ_{10}	1.92×10^{-24}	1.19×10^{-20}
$\sigma_{0\bar{1}}$	2.24×10^{-26}	4.43×10^{-22}

TABLE 5.19: Plasma production cross-sections and energy deposition rates for the JET and ITER beams

Burnett Equations is also apparent in the temperature field exemplified by the centreline temperature plots of figure 5.34. Both equation systems provide a local temperature minima in the vicinity of the gas inlet where cold gas is introduced to the system. This minima is not found in the work by *Surrey*[**?**] since no local gas effects could be modelled, though the magnitude of the temperature rise is found to be similar. Note also, the marked reduction of the gas temperature near the outlet for the Augmented Burnett equations in line with observations previously presented in this thesis, i.e. when outlet pressure is implemented via temperature restriction, the Augmented Burnett equations experience a rapid fall-off in temperature at elevated Knudsen. Note that such a temperature reduction was found for the JET simulations in the absence of beam but not in the presence of beam since flow was fully extrapolated at the outlet boundary for the latter.

Overall, figures 5.33 and 5.34 point to the reduced target loss of the ITER neutraliser design when compared to that seen in the JET neutraliser system in section 5.1. One notes that the fraction of cold target in the presence of beam is significantly larger for ITER ($> 80\%$) than that seen at high powers in JET ($\sim 30\%$). This difference is no doubt linked to the much smaller gas temperature rise found in the ITER system and is further understood via closer examination of the simulations and consideration of each of the source mechanisms for the gas.

Figure 5.36 demonstrates the much larger electron temperature found in the ITER system than within JET neutraliser. Electron temperature is calculated within the model as the ratio of energy deposited in the gas to energy incident upon the neutraliser wall, and the much larger electron temperature for the ITER system results from the differing energy deposition rates and plasma production cross-sections experienced at high beam energies; the energy deposited per beam projectile is reduced by a factor of 2 from that for the JET neutraliser whilst the plasma production rate is reduced by more than a factor of 5 (as in Table 5.19), and therefore the ratio that determines electron temperature is elevated by a significant factor against that seen for JET.

One also notes from figure 5.36 that the plasma density is more than an order of magnitude lower than that presented for the JET neutraliser in section 5.1. The lower plasma density found in the ITER neutraliser is due predominantly to the much lower beam density for the ITER system since neutral gas densities in the presence of beam are actually fairly similar to that encountered

at JET. This reduced beam density is the result of the the significantly reduced current density of the ITER beam, and the partitioning of its total beam current between the neutraliser channels.

Ultimately, though the energy of each plasma ion incident upon the wall is much greater (since the elevated electron temperature corresponds to an elevated sheath potential) the energy that it deposits in the background gas upon neutralisation and reflection from the ITER walls is comparable with that for JET. Demonstrated by figure 5.35, this is due to the much reduced neutraliser width providing a reduced time of flight in which the energetic neutrals are able to deposit energy before accommodation. However, overall one finds a reduced magnitude for the source due to plasma ion reflection in the ITER neutraliser when compared to the JET system; this is the resultant of the much reduced plasma density.

By contrast, the ITER neutraliser is subject to an enhanced gas energy source due to inelastic energy transfer from the stripped electrons to the background gas. Indeed, this stripped electron energy term is, in fact, the largest energy source to the background gas for much of the simulated length of geometry A, surpassing the term due to plasma ion reflection, as can be seen in figure 5.39. This is due largely to the elevated stripped electron densities and energies that result in the system; the stripped electron density, presented in figure 5.38, increases over the length of the neutraliser to reach $\sim 70\%$ of the beam density at the downstream outlet, whilst the characteristic stripped electron energy is of $\sim 300eV$ and therefore enhances the energy transfer rate. This enhanced stripped electron density results from the polarity of the ion beam and the increased stripped electron production cross section associated with negative ions. Indeed it is the inclusion of the stripped electrons, and the magnitude of their contribution to heating in the ITER neutraliser that accounts for the significant difference between this and the author's previously published work[**?**].

Note that primary electron production is negligible at 1MeV beam energies. Thus primary electron production and their associated source mechanisms have been ignored within simulation of the ITER system. Beam dissociation and stripped electron dissociation, though fully evaluated within the model for the ITER neutraliser, are both rendered near negligible contributors as energy sources by the dominance of inelastic collision of the stripped electrons and plasma ion reflection.

Finally, one must acknowledge that the model in HiReCom considers the beam to consist entirely of negative ions at the upstream boundary of the geometry. This is a slightly flawed simulation of the system in this case as the computational geometry ignores $0.5m$ of the neutraliser that lies upstream. Similarly, the beam at the simulated outlet is not that which eventually leaves the neutraliser given the existence of an additional $0.5m$ of neutraliser geometry downstream of the computational boundary. Thus, to gain a more valid estimate of the neutral beam fraction resulting from the neutraliser, extrapolation of the density at the upstream and downstream boundaries has been utilised to quantify the additional gas target offered by the sections of the neutraliser not included in the computational geometry. These additional targets are then used with the outlet beam composition of the computational model, as given in figure 5.40, and to estimate the actual neutral beam fraction resulting from the entire ITER neutraliser.

Table 5.17 indicates the gas target provided in the presence of beam for both the simulated geometry $\int_0^2 n_{hot} dl_b$ and extrapolated to the full $3m$ of the ITER neutraliser design $\int_0^3 n_{hot}\, dl_b$.

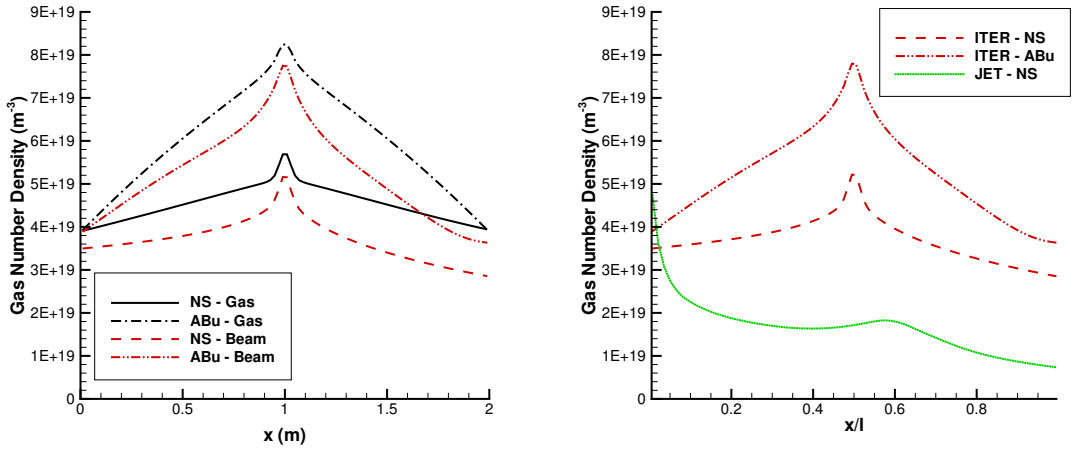

FIGURE 5.33: 2D ITER neutraliser - centreline gas density profiles in the absence and presence of beam, with comparison to 2D JET neutraliser with collar

Within Table 5.17, these gas targets are also compared to that presented in the absence of beam $\int n_{cold} dl_b$ and within the ITER DDD $\int n_{DDD} dl_b$, demonstrating good agreement. Also presented is an estimate of the beam neutral fraction that would result from the gas targets in the presence of beam $\left(\frac{\tilde{n_b^0}}{n_b}, \frac{\widetilde{n_b^0}}{n_b}\right)$. These figures serve to demonstrate that though the ITER neutraliser is subject to gas heating that may remove a significant fraction of the gas target, i.e. $7-19\%$ based upon the model in HiReCom, the neutral fraction exiting the neutraliser is reduced by$<3\%$ if one considers the targets extrapolated to $3m$. This is due to the very flat dependence of the species fractions upon gas target for the $1MV$ negative ion beam of the ITER system, as demonstrated previously by figure 2.6. This is further re-inforced by the observation that if the hot gas target represented only 50% of the optimum, only a 10% loss of the maximum neutral beam fraction is encountered.

Comment on S1 Vs A - Navier-Stokes

Comparisons of results achieved upon symmetric geometry $S1$ and asymmetric geometry A, reveal a minimal difference in the resultant gas targets either in the absence or presence of beam. Though the established flow pattern is significantly different, as outlined by figure 5.41, the target is enhanced by only 1% if symmetric gas inlets are used. This difference results from a locally reduced density and elevated temperature in the beam path near the inlets of geometry A. Characterised by figure 5.42, one can thus conclude that symmetric gas introduction is preferable. Asymmetric gas introduction introduces unwanted local effects but does not produce an excessive increase in the macroscopic effects of gas heating.

	Modelled 2m				Extrapolated to 3m			
	$\int_0^2 n_{hot} dl_b$ (m^{-2})	$\frac{\int_0^2 n_{hot} dl}{\int_0^2 n_{cold} dl}$	$\frac{\int_0^2 n_{hot} dl}{\int_0^2 n_{DDD} ldl}$	$\frac{n_b^0}{n_b}$	$\int_0^{\widetilde{3}} n_{hot} dl$ (m^{-2})	$\frac{\int_0^{\widetilde{3}} n_{hot} dl}{\int_0^{\widetilde{3}} n_{cold} dl}$	$\frac{\int_0^{\widetilde{3}} n_{hot} dl}{\int_0^{\widetilde{3}} n_{DDD} ldl}$	$\frac{\widetilde{n_b^0}}{n_b}$
Augmented Burnett	1.05×10^{20}	0.875	0.891	0.559	1.37×10^{20}	0.932	0.965	0.578
Navier-Stokes	7.42×10^{19}	0.816	0.628	0.498	1.04×10^{20}	0.819	0.732	0.558

TABLE 5.20: 2D ITER neutrlaiser - gas targets in the presence of beam -

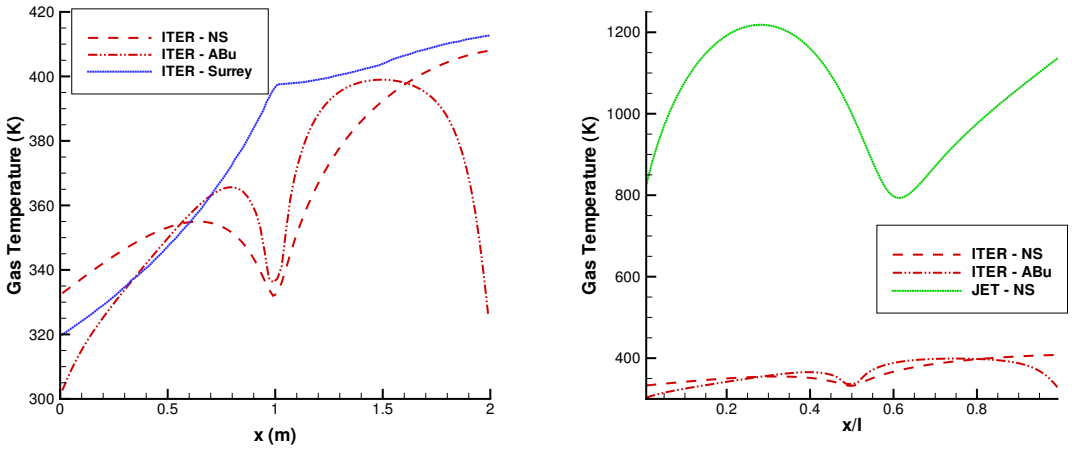

FIGURE 5.34: 2D ITER neutraliser - centreline gas temperature in the presence of beam, with comparison to 2D JET neutraliser with collar

Geometry	N_w (mm)	B_w (mm)	B_d (m)	E_b (kV)	I_b (A)
$S1$	100	70	1.36	1000	10
					20
					30
					40

TABLE 5.21: 2D Symmetric neutraliser - I_b scan model parameters

I_b Scan - Navier-Stokes

The effect of varying current density via varying beam dimensions was explored in the previous Chapter and demonstrated that increasing current density in this fashion induces an enhanced loss of gas target. By contrast, the work presented in this subsection sought to vary current density solely via variation of the beam current I_b, with maintenance of beam dimensions across the differing simulations; undertaken upon the original 100mm wide symmetric neutraliser channel $S1$, this work assumed constant beam dimensions and varied I_b as per the model parameters provided in Table 5.21.

As can be seen from figure 5.43, plots of the centreline gas temperature and gas number density demonstrate similar shapes with varying beam current. However, one notes that with increasing current there is an increased gas temperatue and a reduced gas target presented to the beam. The reduction of gas target with beam current is best demonstrated by figure 5.44, which also indicates the fraction of cold target presented to the beam with increasing beam current.

One can explain the observed relationships as the effect of increased beam current, which in conjunction with maintainence of the beam dimensions, provides an increase in beam density. This elevated beam density in turn serves to enhance plasma and stripped electron production within the neutraliser, as demonstrated by figure 5.45. Since, as noted in section 5.2.3 these form

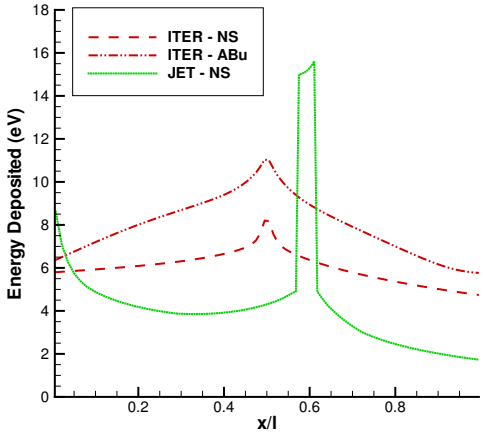

FIGURE 5.35: Energy deposited by energetic neutralised plasma ions for ITER and JET simulations in HiReCom

	Modelled 2m			Extrapolated to 3m		
I_b	$\int_0^2 n_{hot} dl_b$	$\frac{\int_0^2 n_{hot} dl}{\int_0^2 n_{cold} dl}$	$\frac{\tilde{n_b^0}}{n_b}$	$\int_0^{\widetilde{3}} n_{hot} dl$	$\frac{\int_0^{\widetilde{3}} n_{hot} dl}{\int_0^{\widetilde{3}} n_{cold} dl}$	$\frac{\widetilde{n_b^0}}{n_b}$
(A)	(m^{-2})			(m^{-2})		
$10A$	7.50×10^{19}	0.824	0.478	1.05×10^{20}	0.824	0.559
$20A$	7.10×10^{19}	0.780	0.454	9.93×10^{19}	0.780	0.552
$30A$	6.84×10^{19}	0.752	0.435	9.56×10^{19}	0.752	0.546
$40A$	6.65×10^{19}	0.731	0.420	9.29×10^{19}	0.731	0.541

TABLE 5.22: 2D Symmetric neutraliser - I_b scan gas targets and estimated beam neutral fractions

the two dominant heating mechanisms of the ITER neutraliser design, this results in increased energy provision to the background gas and thus enhanced gas heating. The non-linear loss of gas target hints at eventual saturation of this gas heating for extremely large currents. This would most likely be due to the saturation of these heating mechanisms due to increasing loss of gas target.

Obviously the loss of gas target with increasing beam current provides reduced estimates of neutral beam fraction at the neutraliser outlet as detailed in Table 5.22, along with a numerical summary of the gas targets for the simulated geometry and extrapolations to the full $3m$ of the ITER neutraliser channel. Overall, one concludes that with fixed beam dimensions, minimisation of beam current reduces the effect of gas heating and provides the maximal gas target to the beam.

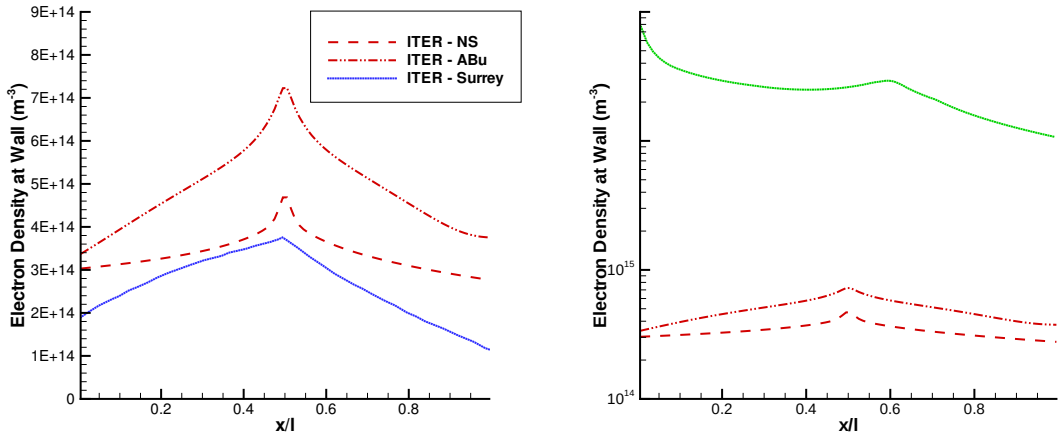

FIGURE 5.36: 2D ITER neutraliser - plasma density, with comparison to 2D JET neutraliser with collar

Geometry	N_w (mm)	B_w (mm)	B_d (m)	E_b (kV)	I_b (A)
$S1$	100	70	1.36	1000	10
$S2$	200				
$S3$	400				

TABLE 5.23: 2D Symmetric neutraliser - N_w scan model parameters

N_wScan - Navier-Stokes

An investigation into the effect of modifying the neutraliser dimensions was sought via variation of the neutraliser width N_w. This work was undertaken in two parts for each of the differing computational geometries outlined in Table 5.24 and figure 5.46 - i.e. firstly in the absence and then in the presence of a 10A 70mm beam. Throughput at the gas inlets was considered constant for each of the geometries, with the same outlet pressure specified for each, as summarised in Table 5.23.

In the absence of beam, it was noted that increasing the neutraliser width resulted in a significantly reduced gas density for the same inlet throughput; this is due to the increased conductance of the system, which encourages a smaller pressure drop from inlet to outlet. The resultant loss of gas target is indicated in figure 5.47 and Table 5.24. Thus one concludes that to provide equivalent gas targets, one requires significantly elevated gas throughput for wider neutralisers.

In the presence of beam, neutraliser width demonstrates elevated gas temperatures and the reduction of gas target as shown in figure 5.47. Examining in further detail, one reasons that the elevation in gas temperature is driven by an increasing total energy source term to the background gas, shown in figure 5.49. In particular, the energy source term due to plasma ion reflection increases with N_w, which is interesting given the apparent reduction of wall plasma density figure

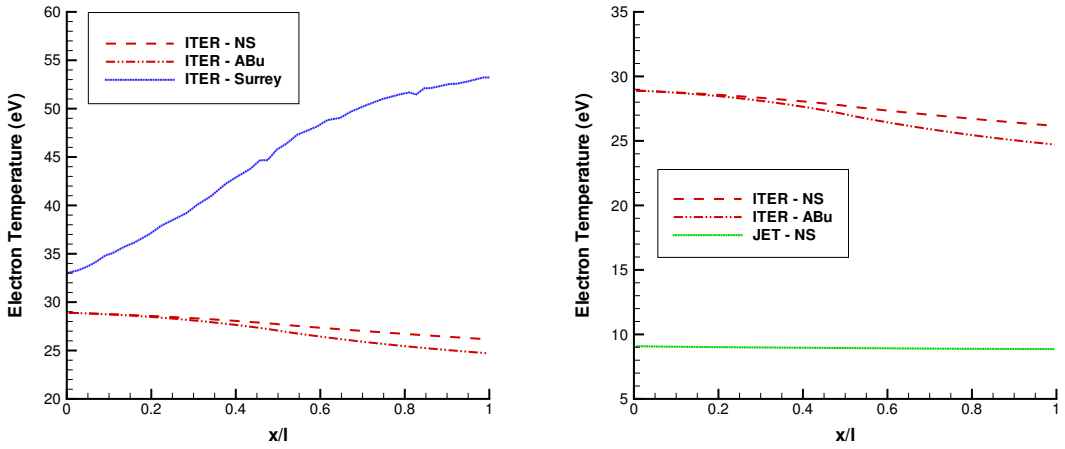

FIGURE 5.37: 2D ITER neutraliser - electron temperature, with comparison to 2D JET neutraliser with collar

	Modelled 2m			Extrapolated to 3m		
N_w	$\int_0^2 n_{hot} dl_b$	$\frac{\int_0^2 n_{hot} dl}{\int_0^2 n_{cold} dl}$	$\frac{\bar{n_b^0}}{n_b}$	$\int_0^3 \widetilde{n_{hot}} dl$	$\frac{\int_0^3 \widetilde{n_{hot}} dl}{\int_0^3 \widetilde{n_{cold}} dl}$	$\frac{\widetilde{n_b^0}}{n_b}$
(mm)	(m^{-2})					
100	7.50×10^{19}	0.824	0.478	1.05×10^{20}	0.825	0.559
200	7.16×10^{19}	0.824	0.468	1.01×10^{20}	0.816	0.553
400	6.65×10^{19}	0.813	0.451	9.52×10^{19}	0.797	0.546

TABLE 5.24: 2D Symmetric neutraliser - N_w scan gas targets and estimated beam neutral fractions

5.48. In fact, the increase of the plasma energy source term is due to the significant gain in the energy deposition fraction with N_w as demonstrated in figure 5.50; the increased N_w allows longer path through the background gas for the fast neutrals before reflection and accomodation at the walls, thus enhancing the overall fraction of energy that is delivered to the background gas in the computational slice.

The Effect of Neutraliser Channels - Navier-Stokes

The partitioning of the ITER neutraliser was assessed for its effect on gas heating via contemplating the effect upon the gas if instead of equipartition of the beam amongst four channels,the

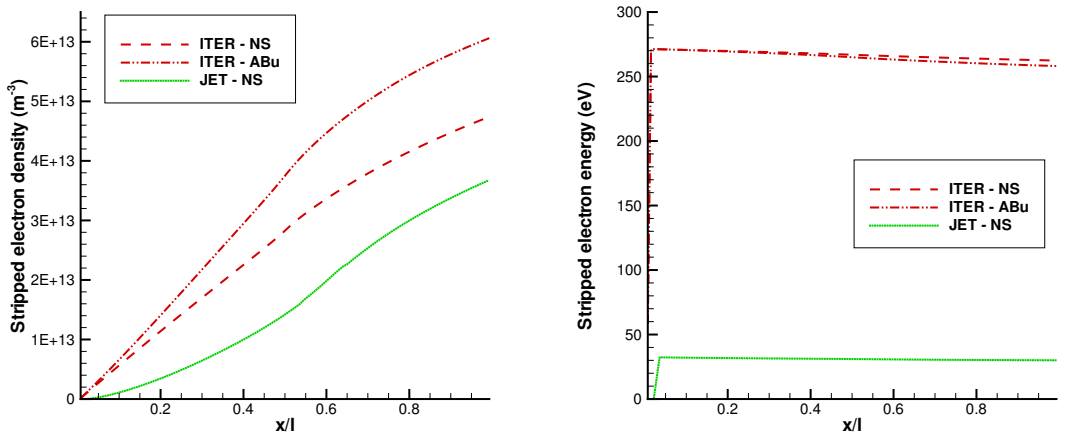

FIGURE 5.38: 2D ITER neutraliser - stripped electron density and temperature, with comparison to 2D JET neutraliser with collar

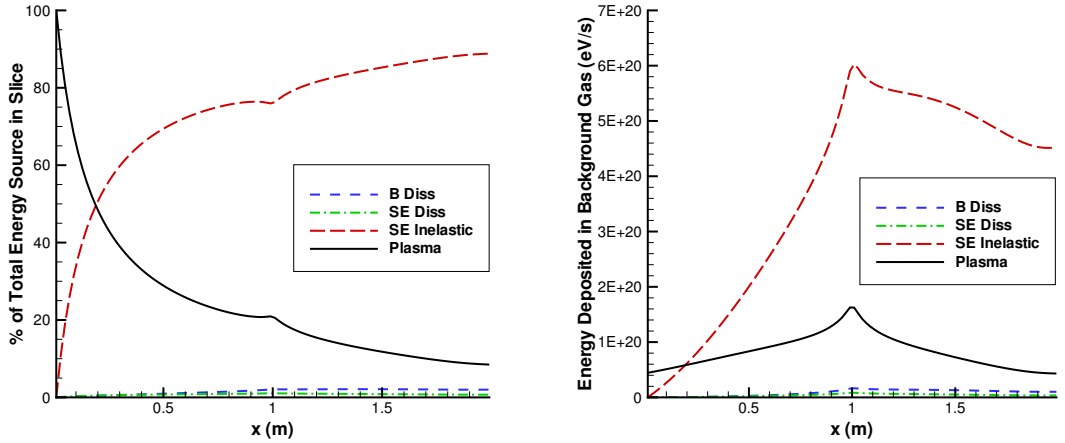

FIGURE 5.39: 2D ITER neutraliser - fractional and actual contribution of each source type to total Energy source

Geometry	N_w (mm)	B_w (mm)	E_b (kV)	I_b (A)	α_{hot}
$S1$	100	70	1000	10	0.37
$S2$	200	140		20	
$S3$	400	280		40	

TABLE 5.25: 2D Symmetric neutraliser - partitioning study parameters

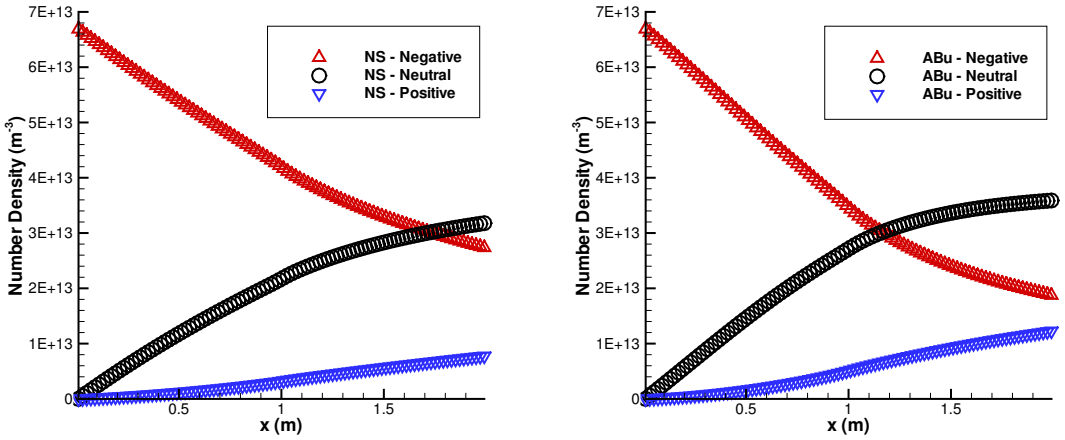

FIGURE 5.40: 2D ITER neutraliser - beam composition along the neutraliser

beam were partitioned into two or perhaps not partitioned at all. These three scenarios, summarised via Table 5.23, serve to vary both beam current and the neutraliser width.

The results correspond to section 5.2.3 in the effect of increasing current against the simulations of section 5.2.3. With fewer channels, one finds a larger neutraliser width and larger fraction of the total current and therefore a significantly reduced gas target. Indeed one notes that if no partitions are used and the neutraliser instead forms a single channel, the gas target loss $F_c = 0.617$ is akin to that experienced in the JET neutraliser. One concludes therefore from Table 5.26 that minimsing both the current and neutraliser width appears a successful strategy in minimising the loss of gas target due to heating.

5.3 3D JET Neutraliser

As discussed in the introductory chapters of this thesis, an historical attempt to alleviate the effects of gas heating in the JET neutraliser sought to use a midplane septum plate. This modification effectively bisected the first stage neutraliser, and was guided by the works of *Pamela*[**? ?**]. Testing of the modified neutralisers proved inconclusive. The coupled solver has thus been utilised to understand the changes in neutral gas dynamics and to further assess the impact of this modification strategy. Requiring the extension of the coupled solver to consider three-dimensional geometries, simulations both with and without a septum have been undertaken. Good agreement with experimental data reinforces the resulting conclusions. Simulations have only been undertaken with the Navier-Stokes equations due to the prohibitive expense of the Augmented Burnett simulations in the presence of beam, as highlighted in the previous section.

				Modelled 2m			Extrapolated to 3m		
Number Channels	N_w	B_w	I_b	$\int_0^2 n_{hot} dl_b$	$\frac{\int_0^2 n_{hot} dl}{\int_0^2 n_{cold} dl}$	$\frac{\bar{n_b^0}}{n_b}$	$\widetilde{\int_0^3 n_{hot} dl}$	$\frac{\widetilde{\int_0^3 n_{hot} dl}}{\widetilde{\int_0^3 n_{cold} dl}}$	$\frac{\widetilde{n_b^0}}{n_b}$
	(mm)	(mm)	(A)	(m^{-2})					
4	100	70	10	1.05×10^{20}	0.824	0.478	1.05×10^{20}	0.825	0.559
2	200	140	20	9.10×10^{19}	0.747	0.446	9.10×10^{19}	0.735	0.538
1	400	280	40	5.26×10^{19}	0.643	0.396	7.37×10^{19}	0.617	0.497

TABLE 5.26: 2D Symmetric neutraliser - partitioning study gas targets and estimated beam neutral fractions

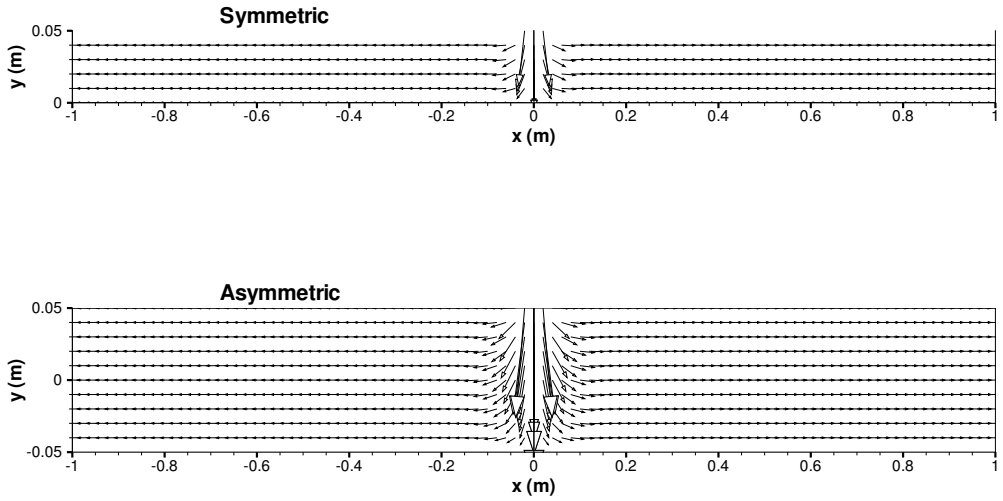

FIGURE 5.41: 2D Symmetric & Asymmetric neutralisers - $S1$ vs A velocity vector comparison

5.3.1 Boundary Conditions and Flow Parameters

This three-dimensional work has sought to simplify the geometry of 5.1, removing the diagnostic collar region and returning to a computational geometry similar to that of 4.5. Inclusion of the upstream gas inlet has been necessary, since standard operating conditions including gas flow from the source have been considered. Centreline symmetry has been utilised to reduce overall computational cost. The computational geometry without septum posesses two symmetry boundaries along $y = 0$ and $z = 0$. By contrast the geometry with septum posesses symmetry only about $y = 0$ in the first stage neutraliser but both $y = 0$ and $z = 0$ for the second stage neutraliser; the septum is included via an additional wall surface for $z = 0$ within the first stage neutraliser. Therefore the two computational geometries can be summarised by the XY and XZ sections of figure 5.51.

Note that Deissler second order boundary conditions have once again been applied for each of the wall surfaces. Deuterium flows with a viscosity interaction model have been considered, with parameters as previously presented in 5.1.1. The boundary condition specification in the presence and absence of beam are also similar to those specified in 5.1.1, differing only in the specification of velocity at the interspace inlet since the considered three-dimensional geometries do not include the diagnostic collar. The boundary condition specification applicable to the three-dimensional simulations are therefore summarised as follows:

Absence of beam

- Outlet: user-specified outlet pressure P_{out}, implemented via temperature specification at the outlet and the use of density extrapolated to the boundary.

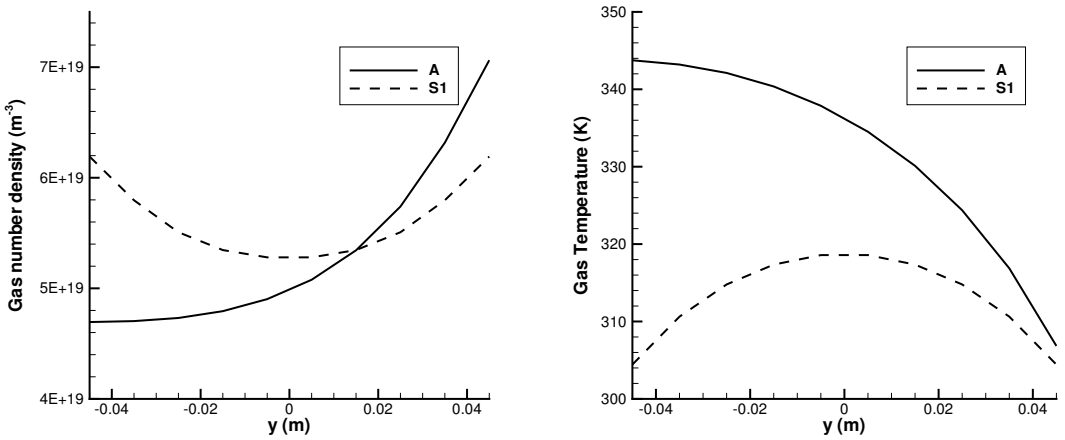

FIGURE 5.42: 2D Symmetric & Asymmetric neutralisers - $S1$ vs A transverse density and temperature comparisons

- Upstream Inlet: user-specified inlet temperature T_{inj} and throughput Q_s. The latter is implemented via the velocity normal to the boundary, with transverse velocities set to zero and density extrapolated to the boundary.

- Interspace Inlet: utilises the same method as the upstream inlet, with user-specified inlet temperature T_{mid} and throughput Q_n.

Presence of beam

- Outlet: all variables extrapolated to the boundary

- Upstream Inlet: user-specified inlet temperature T_{inj}, pressure p_{inj} and throughput $Q_s^{'}$. The latter is implemented via the velocity normal to the boundary, whilst transverse velocities are set to zero. Density is resultant from the equation of state and the specified inlet temperature and pressure. $Q_s^{'}$ follows from Q_s via (5.2), and represents the surplus source gas that does not form part of the beam, and instead streams into the source un-ionised.

- Interspace Inlet: is similar to that in the absence of beam but differs in specication of the gas temperature at the boundary. In order to account for the temperature plateau and the gradual reduction of temperature noted in the diagnostic collar for the simulations of section 5.1 (see figure 5.13), the temperature at the boundary is not restricted to user-specified inlet temperature T_{mid}. Instead an accommodated temperature $T_{mid}^{'}$ is utilised, specified via (5.5) from the temperature extrapolated to the boundary T_{mid}^{extrap}. This allows for the heating of gas in the collar region before entry into the neutraliser.

$$T_{mid}^{'} = (T_{mid}^{extrap} - T_{mid})\alpha + T_{mid} \tag{5.5}$$

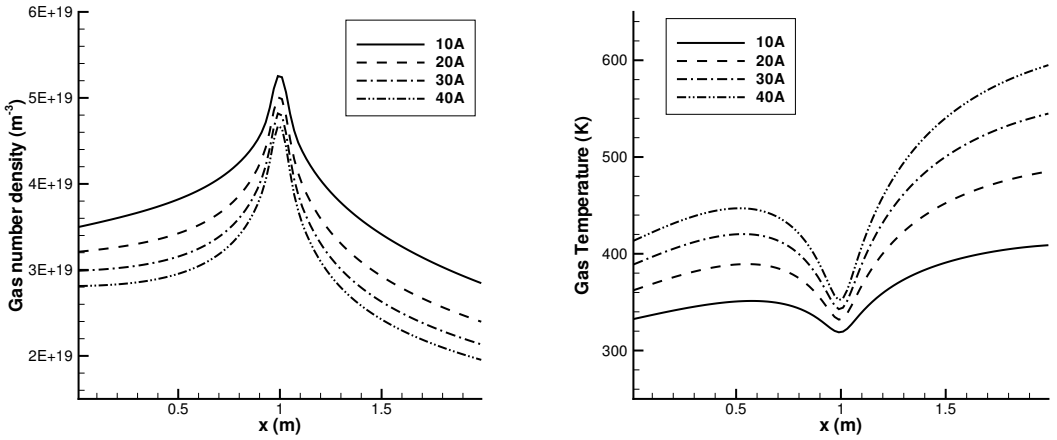

FIGURE 5.43: 2D Symmetric neutraliser - I_b scan centreline gas density and temperature profiles

Note that values for outlet pressure condition in the absence of beam, and the upstream pressure and temperature conditions in the presence of beam, are provided in Appendix **??** from the experimental work undertaken in support of this thesis. Also be aware that the results in this section are steady-state solutions and utilise the same convergence criteria as stated in section 5.1.1, i.e. convergence is deemed to have occurred when inlet-to-outlet pressure drop reaches 10^{-5} of that encountered at the initial timestep.

5.3.2 In the Absence of Beam

The two dimensional simulations of section 5.1 correspond approximately to the three-dimensional geometry without septum. For the same inlet throughputs $Q_s = 12mbarls^{-1}$ and $Q_n = 13mbars^{-1}$, comparisons of simulations in the absence of beam offer good agreement, as demonstrated by the centreline pressure and density profiles of figure 5.52. Indeed, the gas targets over the simulated $1.4m$ differ by only $\sim 10\%$; the two-dimensional simulation initially presented in section 5.1 provides $8.03 \times 10^{19} m^{-2}$ and the three-dimensional simulation higher at $9.03 \times 10^{19} m^{-2}$.

Considering the three-dimensional geometries with and without septum, reveals that the presence of the septum significantly reduces the conductance of the first stage neutraliser. This alters the flow properties in this region as exemplified by examination of the longitudinal velocity profile that develops along the $y = 0$ centreline at $x = 0.4m$, as shown in figure 5.53. Ultimately, the presence of the septum serves to significantly raise the gas target in the absence of beam as shown in figure 5.52. For the flow conditions considered, an increase of $\sim 20\%$ is found in the simulated gas target, with the neutraliser with septum providing $10.56 \times 10^{20} m^{-2}$.

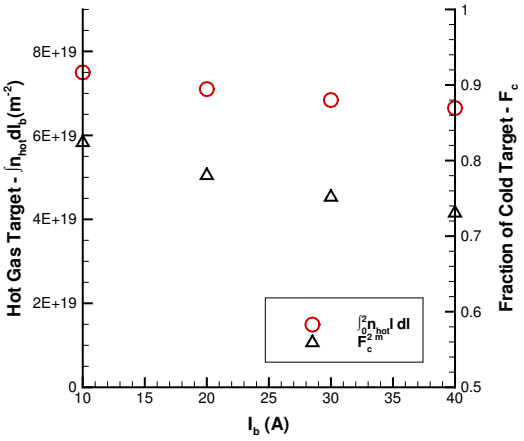

FIGURE 5.44: 2D Symmetric neutraliser - I_b scan hot gas target and fraction of cold target

5.3.3 In the Presence of Beam

Three-dimensional simulations in the presence of beam were undertaken with model parameters as specified in Table 5.27. One notes once more the correspondence of the three-dimensional simulations without septum with the work of section 5.1 in two-dimensions. This is exemplified by the average gas density in the path of a beam of $P_b = 6MW$, as shown in figure 5.54. The resultant gas targets also correspond very well at $2.34 \times 10^{19} m^{-2}$ and $2.35 \times 10^{19} m^{-2}$ for the two and three dimensional simulations respectively. This is particularly interesting given the gas temperature throughout much of the neutraliser appears markedly higher for the three-dimensional system, as shown for system centreline $y = z = 0$ in figure 5.54. This does not appear due to the newly implemented boundary condition at the interspace inlet since if one compares the transverse temperature profile at $x = 0.03m$ and $z = 0m$, one notes the excellent temperature match at the neutraliser extremity as shown in figure 5.13. Indeed, the elevated centreline temperature occurs inspite of a reduced plasma density, outlined in figure 5.56, and a reduced total source term delivered to each transverse slice of the neutraliser. This may be due instead to the deposition profile aross the transverse slices in the interspace region; in the two dimensional work of section 5.1, almost all of the energy and mass source in the interspace region was deposited beyond the neutraliser in the vicinity of the diagnostic collar whereas for the three dimensional geometry all is deposited within the confines of the neutraliser. This discrepancy is highlighted by comparison of D_{source} at $x = 0.03m$ as in figure 5.57. Note that within this figure the profile plotted for the three-dimensional geometry is $\int D_{source}(y,z)\, dz$ and thus dependent solely upon y. Examination of a three-dimensional geometry with collar to corroborate the effect of the deposition profile has not been possible with the present numerical framework; the surpression of the stable timestep limit due to additional grid refinement and increased grid size has proved prohibitive in this endeavour.

Encouragingly, over the range of beam powers considered, the three-dimensional results both

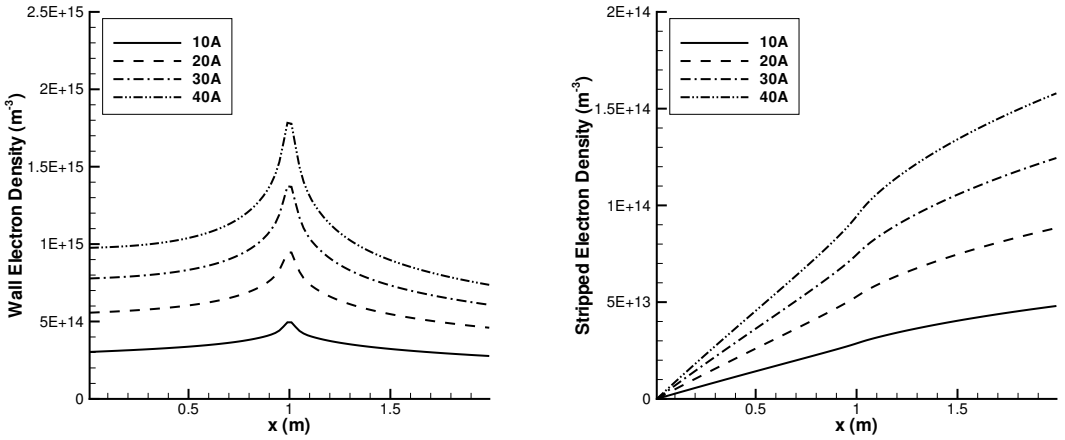

FIGURE 5.45: 2D Symmetric neutraliser - I_b scan wall plasma and stripped electron density

without and with septum show better agreement with experiment than that seen for the two-dimensional work. Compared visually in figure 5.58, consider each of the properties measured at the diagnostic collar in turn:

Electron Density The three-dimensional simulations show excellent agreement with experiment both quantatively and qualitatively. Offering significantly lower number density than the estimates in two dimensions, the model in three dimensions suggests the septum results in slightly elevated electron densities at high power. This is a trend apparent in the experimental data.

Electron Temperature Though the model fails to capture the apparently different electron temperature relationships with beam power for the neutraliser with and without septum, the model predictions fall clearly between the two behaviours suggesting that they are not sufficiently far from experiment to be unrealistic. One should also note the previous comments questioning the characteristic electron temperature extracted from the experimental electron energy distribution function; the solver highlights several distinct contributing energies, which implies the experimental characteristic energy may not truly reflect the sheath electron temperature.

Fraction of Cold Target One observes good agreement of the model results with the experiment data, especially with increasing beam power. Though not as quantitatively accurate as the agreement seen for the two dimensional system, with an error $\sim 20\%$ c.f. $\sim 10\%$ at the highest powers, the three-dimensional still appears to effectively capture the loss of gas target in the presence of beam. Interestingly, due to the much higher cold target, the model actually suggests a lower fraction of cold target for the neutraliser with septum. This is difficult to corroborate with experiment since the empirical law utilised to calculate the approximate cold target has not been fully validated for this neutraliser design. Even so, this observation still implies that the hot target with septum is higher than that seen for the neutraliser without septum.

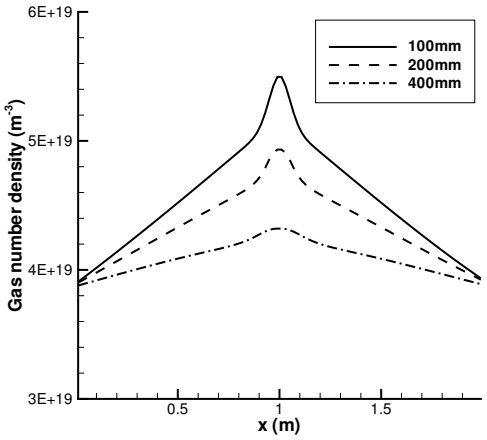

FIGURE 5.46: 2D Symmetric neutraliser - N_w scan centreline gas density profiles in the absence of beam

Gas Temperature The simulated gas temperature agrees very well with the experimental data obtained for the neutraliser without septum. With regards to the available data with septum, significant differences exist between the observed temperatures made upon the JET Neutral Beam Test Bed[**?**] and those inferred via analysis from neutralisation measurements[**?**]. The JET Neutral Beam Test Bed data proposed a much reduced gas temperature for the neutraliser with septum, thus motivating predictions of a significant improvement in the neutral beam fraction obtained. Observation of this improved neutral fraction could not be straightforwardly provided from the Test Bed's diagnostic capabilities. As discussed previously, the neutral beam fraction was instead deduced from neutrlaisation measurements utilising the JET tokamak. This latter series of experimentation revealed only a minimal increase in neutral beam fraction for the neutraliser with septum, with analytical work thus suggesting that the reduction in gas temperature was in fact much less than that found for the JET Neutral Beam Test Bed[**?**]. The temperatures with septum provided by the developed solver present only a slight reduction on those without septum and therefore appear to concur more closely with the neutralisation measurements of *Surrey et al.*[**?**]. Given the excellent agreement of the solver in three dimensions with the other experimental parameters it may therefore be prudent to re-examine the data from both septum experiments in order to assess why they differ so extremely. This lies outside of the scope of this research as they both rely upon detailed analysis and is perhaps instead a topic for further work.

Comparsion of the three-dimensional computational geometries suggests that the septum offers an increase in gas target in the presence of beam. This increase becomes substantial with increasing beam power. Exemplified by considering the simulations with and without septum for $P_b = 6MW$, the septum serves to elevate gas density in the first stage neutraliser whilst reducing gas temperature as shown in figure 5.59. One notes that beyond the first stage neutraliser, once the end of the septum is reached, the flow quickly returns to a very similar distribution for

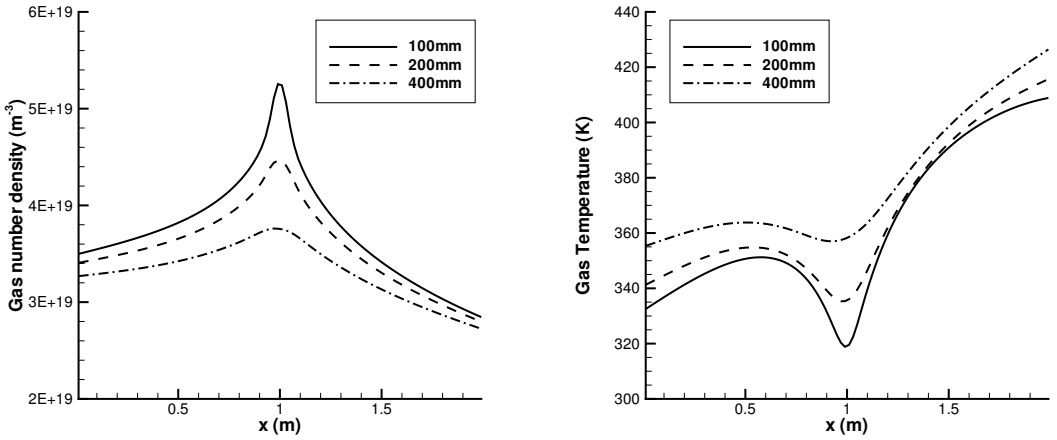

FIGURE 5.47: 2D Symmetric neutraliser - N_w scan centreline gas density and temperature profiles in the presence of beam

both neutraliser designs.

Though gas density is higher in the first stage neutraliser region, the total energy source to the gas is markedly lower with the septum, as in figure 5.60. Each of the constituent source terms, with the exception of inelastic collision of stripped electrons with the background gas, is lower for the neutraliser with septum. This is even though the gas density is larger and thus inspite of the larger number of energetic source particles produced. Instead, the presence of the septum results in each of the energetic source particles created in the first stage neutraliser depositing a smaller amount of their energy in the background gas; the septum serves to reduce their typical path length across the transverse slice, offering a reduced number of collisions with the background gas on each pass and thus a greater amount of energy is lost in accommodation at the wall. An effect noted within 5.2 when examining the effects of varying neutraliser width and of neutraliser paritioning, this reduced energy deposition is exemplified for the three-dimensional JET neutraliser simulations in figure 5.61; the energy deposited by each plasma ion reflection source particle before equilibrium with the background gas molecules is presented. The clear correspondence with the averaged neutraliser half width can be seen via comparison with figure 5.62.

Therefore one concludes that the introduction of the septum, from the perspective of the developed solver, does locally alleviate the effects of gas heating and can improve the observed neutralisation efficiency. With regards to its effectiveness, in the presence of a beam with $P_b = 6MW$ the septum increases the gas target over the simulated neutraliser length by $\sim 10\%$ from $2.34 \times 10^{19} m^{-2}$ to $2.58 \times 10^{19} m^{-2}$. This provides an estimated increase in the neutral fraction of the beam from 21.3% to 22.9% over the simulated length, with a similar improvement predicted fif one considers the extraneous portion of the neutraliser not simulated by the model. One must of course note that the model does not include the additional ionic species within the initial beam and any differences in source pressure due to the presence or absence of the septum affects; any

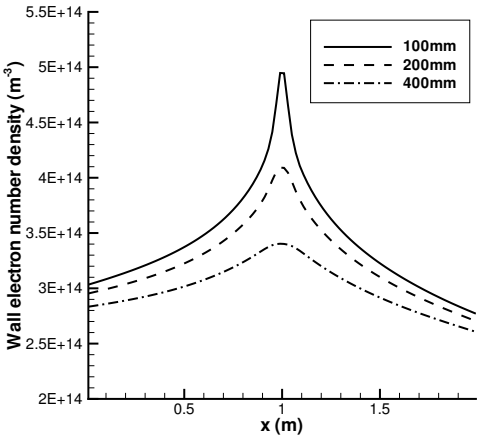

FIGURE 5.48: 2D Symmetric neutraliser - N_w scan wall plasma electron density profiles in the presence of beam

elevation in source pressure due to the presence of the septum would serve to increase the fraction of the beam encompassed by these additional ionic species and therefore may have a minor effect on the predicted neutral fraction.

In comparison to other possible strategies to address the effects of gas heating within the JET neutraliser, if one trusts the quantitative predictions of improvement in both the two and three dimensional works, the septum is perhaps not preferable. By comparison, the introduction of additional gas to the system appears to offer a more substantial boost in target. However, Q_n cannot be increased ad infinitum due to increased high voltage breakdowns reducing the quality and continuity of the extracted beam. The septum certainly combats the underlying effects of neutraliser gas heating and ensures a larger gas target in the presence of beam, therefore perhaps it offers a means of additional gas heating mitigation once the increase of Q_n induces excessive side-effects.

5.4 JET Neutraliser Optimisation

Additional work has been undertaken to modify the JET neutraliser geometry to mitigate the effects of neutraliser gas heating. Initiated by the observations of this research, this EFDA Fusion Technology Task[**?**] seeks to implement an additional gas inlet in the second stage neutraliser in order to increase the gas target available to the beam. This research endeavour will seek to experimentally measure the effect upon neutral beam fraction via use upon the JET Neutral Beam Test Bed.

This work is supported by the work presented in Appendix **??**, which examines two computational geometries with additional gas inlets; simulations in the absence of beam demonstrate a $\sim$ 7% improvement in gas target for the modified neutraliser design. Evaluation in the presence of beam has not been possible with the present solver due to the neccesity for additional code

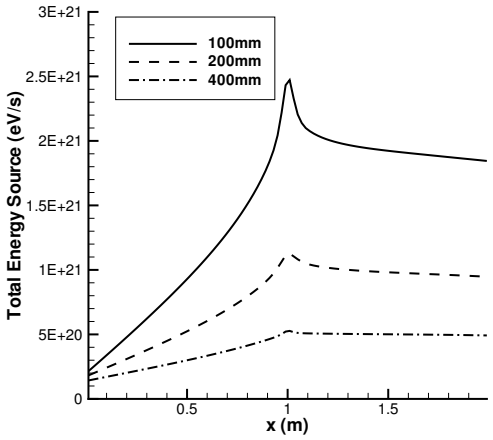

FIGURE 5.49: 2D Symmetric neutraliser - N_w scan total energy source to each computational slice

development, representing a potential area for future work.

5.5 Summary

Comparison of the developed solver with experimental data reveals good agreement for both two and three dimensional simulations of the JET neutraliser in the presence of beam. The solver therefore appears to successfully capture the effect of gas heating and associated loss of gas target. The plasma has been identified as the key energy source for the JET system, whilst predictions for the ITER system suggest that inelastic collision of the stripped electrons with the background gas is the most significant source mechanism.

Parameter scans have identified various design factors and operational parameters that influence the magnitude of target loss. Variation of current density, beam power, inlet gas flow and neutraliser width have all been shown to influence the magnitude of gas heating. By contrast, variation of the wall temperature has been shown to have little impact. Symmetric gas introduction has been found to be slightly advantageous over asymmetric introduction.

The partitioning of a neutraliser into a series of channels, through each of which only a fraction of beam current passes, has been shown to alleviate target loss. This approach is used in the ITER neutraliser design and as such this system should not suffer significant neutraliser efficiency loss due to gas heating.

The use of a septum plate, as previously attempted at JET, was found by the developed solver to provide some improvement over a blank neutraliser, though to only locally restrict gas heating. Interestingly, the results of the developed solver have served to highlight discrepancies in the previously collected experimental data. The solver predicts that the septum induces only minor reductions in the effects of gas heating, appearing to thus agree with experimental neutralisation measurements. However, the results of the solver fail to match neutraliser gas temperature data

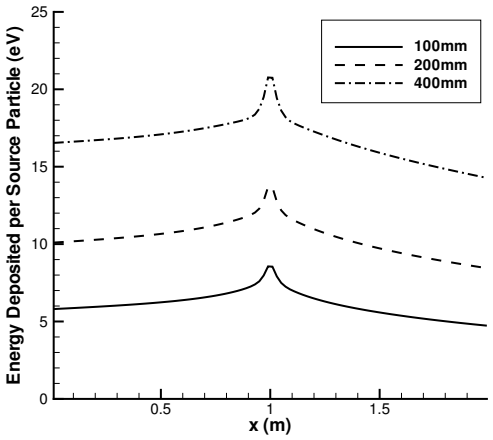

FIGURE 5.50: 2D Symmetric neutraliser - N_w scan energy deposition by plasma source particles

collected in other experimentation, which served to predict a much more substantial influence upon gas heating. This presents an area for possible future attention.

Q_s $\left(Pa.m^3s^{-1}\right)$	Q_n $\left(Pa.m^3s^{-1}\right)$	P_b (MW)	T_w (K)	α	α_{Hot}	P_{inj} (Pa)	T_{inj} (K)	T_{mid} (K)
WITHOUT SEPTUM:								
12	13	2	300	0.37	0.37	0.664	637	300
3			680		0.675			
4			722		0.685			
5			754		0.666			
6			786		0.646			
WITH SEPTUM:								
12	13	2	300	0.37	0.37			300
2	12	13	613	300	0.617			
3			660		0.618			
4			707		0.619			
5			726		0.630			
6			745		0.642			

TABLE 5.27: 3D JET neutraliser with and without septum - model parameters

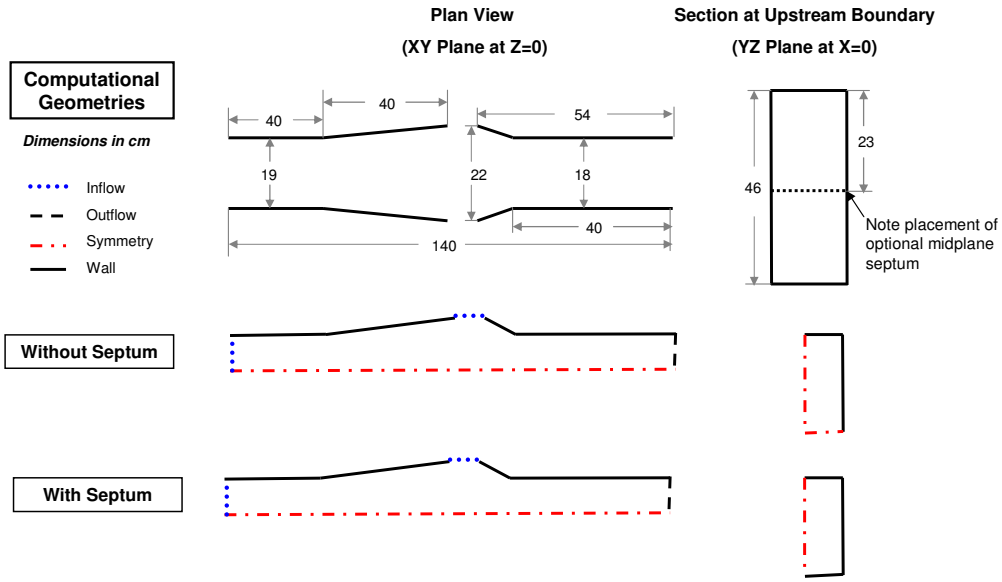

FIGURE 5.51: 3D JET neutraliser computational geometries

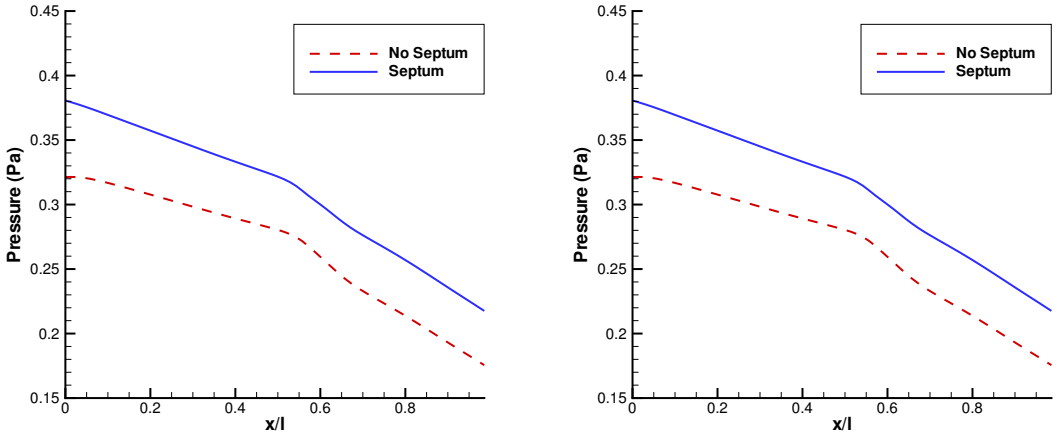

FIGURE 5.52: 3D JET neutraliser with and without septum - $y = z = 0$ centreline pressure and target

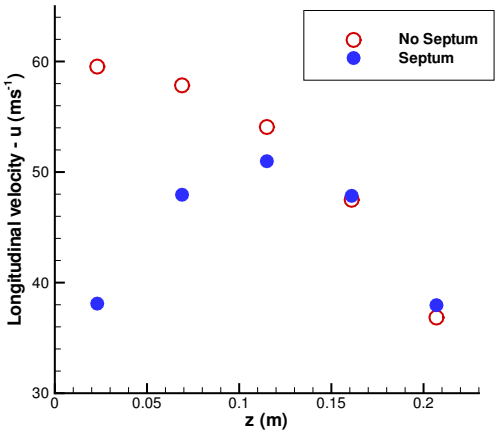

FIGURE 5.53: 3D JET neutraliser with and without septum - longitudinal velocity at $y = 0$, $x = 0.4m$

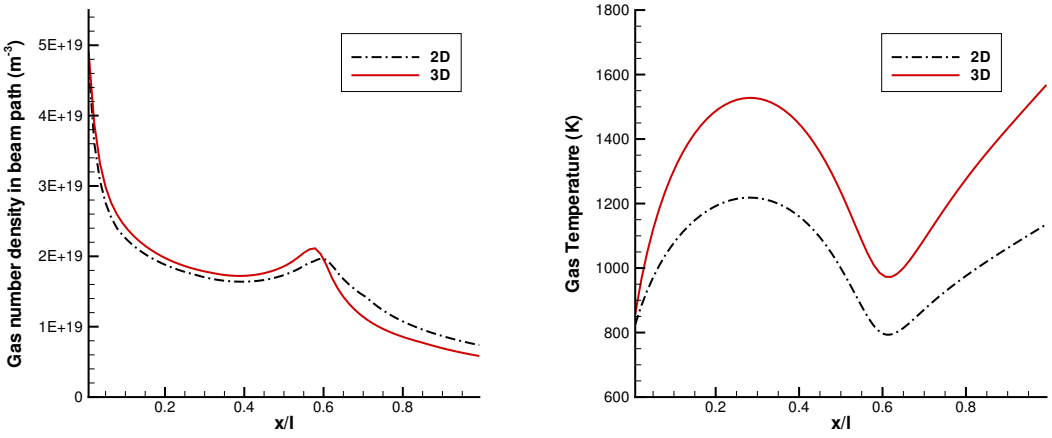

FIGURE 5.54: 2D and 3D JET neutraliser - gas density and temperature profiles at $y = z = 0$

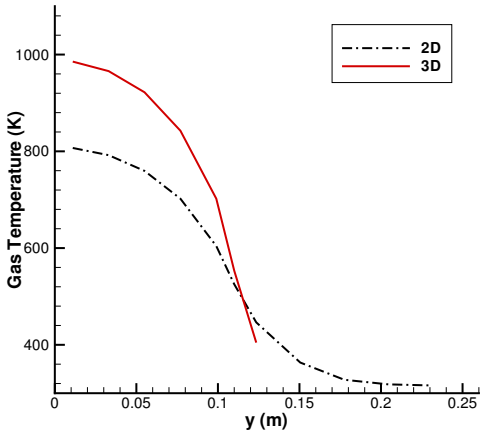

FIGURE 5.55: 2D and 3D JET neutraliser - transverse temperature profiles at $(x, z) = (0.03, 0)$

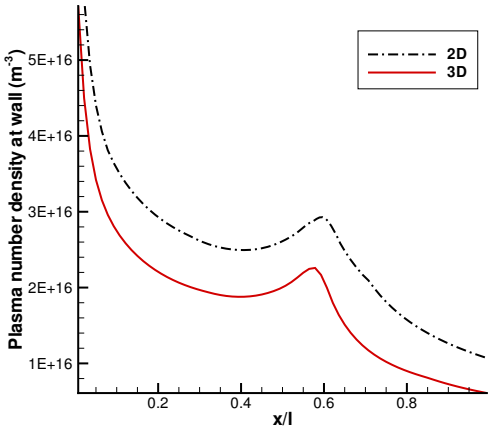

FIGURE 5.56: 2D and 3D JET neutraliser - wall plasma density profiles at $y = z = 0$

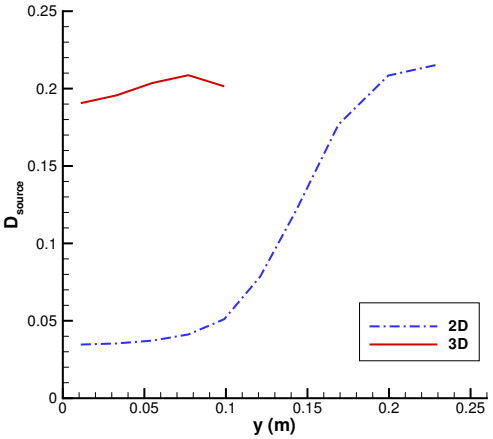

FIGURE 5.57: 2D and 3D JET neutraliser - D_{source} at the midpoint interspace $(x = 0.03m)$

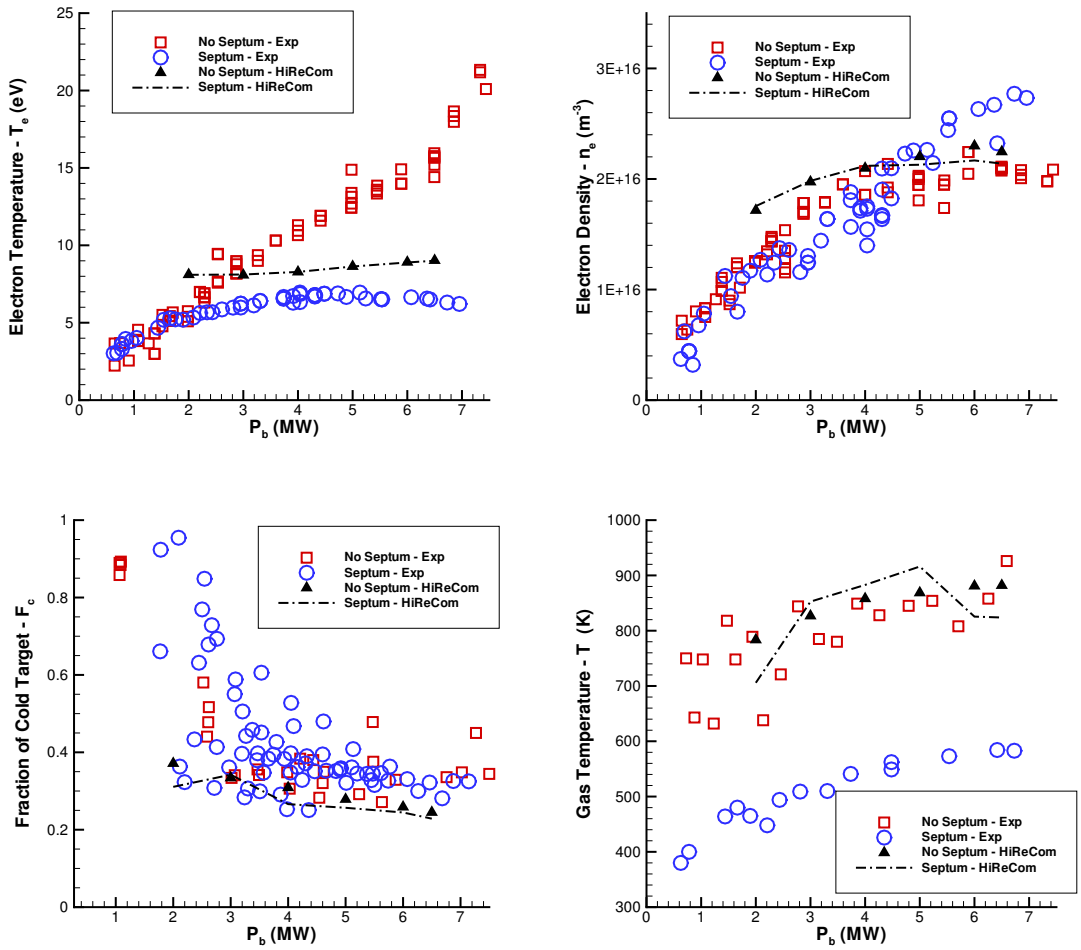

FIGURE 5.58: 3D JET neutraliser with and without Septum - Comparison to experiment

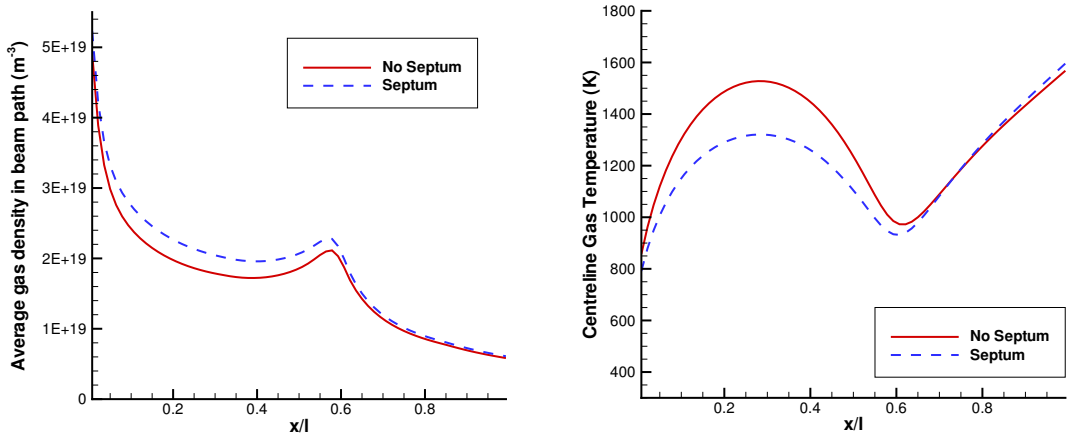

FIGURE 5.59: 3D JET neutraliser with and without Septum - gas density in beam path and centreline temperature (at $y = z = 0$)

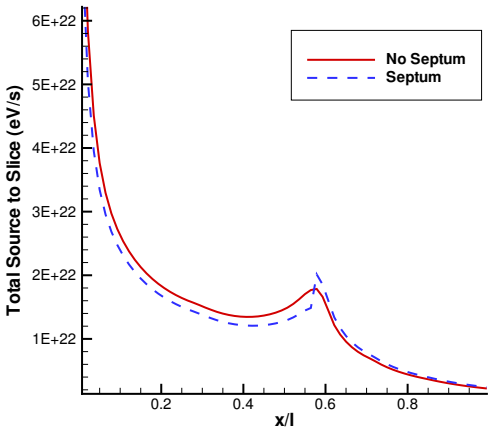

FIGURE 5.60: 3D JET neutraliser with and without Septum - total energy source to slice

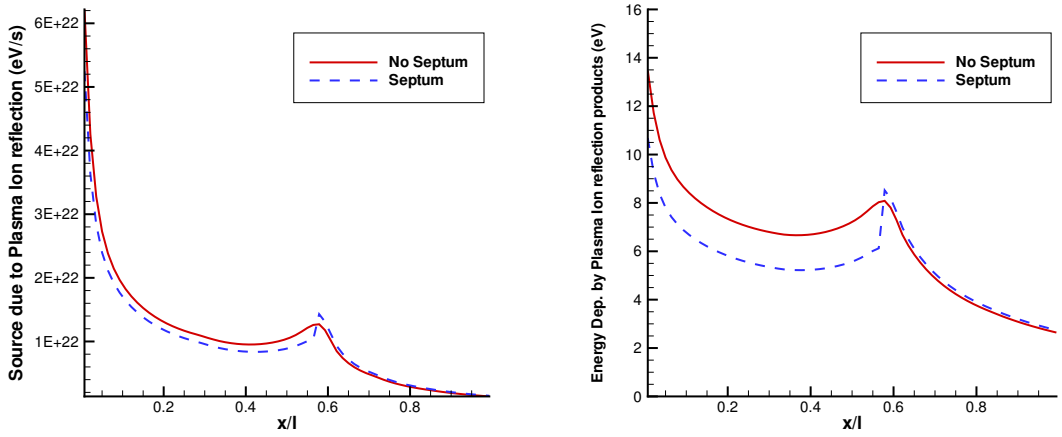

FIGURE 5.61: 3D JET neutraliser with and without Septum - plasma ion reflection energy source to slice and energy deposited per source particle

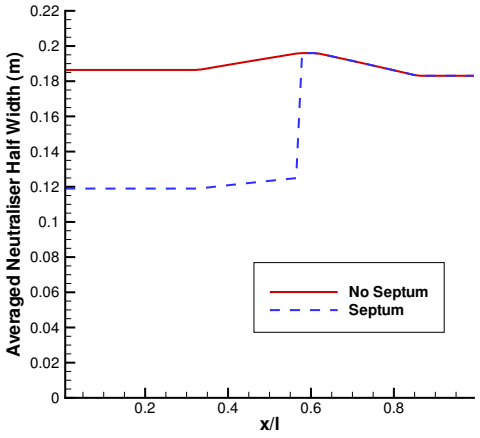

FIGURE 5.62: 3D JET neutraliser with and without Septum - average neutraliser half width $\overline{N_{hw}}$

6

Conclusions and Future Work

This thesis represents the first detailed attempt to apply computational techniques to evaluate neutral gas flow within gas neutraliser systems. These systems represent complex environments within which the incoming ion beam, background plasma and neutral gas all interact. Attempts to model neutral gas flow is further complicated by the continuum-transition gas flow regime typically encountered during operation, wherein typical continuum fluid approaches prove inaccurate.

The research began with the identification of the Burnett equations as the most suitable system with which to simulate neutral gas flow. Extension of the existing in-house HiReCom code to include the higher order metrics, curvilinear transformations, additional viscous flux terms and necessary slip boundary equations, resulted in a continuum-transition solver capable of applying the Navier-Stokes, Conventional Burnett and Augmented Burnett equations. Incremental validation against a series of test cases offered means to further clarify the stability properties of each system of equations via numerical investigation. For the Conventional Burnett equations, the effect of variable reconstruction upon the onset of instability due to excessive grid refinement was sought. For both the Navier-Stokes and Augmented Burnett equations, work sought to assess newly derived novel timestep limits.

The developed gas solver was utilised to provide two and three dimensional simulations of the JET neutraliser. Compared against experimental pressure profile data, both the Augmented Burnett and the Navier-Stokes equations were demonstrated to maintain reasonable levels of accuracy even at high levels of rarefaction approaching the molecular limit and therefore justified their application within this thesis.

Creation of a detailed interaction model for the various neutraliser species facilitated the development of a fully consistent, coupled beam-plasma-gas solver capable of simulating neutral gas dynamics in the presence of beam; steady state analytical models of the beam and plasma for a supplied gas profile allow the formulation of gas mass/energy sources and sinks. Validation was attempted against experimental data for the JET neutraliser in both two and three dimensions. Utilising both historical and additional data generated in support of this thesis, the solver demonstrated good correspondence with experiment.

As well as application to the ITER neutraliser design, the effects of various model and geometry parameters were considered via a series of parameter scans. These additional works also included evaluation of the effects of neutraliser partitioning and an examination of the JET neutraliser design with septum.

6.1 Conclusions

Given the wide arc of the work undertaken, the following are a series of conclusions that are applicable to various themes of the work:

Continuum-Transtion Gas Simulation

- Though provided from simplistic assumptions, the newly developed timestep stability criteria for the Navier-Stokes and Augmented Burnett equations were found to offer good agreement with hypersonic shocks in both one and two dimensions. The criteria serve to bypass the need for an exhaustive CFL search that results from application of the traditional eigenvalue-based timestep limit of explicit schemes when examining rarefied flows.
- The effect of variable reconstruction has been demonstrated to significantly influence the onset of instability observed in the Conventional Burnett equations. Of the schemes examined, first-order interpolation was found to facilitate stable solution of the most refined grids, whilst the fifth-order WENO scheme required significantly coarser grids to provide stability.
- The accuracy of both the Navier-Stokes and Augmented Burnett equations is hampered as the molecular limit $Kn \sim 1$ is approached. The superiority of the latter for higly rarefied flow has been confirmed against experimental pressure profile data, as has the heavy reliance upon the implemented boundary conditions.
- Complete and consistent boundary specification for the Augmented Burnett equations are of great importance, as has been highlighted by problems arising in this thesis from application to unorthodox geometries.

The JET Neutraliser

- The loss of neutralisation efficiency in the presence of beam has been shown to be the result of indirect gas heating effects involving interaction of the various neutraliser constituents.

- The most significant heating mechanism in the JET neutraliser has been identified as due to the acceleration and reflection of plasma ions at the neutraliser wall. Both dissociation by primary electrons and dissociation by positive beam ions were found to be significant additional sources of energy for the background gas, with inelastic collision of stripped electrons providing an increased source term along the neutraliser length.
- The effects of plasma pressure were found to be insignificant due to the low level of ionisation found in the neutraliser.
- In agreement with experiment, the developed model in HiReCom outlined that with increasing beam power, the effects of gas heating were found to be enhanced and result in a further reduction in gas target.
- Inclusion of a midplane septum within the first stage neutraliser was found to significantly increase the gas target provided by the model, both in the absence and presence of beam.

The ITER Neutraliser

- This system has been shown to result in significantly reduced gas heating effects, and a minimal loss in neutralisation efficiency.
- By contrast to the JET system, inelastic collision of the stripped electrons upon the gas molecules is found to be the dominant energy source, followed by the reflected plasma ions. Dissociation presents a near negligible fraction of the total energy source to the gas. This alternative balance of heating contributions is due to two factors: the enhanced stripped electron production of the negative polarity beam; and the reduced plasma production resulting from much reduced beam current.

Gas Neutraliser Optimisation

- The neutraliser gas target in the absence of beam is maximised for a given inlet flow by reduction of the transverse neutraliser dimensions.
- In the presence of beam, the effects of gas heating and loss of neutralisation efficiency may be alleviated via the following:
  - Reduced beam current density, achievable either by reduced current passing through the system or increased beam dimensions
  - Reduced neutraliser transverse dimensions
  - Increased gas flow into the neutraliser (either from the main neutraliser inlet or from a closely coupled source)
  - Increased energy accommodation at the neutraliser walls
  - Inclusion of additional gas inlets

- By contrast, the reduction of wall temperature was found to provide minimal effect upon gas heating. Similarly, symmetric gas introduction was found to offer only a minimal improvement over asymmetric introduction.

- Overall, the strategy of neutraliser partitioning into a series of channels serves to maximise the gas target. These should remain separate for the entire length of the neutraliser, since the use of a midplane septum such as that at JET was found to alleviate only local gas heating effects and do little to combat the loss of neutraliser efficiency further downstream.

6.2 Future Work

The research naturally leads in two directions from this point. The first is to enhance the numerical method of the developed code, whilst the other would seek to utilise additional modelling and experimental endeavour to better inform the existing model.

From the research it is obvious that the existing numerical framework is hampered by the use of explicit timestepping. The Augmented Burnett equations have proved prohibitively expensive in application to refined grids in the presence of beam with only the less accurate and less computationally expensive Navier-Stokes applied in three-dimensional simulations. Implementation of an implicit-explicit timestepping approach would allow much larger timesteps and therefore application to more detailed grids; the stiff viscous terms would be the subject of implicit timestepping whilst the gas mass/energy source and sink terms resulting from the interaction model would be explicitly stepped. Such an approach would represent a significant code enhancement and reduce significantly the computational demands of the existing model.

In light of both the surpressed stable timestep limit and the reduced accuracy of the continuum based methods with increasing rarefaction, it has not been possible to model the most rarefied regions of the neutralisers considered. Therefore, it would be desirable to couple the developed gas solver with a modelling technique more suited to the evaluation of molecular flow in order to allow the inclusion of the outlet regions in future simulations.

This work has sought to utilise the full body of existing gas neutraliser knowledge in order to formulate the resultant coupled beam-plasma-gas solver. However, this effort has been hampered by the remaining gaps in knowledge concerning the dynamics of gas-surface and ion-surface interaction. As outlined in this thesis, these dynamics heavily influence the developed neutraliser model via description of the reflected ion energy source to the gas and the underlying continuum-transition gas model which relies upon slip boundary conditions in order to capture the nonequilibrium effects of rarefied gas near wall surfaces. Unfortunately, in either case there exists little knowledge of the behavior of accommodation effects with varying incident temperature and/or surface properties. Therefore, this represents an area where further modelling or experimental endeavour would significantly enhance understanding of a phenomena applicable to gas neutralisers; this improved understanding could then conceivably be included in an enhanced version of the solver in order to provide a more accurate description of this process.

Similarly, the author notes that the developed interaction model of the various neutraliser

species, which provides the gas mass/energy source and sink terms for the neutral gas, has been the subject of several simplifying assumptions. Given the conclusions concerning the implementation of a septum within the JET system, it would be sensible to review these assumptions in order to ensure the full capture of all the necessary physics within the model. In particular it would be beneficial to extend the beam model to consider the additional ionic species that it contains, in order to correctly evaluate their contribution to the resultant neutral power of the system.

Finally, this research has provided conclusions that point to ways in which neutraliser design might be optimised for the puposes of minimising the effects of gas heating. Comparison of future experimental work upon the JET neutraliser implementing these neutraliser optimisation techniques would serve to further validate the developed solver and demonstrate whether it might form the basis of a predictive neutraliser design tool.